Engineering Materials

Mokhtar Awang
Ehsan Mohammadpour
Ibrahim Dauda Muhammad

Finite Element Modeling of Nanotube Structures

Linear and Non-linear Models

Springer

Engineering Materials

More information about this series at http://www.springer.com/series/4288

Mokhtar Awang · Ehsan Mohammadpour
Ibrahim Dauda Muhammad

Finite Element Modeling of Nanotube Structures

Linear and Non-linear Models

Springer

Mokhtar Awang
Department of Mechanical Engineering
Universiti Teknologi Petronas
Seri Iskandar, Perak
Malaysia

Ibrahim Dauda Muhammad
Department of Mechanical Engineering
University of Abuja
Abuja
Nigeria

Ehsan Mohammadpour
Department of Mechanical Engineering
Universiti Teknologi Petronas
Seri Iskandar, Perak
Malaysia

ISSN 1612-1317 ISSN 1868-1212 (electronic)
Engineering Materials
ISBN 978-3-319-03196-5 ISBN 978-3-319-03197-2 (eBook)
DOI 10.1007/978-3-319-03197-2

Library of Congress Control Number: 2015950438

Springer Cham Heidelberg New York Dordrecht London

Printed on acid-free paper

Springer International Publishing AG Switzerland is part of Springer Science+Business Media (www.springer.com)

To our wives, children and parents

Preface

The purpose of this book is to explain the application of the finite element modeling or analysis (FEM or FEA) with special emphasis on the mechanics of carbon and inorganic nanotubes and related solids, such as nanocomposites. It is intended for those who require modeling and stress analysis of nanotubes using finite element modeling with specific explanations and the book is designed as a textbook or reference material for related graduate engineering courses.

Models of the nanotubes are made using *Nanotube Modeler*© and *Surface Builder* tool of *Material Studio*© package with application of the finite element method demonstrated using *ANSYS*©. Step-by-step instructions for the use of *ANSYS* Parametric Design Language (APDL) in relation to nanotubes are given under different structural and boundary conditions.

This book is not anticipated as an exhaustive reference book on the use of ANSYS, but as a guide for simulation of mechanical properties of nanotubes and nanocomposites that are carbon and inorganic based. Thus, Chaps. 1 and 2 give required information about the atomic structures of nanotubes and how the concept of interatomic potential energy functions are utilized in determining mechanical properties. In other to simplify the procedures to be followed in modeling and meshing of nanotubes, Chaps. 3 and 4 explain the geometrical structure of nanotubes and the options for the elements to be used. An overview of ANSYS is given in Chap. 5 with step-by-step guidelines on how to carry out linear FEA on nanotubes. Chapters 6–10 deal with some specific applications of ANSYS in determining mechanical properties of nanotubes, such as nonlinear analysis, effect of geometrical parameters, effect of defects and multi-walled structures and behaviour of nanocomposites. Most of the simulations presented in this book were made using Version 14.5 of ANSYS; however, many of the examples can be conducted using earlier versions.

During the preparation of this book, necessary attempts were made to cover only essentials of the subject and to provide required tools for understanding of some theoretical background and the skills for using related software. Therefore, apology is offered in advance to all those concerned whose materials are not referenced.

Acknowledgments

We would like to take this opportunity to thank all those who assisted during the preparation and editing of the manuscript, especially Nor Fakhrul M. Noor and Nor Azlinda Azmi. This work would not be possible also without the support from Unversiti Teknologi PETRONAS, Malaysia.

Contents

Chapter 1
Nanotubes

1.1 Introduction

A nanometer is one-billionth of a meter, or relatively one ten-thousandth of the thickness of a human hair. A nanometer-scale tube-like structure is called nanotube. It may represent carbon nanotube (CNT), silicon nanotube, boron nitride nanotube, inorganic nanotube, DNA nanotube and membrane nanotube comprising of tubular membrane connected in the middle of cells. Nanotubes are similar to a powder or black soot. The CNTs, representing others, are in reality rolled-up sheets of graphene that establish hollow threads having walls with one atom thickness [1].

Structurally, nanotubes (NTs) have one dimensional nanostructure with the lateral dimension in nanometer scale. The tube-like configuration is specifically attractive as it makes available access to three separate contact areas: internal and external surfaces together with both ends. Nanotubes can be categorized based on some factors [1–5]: structures having single-walled, double walled and multiple walled as options and composition having carbon NTs and inorganic nanotubes (INTs) as examples.

Both single and multicomponent NTs have been synthesized using various methods [5] with the products have diverse conformations. Nanotubes can be utilized for wide-ranging new and existing applications [6] such as conductive plastics, structural composite materials, flat-panel displays, gas storage, antifouling paint, micro- and nano-electronics, radar-absorbing coating, technical textiles, ultra-capacitors, Atomic Force Microscope (AFM) tips, batteries with improved lifetime, biosensors for harmful gases, extra strong fibers, etc.

Despite the potential impact of NTs in vast areas of nanomaterial and nanotechnology, a deep understanding of their mechanical behavior is missing. This limitation affects the design and optimization of NT-enhanced materials. In this chapter, the recent breakthroughs in mechanical evaluation of NTs are highlighted. Thus emphasis is on the outstanding mechanical properties of CNTs which is essential toward the fabrication of CNT reinforced polymer composite. Moreover,

M. Awang et al., *Finite Element Modeling of Nanotube Structures*,
Engineering Materials, DOI 10.1007/978-3-319-03197-2_1

recent reports on CNT embedded polymer composites are reviewed from both theoretical and experimental aspects, with brief explanation relevant areas on INTs.

1.2 Carbon Nanotubes

It was at mid-1980s that Smalley and Yacobson [7] discovered the fullerenes structures. According to his reports, fullerenes are structures with carbon atoms in geometrical shape of a spherical cage. This cage is composed of hexagonal and pentagonal rings of carbon atoms [12]. Only a few years later, CNTs are introduced by Ijima [8]. CNTs could be defined as a relatively long and thin fullerene structures. Their tubular walls are made of hexagonal carbon cells and could have spherical capes at ends. If these two caps join together, they can form a fullerene [9]. Since 1991, huge attentions have been paid to their atomic structures and their applications in material science, chemistry, physics and engineering. They have been used in a wide range of applications including ultra-strong composite materials, nanofibers, catalysts, and as components of novel electronic and thermal devices [10–16]. CNTs are considered as the revolutionary material that has displayed this combination of superior mechanical, thermal and electronic properties [17]. Their good chemical stability, large surface area, small size, low density, high stiffness, high strength and excellent electronic, optical and thermal properties have demonstrated high potentials in advanced material and nanomechanical devices [12, 16, 18–20].

These exceptional material properties are convinced to be a result of the symmetrical structure of CNTs [12]. From almost the first analogy studies on the CNT's graphite like structure, it was anticipated that they would represent superlative mechanical properties which exceed those of all known materials. It was determined long before, that graphite poses a modulus of about 1 TPa in longitudinal direction [21] and CNTs were conceived to exhibit similar strength.

1.3 Atomic Structure and Morphology of CNTs

Carbon with four valence electrons is known as the sixth element in the periodic table. Having similar energies, these electrons could easily mix their wave functions in order to form hybridized orbits. For example, they can hybridize into sp, sp^2 and sp^3 form which are known as amorphous carbon, graphite and diamond, respectively. Diamond, which is the most famous allotrope of carbon, has four covalent bonds in form of sp^3. These bands connect neighboring carbon atoms into a face-centered cubic atomic structure. Graphite has very different physical properties due to its sp^2 bond type and forms 3 covalent bonds with the neighboring carbons. Diamond and graphite substantially are made from carbon atoms exhibits

completely different properties. While diamond is one of the hardest materials, highly transparent, and has very low electrical conductivity, graphite is black, very soft and a very good conductor [14, 21].

Later on, more interesting classes of carbon have been introduced which are fullerenes, CNTs and graphene. Graphene is a single honeycomb lattice which is packed with hexagonal cells of carbon atoms. To be more concise, it could be assumed as a single layer of graphite. From theoretical point of view, CNT could be seen as a single-wall tubule which is cylindrical in shape with caps at each end. All these materials are made of sp^2 bonds which are interesting and similar to graphite. Figure 1.1a demonstrates graphene as the origin of all graphitic structures [22]. Graphene can be wrapped up to build fullerenes (Fig. 1.1b). It can be rolled into a CNT (Fig. 1.1c) or piled up into graphite form (Fig. 1.1d). These materials have drawn so many researches intention to themselves. For instance, it was pointed out that CNTs and graphene could be an excellent replacement for silicon as a substantial material for electronic devices [11].

The sp^2 hybridized carbon has three valence electrons. Hence, each atom can establish three covalent bonds with its closest neighbors so-called σ bonds. They are

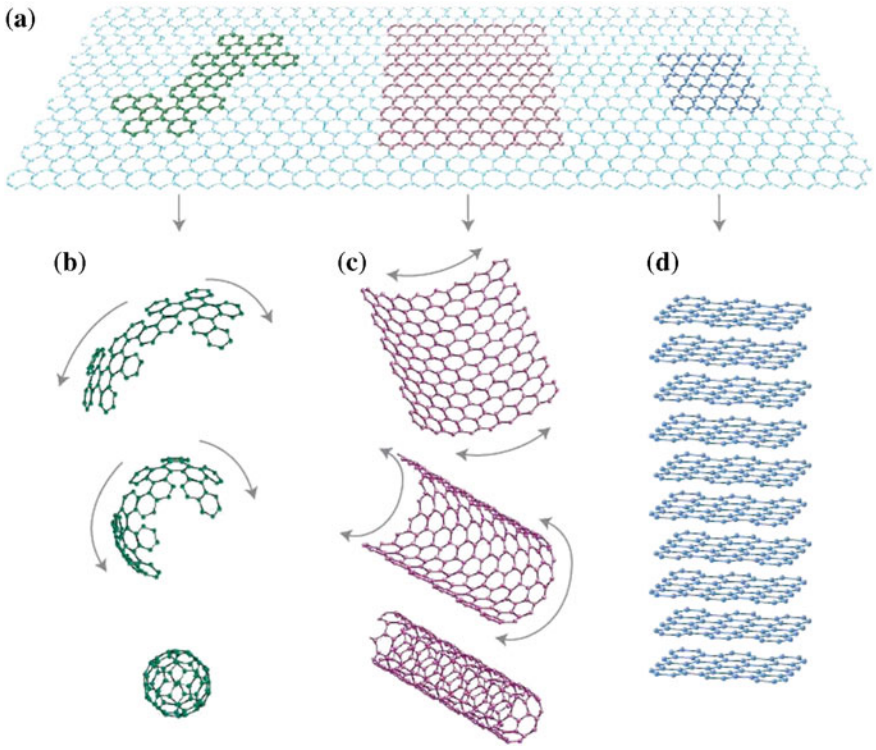

Fig. 1.1 **a** Graphene structure which is the source of other graphitic forms, **b** Fullerenes, **c** CNT and **d** Graphite [22]

just as strong as the sp^3 bonds which put diamonds in the list of the hardest materials. Graphene shows extraordinary mechanical properties and very high thermal conductivity are a consequence of σ bonds presence [23–25].

The fourth electron is in $2p_z$ orbital and can forms a bond perpendicular to the plane. These so-called π bonds are responsible for remarkable properties [23–25]. Figure 1.2 shows the crystal structure of graphene. The lattice vectors in the *x, y* coordinates can be written as in Eq. 1.1.

$$\vec{\mathbf{a}}_1 = \left(\frac{\sqrt{3}a}{2}, \frac{a}{2}a\right), \vec{\mathbf{a}}_2 = \left(\frac{\sqrt{3}a}{2}, -\frac{a}{2}\right) \tag{1.1}$$

The lattice constant, $a = \sqrt{3}a_{C-C} = 2.46$ Å, and $a_{C-C} = 1.42$ Å is the bond length. Figure 1.2 shows that there are theoretically two carbon atoms in each unit cell of graphene lattice and referred as A and B atoms. Each distinct atom forms a sub-lattices, so that graphene can be imagined as A and B sub-lattices (Fig. 1.3).

The diameter, d_t and chiral angle, θ which is the angle between the chiral vectors and lattice vector, a_1, can be derived from the chiral indices:

$$d_t = a\sqrt{n^2 + m^2 + nm} \tag{1.2}$$

$$\cos\theta = \frac{2n + m}{2\sqrt{n^2 + m^2 + nm}} \tag{1.3}$$

In particular, armchair and zigzag CNTs as illustrated in Fig. 1.4 correspond to $\theta = 30^\circ$ and zero, respectively. The chirality could have significant impact on the material properties of the CNT [19]. Although graphite is listed as a semi-metal material, it was shown that CNTs can be metallic, semi-metallic or semi-conducting, depending on tube chirality [26]. The translation vector, **T** as the unit vector of CNTs, also can be expressed on the basis of unit vectors of graphene sheet:

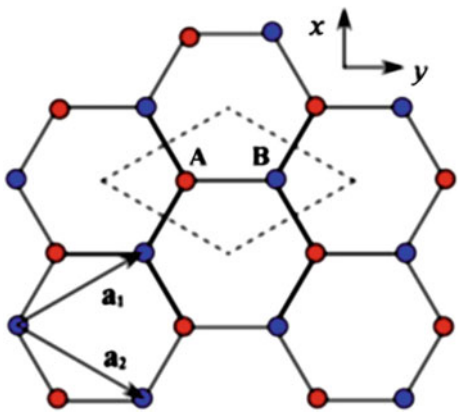

Fig. 1.2 Crystal structure of graphene [23]

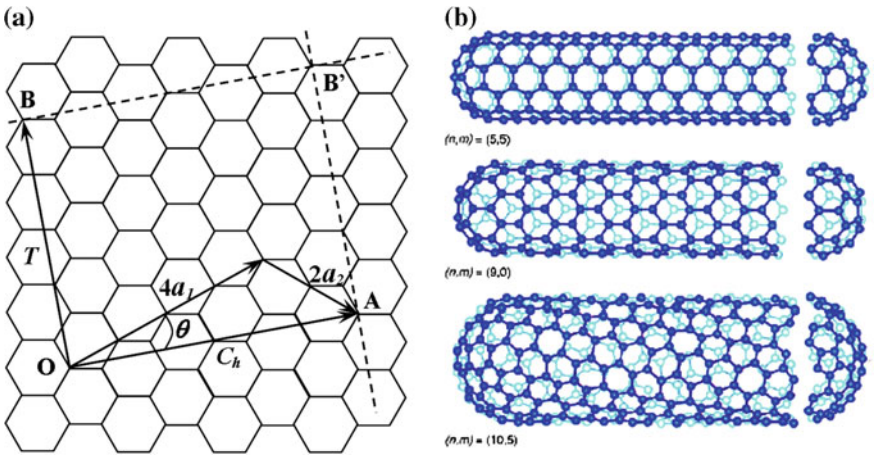

Fig. 1.3 **a** A (4, 2) SWCNT is constructed from graphene sheet. **b** Examples for armchair (5,5), zigzag (90) and chiral (10,5) CNTs [25]

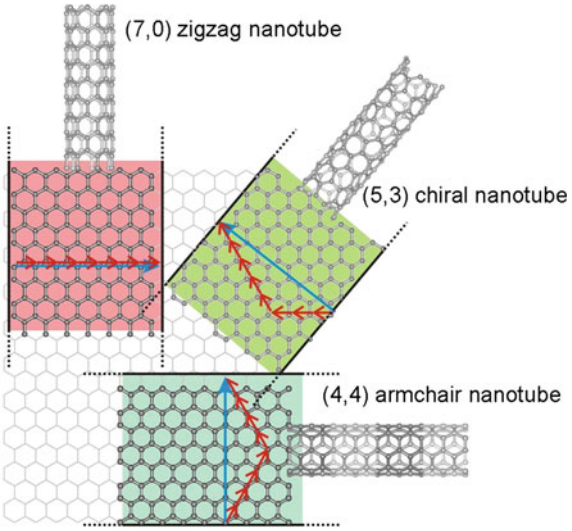

Fig. 1.4 Illustrations of the atomic structure of armchair (4,4), zigzag (7,0) and chiral (5,3) CNTs [27]

$$\mathbf{T} = \frac{2m+n}{d_R}\mathbf{a}_1 + \frac{2n+m}{d_R}\mathbf{a}_2 \tag{1.4}$$

where d_R is the greatest common divisor of $2n + m$ and $2\ m + n$ terms.

To construct a seamless cylindrical single walled carbon nanotube (SWCNT), graphene sheet can be easily roll up and coincide the points equivalently as shown

in Fig. 1.4. SWCNT diameter is usually about 0.7–10 nm and can reach centimeter in length. Hence, they are referred as one-dimensional structure. Graphene layers can stack up to bilayer, trilayer to multilayer structures and construct multi walled carbon nanotube (MWCNT). MWCNT consist of several SWCNT cylinders which are arranged concentrically and separated by 0.35 nm as shown in Fig. 1.5. There is a similar separation space in the basal plane of graphite. MWCNTs have diameters from 2 to 100 nm and lengths of tens of microns [8]. These concentric CNTs are bonded to each other through van der Waals forces. Figure 1.5a illustrates a high resolution transmission electron microscope (HRTEM) image which shows a MWCNT. Several layers of graphitic carbon and a hollow core are evident. There is a 0.34 nm separation between parallel layers.

Since the interactions between concentric layers in MWCNTs further complicate the properties of CNTs, SWCNTs are most used to determine structure-property relationships of CNTs. Indeed, both SWCNTs and MWCNTs exhibit unique properties that can be successfully employed in composite fabrication. Figure 1.5b shows a 3-layered MWCNT and its tip structure. Again, the layer separation is measured as 0.34 nm. Figures 1.5c belongs to a multi-layered CNT and enlarged the tip structure of its conical end. In Fig. 1.5d a detached SWCNT with diameter of 1.2 nm is shown. Tube bundles covered with amorphous carbon are also evident. Finally, a geometric change due to the presence of five and seven membered rings is

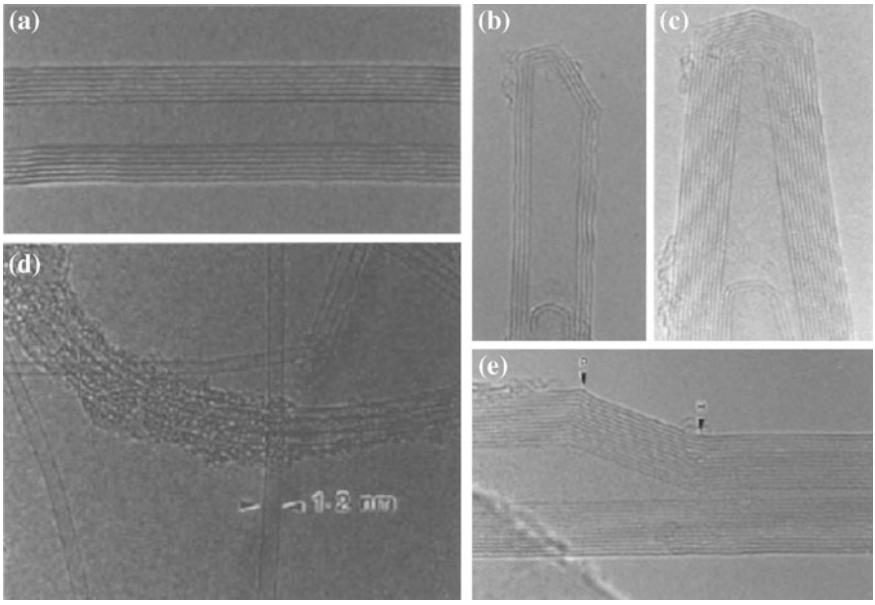

Fig. 1.5 HRTEM images of: **a** an individual MWCNT, **b** The tip structure of a conical end, **c** the tip structure of a closed MWCNT, **d** isolated SWCNT and tubes bundles covered with amorphous carbon and **e** geometric changes caused by five and seven membered defects [28]

Table 1.1 Types of inorganic nanotubes [29]

Type of INTs	Examples
Chalcogenides	HfS_2, MoS_2, $MoSe_2$, NbS_2, $NbSe_2$, TiS_2, $TiSe_2$, WS_2, WSe_2, ZrS_2
Oxides	$BaTiO_3$, Ga_2O_3, $PbTiO_3$, SiO_2,TiO_2, VO_x, ZnO, ZrO_2
Nitrides	BN, GaN
Halides	$NiCl_2$
Metals	Bi, Co, Cu, Fe, Ni, Te

shown in Fig. 1.5e. Defects are noted by *P* for pentagon and *H* for heptagon on the MWCNT outmost layer.

1.4 Inorganic Nanotubes

An inorganic nanotube is a molecule having cylindrical structure composed of material(s) other than carbon and morphologically similar to a carbon nanotube. Inorganic nanotubes (INTs) occur naturally and have also been synthesized [1]. Some minerals such as white asbestos (or chrysotile) and imogolite were discovered to have tubular configuration [4, 5]. The pioneer synthesis of INTs occurred in 1992 when nanotubes made from tungsten disulfide (WS_2) were produced [12]. Several inorganic nanotubes (INTs) has been produced and characterized in the last few years [29], as summarized in Table 1.1.

The atomic structures of some INTs are illustrated in Figs. 1.6 and 1.7.

INTs are regarded as alternative material to better-explored carbon nanotubes, displaying benefits such as simple synthetic approach and extraordinary crystallinity, suitable consistency and distribution, needle-like morphology, effective connection to several polymers and superior impact-resistance. Thus, they are favorable options as fillers for polymer composites with enhanced mechanical, electrical and thermal properties. Specific uses for this type of composites are materials for photovoltaic elements, heat management, electrostatic dissipators, wear protection materials, etc. INTs are heavier than CNTs and not as strong under tensile stress, but they are particularly strong under compression, leading to potential applications in impact-resistant applications such as bulletproof vests [1–6, 29–32] (Fig. 1.8).

1.5 Mechanical Properties of Nanotubes

Since two decades ago, there was a steady progress in the field of CNT characterization and exploring their mechanical properties. It is reported that specific tensile strength of a CNT can be 100 times higher than that of steel. These kind of

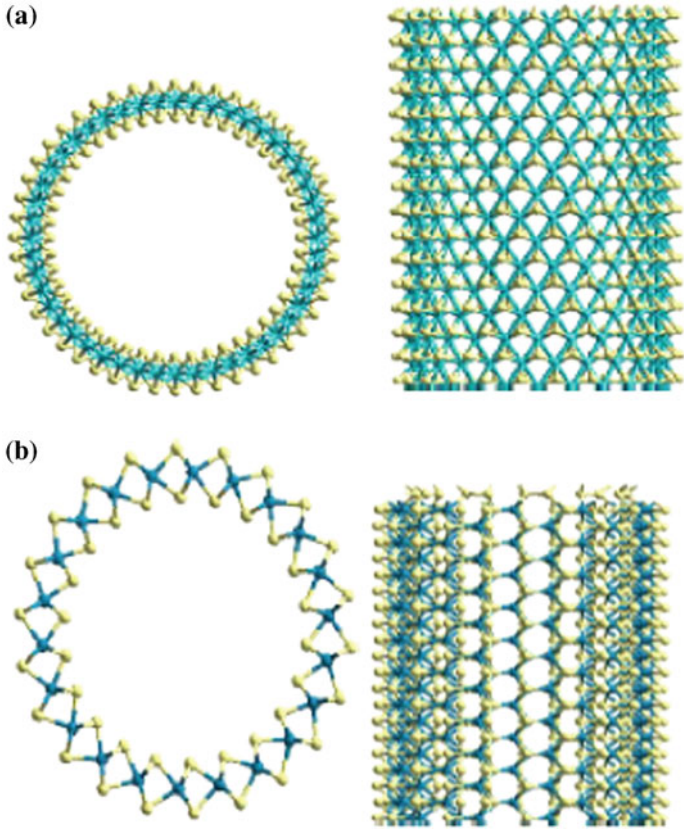

Fig. 1.6 Nanotubes for transition-metal disulfides of TMS_2 type (TM = Mo, W) with **a** being zigzag and **b** armchair types [30]

astonishing mechanical properties ignited further interest to employ CNTs in lightweight and high strength materials [9]. Elastic properties of MWCNTs and SWCNTs have been investigated extensively through experimental work. Theoretical investigations, on the other hand, reported a wide range of elastic property predictions. While the predicted Young's modulus of SWCNT alter in an wide interval of 0.5–5.5 TPa, experimentally determined Young's modulus scatter between 2.8 and 3.6 TPa [10].

In the experimental part, researchers investigated the elastic modulus of isolated MWCNTs by measuring the amplitude of their intrinsic thermal vibration via transmission electron microscopy-TEM [11] or directly measure the properties such as stiffness and strength for individually isolated MWCNTs using atomic force microscopy-AFM [12–14]. Table 1.2 briefly describes particular efforts in this area. Figure 1.9a shows a scanning electron microscope (SEM) image of a MWCNT which was attached to the oppositely aligned tips of an AFM. They used electron

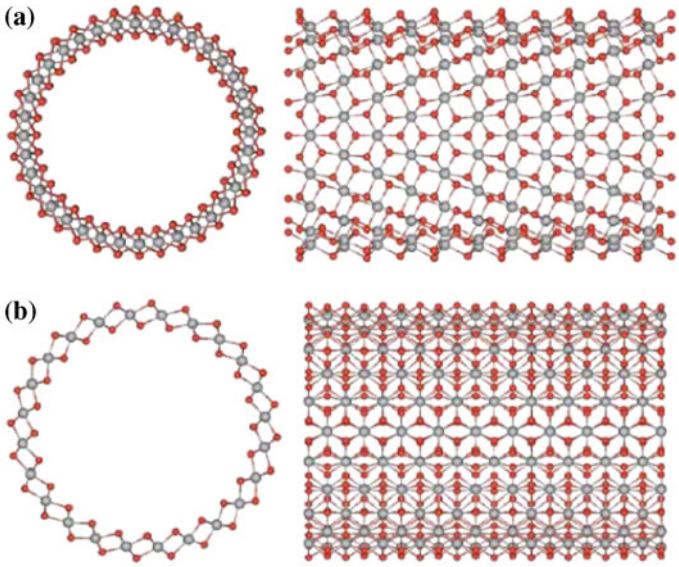

Fig. 1.7 Single-walled TiO_2 nanotubes for (18,0) in **a** and (12,12) in **b** having different configuration but similar diameter [31]

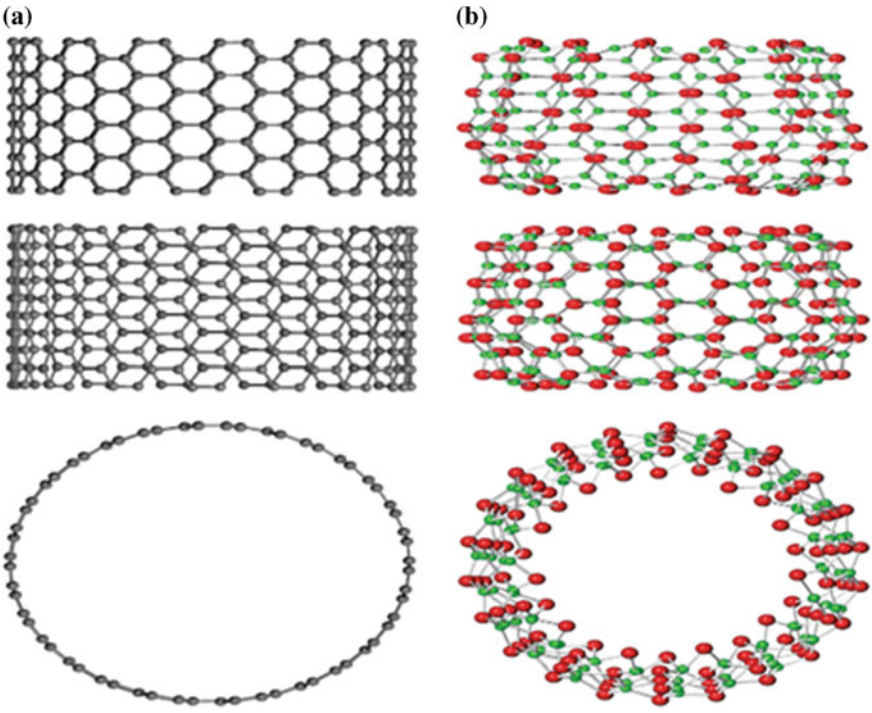

Fig. 1.8 Front, side, and top views for **a** 15 × 15 CNT and **b** 11 × 11 ZrO_2 NT [31]

Table 1.2 Experimental studies of mechanical properties of CNTs

Authors	Elastic modulus	Strength
Treacy et al. [12]	1.8 TPa	n/a
Wong et al. [13]	1.26 TPa	n/a
Salvetat et al. [14]	1 TPa	n/a
Walters et al. [15]	1.25 TPa	–
Yu et al. [16]	270–950 GPa for MWCNTs	11–63 GPa
	320–1470 GPa for SWCNTs	13–52 GPa
Xie et al. [17]	450 GPa	4 GPa

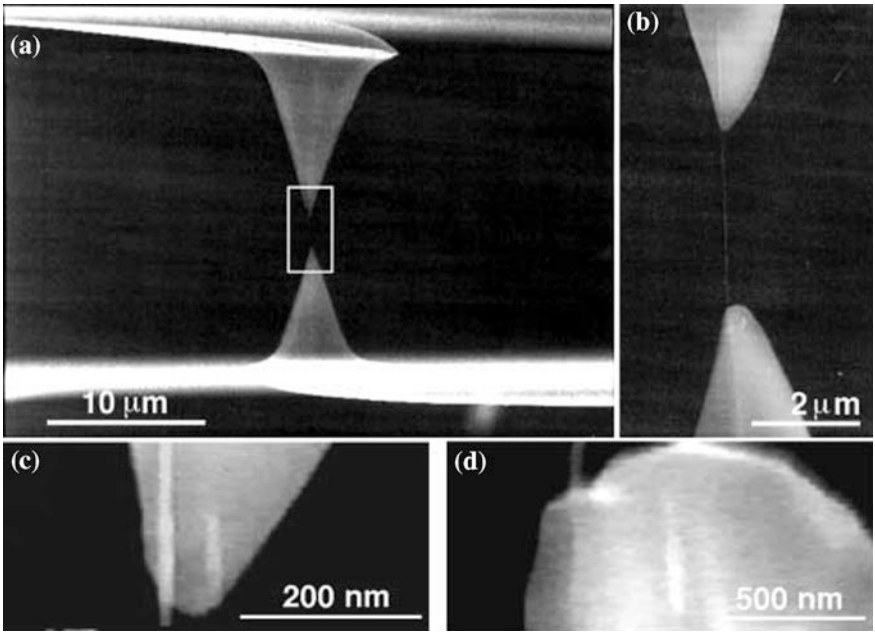

Fig. 1.9 SEM images of: **a** MWCNT is held by two oppositely aligned AFM tips, **b–d** the AFM tips in pointed rectangle and the welding of the MWCNT to the AFM tip

beam deposition to paste the MWCNT on the AFM silicon tip surface. The lower AFM tip in the image is placed on a soft cantilever beam whose deflection was used to measure the applied force on the MWCNT. Figure 1.9b–d are large magnification SEM image of the mentioned region in Fig. 1.9a and the welding of the MWCNT to the AFM tip [16], respectively.

Table 1.3 Young's modulus of various INTs measured using different methods [33–38]

Types of nanotube	Method	Young's modulus
TiO_2	Compression test in AFM–TEM	23–44 GPa
TiO_2	Nano indentation	36–43 GPa
TiO_2	Nano indentation	4–30 GPa
ZrO_2	Micro nano-indentation	30–62 GPa
WS_2	Tensile test in SEM	150–17 GPa
MoS_2	Tensile and bending tests in SEM	170–250 GPa
BN	Thermal vibration in TEM	1.22 ± 0.24 TPa
BN	Direct measurement using TEM	0.5–0.6 TPa
BN	Electric field induced-resonance in TEM	850 GPa

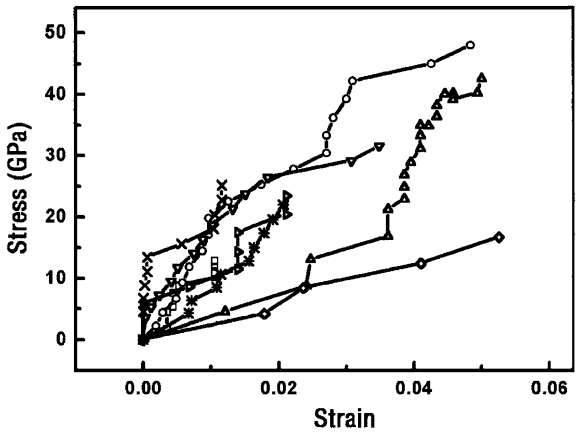

Fig. 1.10 Experimentally determined stress-strain curves from tensile loading of isolated SWCNT ropes [18]

Yu et al. [18] determined the mechanical behavior of several SWCNT ropes under tensile load. Their results showed that 8 of these ropes broke at strains below 5.3 % as depicted in Fig. 1.9. The stress-strain data were further fit by a model that assumed the tensile load was supported by the perimeter surface of the SWCNTs ropes. This model provided mean fracture strength of 30 GPa for SWCNTs on the perimeter region. The virtual values can be seen in the Fig. 2.7 in range of 13–52 GPa. Average Young's modulus values was also calculated in range of 320–1470 GPa, based on the same model.

Variations in the values of measured Young's modulus for INTs as shown in Table 1.3 are similar to what was obtained for CNT (Table 1.2). It should be noted that INTs have large size in comparison to CNTs, thus they have less strength and other mechanical properties [33] (Fig. 1.10).

References

1. P.J.F. Harris, *Carbon Nanotubes and Related Structures*, 1st edn. (Cambridge University Press, Cambridge, 2001)
2. C. Yan, J. Liu, F. Liu, J. Wu, K. Gao, D. Xue, Tube formation in nanoscale materials. Nanoscale Res. Lett. **3**(12), 473–480 (2008)
3. S.V. Kuchibhatla, A.S. Karakoti, D. Bera, S. Seal, One dimensional nanostructured materials. Prog. Mater Sci. **52**(5), 699–913 (2007)
4. P. Yang (ed.), *The Chemistry of Nanostructured Materials, v*ol. 2 (World Scientific, Singapore, 2011)
5. C.C. Koch, *Nanostructured Materials: Processing, Properties and Applications* (William Andrew, Norwich, 2006)
6. R.R.H. Coombs and D.W. Robinsons (eds.), *Nanotechnology in Medicine and Biosciences* (Gordon and Breach, New York, 1996)
7. R.E. Smalley, B.I. Yakobson, The future of the fullerenes. Solid State Commun. **107**, 597–606 (1998)
8. S. Iijima, Helical microtubules of graphite carbon. Nature **354**, 56–58 (1991)
9. Z. Spitalsky, D. Tasis, K. Papagelis, C. Galiotis, Carbon nanotube–polymer composites: Chemistry, processing, mechanical and electrical properties. Prog. Polym. Sci. **35**, 357–401 (2010)
10. E.T. Thostenson, T.-W. Chou, Aligned multi-walled carbon nanotube-reinforced composites: processing and mechanical characterization. J. Phys. D Appl. Phys. **35**, 77–80 (2002)
11. M.M.J. Treacy, T.W. Ebbesen, J.M. Gibson, Exceptionally high Young's modulus observed for individual carbon nanotubes. Nature **381**, 678–680 (1996)
12. E.W. Wong, P.E. Sheehan, C.M. Lieber, Nanobeam mechanics: elasticity, strength, and toughness of nanorods and nanotubes. Science **277**, 1971–1975 (1997)
13. J.-P.B. Salvetat, G.A.D. Briggs, J.-M. Bonard, R.R. Bacsa, A.J. Kulik, T. Stöckli, N.A. Burnham, L. Forró, Elastic and shear moduli of single-walled carbon nanotube ropes. Phys. Rev. Lett. **82**, 944–947 (1999)
14. D.A. Walters, L.M. Ericson, M.J. Casavant, J. Liu, D.T. Colbert, K.A. Smith et al., Elastic strain of freely suspended single-wall carbon nanotube ropes. Appl. Phys. Lett. **74**, 3803–3805 (1999)
15. B.I. Yakobson, P. Avouris, Mechanical properties of carbon nanotubes. Topics Appl. Phys **80**, 287–327 (2001)
16. M.-F. Yu, O. Lourie, M. J. Dyer, K. Moloni, T. F. Kelly, and R. S. Ruoff, Strength and breaking mechanism of multiwalled carbon nanotubes under tensile load. Science **287**, 637–640 (2000)
17. W. Li, S. Xie, Z. Pan, B. Chang, L. Sun, Mechanical and physical properties on carbon nanotube. J. Phys. Chem. Solids **61**, 1153-1158 (2000)
18. M.-F. Yu, B.S. Files, S. Arepalli, R.S. Ruoff, Tensile loading of ropes of single wall carbon nanotubes and their mechanical properties. Phys. Rev. Lett. **84**, 5552–5555 (2000)
19. E.T. Thostensona, Z. Renb, T.-W. Choua, Advances in the science and technology of carbon nanotubes and their composites a review. Compos. Sci. Technol. **61**, 1899–1912 (2001)
20. M.S. Dresselhaus, G. Dresselhaus, R. Saito, Physics of carbon nanotubes. Carbon **33**, 883–891 (1995)
21. J. Vera-Agullo, A. Glória-Pereira, H. Varela-Rizo, J.L. Gonzalez, I. Martin-Gullon, Comparative study of the dispersion and functional properties of multiwall carbon nanotubes and helical-ribbon carbon nanofibers in polyester nanocomposites. Compos. Sci. Technol. **69**, 1521–1532 (2009)
22. I. Janowska, S. Hajiesmaili, D. Bégin, V. Keller, N. Keller, M.-J. Ledoux et al., Macronized aligned carbon nanotubes for use as catalyst support and ceramic nanoporous membrane template. Catal. Today **145**, 76–84 (2009)
23. A.K. Geim, K.S. Novoselov, The rise of graphene. Nat. Mater. **6**, 183–191 (2007)

24. R. Sengupta, M. Bhattacharya, S. Bandyopadhyay, A.K. Bhowmick, A review on the mechanical and electrical properties of graphite and modified graphite reinforced polymer composites. Prog. Polym. Sci. **36**, 638–670 (2011)
25. D. Qian, G.J. Wagner, W.K. Liu, M.-F. Yu, R.S. Ruoff, Mechanics of carbon nanotubes. Appl. Mech. Rev. **55**, 495–533 (2002)
26. J. Coleman, U. Khan, W. Blau, Y. Gunko, Small but strong: a review of the mechanical properties of carbon nanotube–polymer composites. Carbon **44**, 1624–1652 (2006)
27. S. Wijewardane, Potential applicability of CNT and CNT/composites to implement ASEC concept: a review article. Sol. Energy **83**, 1379–1389 (2009)
28. P.M. Ajayan, T.W. Ebbesen, Nanometre-size tubes of carbon. Rep. Prog. Phys. **60**, 1025–1062 (1997)
29. R. Tenne, C.N.R. Rao, Inorganic nanotubes. Philos. Trans. R. Soc. A: Math. Phys. Eng. Sci. **362**(1823), 2099–2125 (2004)
30. N. Zibouche, A. Kuc, T. Heine, From layers to nanotubes: transition metal disulfides TMS 2. Eur. Phys. J. B: Condens. Matter. Complex Syst. **85**, 1–7 (2012)
31. I.D. Muhammad, M. Awang, O. Mamat and K.Z.K Shaari, Estimating young's modulus of single-walled zirconia nanotubes using nonlinear finite element modeling. J. Nanomater. (2015)
32. L. A. Girifalco, M. Hodak, and R. S. Lee, Carbon nanotubes, buckyballs, ropes, and a universal graphitic potential. Phys. Rev. B **62** (2000)
33. J. Eichler, U. Eisele, J. Rodel, Mechanical properties of monoclinic zirconia. J. Am. Ceram. Soc. **87**(7), 1401–1403 (2004)
34. E.W. Wong, P.E. Sheehan, C.M. Lieber, Nanobeam mechanics: elasticity, strength and toughness of nanorods and nanotubes. Science **277**, 1997 (1971)
35. T. Shokuhfar, G.K. Arumugam, P.A. Heiden, R.S. Yassar, C. Friedrich, Direct compressive measurements of individual titanium dioxide nanotubes. ACS Nano **3**(10), 3098–3102 (2009)
36. K. Ashiri, R. Tenne, Mechanical properties of WS_2 nanotubes. J. Cluster Sci. **18**(3), 549–563 (2007)
37. S. Bertolazzi, J. Brivio, A. Kis, Stretching and breaking of ultrathin MoS_2. ACS Nano **5**(12), 9703–9709 (2011)
38. A.P. Suryavanshi, M.F. Yu, J. Wen, C. Tang, Y. Bando, Elastic modulus and resonance behavior of boron nitride nanotubes. Appl. Phys. Lett. **84**(14), 2527–2529 (2004)

Chapter 2
Interatomic Bonding

In computational nanoscale science, we deal with many body nanostructures of all types composed of N atoms or molecules. The value of N can range from several hundred to several billions. To handle the energetics of these structures computationally, the most efficient way is to express the total interaction energies in these systems in terms of interatomic potentials that are functions of the atomic coordinates. The reason is that, even with the high-performing computing platforms and sophisticated simulation techniques available today, the existing quantum mechanical-based, or ab initio, strategies can handle nanoscale systems composed of, at most, a few hundred atoms. Interatomic potential energy functions will, therefore, be indispensable in modeling and simulation studies for a long time to come.

2.1 Potential Energy Function (PEF)

The total potential energy function, H_{I} of an N-body nanostructure, refers to the configurational potential energy that can be expressed in terms of the position coordinates r of its constituent atoms. The simplest way is to express this energy as a cluster expansion involving two, three-body etc. The total potential energy functions H_I is as follow,

$$H_I = \frac{1}{2!}\sum_i \sum_{j\neq i} V_2(\mathbf{r}_i, \mathbf{r}_j) + \frac{1}{3!}\sum_i \sum_{j\neq i} \sum_{k\neq i,j} V_3(\mathbf{r}_i, \mathbf{r}_j, \mathbf{r}_k) + \ldots \tag{2.1}$$

where Vn are n-body interatomic potential functions. In (Eq. 2.1), V_2 is the pair-wise potential between atoms i and j, and V_3 is the three-body potential involving atoms i, j and k.

Potential energy functions that are constructed should satisfy a set of criteria so that they are effective in computational modeling applications. Brenner [1] has succinctly summarized the critical properties that a potential energy function must possess. The properties are as follows:

M. Awang et al., *Finite Element Modeling of Nanotube Structures*,
Engineering Materials, DOI 10.1007/978-3-319-03197-2_2

(1) Flexibility. A PEF must be sufficiently flexible that it accommodates as wide a range as possible of fitting data. For solid systems, the data might include crystalline lattice constants, cohesive energies, elastic properties, vacancy formation energies and surface energies.
(2) Accuracy. A PEF should be able accurately to reproduce an appropriate fitting database.
(3) Transferability. A PEF should be able to describe, at least qualitatively, if not with quantitative accuracy, structures that were not included in the fitting database.
(4) Computational efficiency. Evaluation of the PEF should be relatively efficient, vis-à-vis such quantities as the system size and time-scale of interest, as well as the available computing resources.

In this chapter, we present a rather thorough description of most of the state-of-the-art PEFs that have been developed and used in the computational modeling of the mechanical, thermal, structural, transport and storage properties of carbon nanotubes. These potentials have been extensively used in many simulation studies. In the early molecular mechanics studies in both inorganic and organic chemistry the strain energy, U_{total} is defined as arising from four principle energy terms (Eq. 2.2),

$$U_{\text{total}} = \sum_{\text{molecule}} (E_b + E_\theta + E_\phi + E_{nb}) \tag{2.2}$$

where $\sum E_b$ is the total bond deformation energy, $\sum E_\theta$ the total valence angle deformation energy, $\sum E_\phi$ the total torsional (or dihedral) angle deformation energy and $\sum E_{nb}$ the total nonbonded (van der Waals) interaction energy. The individual energy terms are calculated using simple functions. Bonds are modeled as elements that obey Hooke's law (Eq. 2.3),

$$E_b = \frac{1}{2} k_b (r_{ij} - r_0)^2 \tag{2.3}$$

Where k_b is the force constant or spring 'strength' and r_0 is the ideal bond length or the preferred spring's length. Valence angles are modeled in a very similar way (Eq. 2.4),

$$E_\theta = \frac{1}{2} k_\theta (\theta_{ij} - \theta_0)^2 \tag{2.4}$$

where k_θ is the strength of the 'spring' holding the angle at its ideal value of θ_0.

Torsion or dihedral angles cannot be modeled in the same manner since a periodic function is required (Eq. 2.5),

$$E_{\phi} = \frac{1}{2} k_{\phi}(1 + \cos(m(\phi_{ijkl} + \phi_{\text{offset}}))) \tag{2.5}$$

where k_{ϕ} is the height of the barrier to rotation about the torsion angle $\phi_{ijkl,}$ m is the periodicity and ϕ_{offset} is the offset of the minimum energy from a staggered arrangement. Nonbonded interactions are calculated using a function that includes a repulsive and an attractive (London dispersion) component (Eq. 2.6),

$$E_{\text{nb}} = Ae^{-Bd_{ij}} - Cd_{ij}^{-6} \tag{2.6}$$

where d_{ij} is the distance between the two nuclei and A, B and C are atom based constants discussed later in this book.

More recently a number of additional components have been added to the calculation of the strain energy. Out-of-plane deformation terms E_{δ} have been included in models of aromatic or sp^2 hybridized systems (Eq. 2.7),

$$E_{\delta} = \frac{1}{2} k_{\delta} \delta^2 \tag{2.7}$$

where δ is the angle between the plane defined by three atoms and the vector from the center of these atoms to a fourth bonded atom, and k_{δ} is the corresponding force constant. Modeling the interaction of metal complexes with biological systems has necessitated the inclusion of electrostatic and hydrogen bonding interaction terms. The electrostatic interactions are modeled based on the Coulomb's law (Eq. 2.7),

$$E_{\varepsilon} = \frac{q_i q_j}{\varepsilon d_{ij}} \tag{2.8}$$

where q_i and q_j are the partial charges on atoms i and j, ε is the dielectric constant and d_{ij} is the interatomic separation. Hydrogen bonding, E_{hb} interactions are generally modeled using a function of the type given in (Eq. 2.9),

$$E_{\text{hb}} = Fd_{ij}^{-12} - Gd_{ij}^{-10} \tag{2.9}$$

where F and G are empirically derived constants that reproduce the energy of a hydrogen bond and $d_{jj,}$ is the donor-acceptor distance. The addition of these terms give rise to the revised definition of U_{total} given in (Eq. 2.10),

$$U_{\text{total}} = \sum_{\text{molecule}} (E_b + E_{\theta} + E_{\phi} + E_{nb} + E_{\delta} + E_{\varepsilon} + E_{\text{hb}}) \tag{2.10}$$

The set of functions together with the collection of terms that parameterize them (k_b, r_0, etc.) is referred to the force field. In some cases force field parameters can be related to experimentally determinable values. For example, the bond stretching force constant k_b is approximately equivalent to the vibrational force constant

derived from an infrared spectrum. However, in general the force field terms are derived empirically with the target of reproducing experimental structures and energy distributions.

Once a model and a force field have been chosen for a particular problem, the goal of molecular mechanics is to find the geometry with the minimum strain energy. This can be achieved by a variety of mathematical techniques described elsewhere in this book. The value of the strain energy is dependent on the force field and therefore has little meaning in absolute terms. However, because isomers have the same bond, bond angle and torsional angle types, strain energies of isomers can be compared to each other and differences correlated with experimentally determined isomer populations.

This has formed the justification of many molecular mechanics studies. In recent studies of more complex systems the primary goal has been to produce reasonable models that allow the investigator to visualize the interactions of metal ions with large molecules. Also, methods where molecular mechanics is used in combination with experimental data to determine molecular structures, for example in solution, are receiving increasing attention.

2.2 Harmonic Functions for Carbon Nanotubes

It has been proved through chemical calculations that harmonic functions provide a reasonable approximation to the potential energy of molecular systems in which the bond length is near its equilibrium position [2]. In this particular formula, the energy terms associated to bond stretching (Eq. 2.11), angle bending (Eq. 2.12) and inversion (Eq. 2.13) are described as [3, 4],

$$\mathrm{U}_b = \frac{1}{2}\sum_i K_i(r - r_0)^2 \tag{2.11}$$

$$\mathrm{U}_\theta = \frac{1}{2}\sum_j C_j(\theta - \theta_0)^2 \tag{2.12}$$

$$\mathrm{U}_\phi = \frac{1}{2}\sum_k B_k(\varphi - \varphi_0)^2 \tag{2.13}$$

where $r - r_0$, $\theta - \theta_0$, $\varphi - \varphi_0$ are the elongation of bond i, variance of bond angle j and inversion angle k, respectively. K_i, C_j and B_k are force constants associated with bond stretching, angle variance and inversion, respectively. Formulation was done by using schematic diagrams as shown in Fig. 2.1.

In such cases, elastic Young's modulus E_n of armchair (n, n) and zigzag (n, 0) CNTs could be expressed as the following,

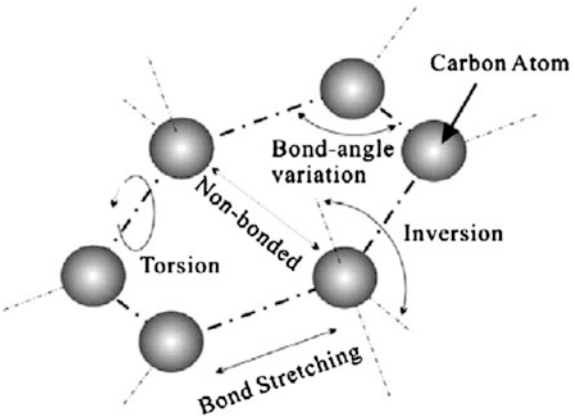

Fig. 2.1 Schematic illustration of atoms and bonds in CNT

$$E_n = \frac{4\sqrt{3}K}{3\lambda K a^2/C + 9},\ \lambda = \frac{7 - \cos(\pi/n)}{34 + 2\cos(\pi/n)} \tag{2.14}$$

where K, C and a are axial stiffness of the carbon–carbon covalent bond (C–C) (742 nN/nm), bending stiffness resulting from the angular distortion of bond angle (1.42 nN/nm) and bond length, respectively [4].

2.3 Morse Potential Functions for CNTs

It is crucial to note that linear functions are only applicable to characterize material properties under relatively small strain conditions. Obviously, a harmonic function is a good approximation of the bond stretching function near the energy minimum as shown in Fig. 2.2 [3, 5]. However, a more complex function must be used to describe the behavior of a chemical bond far from its equilibrium position such as Morse potential which was used to describe the behavior from equilibrium to bond dissociation [3]. Among presented models, Morse potential function was selected in this study mostly due to its simplicity over many-body potentials such as Brenner function and its compatibility with the finite element method [5–8]. For a SWCNT subjected to axial loadings at large strains, with the proper set of constants, it is possible to simulate all potentials including torsion, inversion, van der Waals and electrostatic interactions [3]. To make the simulation as simple as possible in agreement with [9], those potentials with minor effects were neglected.

After neglecting non effective force fields, the bond total energy could be expressed by the interatomic functions defined by Morse potential. A modified Morse potential function has been established for CNT [6].

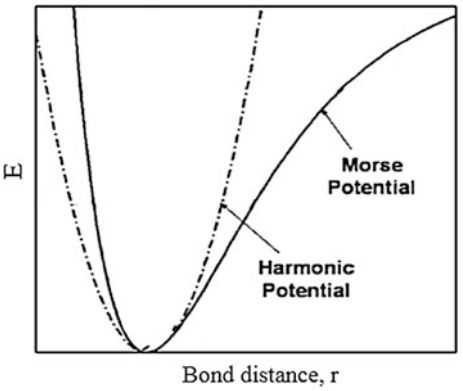

Fig. 2.2 The schematic of the Morse and the harmonic potentials [10]

The main improvement was that a bond angle bending potential was added in Morse potential. This modification has been mainly done to facilitate theoretical studies of CNT fracture. It can be written as

$$U = U_{\text{stretch}} + U_{\text{angle}} \tag{2.15}$$

where $U_{stretch}$ and U_{angle} are the bond energy due to bond stretching and bond energy due to bond angle bending. These potentials are shown in Fig. 2.3. In which,

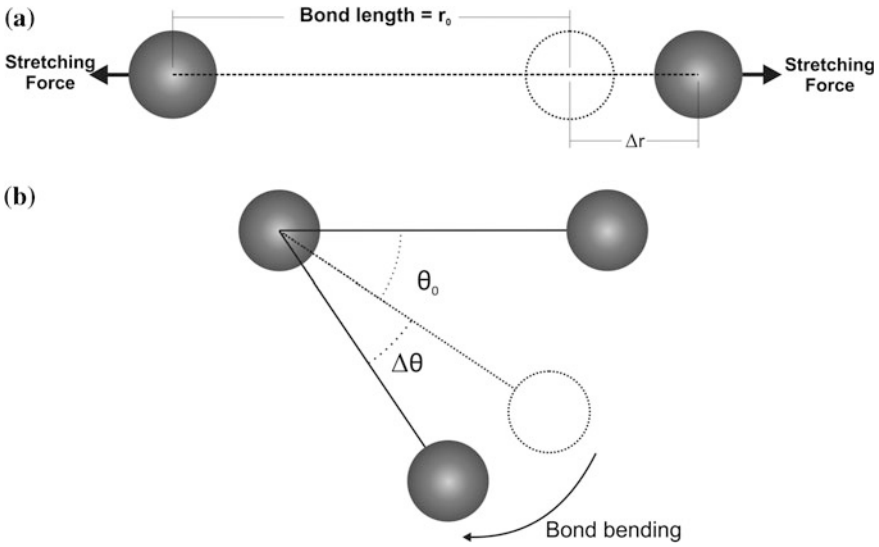

Fig. 2.3 Interatomic interactions according to modified Morse potential for C–C bonds: **a** bond stretching, **b** bond bending

Table 2.1 Associated values of force constants

Symbol	Name	Value
r_0	C–C bond length	1.421×10^{-10} m
θ_0	Bond angle	2.094 rad
D_e	well depth	6.03105×10^{-19} nm
β	Controls the width of the potential	2.625×10^{10} m^{-1}
k_θ	force constant	0.9×10^{-18} N/rad^2
k_{sexic}	force constant	0.754 rad^{-4}

$$U_{\text{stretch}} = D_e\left[\left(1 - e^{-\beta(r-r_0)}\right)^2 - 1\right] \tag{2.16}$$

$$U_{\text{angle}} = \frac{1}{2}k_\theta(\theta - \theta_0)^2\left[1 + k_{sexic}(\theta - \theta_0)^4\right] \tag{2.17}$$

where r *and* θ are the current bond length and angle of the adjacent bond, respectively. The parameters of the potential are summarized in Table 2.1 [6, 8, 9].

The stretching force and required bending moment to deform C–C bonds were obtained by differentiating bond stretching and angle bending potentials against bond length and bending angle, respectively,

$$F(r) = \frac{\partial U_{\text{stretching}}}{\partial r} = 2\beta D_e\left[1 - e^{-\beta(r-r_0)}\right]e^{-\beta(r-r_0)} \tag{2.18}$$

$$M(\theta) = \frac{\partial U_{\text{bending}}}{\partial \theta} = k_\theta(\theta - \theta_0)\left(1 + 3k_{sextic}(\theta - \theta_0)^4\right) \tag{2.19}$$

2.4 Potential Interactions for Inorganic Nanotubes

The initial stage in the majority of the atomistic molecular modeling methods (molecular mechanics) is the computation of the energy (Lattice energy in this case). The lattice energy of a crystal can be determined by summing all separate kinds of interactions that may likely occur in a system containing a number of atoms in it [11]. But, the lattice energy calculated is accurate only if higher orders of interactions are also taken into consideration during the calculation process. On the other hand, it is unrealistic to take account of the higher orders of interaction for computation as it will turn out to be exceedingly time consuming [12]. Furthermore since contributions decreases progressively with increasing order of interactions, it is realistic to shorten the increase to two body and three body interactions. The atomic interactions turn out to be weaker as the distance in the middle of the atoms spread wider [11].

Potentials of atoms/molecules are determined using empirical equations (based on interatomic distance) in order to calculate the energy related with the particular atomic interactions. Potentials perform a significant task in defining the precision of the computational modeling investigations [13]. There are various types of chemical bonds occurring in numerous elements for binding the material together, viz. covalent bonds, ionic bonds, metallic bonds, Van der Waals bonds and hydrogen bonds. Every form of bonds will have varied strength. Bonds may also be categorized as intramolecular bonds and intermolecular bonds. Intramolecular bonds keep the atoms together in a molecule. In addition, intramolecular bonds are those that exist between the molecules as in Van der Waals bonding, ionic bonding, covalent bonding, dipole—dipole interaction and hydrogen bonding [11]. In ionic bonding, the ions of opposite charges are attracted to each other. Zirconia (ZrO_2) is an example of ionic bonding. In covalent bonding, the valence electrons are mutual in the middle of atoms not like electron transfer witnessed in ionic bonding. Covalent bonding is witnessed in water and diatomic molecules like O_2, H2 etc. These atomic interactions may well be categorized as long and short range interactions [14].

2.4.1 Long Range Interactions

In ionic crystals such as Zr-O, the long range (Coulomb) interactions accounts for most of the total energy of the structure [11]. Considering the ions as specific point charges, the Coulomb's law may be specified as [12]

$$U_{ij}^{\text{Coulomb}} = \frac{q_i q_j}{4\pi\varepsilon_0 r_{ij}} \tag{2.20}$$

where U_{ij}^{Coulomb} is the Coulomb's energies, q_i, q_j represent the charges on the pairs of ions, ε_o is the permittivity of free space and r_{ij} is the inter-ionic distance.

The computation of Coulomb energy turns out to be tedious for a 3D bulk material [12]. Exchanges involving ions progressively decrease in the midst of increase in the inter-ionic distances. On the other hand, the amount of ions and therefore the number of interactions among ions increases as the cut-off radius increases. This eventually affects the increase of energy density of interactions with increase in distance [12]. This hindrance may well be fixed by using Ewald summation technique [11, 15, 16], which requires two vital conditions for convergence: (a) Sum of all the charges in the system should be zero (b) Dipole moment should be zero. Ewald summation technique is fundamentally obtained by using Laplace transformation on Eq. 2.22. The Coulomb energy computation occurs in two sections: (a) Real space summation (b) Reciprocal space summation. Real space summation section converges promptly and the reciprocal space summation section decays rapidly. A Gaussian charge distribution is included and deducted from each ion. The expression for the approximation of Coulomb energy (U^{CE}) as the sum

total of inputs from real space (U^{real}), reciprocal space ($U^{\text{reciprocal}}$) and self-energy ($U^{\text{selfenergy}}$) of the ions is specified by [13]:

$$U^{CE} = \frac{1}{2}\sum_{i=1}^{N}\sum_{j-1}^{N}\frac{q_i q_j}{r_{ij}} erfc(\eta^{\frac{1}{2}} r_{ij}) + \frac{1}{2}\sum_{i=1}^{N}\sum_{j-1}^{N}\sum_{G}\frac{4}{\pi} q_i q_j \exp(iGr_{ij})\frac{\exp\left(\frac{G^2}{4\pi}\right)}{G^2} - \sum_{i=1}^{N} q_i^2\left(\frac{\eta}{\pi}\right)^{0.5} \tag{2.21}$$

$$U^{CE} = U^{\text{real}} + U^{\text{reciprocal}} - U^{\text{selfenergy}} \tag{2.22}$$

From Eq. 2.22, q represents the charge of the ion, G is equal to the reciprocal lattice vector, V is the unit cell volume, N is the number of atoms in the system and η represents the ratio of task among real and reciprocal space.

2.4.2 Short Range Interactions

Short range (non-Coulombic) interactions perform a critical part in approximating the position and profile of the minimum energy [11]. Mostly, the two body terms influence the short range interactions. Two body terms consist of interactions amongst atoms that are ions or attached. The three most prevalently used two- body potentials are Buckingham potential, Lennard-Jones potential and Morse potential [13]. The expressions for the potentials are given by:

$$U_{ij}^{\text{Buckingham}} = A\exp\left(\frac{-r_{ij}}{\rho}\right) - \frac{C_6}{r_{ij}^6} \tag{2.23}$$

$$U_{ij}^{\text{Lennard-Jones}} = \frac{C_m}{r_{ij}^m} - \frac{C_6}{r_{ij}^6} \tag{2.24}$$

$$U_{ij}^{\text{Morse}} = D_e\left[(1-\exp(-a(r-r_0)))^2\right] - 1 \tag{2.25}$$

where, r_{ij} is the inter-atomic distance and all the other terms are the parameters of the potential.

The Buckingham potential and Lennard-Jones potential include comparable terms in Eqs. (2.23) and (2.24) i.e., a repulsive part and attractive part. The C_6 portion obtained in all the potentials is the attractive part of the potential and it is not required to model in relation to ionic bonds [17]. Thus for ZrO_2, the potential energy is obtained as a sum of two-body interactions of the form [11]:

Table 2.2 Parameters for atomic interactions in ZrO_2 [11]

Pair	A_{ij} (eV)	ρ_{ij} (Å)	C_{ij} (eVÅ^{-6})
Zr-O	985.87	0.3760	0.0
Zr-Zr	22764.3	0.1490	27.89
O-O	0.0	0.0	0.0

$$U = U^{\text{bonded}} + U^{\text{nonbonded}}$$

$$U = A\exp\left(\frac{-r_{ij}}{\rho}\right) - \frac{C_6}{r_{ij}^6} + \frac{q_i q_j}{4\pi\varepsilon_0 r_{ij}} \tag{2.26}$$

Parameters in Eq. 2.26 for ZrO_2 have been developed by empirical method [11, 18] and are indicated in Table 2.2.

The electric permittivity of vacuum, ε_o = 0.55263614 × 10^{-12} $C^2eV^{-1}Å^{-1}$; $q_{Zr} = 4e$; $qO_2 = -2e$; where e is the magnitude of electronic charge, 1.602 × 10^{-19} C [11, 18]. The Morse potential is used for atomic interactions where covalent bond dominates in the total energy for the system such CNT, BN and others [17].

References

1. D.W. Brenner, Empirical potential for hydrocarbons for use in simulating the chemical vapor deposition of diamond films. Phys. Rev. B **42**, 9458–9471 (1990)
2. N.L. Allinger, *Molecular Structure: Understanding Steric and Electronic Effects from Molecular Mechanics* (Wiley, 2010)
3. T. Chang, H. Gao, Size-dependent elastic properties of a single-walled carbon nanotube via a molecular mechanics model. J. Mech. Phys. Solids **51**, 1059–1074 (2003)
4. G.M. Odegarda, T.S. Gatesb, L.M. Nicholsonc, K.E. Wised, Equivalent-continuum modeling of nano-structured materials. Compos. Sci. Technol **62**, 1869–1880 (2002)
5. H. Wan, F. Delale, A structural mechanics approach for predicting the mechanical properties of carbon nanotubes. Meccanica **45**, 43–51 (2010)
6. T. Belytschko, S.P. Xiao, G.C. Schatz, R.S. Ruoff, Atomistic simulations of nanotube fracture. Phys. Rev. B **65**, 235–430 (2002)
7. J. Xiao, B. Gama, J. Gillespiejr, An analytical molecular structural mechanics model for the mechanical properties of carbon nanotubes. Int. J. Solids Struct. **42**, 3075–3092 (2005)
8. K. Tserpes, P. Papanikos, G. Labeas, S. Pantelakis, Multi-scale modeling of tensile behavior of carbon nanotube-reinforced composites. Theoret. Appl. Fract. Mech. **49**, 51–60 (2008)
9. M. Rossi, M. Meo, On the estimation of mechanical properties of single-walled carbon nanotubes by using a molecular-mechanics based FE approach. Compos. Sci. Technol. **69**, 1394–1398 (2009)
10. G. Cao, X. Chen, J.W. Kysar, Thermal vibration and apparent thermal contraction of single-walled carbon nanotubes. J. Mech. Phys. Solids **54**, 1206–1236 (2006)
11. M.A. Caravaca, J.C. Mino, V.J. Pérez, R.A. Casali, C.A.Ponce, Ab initio study of the elastic properties of single and polycrystal TiO_2, ZrO_2 and HfO_2 in the cotunnite structure. J. Phys.: Condens. Matter 21(1), (2009)
12. M.C. Payne, M.P. Teter, D.C. Allan, T.A. Arias, J.D. Joannopoulos, Iterative minimization techniques for ab initio total-energy calculations: molecular dynamics and conjugate gradients. Rev. Mod. Phys. **64**(4), 1045 (1992)

13. G.V. Lewis, C.R.A. Catlow, Potential models for ionic oxides. J. Phys. C: Solid State Phys. **18** (6), 1149–1156 (1985)
14. D. Fang, Z. Luo, S. Liu, T. Zeng, L. Liu, J. Xu, W. Xu, Photoluminescence properties and photocatalytic activities of zirconia nanotube arrays fabricated by anodization. Opt. Mater. **35** (7), 1461–1466 (2013)
15. S.J. Clark, M.D. Segall, C.J. Pickard, P.J. Hasnip, M.I. Probert, K. Refson, M.C. Payne, First principles methods using CASTEP. Z. Kristallogr. **220**, 567–570 (2005)
16. M.C. Payne, M.P. Teter, D.C. Allan, T.A. Arias, J.D. Joannopoulos, Iterative minimization techniques for ab initio total-energy calculations: molecular dynamics and conjugate gradients. Rev. Mod. Phys. **64**(4), 1045 (1992)
17. A.R. Yavari, J.J. Lewandowski, J. Eckert, Mechanical properties of bulk metallic glasses. MRS Bull. **32**(08), 635–638 (2007)
18. A. Dwivedi, A.N. Cormack, A computer simulation study of the defect structure of calcia-stabilized zirconia. Philos. Mag. A **61**(1), 1–22 (1990)

Chapter 3
Finite Element Modeling of Nanotubes

In order to develop a finite element model for a given nanotube, it is necessary to set few things. Geometry of the nanotube should be well understood. As discussed in the previous chapters, atomic coordinates in a nanotube structure should be determined. The atomic coordinates is the base of any atomic modeling. Bonding between atoms should be established with respect to the experimental observations. Chemical bonds will be replaced with a proper structural element. After creating the frame-like structure of the nanotube, we can apply boundary conditions and carry out the simulation process.

In order to make a clear image of the modeling process, we will try to model a typical nanotube such as SWCNT in the following section. First of all, description of the geometry of SWCNT will be given. Different types of bonds exist between atoms in a given nanotube structure. For example, in a CNT there are covalent bonds that connect two neighboring carbon atoms. These bonds should be replaced with structural elements such as springs, beam, shell, plates. In the following section, a more detailed geometrical description will be presented for CNT. Similar approach should be utilized for modeling of other nanotubes. Type of bonding between atoms in the nanotube should be studied carefully. The bonding characteristics play a significant role on the rest of modeling approach and simulation results as well. Accuracy of the model mainly depends on the understanding of the nanotube structure and interatomic interactions of the atoms. Later, the modeling of INTs is also considered.

3.1 Geometry and Structure of Nanotubes

First step of the modeling process is to create the geometry of the nanotube. To begin with, let's consider CNT. Atomic structure of CNT is described in the first chapter. CNTs can be imaged as graphene sheets which are rolled into hollow cylindrical hexagonal carbon rings. When the hexagonal pattern is repeated in particular directions, carbon atoms are bond to neighboring rings via covalent bonds. In this way, CNTs can be constructed as a frame-like structure with their bonds as beam members and carbon atoms as joints [1]. This process is shown in

M. Awang et al., *Finite Element Modeling of Nanotube Structures*,
Engineering Materials, DOI 10.1007/978-3-319-03197-2_3

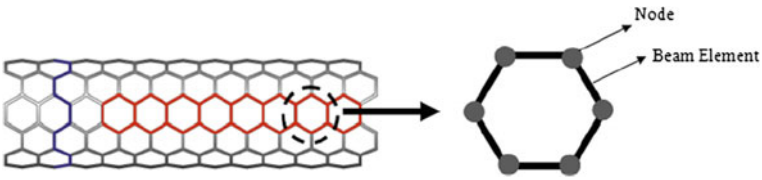

Fig. 3.1 The FE representation of the hexagonal structure of a typical CNT [1]

Fig. 3.1. In the present approach, it is assumed that CNTs are defect free molecular structures.

The parameters related to various components of CNT is shown in Table 3.1.

Atomic structure of a SWCNT follows a regular expression,

$$(x, y, z) = \left(r_n \cos\left(\frac{x'}{r_n}\right), r_n \sin\left(\frac{x'}{r_n}\right), y' \right)$$

where in this equation, x' and y' are the original coordinates of carbon atoms on the corresponding graphene sheet.

Nanotube Modeler is the most widely software for generating *xyz*-coordinates for nanotubes and nanocones. The Fullerene library by M.Yoshida may be accessed as well. Generated geometries may be viewed using the integrated viewer or by calling a viewer program of your choice. This program is based on the *JNanotubeApplet* but has improved and extended features as Fig. 3.2.

The main features of *Nanotube Modeler* include [3]:

- Interactive graphics (rotate structure by mouse drag)
- Creation of Nanotubes, Nanocones, Buckyball, Graphene Sheets
- Creation of capped (9,0) and (5,5) tubes
- Application of tube distortions
- Creation of single- or multi-walled nanotubes (SWNT, MWNT)
- Export of XYZ, JPG, BMP, PDF, MOL, XMOL, PDB, CIF, VRML, POV files
- Import of XY-Sheet coordinate files (can be rolled into tube)
- Display of Drexler-Merkle molecular machines from IMM
- XY-Sheet generation tool (image search/manual assembly)
- Nanotube Hetero-Junctions (using CoNTub plug-in)
- Import of XMOL coordinate files (distortions can be applied to nanotube data)
- More capped tubes (6,6), (10,0) and (10,10)
- Create tubes by number of translational units
- Custom MWNT input/Radius calculator/MWNT sequence finder
- Expanded number of atoms for longer tubes
- Rainbow color mode
- New CIF output option for ICSD style atom data block
- User-assigned bond order for MOL file export

Table 3.1 Parameters of carbon nanotubes [2]

Symbol	Name	Formula	Value
$a_{c\text{-}c}$	Carbon–carbon distance		1.421
a	Length of unit vector	$\sqrt{3}a_{c-c}$	2.46
$\boldsymbol{a}_1$, $\boldsymbol{a}_2$	Unit vectors	$\left(\frac{\sqrt{3}}{2},\frac{1}{2}\right)a,\ \left(\frac{\sqrt{3}}{2},-\frac{1}{2}\right)a$	in (x,y) coordinates
$\boldsymbol{b}_1$, $\boldsymbol{b}_2$	Reciprocal lattice vectors	$\left(\frac{1}{\sqrt{3}},1\right)\frac{2\pi}{a},\ \left(\frac{1}{\sqrt{3}},-1\right)\frac{2\pi}{a}$	in (x,y) coordinates
$\mathbf{C}_\mathrm{h}$	Chiral vector	$\mathbf{C}_h = n\mathbf{a}_1 + m\mathbf{a}_2 = (n,m)$	n, m are integers
L	Circumference of nanotube	$L = \lvert\mathbf{C}_h\rvert = a\sqrt{n^2+m^2+nm}$	$0 \le \lvert m\rvert \le n$
d_t	Diameter of nanotube	$d_t = \frac{L}{\pi}\frac{a\sqrt{n^2+m^2+nm}}{\pi}$	
θ	Chiral angle	$\sin\theta = \frac{\sqrt{3}m}{2\sqrt{n^2+m^2+nm}}$ $\cos\theta = \frac{2n+m}{2\sqrt{n^2+m^2+nm}}$ $\tan\theta = \frac{\sqrt{3}m}{2n+m}$	$0 \le \lvert\theta\rvert \le 30^\mathrm{o}$
d	The highest common divisor of (n,m)	$d_R = \{d$ if $n-m$ not a multiple of $3d$ $d_R = \{3d$ if $n-m$ a multiple of $3d$	
d_R	The highest common divisor of $(2n,m,\ 2\ \mathrm{m},n)$		
$\boldsymbol{T}$	Translational vector of 1D unit cell	$\mathbf{T} = t_1\mathbf{a}_1 + t_2\mathbf{a}_2 = (t_1,t_2)$ $t_1 = \frac{2m+n}{d_R}$ $t_2 = -\frac{2n+m}{d_R}$	t_1, t_2 are integers
T	Length of vector $\boldsymbol{T}$	$T = \frac{\sqrt{3}L}{d_R}$	
N	Number of hexagons per 1D unit cell	$N = \frac{2(n^2+m^2+nm)}{d_R}$	$2\ N = n_C$/ unit cell
$\boldsymbol{R}$	Symmetry vector	$\mathbf{R} = p\mathbf{a}_1 + q\mathbf{a}_2 = (p,q)$ $d = mp - nq,\ 0 \le p \le n/d, 0 \le q \le m/d$	p, q are integers
M	Number of 2π revolutions	$M = [(2n+m)p + (2m+n)q]/d_R$ $N\mathbf{R} = M\mathbf{C}_h + d\mathbf{T}$	M is integers
R	Basic symmetry operation	$R = (\psi/\tau)$	
ψ	Rotation operation	$\psi = 2\pi\frac{M}{N}, (x = \frac{\psi L}{2\pi})$	ψ in radians
τ	Translation operation	$\tau = \frac{d\mathbf{T}}{N}$	τ, x are unit lengths

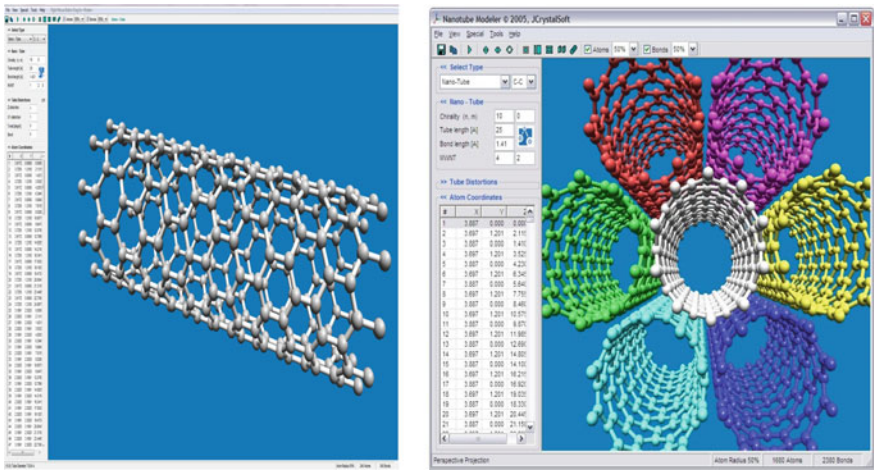

Fig. 3.2 CNTs generated from *Nanotube Modeler*

- Modified for European customers (decimal point/comma issue)
- Select one or both caps for capped tubes
- Extra-long tubes (>100 000 A)
- Export bond connection files
- Export MLM files (Agile Molecule)
- Export Nano-Hole Arrays
- Export VRML1.0 (in addition to VRML2.0)
- Multi-Layer Graphene Sheets
- Rotation option for Multi-Layer Graphene Sheets

Nanotube Modeler can also be used to generate some INTs: B-N, Ga-N, Al-N, Al-P and Ga-P. Free version of *Nanotube Modeler* is available in the link: http://jcrystal.com/products/wincnt/ except for the above mentioned export functions and the Copy Functions. The full version of *Nanotube Modeler* with all features has to be purchased through single user license or classroom/multi user license.

There are a series of other free online codes for generating CNTs based on the specific chilarity and other parameters such as C-C bond length, length/height of the nanotube, tube distortion and others. These coordinates can be imported to other software for furthers analysis. Other available software for modeling CNTs are summarized in Table 3.2.

For INTs, *Materials Studio* is the preferable software for modeling. It is developed and distributed by Biovia (formerlyAccelrys), a company specializing in research software for computational chemistry, bioinformatics, cheminformatics, molecular simulation, and quantum mechanics [4]. This software is used in advanced research of various materials, such as polymers, nanotubes, catalysts, metals, ceramics, and so on, by universities, research centers and hi-tech companies. *Materials Studio* is

Table 3.2 Available FE software for modeling of CNTs

Name	Description	Source	Link
TubeASP	Web-accessible carbon nanotube generation applet	Roberto Veiga	http://www.nanotube.msu.edu/tubeASP/
TubeGen	Web-accessible nanotube structure generator	Doren Research Group, University of Delaware	http://turin.nss.udel.edu/research/tubegenonline.html
CoNTub	Java-based code to generate nanotube junction geometries	GMDM group at the University of Granada, Spain	http://www.ugr.es/~gmdm/java/contub/contub.html
Fullerene isomers	Generation of fullerene geometries based on structures in the Fullerene Library that has been created by M. Yoshida	David Tomanek and Nick Frederick at the Michigan State University Com-putational Nanotechnology Lab	http://www.nanotube.msu.edu/fullerene/fullerene-isomers.html

a client–server software package with Microsoft Windows-based PC clients and Windows and Linux-based servers running on PCs, Linux IA-64 workstations (including Silicon Graphics (SGI) Altix) and HP XC clusters.

Materials Visualizer is the core product of the *Materials Studio* (MS) software suite, which is designed to support the materials modeling needs of the chemicals and materials-based industries. *Materials Visualizer* provides all of the tools that are required to construct graphical models of molecules, crystalline materials, and polymers. You can manipulate, view, and analyze these models. *Materials Visualizer* also handles graph, tabular, and textual data and provides the software infrastructure and analysis tools to support the full range of *Materials Studio*® products. Nanotechnology building tools include [4]:

- Tools available for both single and multi-walled nanotubes
- Specify carbon or boron Nitride tubes
- Build nanoropes
- Create nanoclusters from crystals

3.1.1 Modeling of CNTs with Specific Chirality

Let us consider a SWCNT with chilarity of (10,0) and length of 10 Å. Figure 3.3 shows the parameters required to generate the specified nanotube. From the structure, the atomic coordinates of the nanotube is generated and then the

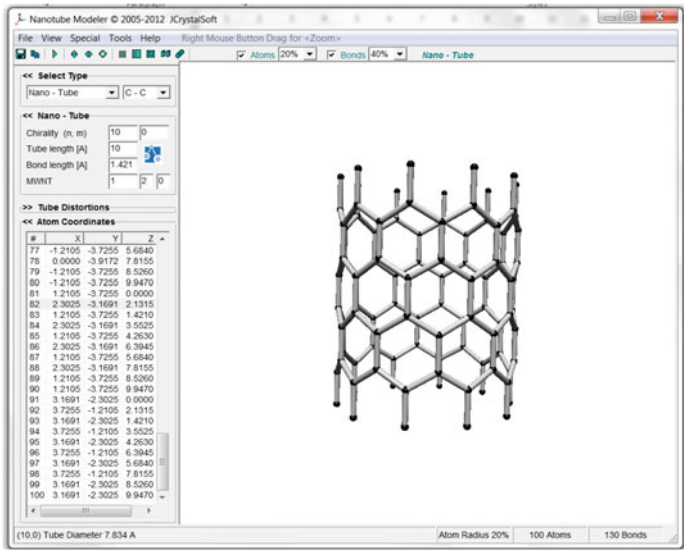

Fig. 3.3 Parameters for generating (10,0) CNT using *Nanotube modeler*

coordinates are inserted into a commercial finite element software such as ANSYS. In this entry, *Nanotube modeler* is used to create the coordinates.

A simple zigzag nanotube (10, 0) will be created using the *Nanotube modeler* and the (x,y,z) coordinates will be transferred to ANSYS. The (10,0) CNT with length of 10 Å has 100 carbon atoms in hexagonal cell arrangements. The hexagonal rings of carbon is illustrated in the Fig. 3.4.

The coordinates for CNT models generated using *Nanotube modeler* will be used in this book.

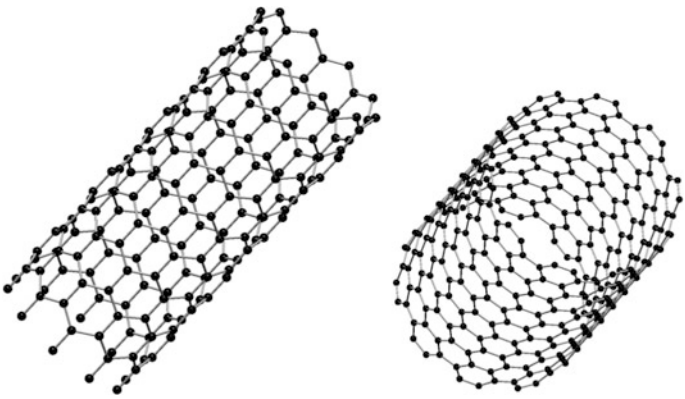

Fig. 3.4 (10, 0) CNT indicating all the atoms and bonds

3.1.2 Geometries of Multi-walled Carbon Nanotubes

As explained earlier, MWCNTs are centrically arranged SWCNTs that connect together with weak van der Waals forces. Some of mentioned codes are capable of producing MWCNTs with particular geometries. Using procedures as stipulated in Sect. 3.1.1, MWCNTs are generated with different parameters. In addition to chirality, tube length and bond length; the other parameters required for modeling MWCNTs are the number of walls and increment per wall. Some generated MWCNTs are illustrated in Figs. 3.5 and 3.6.

The models generated using *Nanotube modeler* (Figs. 3.5 and 3.6) are similar to TEM images of MWCNTs obtained experimentally as shown in Fig. 3.7.

3.1.3 Geometry of Inorganic Nanotubes

Structural models of INTs such as ZrO_2 nanotube (ZNT) can be created using the default of CNT or BN nanotube available in *Materials Studio* (MS), so we will make nanotube with BN and then replace B by Zr and N by Oxygen as indicated in Fig. 3.8.

Then select all B atom by pressing Alt key and double click any B atom, all of them (B atoms) will be selected, then change them to Zr; follow similar with N and replace them (N atoms) with O. Thereafter use "clean" tool to adjust the bond

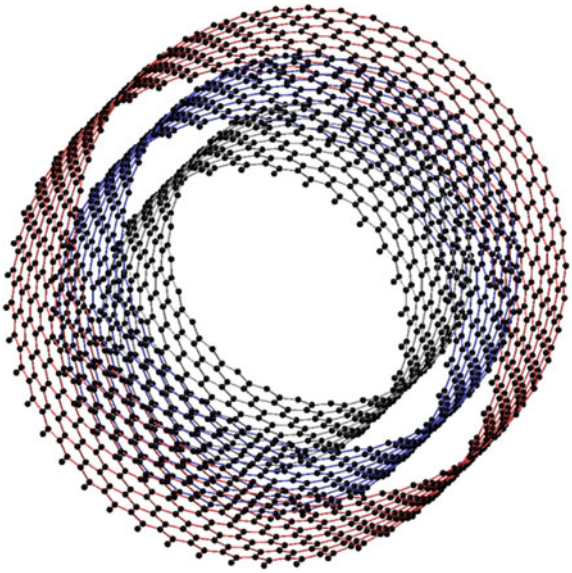

Fig. 3.5 MWCNT having (29,0) (38,0) (47,0) configuration

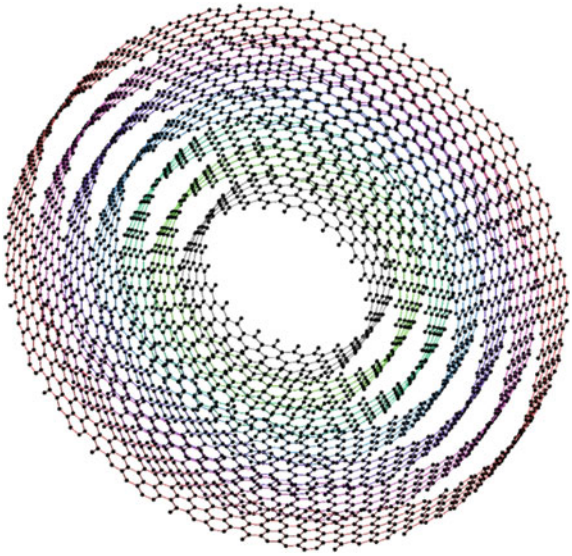

Fig. 3.6 MWCNT having (29,0) (38,0) (47,0) (48,13) (55,16) (63,17) (70,20) configuration

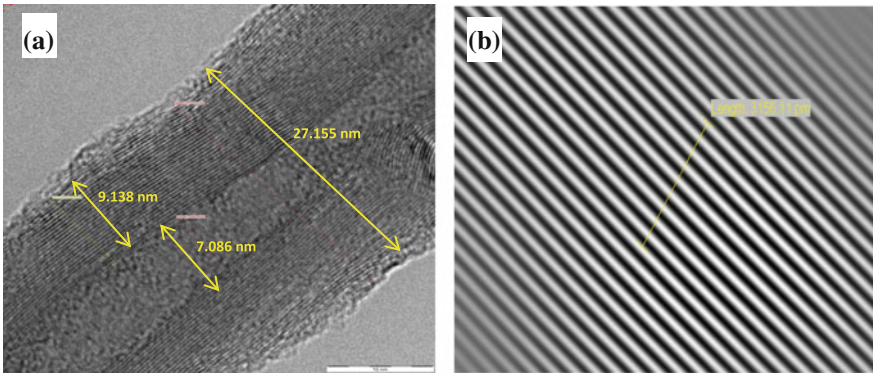

Fig. 3.7 TEM micrographs of **a** typical MWCNT, **b** interlayer distances in a MWCNT wall [5]

length from that of B-N to Zr-O. Example of generated model for ZrO_2 nanotube (10, 10) is illustrated in Fig. 3.9.

In order to transfer the model of INTs to ANSYS for simulation, a (35, 0) ZNT was generated and the structure was then exported and saved as PDB file as shown in Fig. 3.10.

Based on the PDB file generated, specific data required were extracted using code developed by *Python* software to carry out the following tasks [6]:

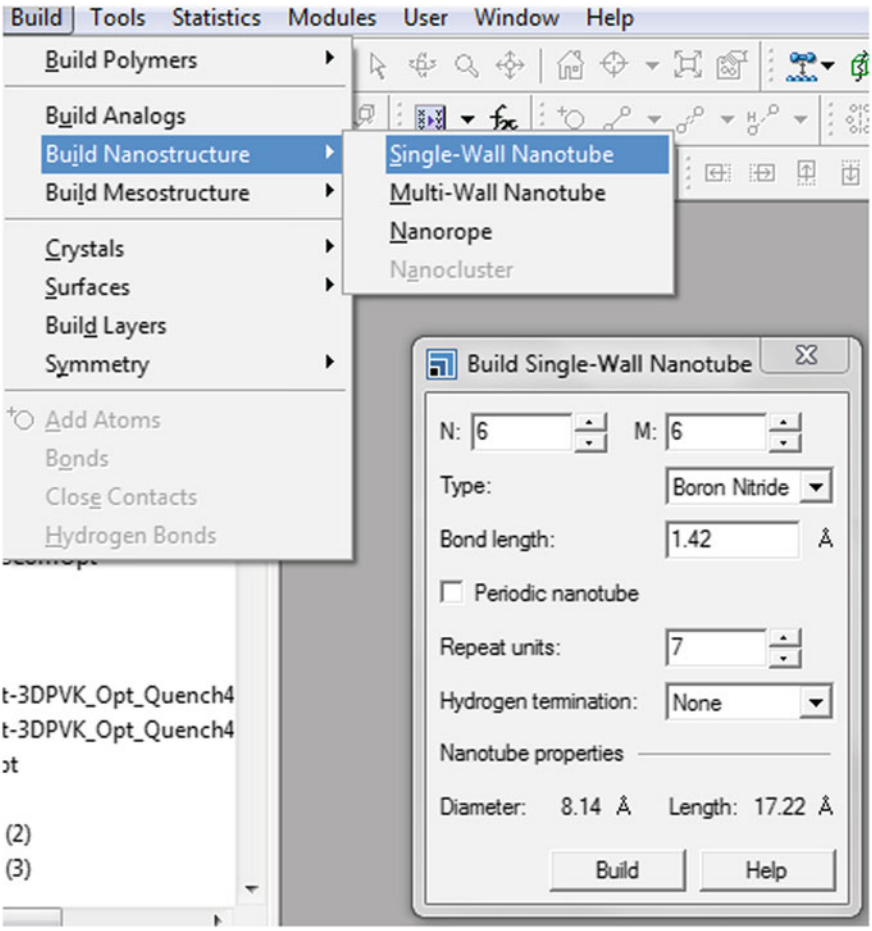

Fig. 3.8 Building of single-walled BN nanotube with (6,6) chirality using *Material Studio*

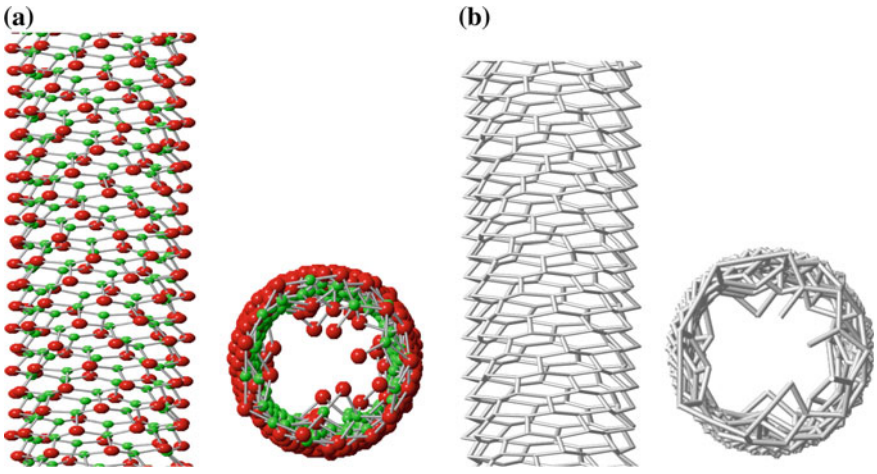

Fig. 3.9 Ball and stick **a** and stick **b** models of ZrO_2 NT generated from *Material Studio*

```
REMARK   Materials Studio PDB file
REMARK   Created:  Mon Sep 22 06:47:27 Malay Peninsula Standard Time 2014
ATOM      1 Zr   MOL     1      13.560   0.607   0.658  1.00  0.00          Zr4+
ATOM      2  O   MOL     1      14.697   1.984   1.204  1.00  0.00           O2-
|
|
ATOM   3358 Zr   MOL     1      13.254  -3.027 101.248  1.00  0.00          Zr4+
ATOM   3359  O   MOL     1      13.829  -1.873 102.814  1.00  0.00           O2-
ATOM   3360 Zr   MOL     1      13.586  -0.610 101.245  1.00  0.00          Zr4+
TER    3361
CONECT    1    2  137
CONECT    2    1    4    6
CONECT    3    6  140  141
|
|
CONECT 3357 3221 3356 3360
CONECT 3358 3355 3353 3359
CONECT 3359 3358 3360
CONECT 3360 3223 3359 3357
END
```

Fig. 3.10 PDB File for 10 × 10 cubic zirconia nanotube from *Material Studio*

(1) Open the PDB file and read each line.
(2) Select out lines having the word "ATOM".
(3) Get the X, Y and Z coordinates of those atoms.
(4) Store the coordinates as nodes.
(5) Select out lines with the word "CONECT".
(6) Separate each line into pair connections only, with the first atom connected to others in twos serially.
(7) Print out the results in a formatted table.

The output in txt file (Fig. 3.11) was thereafter exported into ANSYS.

3.2 Modeling the Mechanical Properties of Carbon Nanotubes

As mentioned previously, CNTs can be constructed as a frame-like structure with their bonds as beam members and carbon atoms as joints [1]. This process is shown in Fig. 3.1. In the present approach, it is assumed that CNTs are defect free molecular structures.

A rather extensive part of the modeling concentrates on the computation of the elastic constants, Poisson's ratios and Young's moduli of SWCNTs, MWCNTs and their respective bundles (ropes), aiming to show the dependence of these properties on the diameter and chirality of the nanotubes. A very interesting aspect of the computational modeling of the mechanical properties of nanotubes that has clearly

Fig. 3.11 Output file in macro APDL for modeling 35 × 0 SWZNT

```
/prep7
k, 1, 13.560, 0.607,0.658
k, 2, 14.697, 1.984,1.204
k, 3, 14.831, 0.665,3.705
k, 4, 13.244, 3.021,0.661
k, 5, 14.111, 4.585,1.199
:
:
k, 3358, 13.254, -3.027,101.248
k, 3359, 13.829, -1.873,102.814
k, 3360, 13.586, -0.610,101.245
l, 1, 2
l, 1, 137
l, 2, 1
l, 2, 4
l, 2, 6
l, 3, 6
l, 3, 140
:
:
:
l, 3359, 3360
l, 3360, 3223
l, 3360, 3359
l, 3360, 3357
```

emerged from the research in this area of nanotube physics is the relevance of the well-established continuum-based theories of curved plates, thin shells, beams and vibrating rods, to model and interpret the response of nanotubes to external influences, such as large strains, or the flow of fluids inside nanotubes.

These continuum-based theories have been successfully employed both in their own right, i.e. as independent computational tools to compute the elastic properties and deformation modes of nanotubes, and also in conjunction with the atomistic based models to provide the input data for these models and interpret the results obtained from them.

Continuum-based theories dealing with vibration, bending and buckling of beams and rods, have been also employed to model a range of mechanical properties of carbon nanotubes. They also provide a theoretical framework to interpret the results from nanoscale experiments designed to measure the stiffness of nanotubes. Here the theories pertinent to the dynamics of a thin beam (the Euler–Bernoulli beam) and a thick beam (the Timoshenko beam) are presented.

3.2.1 Analytic Solution

Based on equivalent continuum modeling techniques [7], each carbon–carbon bond is treated as load bearing beam undergoing tension and bending. A graphene sheet can be considered as a honeycomb frame structure. The displacement field of the unit element of the structure is investigated using complementary potential energy of the structure and the Young's modulus of a graphene sheet will be derived, accordingly. The developed formulation of a graphene sheet will be enhanced to a CNT, based on rolling a graphene sheet virtually and reorganizing the governing equations.

A CNT can be treated as schematically rolled graphene sheet. Analysis of zigzag and armchair CNTs can be performed using mentioned load distribution in Fig. 3.12, while variations of π angle in term of nanotube diameter is needed to be characterized. Orientation of zigzag and armchair nanotubes including corresponding angles are depicted in Fig. 3.12. The n–n' is a line of intersection between the plane perpendicular to the axes of nanotube and BAC plane [8].

Relationship between mentioned angles in Fig. 3.12 can be expressed for zigzag and armchair configurations in Eqs. 3.1 and 3.2 respectively [8].

$$\sin(\beta/2) = \sin(\theta)\cos(\pi/2n) \tag{3.1}$$

$$\cos(\beta) = -\cos(\theta)\cos(\pi/2n) \tag{3.2}$$

where n is characterized by chiral index of either armchair or zigzag in the form of (n, n) or (n, 0), respectively. As it can be seen from Eqs. 3.1 and 3.2, when n goes to infinity, the equations account for a graphene sheet. Composing moment and force equilibrium for each load case, the variation of h can be obtained for zigzag and armchair nanotubes. Detailed description of the calculation procedure can be found in [8]. Rearranged forms of equations stating variation of h with respect to the

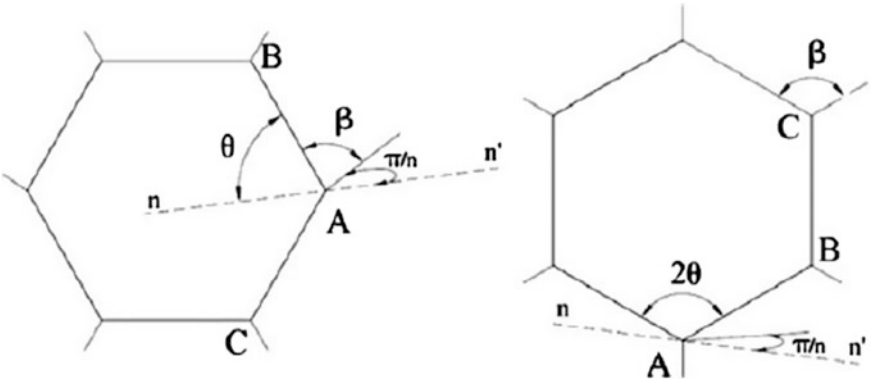

Fig. 3.12 Angle orientations of armchair (*left*) and zigzag (*right*) nanotubes [8]

developed method are specified in Eqs. (3.3a) and (3.3b) for zigzag and armchair geometrical configurations, respectively.

$$\Delta\theta_Z = \frac{HL^2}{2EI}\sin\theta\left[1+\frac{\cos^2\theta\cos^2(\pi/2n)}{1-\sin^2\theta\cos^2(\pi/2n)}\right]^{-1} \tag{3.3a}$$

$$\Delta\theta_A = \frac{VL^2}{2EI}\cos\theta\left[2+\frac{\sin^2\theta\cos^2(\pi/2n)}{1-\cos^2\theta\cos^2(\pi/2n)}\right]^{-1} \tag{3.3b}$$

Again it can be observed from Eqs. (3.3a) and (3.3b) that when n goes to infinity, the corresponding HL leads to the associated amount of graphene sheet. Using ab initio simulation, Yu et al. [9] showed that h is approximately equal to 60 Å for both armchair and zigzag nanotubes.

Now, we can rearrange Eqs. (3.3a) and (3.3b) and adopt it for zigzag and armchair CNTs which were previously developed for graphene sheet as shown in Eqs. (3.4a) and (3.4b).

$$\delta_Z = \frac{L\Delta\theta_Z}{3}\sin\theta + \frac{HL\cos^2\theta}{EA} + \frac{2HL}{EA} \tag{3.4a}$$

$$\delta_A = \frac{L\Delta\theta_A}{2}\cos\theta + \frac{VL\sin^2\theta}{EA} \tag{3.4b}$$

where δ_Z and δ_A are the deformations of zigzag and armchair nanotubes along their axial axes, respectively. Strain and stress fields can be expressed using following equations:

$$\varepsilon_Z = \frac{\delta_Z}{L(1+\cos\theta)},\ \sigma_Z = \frac{H}{tL\sin\theta} \tag{3.5a}$$

$$\varepsilon_A = \frac{\delta_A}{L\sin\theta},\ \sigma_A = \frac{V}{tL(1+\cos\theta)} \tag{3.5b}$$

where ε_Z, σ_Z, ε_A and σ_A are strains and stresses of zigzag and armchair nanotubes all along tube axial axes, respectively. Finally, axial Young's moduli of hollow CNTs can be obtained using the following formulation:

$$E_Z = \frac{16\sqrt{3}}{t}\left[\frac{k_r k_0(3-\cos\frac{\pi}{n})}{5k_rL^2+108k_\theta-(3k_rL^2+36k_\theta)\cos\frac{\pi}{n}}\right] \tag{3.6a}$$

$$E_A = \frac{16}{t\sqrt{3}}\left[\frac{k_r k_0(17+\cos\frac{\pi}{n})}{7k_rL^2+204k_\theta+(12k_\theta-k_rL^2)\cos\frac{\pi}{n}}\right] \tag{3.6b}$$

Both Eqs. (3.6a) and (3.6b) will converge to when n goes to infinity. This mathematical behavior can be interpreted as a logical physical behavior that Young's modulus of larger nanotubes in diameter will approaches to the Young's modulus of a graphene sheet as a bounding value. The reason for this behavior can be found in distortion of carbon–carbon bonds in smaller diameter which are much more significant than it in larger diameter and when diameter is large enough, the mentioned influence diminishes [10].

3.2.2 *Computing Some Mechanical Properties of Carbon Nanotubes*

To calculate the mechanical properties of a CNT, one CNT's end was restrained and axial displacement was applied on the other end (Fig. 3.14). The axial strain, ε_Z, is defined as tube length at each substep, l, divided by initial length of the tube, l_0. The corresponding external force, F, is calculated from the summation of nodal reactions at fixed end [1].

Then, the properties can be calculated as follows:

$$\varepsilon_Z = \frac{u}{l_0} = \frac{l - l_0}{l_0} \tag{3.7}$$

$$\sigma = \frac{F}{A} \tag{3.8}$$

$$E = \frac{d\sigma}{d\varepsilon} \tag{3.9}$$

$$v = \frac{(r - r_0)/r_0}{u/l_0} \tag{3.10}$$

where E, σ, F, A, v, r, r_0 are the Young's modulus, axial stress, reaction force, cross sectional area, Poisson's ratio, current and initial radius of the tube.

From the theoretical point of view, tensile properties of CNTs are strongly based on its wall thickness assumptions [11]. This may explain wide range of reported property values such as Young's modulus of the SWCNT. In fact, there has been no consensus on the exact values of CNT wall thickness in theoretical calculations. Different values have been considered for CNT wall thickness such as the graphite inter-layer spacing (0.34 nm) or the double C–C bond length. Most of reported thicknesses are vary in a range of 0.06–0.69 nm. In this work, the wall thickness is defined equal to 0.34 nm, according to electron density distributions [12]. With this assumption, the CNT cross section is defined as πDt where D and t are CNT diameter and thickness as shown in Fig. 3.13.

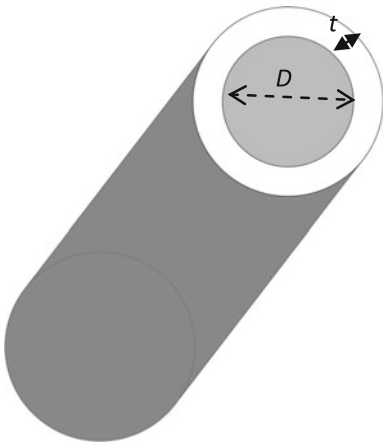

Fig. 3.13 Illustration of the diameter and cross section of the carbon nanotube

3.3 Modeling the Mechanical Properties of Inorganic Nanotubes

Due to ionic bonds in inorganic nanotubes, their structure buckles when exposed to deformation [13]. This buckling, which is lacking in carbon nanotubes, may well produce a consequence on the mechanical properties of ZNT and other inorganic nanotubes [14]. Thus analytical model based on molecular mechanics method for determining the elastic properties of nanotubes formed by two or more elements is not the same as that of SWCNTs [15].

An inorganic nanotube is structurally represented in Fig. 3.14, with (a) symbolizing the whole (10,10) armchair ZNT, (b) shows the structure observed by the longitudinal path along the nanotube, (c) arrangement, and (d) breakdown of force applied on half of stick b. The dark (or red) balls represent oxygen atoms and the bright (or green) balls represent zirconium atoms.

Considering a single-walled zirconia nanotube (SWZNT) as a ZrO_2 nanosheet rolled into a tube, its geometry and structure is more complex than that of SWCNT. The bonds and bond angles is denoted by a_1, b_1, b_2, α_{O2}, β_{O2}, β_{O2} for oxygen atom and a_2, b_2, b_3, α_{Zr}, β_{Zr}, β_{Zr} for zirconium atom as illustrated in Fig. 3.14c; this is similar to what was used for BN nanotubes [15]. With the force and moment in stick b, the internal forces are based on the axial force F and the axial torque T which are designated by f and s, correspondingly. Thus the connections joining the external and internal forces are generated as

$$F = 2nf, \; T = 2nsR \tag{3.11}$$

where R represents the tube radius with the forces f and s been divided in dual components, p and q as indicated in Fig. 3.14d.

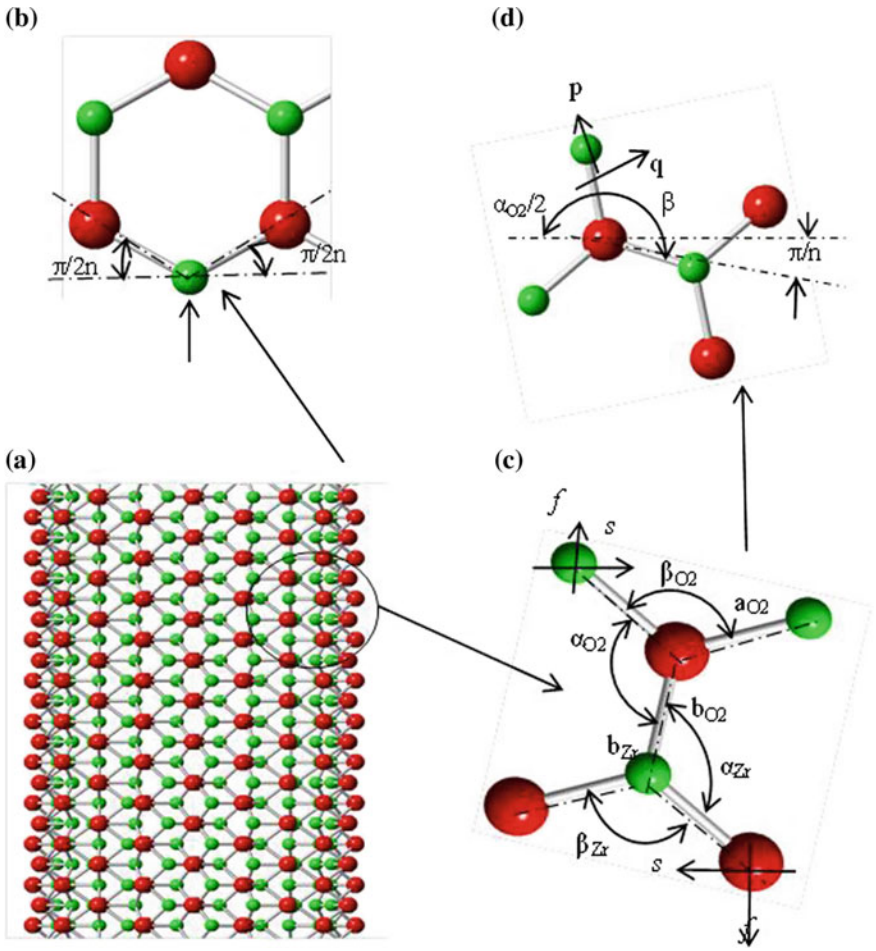

Fig. 3.14 Schematic representation of the forces in a (10,10) zirconia nanotube

Along the b-b plane, the bond stretching by the component $p = f\ sin(\alpha/2) + cos\ (\alpha/2)$ alongside the direction of the bond with the component $q = f\ cos(\alpha/2) + s\ sin\ (\alpha/2)$ which is at right angles to the bond leading into bond angle deformation/ distortion.

The force of equilibrium for the bond, yields

$$f \sin\left(\frac{\alpha O_2}{2}\right) + s\cos\left(\frac{\alpha O_2}{2}\right) = f \sin\left(\frac{\alpha Zr}{2}\right) + s\cos\left(\frac{\alpha Zr}{2}\right) = Kdb \qquad (3.12)$$

When the bond/stick b is divided in two: with O_2 atoms represented by b_{O2} and Zr atoms by b_{Zr}. The bond angle variances $d\alpha$ and $d\beta$ give rise to moments C$d\alpha$ and C$d\beta$ in planes b-b and a-b respectively.

The torsion angles between planes *b-b* and *a-b* can be computed as

$$\cos\phi_{O_2} = -\frac{\tan\left(\frac{\alpha_{O_2}}{2}\right)}{\tan\beta_{O_2}} \tag{3.13}$$

$$\cos\phi_{Zr} = -\frac{\tan\left(\frac{\alpha_{Zr}}{2}\right)}{\tan\beta_{Zr}} \tag{3.14}$$

Then the moment equilibrium becomes

$$b_{O_2}\left[f\cos\left(\frac{\alpha_{O_2}}{2}\right) + s\sin\left(\frac{\alpha_{O_2}}{2}\right)\right] = C_{O_2}d\alpha_{O_2} + C_{O_2}d\beta_{O_2}\cos\phi_{O_2} \tag{3.15}$$

$$b_{Zr}\left[f\cos\left(\frac{\alpha_{Zr}}{2}\right) + s\sin\left(\frac{\alpha_{Zr}}{2}\right)\right] = C_{Zr}d\alpha_{Zr} + C_{Zr}d\beta_{Zr}\cos\phi_{Zr} \tag{3.16}$$

In relation to armchair single-walled inorganic nanotube, the geometry connections fulfill [15]

$$\cos\beta_{O_2} = -\cos\left(\frac{\alpha_{O_2}}{2}\right)\cos\gamma_{O_2} \tag{3.17}$$

$$\cos\beta_{Zr} = -\cos\left(\frac{\alpha_{Zr}}{2}\right)\cos\gamma_{Zr} \tag{3.18}$$

where γ_{O2} and γ_{Zr} are the angles for the bonds a_{O2} and a_{Zr} along the plane b-b. Differentiating Eqs. (3.17) and (3.18)

$$d\beta_{O_2} = -\frac{\sin\left(\frac{\alpha_{O_2}}{2}\right)}{2\sin\beta_{O_2}}\cos\gamma_{O_2}d\alpha_{O_2} \tag{3.19}$$

$$d\beta_{Zr} = -\frac{\sin\left(\frac{\alpha_{Zr}}{2}\right)}{2\sin\beta_{Zr}}\cos\gamma_{Zr}d\alpha_{Zr} \tag{3.20}$$

For simplicity, it is assumed that $a = b$ and $\alpha_{O2} = \alpha_{Zr}$. If the SWZNT is subjected only to axial tensile force F, then $T = 2nsR = 0$ giving the force equilibrium and moment equations as

$$f\sin\left(\frac{\alpha_{O_2}}{2}\right) = f\sin\left(\frac{\alpha_{Zr}}{2}\right) = Kdb \tag{3.21}$$

$$b_{O_2} = f\cos\left(\frac{\alpha_{O_2}}{2}\right) = C_{O_2}d\alpha_{O_2} + C_{O_2}d\beta_{O_2}\cos\phi_{O_2} \tag{3.22}$$

$$b_{Zr} = f\cos\left(\frac{\alpha_{Zr}}{2}\right) = C_{Zr}d\alpha_{Zr} + C_{Zr}d\beta_{Zr}\cos\phi_{Zr} \tag{3.23}$$

Merging Eqs. (3.22) and (3.23), then substituting Eqs. (3.16)–(3.19) and Eq. (3.21) into it, we attain

$$d\alpha = \frac{2Kb^2}{C_{O_2}\lambda_{O_2} + C_{Zr}\lambda_{Zr}} \cot\left(\frac{\alpha}{2}\right) \frac{db}{b} \tag{3.24}$$

where,

$$\lambda_{O_2} = \frac{2 - 2\cos^2\left(\frac{\alpha}{2}\right)\cos^2\gamma_{O_2} + \sin^2\left(\frac{\alpha}{2}\right)\cos^2\gamma_{O_2}}{1 - \cos^2\left(\frac{\alpha}{2}\right)\cos^2\gamma_{O_2}} \tag{3.25}$$

$$\lambda_{Zr} = \frac{2 - 2\cos^2\left(\frac{\alpha}{2}\right)\cos^2\gamma_{Zr} + \sin^2\left(\frac{\alpha}{2}\right)\cos^2\gamma_{Zr}}{1 - \cos^2\left(\frac{\alpha}{2}\right)\cos^2\gamma_{Zr}} \tag{3.26}$$

The axial strain ε_3 and the circumferential strain ε_2 of armchair nanotube is expressed as [15]

$$\varepsilon_3 = \frac{d[b\sin\left(\frac{\alpha}{2}\right)]}{[b\sin\left(\frac{\alpha}{2}\right)]}, \; \varepsilon_2 = \frac{d[a + bs\cos\left(\frac{\alpha}{2}\right)]}{[a + b\cos\left(\frac{\alpha}{2}\right)]} \tag{3.27}$$

Substituting Eq. (3.24) into Eq. (3.27), we obtain

$$\begin{aligned} \varepsilon_3 &= \left[1 + \frac{Kb^2}{C_{O_2}\lambda_{O_2} + C_{Zr}\lambda_{Zr}} \cot^2\left(\frac{\alpha}{2}\right)\right] \frac{db}{b}, \\ \varepsilon_2 &= -\left[\frac{Kb^2}{C_{O_2}\lambda_{O_2} + C_{Zr}\lambda_{Zr}} - 1\right] \frac{cos\left(\frac{\alpha}{2}\right)}{1 + cos\left(\frac{\alpha}{2}\right)} \frac{db}{b} \end{aligned} \tag{3.28}$$

Considering a nanotube as a cylindrical thin shell having radius R and thickness t and subjected to an axial tensile force F, its Young's modulus can be expressed as the ratio of axial stress and the axial strain, that is

$$E = \frac{F}{2\pi Rt\varepsilon_s} \tag{3.29}$$

To avoid the problem with variable thickness of nanotubes [14], the equivalent Young's modulus is Y_s is defined as

$$Y_s = Et = \frac{F}{2\pi R\varepsilon_s} \tag{3.30}$$

Additionally, the Poisson's ratio is

$$v = -\frac{\varepsilon_2}{\varepsilon_3} \tag{3.31}$$

In order to obtain the shear modulus G_s, an axial torque T is applied and following the procedure utilized for axial modulus above then

$$G_s = \frac{\tau}{2\pi R^2 \mu} \tag{3.32}$$

Substituting Eqs. (3.28) and (3.29) into Eqs. (3.30) and (3.31), we obtain

$$Y_s = \frac{4\sqrt{3K}}{9 + \frac{3Kb^2}{C_{O_2}\lambda_{O_2} + C_{Zr}\lambda_{Zr}}}, \tag{3.33}$$

$$v = \frac{\frac{Kb^2}{C_{O_2}\lambda_{O_2} + C_{Zr}\lambda_{Zr}} - 1}{3 + \frac{Kb^2}{C_{O_2}\lambda_{O_2} + C_{Zr}\lambda_{Zr}}} \tag{3.34}$$

For the shear modulus,

$$G_s = \frac{2\sqrt{3}K}{3 + \frac{9Kb^2}{C_{O_2}\lambda_{O_2} + C_{Zr}\lambda_{Zr}}} \tag{3.35}$$

From the steps described above, the numerical technique for stress-strain correlation for armchair nanotube is summarized as follows:

(1) Determine/assume any given bond stretch db
(2) Compute f using Eqs. (3.21) and (3.29)
(3) Calculate stress at the most recent position by Eq. (3.33)
(4) Identify balance geometry with dα and dβ for both Zr and O_2 conforming to db using Eqs. (3.30) and (3.31) over a loop with fixed variation [14]
(5) Estimate the strains at the most recent/current state using Eqs. (3.26) and (3.35).
(6) Calculate the Young's modulus, Poisson's ratio and shear modulus using Eqs. (3.33), (3.34) and (3.35) respectively.

The values for the angles α and β for Zr and O_2 of armchair nanotubes for various materials have been determined using ab initio calculations [16]. Similar procedure was followed to determine the values of Y_s, v and G_s for the zigzag nanotubes [13–15].

Determining the stress-strain relationship for nanotubes using Eqs. (3.11)–(3.35) is demanding as hundreds of equations will be generated depending on chirality and number of atoms and bonds available. The best alternative is to use a numerical method with the capability to handle as many atoms/nodes and bonds/elements as possible.

References

1. E. Mohammadpour, M. Awang, M. Abdullah, Predicting the Young's modulus of single-walled carbon nanotubes using finite element modeling. J. Appl. Sci. **11**, 1653–1657 (2011)
2. G.M. Odegarda, T.S. Gatesb, L.M. Nicholsonc, K.E. Wised, Equivalent-continuum modeling of nano-structured materials. Compos. Sci. Technol. **62**, 1869–1880 (2002)
3. JVirusApplet at http://www.jcrystal.com/steffenweber/JAVA/jvirus/index.htm
4. http://accelrys.com/products/materials-studio/
5. B.I. Yakobson, P. Avouris, Mechanical properties of carbon nanotubes. Topics Appl. Phys. **80**, 287–327 (2001)
6. I.D. Muhammad, M. Awang, Extracting the atomic coordinates and connectivity of zirconia nanotubes from PDB files for modelling in ANSYS. Adv. Nanopart. **3**, 92–98 (2014)
7. W.L.S. Xie, Z. Pan, B. Chang, L. Sun, Mechanical and physical properties on carbon nanotube. J. Phys. Chem. Solids **61,** 1153–1158 (2000)
8. K. Ahmad, W. Pan, Dramatic effect of multiwalled carbon nanotubes on the electrical properties of alumina based ceramic nanocomposites. Compos. Sci. Technol. **69**, 1016–1021 (2009)
9. M.-F. Yu, B.S. Files, S. Arepalli, R.S. Ruoff, Tensile loading of ropes of single wall carbon nanotubes and their mechanical properties. Phys. Rev. Lett. **84**, 5552–5555 (2000)
10. I. Janowska, S. Hajiesmaili, D. Bégin, V. Keller, N. Keller, M.-J. Ledoux et al., Macronized aligned carbon nanotubes for use as catalyst support and ceramic nanoporous membrane template. Catal. Today **145**, 76–84 (2009)
11. E. Mohammadpour, M. Awang, Nonlinear finite-element modeling of graphene and single-and multi-walled carbon nanotubes under axial tension. Appl. Phys. A **106**(3), 581–588 (2012)
12. C.Y.J. Cai, T. Yu, S. Yu, Wall thickness of single-walled carbon nanotubes and its Young's modulus. Phys. Scr. **79** (2009)
13. X. Blase, A. Rubio, S.G. Louie, M.L. Cohen, Stability and band gap constancy of boron nitride nanotubes. Eur. Phys. Lett. **28**(5), 335 (1994)
14. H.X. Zhang, C. Feng, Y.C. Zhai, K.L. Jiang, Q.Q. Li, S.S. Fan, Cross-stacked carbon nanotube sheets uniformly loaded with SnO_2 nanoparticles: a novel binder-free and high-capacity anode material for lithium-ion batteries. Adv. Mater. **21**(22), 2299–2304 (2009)
15. L. Jiang, W. Guo, A molecular mechanics study on size-dependent elastic properties of single-walled boron nitride nanotubes. J. Mech. Phys. Solids **59**(6), 1204–1213 (2011)
16. I.D. Muhammad, M. Awang, O. Mamat and K.Z.K Shaari, Estimating Young's modulus of single-walled zirconia nanotubes using nonlinear finite element modeling. J Nanomater. (2015)

Chapter 4
Nanotube Modeling Using Beam Element

4.1 Introduction

Advances in computing technology have significantly increased the scientific interest in computer based molecular modeling of nano materials [1]. In order to perform any computational study on molecular properties, it is necessary to create a molecular model. In other words, it is essential to create an accurate model of atomic interactions at the first step. This model could be used to investigate the mechanical properties of a material near molecular length scales [2]. It can be derived by taking into account an appropriate crystal structure. Any technique that can produce a valid model for a given compound seems appropriate. Molecular modeling could be a useful tool at this stage. It is widely employed to determine molecular equilibrium structures. In addition, it could be used to design new materials with desirable properties [3]. These theoretical methods can be classified into two board branch which are "bottom up" and "top down". "Bottom up" is based on quantum/molecular mechanics including the classical MD and ab initio methods. In contrast, "top down" approach arose from continuum mechanics.

In the last decade intensive computational investigation has been performed to assess CNT's mechanical properties, either to explain observations or to obtain information which is not accessible through experimental studies. The deformation behavior of CNTs has been subjected to numerous investigations via MD and continuum approaches [4–9]. Since experimental studies at nano length scale are still under development, they have resulted in a scattered range of values for various mechanical properties. A MD model was proposed for CNTs under bending, torsion and axial compression loadings [5]. Simulations were conducted on SWCNTs of various diameters, helicities and lengths with large elastic deformations and results were in good agreement with the experimentally observed patterns. Moreover, the results showed that CNT behaviors could be well described by a continuum model with proper chosen set of parameters, e.g., Poisson's ratio,

M. Awang et al., *Finite Element Modeling of Nanotube Structures*,
Engineering Materials, DOI 10.1007/978-3-319-03197-2_4

ν = 0.19, Young's modulus, E = 5.5 TPa, and CNT thickness, t = 0.66 Å [10]. The results of these simulations indicated that the walls of CNTs can be accurately treated as elastic shells when proper attention is given to the definition of the wall elastic modulus and thickness. Later the strain energy and Young's modulus of SWCNT were estimated by counting the total energy of all the occupied band electrons [11]. At thickness of 0.074 nm, the Young's modulus of simulated CNT was 5.1 TPa. Their results also showed that continuum elasticity theory can serve well to describe the mechanical properties of SWCNTs.

Although, MD has been used widely in studying the deformation mechanism of CNTs, the required computational power for MD simulations restrains the size of the CNTs model [12]. Generally, the main drawback of MD is the limitation in time and length scale of the models. Even short length scale in range of nanometer for small times in range of picosecond (10–12 s) needs great deal of time and effort. MD is not practical for models that include large number of atoms [12]. Great amount of computing power and extremely complex formulations makes them suitable for small systems with at most few hundreds of atoms. It was noted that although computational power constantly increases and numerical algorithms are improved quickly, the molecular dynamics approaches are still bounded to models with just around 106–108 atoms for a fraction of seconds [13]. Therefore, it seems the evaluation of larger compounds or longer periods should be done via continuum methods.

Molecular mechanics is one such a technique. It is one of the most widely used techniques due to computational simplicity and efficiency [2]. Molecular mechanics are believed to have been developed from the Born-Oppenheimer approximation. It mainly assumes that in a molecule, the nuclei motions are independent of the electrons motions. In molecular mechanics approach, the positions of the nuclei are calculated while the arrangement of the electrons is presumed to be fixed. However, electron positions are calculated in quantum mechanics calculations based on the assumption that nuclei are at fixed positions [3, 14].

In order to create a model, a mechanical approach must be chosen to calculate all the forces between the atoms of a given molecule. In this way, good estimate of the molecule geometry could be obtained. Bonded atoms are assumed to hold together by forces that behave like mechanical springs. Non bonded interactions are replaced by attractive and repulsive forces which are known as van der Waals forces. Experimental observation such as infrared vibrational frequencies and gas compressibility data will be used to define spring stiffness and parameters or the van der Waals curves are derived. However, the defined parameters should be modified empirically to enhance the replication of geometries which are experimentally detected. In order to optimize the geometry of a given molecule, computational methods are employed to minimize its total energy caused by atomic interactions. The molecular strain could be determined by considering minimized total energies so-called the strain energy. It is mainly related to the molecular potential energy and its stable order [15].

4.2 Forces Between Bonds in Nanotubes

Basically, forces between pairs of atoms are the main variables in molecular mechanics calculations which determine the positions of the atoms in a molecule or similar compound and crystal lattice. Various kinds of these forces exist such as covalent bonds, hydrogen bonds, van der Waals and electrostatic interactions are pair of atomic forces. Groups of three atoms could create valence angles. Torsional angles and planes are formed to groups of four atoms.

Several empirical potentials for covalent bonds are available [16] and can be used to estimate physical and mechanical properties of CNTs. The typical empirical models could be classified as force field model [17–19], bond order model [20–23], and semi-empirical model [24]. The calculated energies by mentioned models can be used to determine the positions of the nuclei in a molecule. Consequently, the entire molecular structure is easy to find out.

The total strain energy of a molecule is commonly represented by a set of potential energy functions. It is more convenient to divide the total strain energy into "through bond" and "through space" terms. Therefore, the molecular mechanics model could be expressed as below.

$$U_{\text{total}} = \sum_{\text{molecule}} (U_d + U_{nd}) \tag{4.1}$$

The through bond terms, U_{d}, are called directional terms. In contrary, all non-bonded interactions are summation of repulsive and attractive terms. Repulsive interactions includes through space or non-directional terms, U_{nd},

$$U_{\text{d}} = U_b + E_\theta + U_\phi + U_\delta \tag{4.2}$$

$$U_{\text{nd}} = U_{nb} + U_z + U_{hb} \tag{4.3}$$

These terms are listed in Table 4.1 and shown in Figs. 4.1 and 4.2 [2, 25]. Various potential energy functions are given below.

$$U_{\text{b}} = \frac{1}{2} k_b (r_{ij} - r_0)^2 \tag{4.4}$$

$$U_\theta = \frac{1}{2} k_\theta (\theta_{ijk} - \theta_0)^2 \tag{4.5}$$

$$U_\phi = \frac{1}{2} k_\phi (1 + \cos(m(\phi_{ijkl} - \phi_{\text{offset}})))^2 \tag{4.6}$$

$$U_\delta = A e^{-Ed_{ij} - Cd_{ij}^{-6}} \tag{4.7}$$

Table 4.1 Potential energy functions

Potential type		Energy	Symbol
Through bond terms	Two body interactions	Bonding energy	U_b
	Three body interactions	Valence angle energy	U_θ
	Four body interactions	Torsional angle	U_ϕ
		Out-of-plane energy	U_δ
Through space terms		van der Waals interactions	U_{nb}
		Electrostatic terms	U_ε
		Hydrogen bonding	U_{hb}

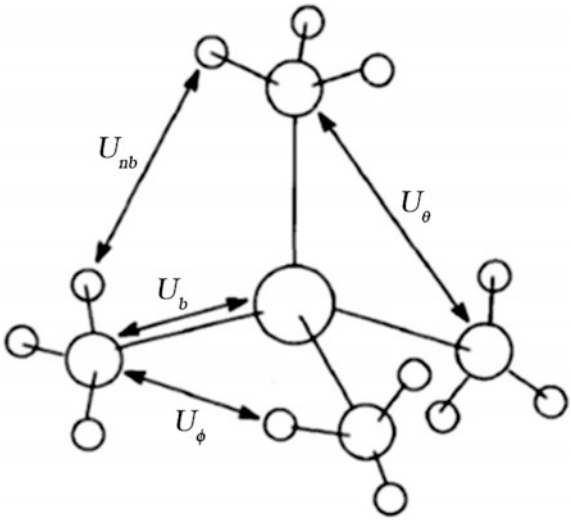

Fig. 4.1 The molecular mechanics model of force field potentials [3]

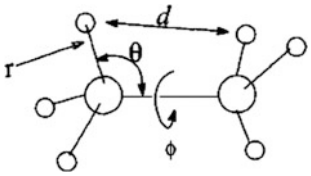

Fig. 4.2 Molecular mechanics force fields and related parameters [3]

where,

$$A = 2014(\varepsilon_i \varepsilon_j)^{\frac{1}{2}} \tag{4.8}$$

$$B = \frac{12.50}{vdw_i + vdw_j} \tag{4.9}$$

$$C = \frac{2.55(\varepsilon_i \varepsilon_j)^{\frac{1}{2}}(vdw_i + vdw_j)^6}{144} \tag{4.10}$$

$$U_\delta = \frac{1}{2} k_\delta \delta^2 \tag{4.11}$$

$$U_\varepsilon = \frac{q_i q_j}{\varepsilon d_{ij}} \tag{4.12}$$

$$U_{hb} = \frac{F}{d_{ij}^1} - \frac{G}{d_{ij}^2} \tag{4.13}$$

Parameters and variables are shown in Fig. 4.2.

Figure 4.3 shows schematic bond structure of a carbon cell and energy terms. Additional energy terms associated with electromechanical or optomechanical interactions can be likewise included [1].

Recently, great efforts have been made to employ continuum mechanics in computational modeling of CNTs. For instance, to show the validity of the classical shell theory, [25] the deformation of SWCNTs and MWCNTs were studied [using the continuum limit from the local density approximation (LDA) model developed earlier [26]. The obtained values were Young's modulus, E = 5.470 TPa, Poisson's ratio, ν = 0.34, and thickness, t = 0.75 Å. Young's modulus of the MWCNT is obviously found to be a function of the number of layers which varies from 1.04 to 4.70 TPa. Nanoscale continuum theory was proposed to directly incorporate interatomic potentials into a continuum analysis [27]. The predictions for the linear elastic modulus of a SWCNT with t = 0.335 nm yielded E = 475 GPa and E = 705 GPa for different set of parameters. Afterwards, the same theory was also applied for fracture nucleation in SWCNTs under tension [27]. Another approach was proposed to determine relationships between nanomaterials structure and properties [28]. This method connected computational chemistry and solid mechanics and

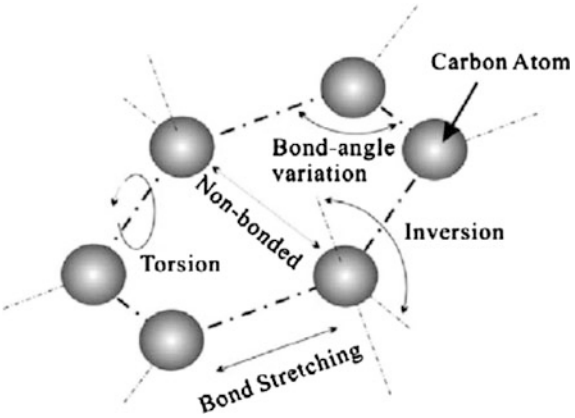

Fig. 4.3 Bond structures of a graphene cell and corresponding energy terms [12]

successfully replaced molecular structures with equivalent-continuum models. In another attempt, a structural mechanics was presented to simulate the deformation of CNTs [29]. The sectional parameters of structural members were obtained by connecting structural mechanics to molecular mechanics. Young's modulus and shear modulus of CNTs were found in increasing trend of 0.9–1.03 TPa when CNT diameter increases.

An elastic finite element approach based on molecular mechanics was later introduced using elastic beam elements to simulate the carbon-carbon chemical bonds [30]. The approach was based on an equivalency between the beam sectional stiffness and force field constants. The estimated Young's modulus of 1.033 TPa showed good agreement with what was obtained in other studies. The buckling of SWCNTs was also studied with emphasis on the out-of-plane deformation of the bonds with a rectangular cross sectional beam was assumed for the structural elements [31]. Using the same concept, a finite element model for SWCNTs was built and then upgraded to MWCNTs [32, 33]. Spring elements were used to simulate van der Waals interactions between layers of the MWCNTs.

Most of the above mentioned computational methods are limited to elastic constants like Young's modulus or Poisson's ratio of CNTs. It is mainly caused by employing harmonic potential functions. In order to obtain more realistic results on the mechanical behavior of nanotubes up to or beyond bond breaking, a more complex interatomic potential function has to be used [1, 2].

The unrolled graphene sheet subjected to axial tension in two orthogonal directions is shown in Fig. 4.4. This lattice structure can be substituted with equivalent honeycomb-like continuum structure conventionally utilized as a core material in composite sand.

The structure of honeycomb consists of several thin strut elements assembled together in hexagonal cells. Using the same analogy, the carbon–carbon bonds in molecular system of a graphene sheet can be simulated as constitutive struts of the honeycomb. The simulation procedure will be accomplished successfully, if the carbon–carbon bonds in the lattice structure of molecular system are properly

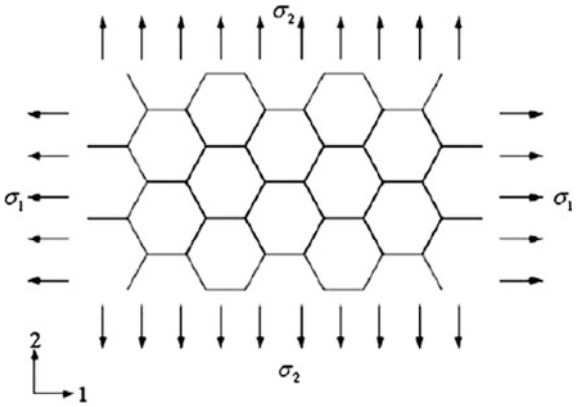

Fig. 4.4 Graphene sheet subjected to bi-axial tension loading

replaced with load bearing struts in the imaginary honeycomb configuration. As it was stated in the preceding section, the employed inter atomic potential energy of the molecular structure consists of bond stretching and angle variation. Hence, the substituted structural member for the carbon–carbon bond should be able to capture both axial and bending deformations. Frame elements are suitable structural members to fulfill these requirements. A frame structure is identified by its cross sectional area, modulus of elasticity, moment of Inertia and length. A linkage between structural mechanics and molecular mechanics was developed to obtain sectional stiffness parameters based on the constants of force fields [34]. A correlation between inter-atomic molecular potential energies and strain energies of a beam was established using equivalence of energies and thus the graphene sheet can be analyzed using solid mechanics.

4.3 Beam and Frame Elements

In structure analysis, most element types are structural elements, ranging from simple spars and beams to more complex layered shells and large strain solids. For example, the types of structural elements used in ANSYS are summarized in Table 4.2 [3]. Some of the element types have been removed in the latest version.

Beams play significant roles in many engineering applications, including buildings, bridges, automobiles, and airplanes structures. A beam is defined as a structural member whose cross-sectional dimensions are relatively smaller than its length. Beams are commonly subjected to transverse loading, which is a type of loading that creates bending in the beam. A beam subjected to a distributed load is shown in Fig. 4.5. The deflection of the neutral axis at any location x is represented by the variable u. For small deflections, the relationship between the normal stresses at a section, the bending moment at that section M, and the second moment of area I is given by the flexure formula. The flexure formula can be written as,

$$\sigma = -\frac{My}{I} \tag{4.14}$$

where y locates a point in the cross section of the beam and represents the lateral distance from the neutral axis to that point.

The deflection of the neutral axis v is also related to the internal bending moment $M(x)$, the transverse shear $V(x)$, and the load $w(x)$ according to the equations

$$EI\frac{d^2v}{d^2x} = M(x) \tag{4.15}$$

Table 4.2 Types of structural elements used in ANSYS

Category	Element name(s)
Spars	LINK1, LINK8, LINK10, LINK180
Beams	BEAM3, BEAM4, BEAM23, BEAM24, BEAM44, BEAM54, BEAMI88, BEAMI89
Pipes	PIPE16, PIPE17, PIPE18, PIPE20, PIPE59, PIPE60
2-D Solids	PLANE2, PLANE25, PLANE42, HYPER56, HYPER74, PLANE82, PLANE83, HYPER84, VISC088, VISCO106, VISC0108, PLANE145, PLANE146, PLANE182, PLANE183
3-D Solids	SOLID45, SOLID46, HYPERS8, SOLID64, SOLID65, HYPER86, VISC089, SOLID92, SOLID95, VISCO107, SOLID147, SOUD148, HYPER158, SOLID185, SOLID186, SOLID187, SOLID191
Shells	SHELL28, SHELL41, SHELL43, SHELL51, SHELL61, SHELL63, SHELL91, SHELL93, SHELL99, SHELL150, SHELL181
Interface	INTER192, INTER193, INTER194, INTER195
Contact	CONTAC12, CONTAC52, TARGE169, TARGE170, CONTA171, CONTA172, CONTA173, CONTA174, CONTA175
Coupled-field	SOLID5, PLANE13,FLUID29, FLUID30, FLUID38, SOLID62, FLUID79, FLUID80, FLUID81,SOLID98, FLUID129, INFIN110, INFIN111, FLUID116, FLUID130
Specialty	COMBIN7, LINK11, COMBIN14, MASS21, MATRIX27, COMBIN37, COMBIN39, COMBIN40, MATRIX50, SURF153, SURF154
Explicit dynamics	LINK160, BEAM161, PLANE162, SHELL163, SOLID164, COMBI165, MASS166, LINK167, SOLID168

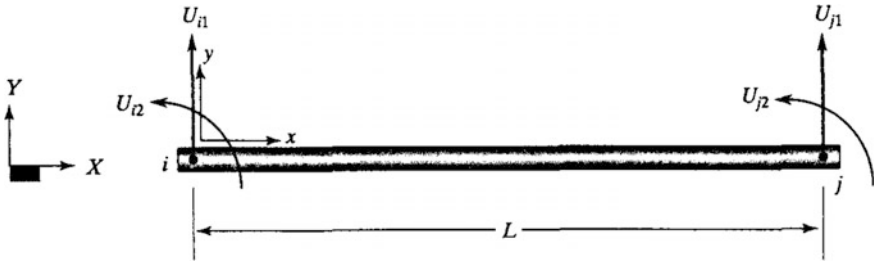

Fig. 4.5 Cross section of uniformly loaded beam

$$EI\frac{d^3v}{d^3x} = \frac{dM(x)}{dx} = V(x) \tag{4.16}$$

$$EI\frac{d^4v}{d^4x} = \frac{dV(x)}{dx} = w(x) \tag{4.17}$$

In the following derivation, we will neglect the contribution of shear stresses to the strain energy. The strain energy for an arbitrary beam element (e) then becomes:

$$\Lambda^{(a)} = \int_v \frac{\sigma\varepsilon}{2} dV = \int_v \frac{E\varepsilon^2}{2} dV = \frac{E}{2} \int_v \left(-y \frac{d^2v}{dx^2}\right)^2 dV \tag{4.18}$$

$$\Lambda^{(a)} = \frac{E}{2} \int_v^l \left(\frac{d^2v}{dx^2}\right)^2 dx \int_v y^2 dA \tag{4.19}$$

$$\Lambda^{(a)} = \frac{EL}{2} \int_0^L \left(\frac{d^2v}{dx^2}\right)^2 dx \tag{4.20}$$

Before integrating Eq. (4.7), beam element has to be specified. A simple beam element consists of two nodes. At each node, there are two degrees of freedom, a vertical displacement, and a rotation angle (slope), as shown in Fig. 4.6.

There are four nodal values associated with a beam element. Therefore, a third-order polynomial with four unknown coefficients is used to represent the displacement field. Moreover, the first derivatives of the shape functions should be continuous. The resulting shape functions are commonly referred to as *Hermite shape* functions.

Frames represent structural members that may be rigidly connected with welded or bolted joints. For such structures, in addition to rotation and lateral displacement, we also need to be concerned about axial deformations. Here, we will focus on plane frames.

The frame element, shown in Fig. 4.6, consists of two nodes. At each node, there are three degrees of freedom: a longitudinal displacement, a lateral displacement, and a rotation [35].

Referring to Fig. 4.6, note that u_{i1}, represents the longitudinal displacement and u_{i2} and u_{i3}, represent the lateral displacement and the rotation at node i, respectively. In the same manner, u_{ji}, u_{j2} and u_{j3} represent the longitudinal displacement, the lateral displacement and the rotation at node i, respectively. In general, two frames of reference R will be required to describe frame elements: a global

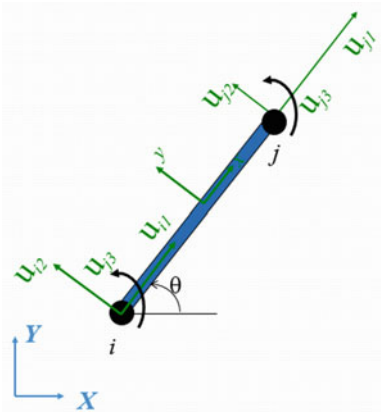

Fig. 4.6 Frame element with two nodes

coordinate system and a local frame of reference. We choose a fixed global coordinate system (X, Y) for several uses: (1) to represent the location of each joint (node) and to keep track of the orientation of each element using angles such as 0; (2) to apply the constraints and the applied loads in terms of their respective global components; and (3) to represent the solution. We will also need a local, or elemental, coordinate system to describe the axial-load behavior of an element. The relationship between the local coordinate system (x, y) and the global coordinate system (X Y) is shown in Fig. 4.6. Because there are three degrees of freedom associated with each node, the stiffness matrix for the frame element will be a 6×6 matrix. The local degrees of freedom are related to the global degrees of freedom through the transformation matrix [*T*], based on the relationship,

$$[\mathrm{u}] = [\mathrm{T}][\mathrm{U}]$$

where the transformation matrix is

$$[\mathrm{T}] = \begin{bmatrix} \cos\theta & \sin\theta & 0 & 0 & 0 & 0 \\ -\sin\theta & \cos\theta & 0 & 0 & 0 & 0 \\ 0 & 0 & 1 & 0 & 0 & 0 \\ 0 & 0 & 0 & \cos\theta & \sin\theta & 0 \\ 0 & 0 & 0 & -\sin\theta & \cos\theta & 0 \\ 0 & 0 & 0 & 0 & 0 & 1 \end{bmatrix} \tag{4.21}$$

In the previous section, we developed the stiffness matrix attributed to bending for a beam e1ement. *U* matrix accounts for lateral displacements and rotations at each node,

$$[K]_{xy} = \frac{EI}{L^3} \begin{bmatrix} 0 & 0 & 0 & 0 & 0 & 0 \\ 0 & 12 & 6L & 0 & -12 & 6L \\ 0 & 6L & 4L^2 & 0 & -6L & 2L^2 \\ 0 & 0 & 0 & 0 & 0 & 0 \\ 0 & -12 & -6L & 0 & 12 & -6L \\ 0 & 6L & 2L^2 & 0 & -6L & 4L^2 \end{bmatrix} \tag{4.22}$$

To represent the contribution of each term to nodal degrees of freedom, the degrees of freedom are shown above and alongside the stiffness matrix in Eq. (4.9). The stiffness matrix for members under axial loading is represented as

$$[K]_{axial} = \begin{bmatrix} \frac{AE}{L} & 0 & 0 & -\frac{AE}{L} & 0 & 0 \\ 0 & 0 & 0 & 0 & 0 & 0 \\ 0 & 0 & 0 & 0 & 0 & 0 \\ -\frac{AE}{L} & 0 & 0 & \frac{AE}{L} & 0 & 0 \\ 0 & 0 & 0 & 0 & 0 & 0 \\ 0 & 0 & 0 & 0 & 0 & 0 \end{bmatrix} \tag{4.23}$$

Adding Eqs. (4.9) and (4.10) results in the stiffness matrix for a frame element:

$$[K]_{xy}^{(e)} = \begin{bmatrix} \frac{AE}{L} & 0 & 0 & -\frac{AE}{L} & 0 & 0 \\ 0 & \frac{12EI}{L^3} & \frac{6EI}{L^2} & 0 & -\frac{12EI}{L^3} & \frac{6EI}{L^2} \\ 0 & \frac{6EI}{L^2} & \frac{4EI}{L} & 0 & -\frac{6EI}{L^2} & \frac{2EI}{L} \\ -\frac{AE}{L} & 0 & 0 & \frac{AE}{L} & 0 & 0 \\ 0 & \frac{12EI}{L^3} & -\frac{6EI}{L^2} & 0 & \frac{12EI}{L^3} & -\frac{6EI}{L^2} \\ 0 & \frac{6EI}{L^2} & \frac{2EI}{L} & 0 & -\frac{6EI}{L^2} & \frac{4EI}{L} \end{bmatrix} \tag{4.24}$$

Note that we need to represent Eq. (4.11) with respect to the global coordinate system. To perform this task, we must substitute for the local displacements in terms of the global displacements in the strain energy equation, using the transformation matrix and performing the minimization. These steps result in the relationship

$$[\mathrm{K}]^{(e)} = [\mathrm{T}]^{T}[\mathrm{K}]_{xy}^{(e)}[\mathrm{T}] \tag{4.25}$$

4.3.1 Three-Dimensional Beam Element

The 3D beam element used in *ANSYS* is suited for situations wherein the beam may be subjected to loads that can create tension, compression, bending about different axes, and twisting (torsion). At each node, there are six degrees of freedom, displacements in *X, Y*, and *Z* directions, and rotation about *X, Y*, and *Z* axes. Therefore, the elemental matrix for a three-dimensional beam element is a 12 × 12 matrix. ANSYS's three-dimensional elastic beam element is shown in Fig. 4.7 [36].

The element input data include node locations, the cross-sectional area, two moments of inertia (I_{ZZ} and I_{yy}), two thicknesses (*TKY* and *TKZ*), an angle of orientation (θ) about the element x-axis, the torsional moment of inertia ($\mathrm{I_{xx}}$) and the material properties. If $\mathrm{I_{xx}}$ is not specified or is equal to 0.0, ANSYS assumes that it is equal to the polar moment of inertia ($I_{yy} + I_{ZZ}$). The element x-axis is oriented from node *I* toward node *J*. For the two-node option, the default ($\theta = 0°$) orientation of the element y-axis, *ANSYS* automatically sets the orientation parallel to the global *X-Y* plane.

For the case where the element is parallel to the global Z axis, the element y-axis is oriented parallel to the global Y-axis (as shown). For user control of the element orientation about the element x-axis, use the 6 angle (THETA) or the third-node option. If both are defined, the third-node option takes precedence. The third node (K), if used, defines a plane (with I and J) containing the element x and z axes (as shown).

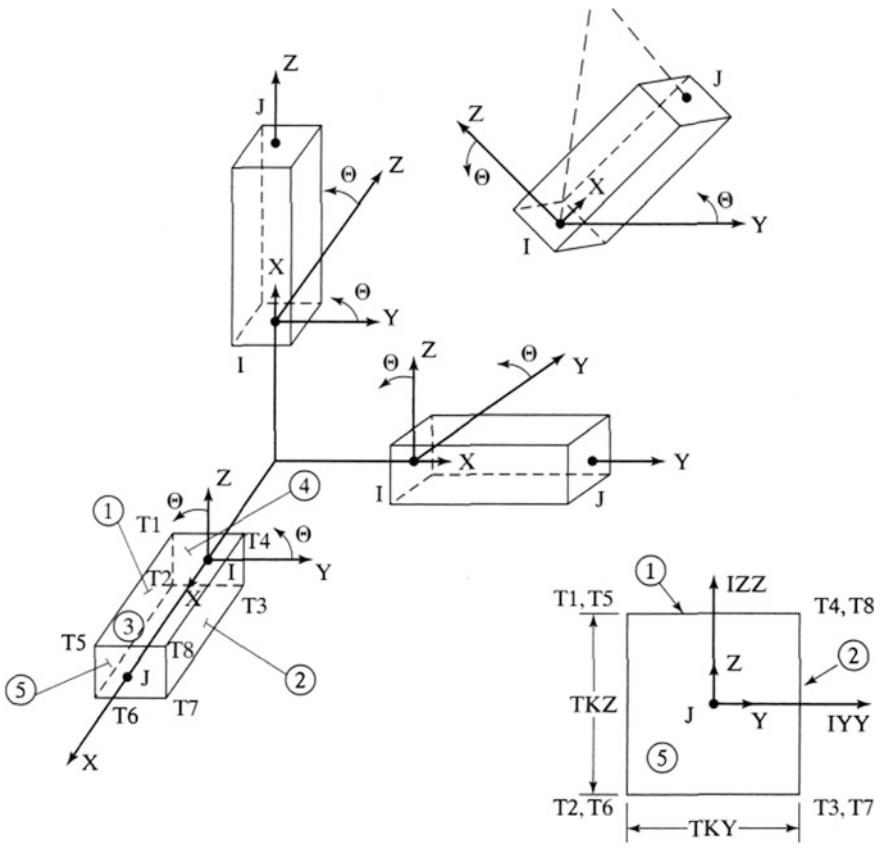

Fig. 4.7 BEAM188 3-D elastic beam

The input data for BEAM188 is summarized below:

Nodes

I, J, K (K orientation node is optional)

Degrees of Freedom

UX, UY, UZ (displacements in X, Y, and Z-directions)

ROTX (rotation about X-axis), ROTY (rotation about Y-axis), ROTZ (rotation about Z-axis)

Real Constants

AREA, I_{zz}, I_{yy}, TKZ, TKY, THETA,

ISTRN (initial strain in the element), I_{xx}

Material Properties

EX (modulus of elasticity), ALPX (Poisson's ratio), DENS (density), GXY (shear modulus), DAMP (damping)

Surface Loads
Pressures
face 1 (I−J) (-Z normal direction)
face 2 (I−J) (—Y normal direction)
face 3 (I−J) (+X tangential direction)
face 4 (I) (+X axial direction)
face 5 (J) (−X axial direction)
(use negative value for opposite loading)
Temperatures
Tl, T2, T3, T4, T5, T6, T7, T8
Stresses

To review stresses in beams, you must first copy these results into element tables, and then you can list them or plot them. These items are obtained using item label and sequence numbers. For a BEAM188 element, the following output information is available: the maximum stress, which is computed as the direct stress plus the absolute values of both bending stresses; the minimum stress, which is calculated as the direct stress minus the absolute value of both bending stresses. BEAM188 output includes additional stress values—examples of these stresses are given in Table 4.3. Once you decide which stress values you want to look at, you can read them into a table using item labels and sequence numbers. Examples of the item labels and sequence numbers for BEAM188 are summarized in Table 4.4.

Table 4.3 Examples of stresses computed by ANSYS

Type	Description
SDIR	Axial direct stress
SB YT	Bending stress on the element + Y side of the beam
SBYB	Bending stress on the element − Y side of the beam
SBZT	Bending stress on the element + Z side of the beam
SBZB	Bending stress on the element − Z side of the beam
SMAX	Maximum stress (direct stress + bending stress)
SMIN	Minimum stress (direct stress − bending stress)

Table 4.4 Item and sequence numbers for the BEAM188 element

Type	Group	Item label	Sequence No
SDIR	LS	1	6
SBYT	LS	2	7
SBYB	LS	3	8
SBZT	LS	4	9
SBZB	LS	5	10
SMAX	NMISC	1	3
SMIN	NMISC	2	4

References

1. T. Chang, H. Gao, Size-dependent elastic properties of a single-walled carbon nanotube via a molecular mechanics model. J. Mech. Phys. Solids **51**, 1059–1074 (2003)
2. P. Comba, T.W. Hambley, B. Martin, *Molecular Modeling of Inorganic Compounds*, 3 edn. (Wiley, 2009)
3. A. Hinchliffe, *Molecular Modelling for Beginners* (Wiley, 2008)
4. B.I. Yakobson, P. Avouris, Mechanical properties of carbon nanotubes. Topics Appl. Phys. **80**, 287–327 (2001)
5. B.I. Yakobson, C.J. Brabec, J. Bernholc, Nanomechanics of carbon tubes: instabilities beyond linear response. Phys. Rev. Lett. **76**, 2511–2514 (1996)
6. S. Iijima, C. Brabec, A. Maiti, J. Bernholc, Structural flexibility of carbon nanotubes. J. Chem. Phys. **104**, 2089–2092 (1996)
7. M.B. Nardelli, B.I. Yakobson, J. Bernholc, Mechanism of strain release in carbon nanotubes. Phys. Rev. B **57**, 4279 (1998)
8. L. Vaccarini, C. Goze, L. Henrard, E. Hernández, P. Bernier, A. Rubio, Mechanical and electronic properties of carbon and boron-nitride nanotubes. Carbon **38**, 1681–1690 (2000)
9. Q. Zeng, A. Yu, G. Lu, Multiscale modeling and simulation of polymer nanocomposites. Prog. Polym. Sci. **33**, 191–269 (2008)
10. B.I. Yakobson, M.P. Campbell, C.J. Brabec, J. Bernholc, High strain rate fracture and C-chain unraveling in carbon nanotubes. Comput. Mater. Sci. **8**, 341–348 (1997)
11. Z. Xin, Z. Jianjun, O.-Y. Zhong-can, Strain energy and Young's modulus of single-wall carbon nanotubes calculated from electronic energy-band theory. Phys. Rev. B **62**, 13692 (2000)
12. M.M. Shokrieh, R. Rafiee, On the tensile behavior of an embedded carbon nanotube in polymer matrix with non-bonded interphase region. Compos. Struct. **92**, 647–652 (2010)
13. B.B.Q. Lu, The role of atomistic simulations in probing the small-scale aspects of fracture—a case study on a single-walled carbon nanotube. Eng. Fract. Mech. **72**, 2037–2071 (2005)
14. N.L. Allinger, in *Molecular Structure.* Molecular Structures by Computational Methods (Wiley, 2010)
15. N.L. Allinger, *Molecular Structure: Understanding Steric and Electronic Effects from Molecular Mechanics* (Wiley, 2010)
16. R. Ruoff, Mechanical properties of carbon nanotubes: theoretical predictions and experimental measurements. C.R. Phys. **4**, 993–1008 (2003)
17. T. Belytschko, S.P. Xiao, G.C. Schatz, R.S. Ruoff, Atomistic simulations of nanotube fracture. Phys. Rev. B **65**, 235–430 (2002)
18. S.L. Mayo, B.D. Olafson, W.A. Goddard, DREIDING: a generic force field for molecular simulations. J. Phys. Chem. **94**, 8897–8909 (1990)
19. N.L. Allinger, Conformational analysis. 130. mm2. a hydrocarbon force field utilizing vi and v2 torsional terms. J. Am. Chem. Soc. **99**, 8127–8134 (1977)
20. G.C. Abell, Empirical chemical pseudopotential theory of molecular and metallic bonding. Phys. Rev. B **31**, 6184–6196 (1985)
21. J. Tersoff, Empirical interatomic potential for carbon, with applications to amorphous carbon. Phys. Rev. Lett. **61**, 2879–2882 (1988)
22. D.W. Brenner, Empirical potential for hydrocarbons for use in simulating the chemical vapor deposition of diamond films. Phys. Rev. B **42**, 9458–9471 (1990)
23. D.H. Robertson, D.W. Brenner, J.W. Mintmire, Energetics of nanoscale graphitic tubules. Phys. Rev. B **45**, 12592–15595 (1992)
24. D.G. Pettifor, I.I. Oleinik, Bounded analytic bond-order potentials for sigma and pi bonds. Phys. Rev. Lett. **84**, 4124 (2000)
25. Z.-C. Tu, Z.-C. Ou-Yang, Single-walled and multiwalled carbon nanotubes viewed as elastic tubes with the effective Young's moduli dependent on layer number. Phys. Rev. B **65,** 233407–4 (2002)

26. T. Lenosky, X. Gonze, M. Teter, V. Elser, Energetics of negatively curved graphitic carbon. Nature **355**, 333–335 (1992)
27. L. Zhang, C. Wan, Y. Zhang, Morphology and electrical properties of polyamide 6/polypropylene/multi-walled carbon nanotubes composites. Compos. Sci. Technol. **69**, 2212–2217 (2009)
28. G.M. Odegarda, T.S. Gatesb, L.M. Nicholsonc, K.E. Wised, Equivalent-continuum modeling of nano-structured materials. Compos. Sci. Technol. **62**, 1869–1880 (2002)
29. H. Zhang, J. Wang, X. Guo, Predicting the elastic properties of single-walled carbon nanotubes. J. Mech. Phys. Solids **53**, 1929–1950 (2005)
30. C. Li, A structural mechanics approach for the analysis of carbon nanotubes. Int. J. Solids Struct. **40**, 2487–2499 (2003)
31. H. Wan, F. Delale, A structural mechanics approach for predicting the mechanical properties of carbon nanotubes. Meccanica **45**, 43–51 (2010)
32. K. Tserpes, P. Papanikos, Finite element modeling of single-walled carbon nanotubes. Compos. B Eng. **36**, 468–477 (2005)
33. C.-W. Fan, J.-H. Huang, C. Hwu, Y.-Y. Liu, Mechanical properties of single-walled carbon nanotubes—a finite element approach. Adv. Mater. Res. **33–37**, 937–942 (2008)
34. C.W. Fan, Y.Y. Liu, C. Hwu, Finite element simulation for estimating the mechanical properties of multi-walled carbon nanotubes. Appl. Phys. A **95**, 819–831 (2009)
35. C. Li, T.-W. Chou, Elastic moduli of multi-walled carbon nanotubes and the effect of van der Waals forces. Compos. Sci. Technol. **63**, 1517–1524 (2003)
36. Z. Han, A. Fina, Thermal conductivity of carbon nanotubes and their polymer nanocomposites: a review. Prog. Polym. Sci. **36**, 914–944 (2010)

Chapter 5
Linear Finite Element Analysis of Nanotubes

5.1 Introduction

From proven chemical calculations [1], the harmonic functions provide a reasonable approximation to the potential energy of molecular systems in which the bond length is near its equilibrium position. In this particular formula, the energy terms associated to bond stretching (5.1), angle bending (5.2) and inversion (5.3) are described as [2, 3],

$$\mathrm{U}_r = \frac{1}{2}\sum_i K_i(r - r_0)^2 \tag{5.1}$$

$$\mathrm{U}_\theta = \frac{1}{2}\sum_j C_j(\theta - \theta_0)^2 \tag{5.2}$$

$$\mathrm{U}_\phi = \frac{1}{2}\sum_k B_k(\varphi - \varphi_0)^2 \tag{5.3}$$

where $r - r_0$, $\theta - \theta_0$, $\varphi - \varphi_0$ are the elongation of bond i, variance of bond angle j and inversion angle k. K_i, C_j and B_k are force constants associated with bond stretching, angle variance and inversion, respectively. Formulation was done by using schematic diagram as shown in Fig. 5.1.

In such cases, elastic Young's modulus ($\mathrm{E_n}$) of armchair (n, n) and zigzag (n, 0) CNTs could be expressed as the following,

$$E_n = \frac{4\sqrt{3}K}{3\lambda K a^2/C + 9},\ \lambda = \frac{7 - \cos(\pi/n)}{34 + 2\cos(\pi/n)} \tag{5.4}$$

M. Awang et al., *Finite Element Modeling of Nanotube Structures*,
Engineering Materials, DOI 10.1007/978-3-319-03197-2_5

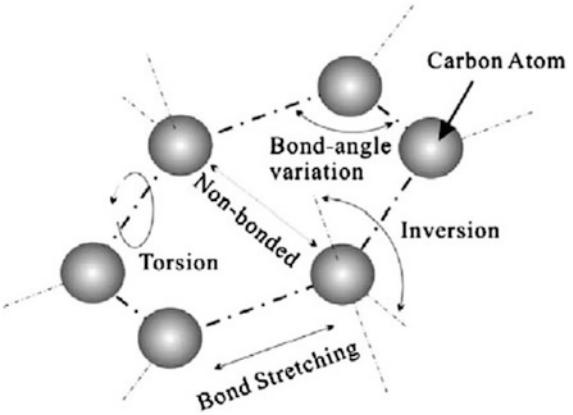

Fig. 5.1 A schematic illustration of atomic interactions in CNT model

where K, C and a are axial stiffness of the carbon–carbon covalent bond (742 nN/nm), bending stiffness resulting from the angular distortion of bond angle (1.42 nN/nm) and bond length, respectively [2].

To calculate the elastic moduli of beam elements, a linkage between molecular and continuum mechanics is used [2, 4, 5]. For clarity, the linkage is illustrated in Fig. 5.2.

From the viewpoint of molecular mechanics, CNTs may be regarded as large molecules consisting of carbon atoms. The atomic nuclei may be regarded as material points and their motions are regulated by a force-field generated by electron–nucleus and nucleus–nucleus interactions. The force-field is expressed in the form of steric potential energy, which depends solely on the relative positions of the nuclei constituting the molecule. The general expression of the total steric potential energy, when omitting the electrostatic interaction, is the following sum of

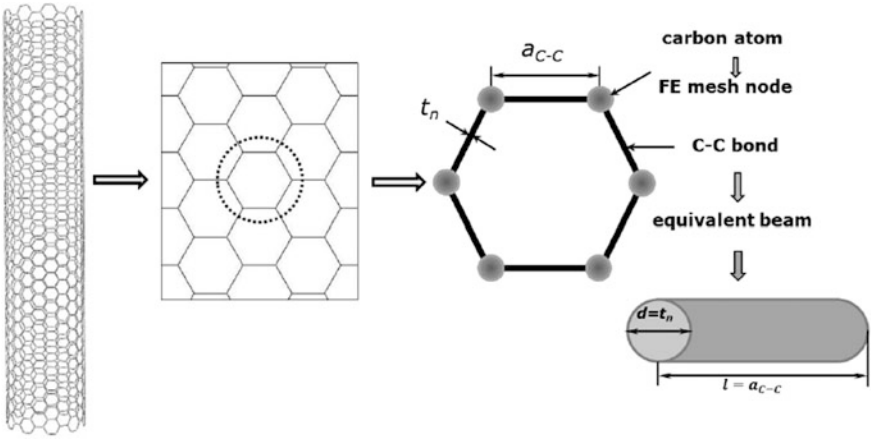

Fig. 5.2 Space-frame structure with beam elements substituting C–C bonds

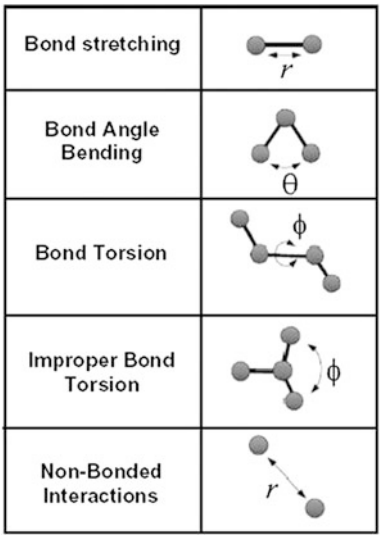

Fig. 5.3 Interatomic interactions in molecular mechanics

energies due to valence of bonded interactions or bonded and non-bonded interactions [6]:

$$U_{\text{Total}} = \sum U_r + \sum U_\theta + \sum U_\phi + \sum U_\omega + \sum U_{vdw} \tag{5.5}$$

where U_r is the energy due to bond stretch interaction, U_θ the energy due to bending (bond angle variation), U_ϕ the energy due to dihedral angle torsion, U_ω the energy due to out-of-plane torsion and U_{vdw} the energy due to non-bonded van der Waals interaction. A schematic representation of the interatomic interactions in molecular mechanics, as taken into account in Eq. (5.2), is shown in Fig. 5.3.

For covalent systems, the main contributions to the total steric energy come from the first four terms of Eq. (5.2). Under the assumption of small deformation, the harmonic approximation is adequate for describing the energy [7]. By adopting the simplest harmonic forms and merging dihedral angle torsion and out-of-plane torsion into a single equivalent term, the expressions for each form of energy is determined (Eq. 5.6).

$$\begin{aligned} U_r &= \frac{1}{2}k_r(r - r_0)^2 = \frac{1}{2}k_r(\Delta r)^2 \\ U_\theta &= \frac{1}{2}k_\theta(\theta - \theta_0)^2 = \frac{1}{2}k_\theta(\Delta\theta)^2 \\ U_\tau &= U_\phi + U_\omega = \frac{1}{2}k_\tau(\Delta\phi)^2 \end{aligned} \tag{5.6}$$

where k_r, k_θ, and k_τ are the bond stretching, bond bending and torsional resistance force constants, respectively, while Δr, $\Delta\theta$ and $\Delta\varphi$ represent bond stretching increment, bond angle variation and angle variation of bond twisting, respectively.

In order to determine the elastic moduli of beam elements, relations between the sectional stiffness parameters in structural mechanics and the force-field constants in molecular mechanics need to be obtained. For simplicity reasons, the sections of the bonds are assumed to be identical and circular, and therefore the moments of inertia are equal, i.e. I_{xz}, I_{yz}. The elastic moduli that need to be determined are the Young's modulus, E and shear modulus, G. The deformation of a space-frame results in changes of strain energies. Thus, the elastic moduli can be determined through the equivalence of the energies due to the interatomic interactions (Eq. 5.6) and the energies due to deformation of the structural elements of the space- frame. As each of the energy terms of Eq. (5.6) represents specific deformations, and no interactions are included, the strain energies of structural elements under specific deformations will be considered.

According to classical structural mechanics, the strain energy of a uniform beam of length, L and cross-section, A under pure axial force, N can be written as

$$U_A = \frac{1}{2}\int_0^L \frac{N^2}{EA}dL = \frac{1}{2}\frac{N^2 L}{EA} = \frac{1}{2}\frac{EA}{L}(\Delta L)^2 \tag{5.7}$$

where dL is the axial stretching deformation. The strain energy of a uniform beam under pure bending moment, M is

$$U_M = \frac{1}{2}\int_0^L \frac{M^2}{EI}dL = \frac{2EI}{L}\alpha^2 = \frac{1}{2}\frac{EI}{L}(2\alpha)^2 \tag{5.8}$$

where α denotes the rotational angle at the ends of the beam. The strain energy of a uniform beam under pure torsion T is

$$U_T = \frac{1}{2}\int_0^L \frac{T^2}{GJ}dL = \frac{1}{2}\frac{T^2 L}{GJ} = \frac{1}{2}\frac{GJ}{L}(\Delta\beta)^2 \tag{5.9}$$

where $\Delta\beta$ is the relative rotation between the ends of the beam and J the polar moment of inertia.

It can be concluded that U_r, U_A represent the stretching energies in the two systems (molecular and structural), U_θ, U_M are the bending energies, and U_τ, U_T are the torsional energies. It can be assumed that the rotation angle 2α is equivalent to the total change Δq of the bond angle, ΔL is equivalent to Δr, and Δβ is equivalent to Δf. Therefore, by comparing Eq. (5.6) with Eqs. (5.7–5.9), the following direct relationships between the structural mechanics parameters EA, EI and GJ and the molecular mechanics parameters k_r, k_q and k_t are obtained

$$\frac{EA}{L} = k_r, \quad \frac{EI}{L} = k_\theta, \quad \frac{GJ}{L} = k_\tau \tag{5.10}$$

Equation (5.10) forms the basis for the application of structural mechanics to the analysis of CNTs and carbon-related nano-structures. By assuming a circular beam

section with diameter d, and setting $A_Z = d^2/4$, $I_Z = d^4/64$ and $J_Z = d^4/32$, Eq. (5.10) give

$$d = 4\sqrt{\frac{-=k_\theta}{k_r}}, \quad E = \frac{k_r^2 L}{4\pi k_\theta}, \quad G = \frac{k_r^2 k_\tau L}{8\pi k_\theta^2} \tag{5.11}$$

Equation (5.11) establishes the basis for the application of continuum mechanics to the analysis of the mechanical behavior of CNTs, and provides the input for simulation of the CNTs as space-frame structures. The values of force constants and input data for the FE model are given in Table 5.1.

Given the force constants k_r, k_θ and k_τ together with the bond diameter (d) and the elastic moduli can be obtained from Eq. (5.11) and thereafter other mechanical properties can be computed. Taking the constants from various sources [2, 4, 5], and using Eq. (5.11) d = 0.147 nm, E = 5.49 TPa and G = 0.871 TPa. The procedure followed above provides a unique value of the bond diameter (equal to wall thickness). However, different values of the wall thickness have been used in the literature. In order to compare the evaluated elastic moduli of the SWCNTs with the literature results, the FE model has been implemented using various values of wall thickness. To satisfy the energy equivalence between molecular and structural approaches, the moment of inertia I was evaluated from Eq. (5.10) and not as $I = d^4/64$.

As stated earlier, the potential use of CNTs and other inorganic nanotubes as reinforcing materials in nano-composites or in present advanced composites, originated the need to investigate their mechanical properties. Two of the properties receiving great attention, because they are appointing the effectiveness of CNTs, are the Young's modulus and tensile strength. Many theoretical and experimental research efforts have been placed on the investigation of Young's modulus of CNTs [2, 3, 8–27]. From the review, it is clear that the values of Young's modulus of CNTs either calculated using theoretical methods or measured using experimental techniques show a very wide scatter. The reasons for that are due to the physical

Table 5.1 Input parameters for the FE model of CNTs

Parameters	Value	Formula
Force constant, k_r	6.52×10^{-7} N nm^{-1}	–
Force constant, k_θ	8.76×10^{-10} N nm rad^{-2}	–
C–C bond or beam length ($l = a_{c-c}$)	0.1421	–
Diameter (d)	0.147 nm	$d = 4\sqrt{k_\theta/k_r}$
Cross section area, A_b	0.01688 nm^2	$A_b = \pi d^2/4$
Moment of inertia, I_b	2.269×10^{-5} nm^4	$I_b = \pi d^4/64$
Young's modulus, E_b	5488 GPa	$E_b = k_r^2 l/4\pi k_\theta$
Tensile rigidity, E_bA_b	92.65 nN	$E_bA_b = k_r l$
Bending rigidity, E_bI_b	0.1245 nN nm^2	$E_bI_b = k_\theta l$

difficulty of direct experimental measurements, the approximation in theoretical methods used and the dependence of Young's modulus to various geometrical and nano-structural parameters. Thus, there is a need to use the FE modeling in order to assess the effect of wall thickness, diameter and chirality on the Young's and shear moduli of nanotubes.

Simulation of some mechanical properties of nanotubes can be carried out using commercial finite element software currently available such as ANSYS, I-IDEAS, NASTRAN, ABAQUS, COSMOS, ALGOR etc. with each having respective capabilities and limitations [28].

5.2 Overview of *ANSYS* Software

ANSYS is a general-purpose finite-element modeling package for numerically solving a wide variety of mechanical problems. These problems include static/dynamic, structural analysis (both linear and nonlinear), heat transfer, and fluid problems, as well as acoustic and electromagnetic problems. In general, a finite-element solution may be broken into the following three stages. (1) Preprocessing: defining the problem. The major steps in preprocessing are (i) define keypoints/lines/areas/volumes, (ii) define element type and material/geometric properties, and (iii) mesh lines/areas/volumes as required [29].

The amount of detail required will depend on the dimensionality of the analysis, i.e., 1D, 2D, axisymmetric, and 3D. (2) Solution: assigning loads, constraints, and solving Here, it is necessary to specify the loads (point or pressure), constraints (translational and rotational), and finally solve the resulting set of equations. (3) Postprocessing: further processing and viewing of the results In this stage one may wish to see (i) lists of nodal displacements, (ii) element forces and moments, (iii) deflection plots, and (iv) stress contour diagrams or temperature maps [30–33].

5.3 Building a Linear Model for a Typical SWCNT

The ANSYS program has many finite-element analysis capabilities, ranging from a simple linear static analysis to a complex nonlinear transient dynamic analysis. Building a finite-element model requires more time than any other part of the analysis as illustrated in Fig. 5.4.

At the onset, a *jobname* and analysis *title* has to be specified. Next, the *PREP7* preprocessor is used to define the element types, element real constants, material properties, and the model geometry. It is important to remember that ANSYS does not assume a system of units for intended analysis. Consider a nanotube with zigzag chilarity (10,0), length of 100 Å and having C–C bond length was 1.14 Å; in order to create an atomic model of this nanotube in ANSYS, we have to follow the steps detailed in subsequent sections.

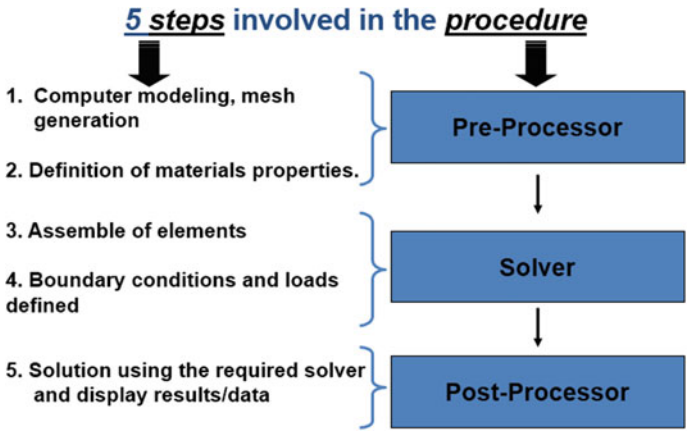

Fig. 5.4 Steps involved for FEM in *ANSYS*

5.3.1 Specifying Units

First of all, activate [A] SI (MKS) button to inform the *ANSYS* program that this system of units is proposed to be used in the analysis. Any system of units can be used so long as it is ensured that units are consistent for all input data. Units cannot be set directly from the GUI. In order to set units as the international system of units (SI) from **ANSYS Main Menu**, select **Preprocessor → Material Props → Material Library → Select** Units. Figure 5.5 shows the resulting window.

Before we feed in the input data of the BEAM 188 elements properties, the dimensions of the parameters stated above should be further adjusted to avoid

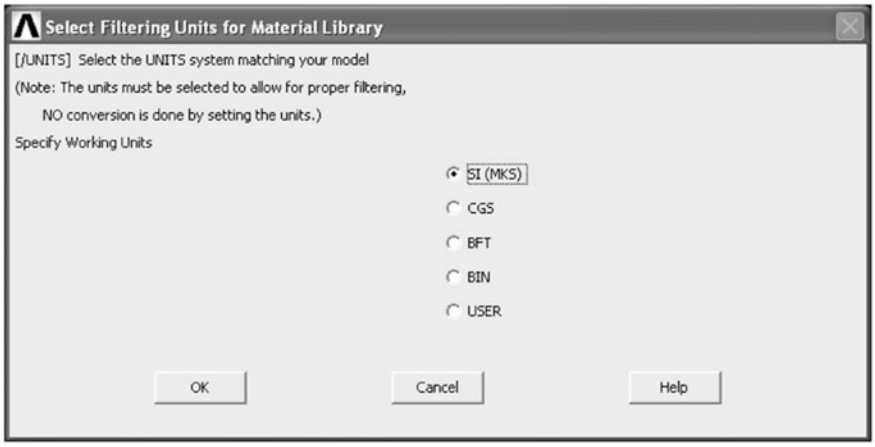

Fig. 5.5 Selection of appropriate unit system in *ANSYS*

possible digits of overflow/underflow error during the computation performed by ANSYS. Thus, we adjust the dimensions as follows:

$$L_{\text{an}} = 10^{10}L, \quad F_{\text{an}} = 10^{20}F, \quad M_{\text{an}} = 10^{26}M,$$

where the original dimensions of length L, force F and mass M are m, N and kg, respectively, and the subscript "an" denotes the associated values in ANSYS. Thereby the adjustment of the derived dimensions which will appear in the present problem can be represented as

$$E_{\text{an}} = E, \quad G_{\text{an}} = G, \quad k_{s,\text{an}} = 10^{10}k_s,$$
$$f_{\text{an}} = 10^{-8}f, \quad P_{\text{cr,an}} = 10^{20}P_{\text{cr}},$$

where E, G, k_s, f and P_{cr} denote respectively the Young's modulus, shear modulus, spring element stiffness, natural frequency and buckling load. After such adjustment, the numerical parts of the input data prepared for the *BEAM188* elements can be listed respectively as $E_{\text{an}} = 5.49 \times 10^{12}$, $A_{\text{an}} = 1.69$, $\nu_{\text{an}} = 0.3$ and $k_{s,\text{an}} = 3.7 \times 10^{10}$, where $A_{\text{an}} = \pi d^2/4$ is the area of the cross section, $d_{\text{an}} = 1.47$ is the diameter of the cross section [4, 5, 34, 35].

5.3.2 Defining Element Types and Real Constants

The *ANSYS* element library contains more than 200 different element types. Each element type has a unique number and a prefix that identifies the element category. In order to define element types, one must be in PREP7. From **ANSYS Main Menu**, select **Preprocessor → Element Type → Add/Edit/Delete**. In response, a pop-up window shown in Fig. 5.6 appears. Click on [A] **Add** button and a new frame, shown in Fig. 5.7, appears. Select an appropriate element type for the analysis performed, e.g., [A] **Beam** and [B] **Beam188** as shown in Fig. 5.7. Thereafter select OK and then Options to change elements settings (Fig. 5.8).

5.3.3 Defining Material Properties

Most element types require material properties. Depending on the application, material properties may be:

- Linear or nonlinear
- Isotropic, orthotropic, or anisotropic
- Constant temperature or temperature-dependent.

As with element types and real constants, each set of material properties has a material reference number. The table of material reference numbers versus material

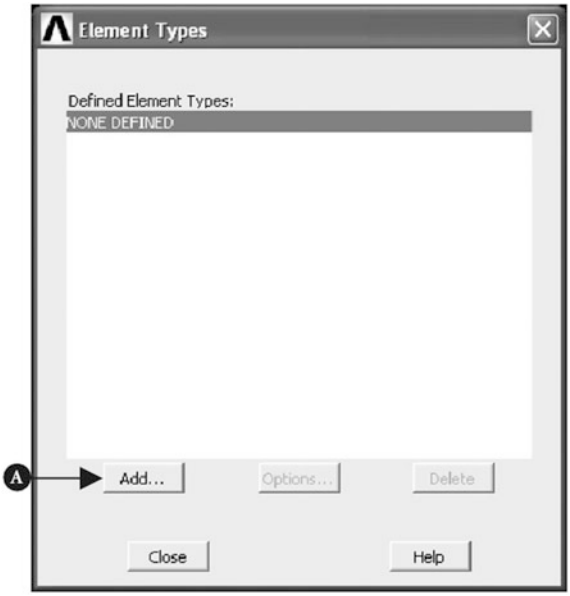

Fig. 5.6 Addition of element type from *ANSYS* library

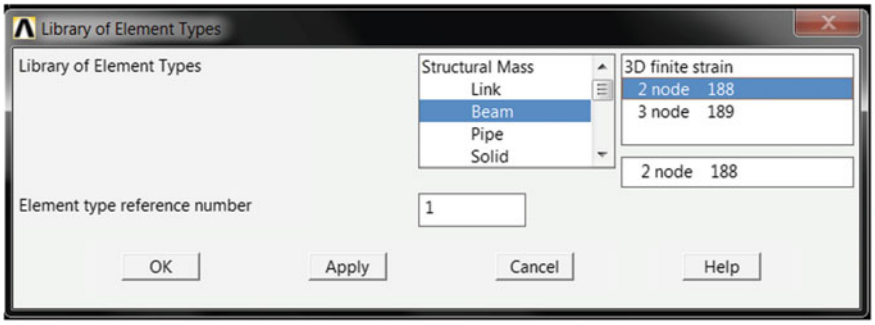

Fig. 5.7 Selection of BEAM 188 element

property sets is called the *material table*. Within one analysis, you may have multiple material property sets (to correspond with multiple materials used in the model). ANSYS identifies each set with a unique reference number.

While defining the elements, point to the appropriate material reference number using one of the following: **Main Menu > Preprocessor > -Attributes-> Define > Default Attribs**. For simple linear material models, the options available are indicated in Fig. 5.9.

For CNT, the input parameters used are shown in Fig. 5.10 with *EX* representing Young's modulus and *PRXY* the Poisso's ratio along x-y axis.

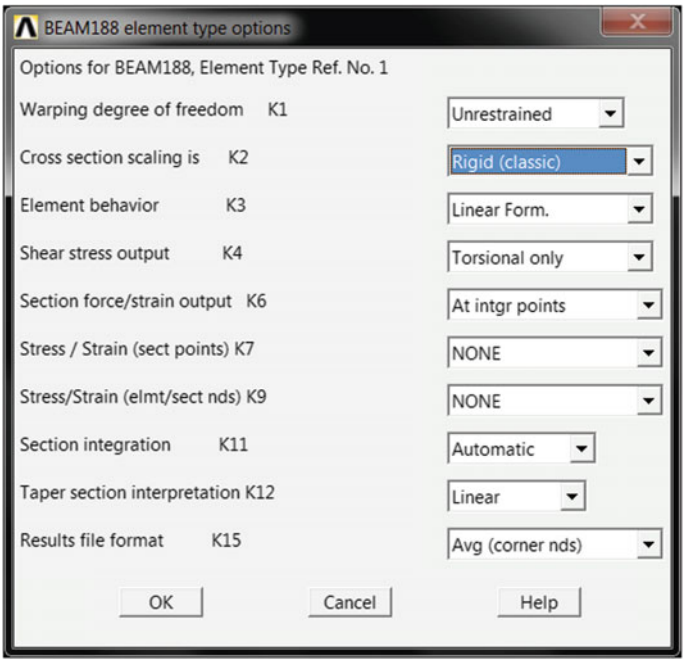

Fig. 5.8 Settings for BEAM188 element type

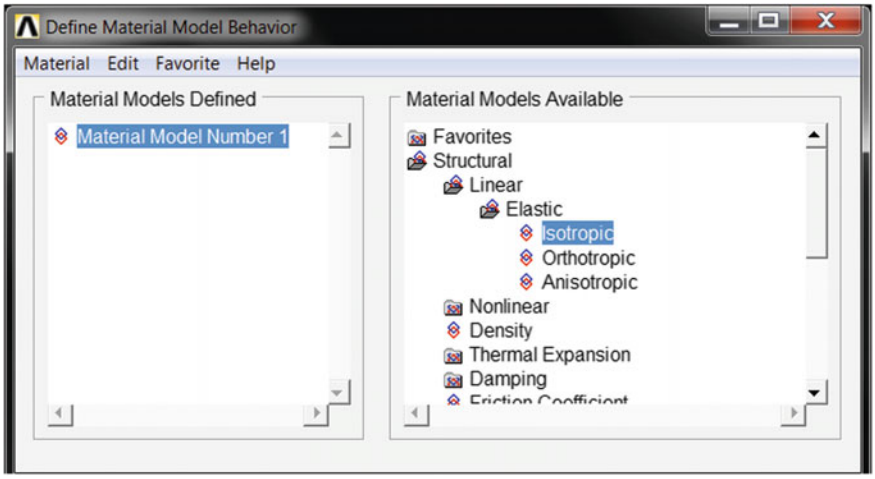

Fig. 5.9 Selecting the material model

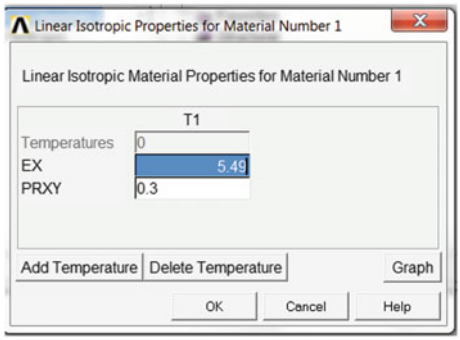

Fig. 5.10 Input data for material properties of CNT

5.3.4 *Defining the Cross Section of the Element*

The ANSYS element library contains more than 200 different element types. Each element type has a unique number and a prefix that identifies the element category: BEAM 188, BEAM188, PLANE77, SOLID96, etc. (Table 5.2).

The element type determines, among other things:

- The degree-of-freedom set (which in turn implies the discipline-structural, thermal, magnetic, electric, quadrilateral, brick, etc.)
- Whether the element lies in two-dimensional or three-dimensional space.

Element real constants are properties that depend on the element type, such as cross-sectional properties of a beam element, which are supposed to be defined using this format: **Main Menu > Preprocessor > Sections > Beam > Common Sections**. The cross section of the beam elements according to the simplified structural model of the carbon-carbon bond is indicated in Fig. 5.11.

Thereafter, the cross section of the element is plotted: **Main Menu > Preprocessor > Sections > Beam > Plot Section** (Fig. 5.12); the sections listed: **Main Menu > Preprocessor > Sections > List Sections** and details obtained (Figs. 5.12 and 5.13).

Table 5.2 Some element types available in *ANSYS*

BEAM	PLANE
COMBINation	SHELL
CONTACt	SOLID
FLUID	SOURCe
HYPERelastic	SURFace
INFINite	TARGEt
LINK	USER
MASS	INTERface
MATRIX	VISCOelastic (or viscoplastic)
PIPE	

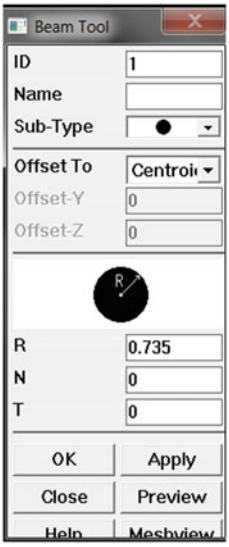

Fig. 5.11 Selected cross section of C–C bond (*BEAM188)*

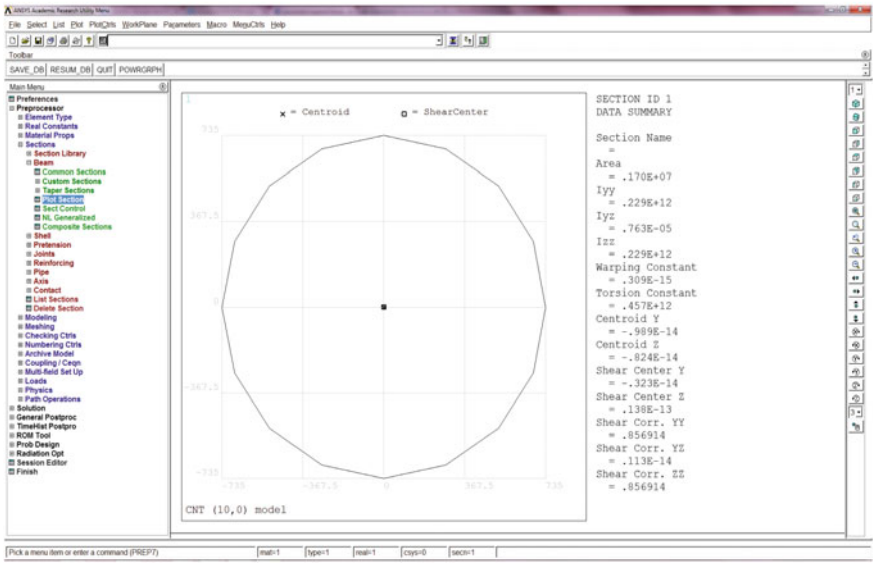

Fig. 5.12 Section of C–C bond cross section

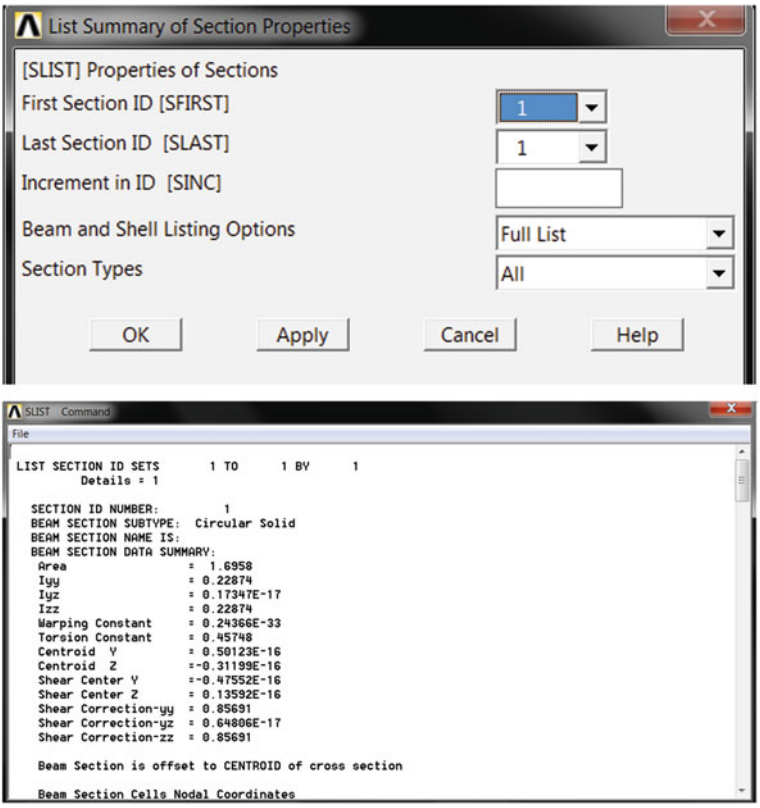

Fig. 5.13 Details of the C–C beam section

5.3.5 *Creating Carbon Nanotube Model*

To create the geometrical model of CNT, we need to generate the atomic coordinates of the nanotube and then insert the coordinates into the *ANSYS* program. Therefore, we will use any suitable software such as *nanotube modeler* to create the coordinates. A simple zigzag nanotube (10,0) will be created using the *nanotube modeler* (Fig. 5.14) and the (x,y,z) coordinates will be transferred to *ANSYS*.

The (10,0) nanotube with length of 10 has 100 carbon atoms in hexagonal cell arrangements. The hexagonal rings of carbon can be seen in Fig. 5.14. There is the need to create a list of keypoints from the coordinates using a simple coding. We can make a simple macro in *ANSYS* to do the modeling job. The macro name will be nanotube. To make sure we are safe we add few lines to the macro and done in the preprocessing section. Otherwise, we will not be able to insert keypoints. The active coordinate system should be global Cartesian.

The (10,0) CNT model developed in *Nanotube Modeler* is then exported as a Protein Data Bank (PDB) file and the coordinates displayed using a *Notepad* text

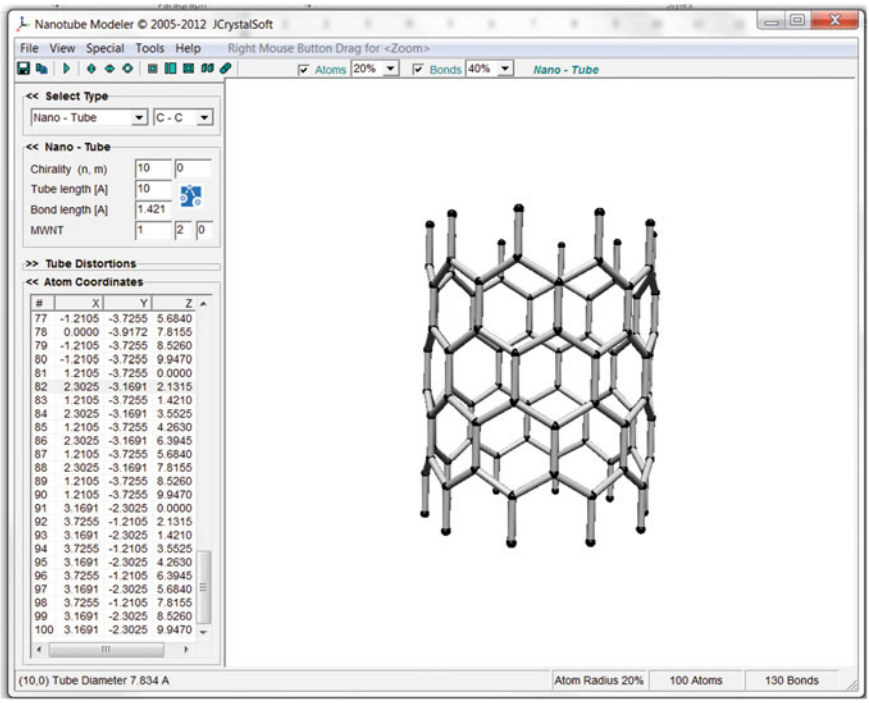

Fig. 5.14 Model of CNT (10,0) developed using *Nanotube Modeler*

editor (Fig. 5.15). Thereafter a file is created to generate the atoms as nodes using *ANSYS* Parametric Design Language (APDL) commands. The command for creating a node has the format: N, NODE, X, Y. Z, THXY, THYZ, THZX. The model of CNT with (10,0) configuration have 100 atoms (nodes) that are connected by bonds regards as elements of *BEAM188* type.

The macro to generate the (10,0) CNT is indicated in Fig. 5.16. The commands are copied and then paste on the command line in *ANSYS APDL*. Then click the isometric view button to obtain the 3D model of generated (10,0) CNT as indicated in Fig. 5.17.

All the nodes and their serial numbers can also be plotted as indicated in Fig. 5.18. The file is saved by pressing the SAVE_DB button on the **Utility menu** and we can resume from any step, in case of any error by pressing RESUME_DB button.

5.3.6 *Creating Inorganic Nanotube Model*

Based on available geometrical parameters, inorganic nanotubes having different dimensions can be developed using the *Surface Builder* tool of *Material Studio*©

```
REMARK   Nanotube Modeler PDB file (JCrystalSoft)
REMARK   Created:5/8/2015 9:22:06 AM
CRYST1    1.000    1.000    1.000  90.00  90.00  90.00 P1
ATOM      1  C    C A   1      3.917   0.000   0.000  1.00  0.00
ATOM      2  C    C A   1      3.725   1.210   2.132  1.00  0.00
ATOM      3  C    C A   1      3.917   0.000   1.421  1.00  0.00
:
:
:
ATOM     98  C    C A   1      3.725  -1.210   7.816  1.00  0.00
ATOM     99  C    C A   1      3.169  -2.302   8.526  1.00  0.00
ATOM    100  C    C A   1      3.169  -2.302   9.947  1.00  0.00
TER
CONECT    1    3
CONECT    2    3    4   13
CONECT    3    1    2   92
:
:
:
CONECT   98    9   96   99
CONECT   99   88   98  100
CONECT  100   99
MASTER        0    0    0    0    0    0    0    0  100    0  100    0
END
```

Fig. 5.15 PDB file of (10,0) CNT indication x,y,z coordinates of atoms and how they are connected

package for armchair and zigzag types. Examples of modelled single walled cubic zirconia nanotubes (SWCZNT) are shown in Figs. 5.19 and 5.20 for armchair and zigzag respectively.

The structure of SWCZNT modelled using the *Surface Builder* of the *Material Studio* can be exported to *CrystalMaker* or any other software with capacity for importing Protein Data Bank (PDB) file. The PDB file(s) contain detailed information such as atomic coordinates, bibliographic citations, primary and secondary structure, information, and crystallographic structure factors [36]. PDB file format

```
nanotube     ! file name

/prep7       !move to preprocessing
CSYS,0       !activate global coordinate system

n, 1, 3.917, 0.000, 0.000    !format: n (node), serial no., x,y,z
n, 2, 3.725, 1.210, 2.132
n, 3, 3.917, 0.000, 1.421
:
:
:
n, 97, 3.169, -2.302, 5.684
n, 98, 3.725, -1.210, 7.816
n, 99, 3.169, -2.302, 8.526
n, 100, 3.169, -2.302, 9.947
e, 1, 3      !format: e(element), first node, second node connected
e, 2, 3
e, 2, 4
e, 2, 13
e, 3, 1
:
:
:
e, 98, 96
e, 98, 99
e, 99, 88
e, 99, 98
e, 99, 100
e, 100, 99
```

Fig. 5.16 APDL Macro for generating (10,0) CNT

is a typical way of data exchange in macromolecular configuration and is commonly accepted by much molecular modeling software. A typical PDB file for a SWZCNT exported from *Material Studio* is shown in Fig. 5.21.

Software such as *MATLAB*, C^{+} and others have been used to extract the required information for modeling nanotubes in *ANSYS* [37]. *Python* (*Wing IDE version 101 v 5*) have additional capabilities such as the availability of predefined modules for 3D structural format including those with periodic setup. A script (code) to extract the required data and print out an APDL macro for finite element modeling is indicated in Fig. 5.22.

All the outputs for all atoms and bonds are recorded in a file. The output file for 35 × 0 SWCZNT with 102.08 Å length is displayed in Fig. 5.23. The */PREP7* is the ANSYS command employed to build and setup the model, **n** labels the node to

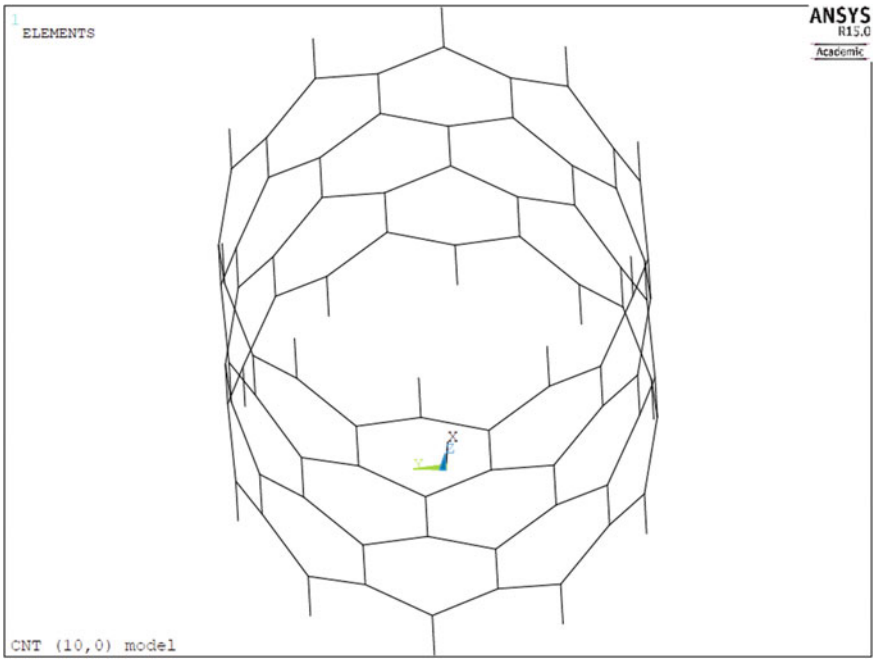

Fig. 5.17 Generated (10,0) CNT showing the elements

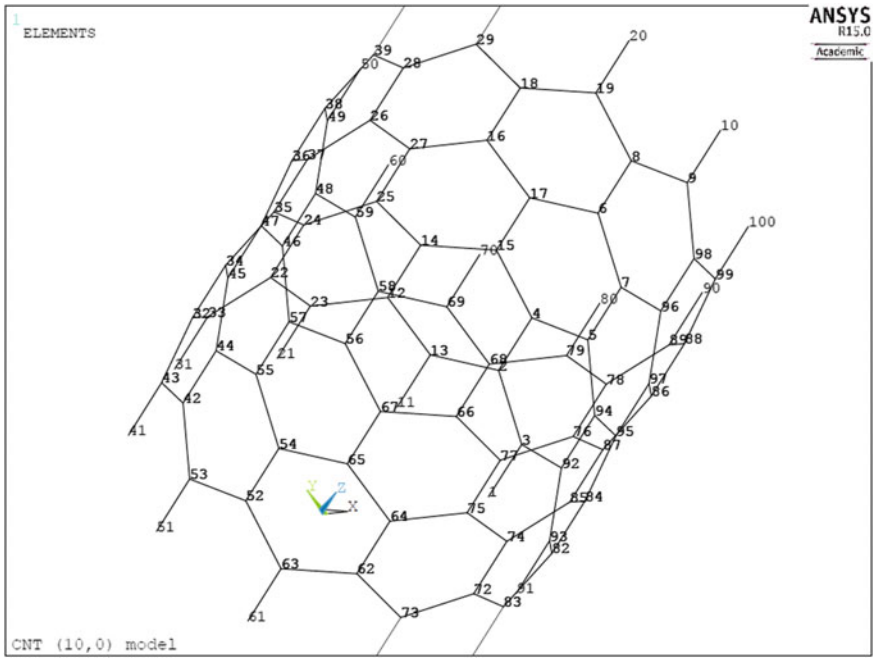

Fig. 5.18 Generated (10,0) CNT showing the elements and numbered nodes

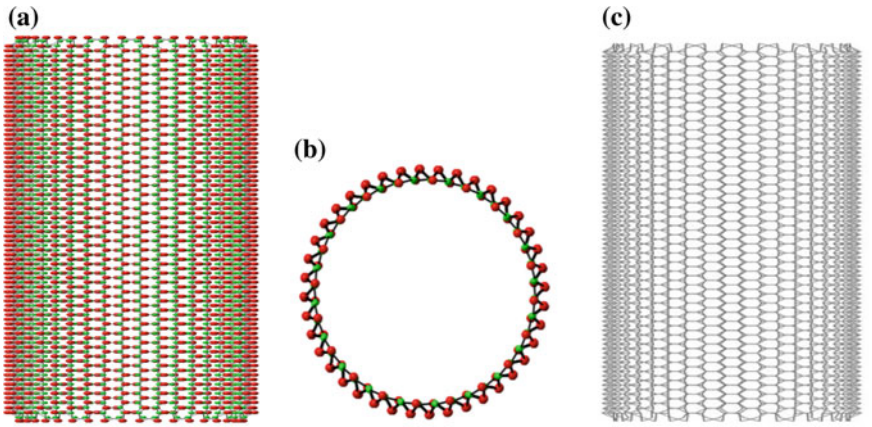

Fig. 5.19 **a** *Front* and **b** *Top* in ball and stick form and **c** *Front* wire frame models for an armchair (20 × 20) SWCZNT

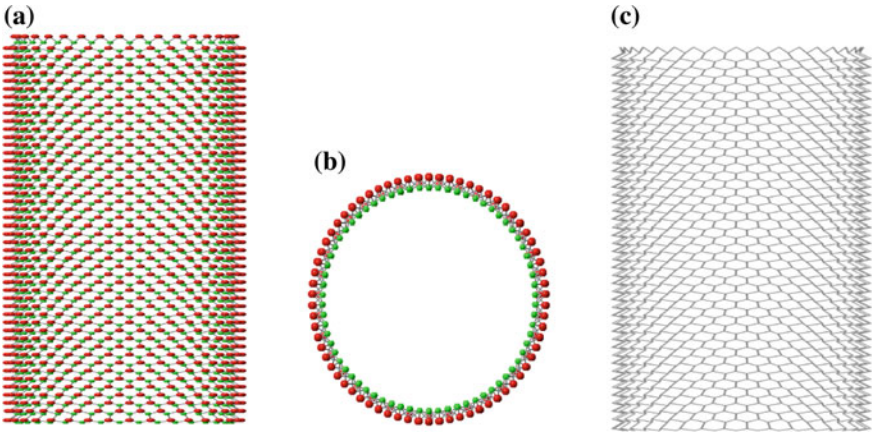

Fig. 5.20 **a** *Front* and **b** *Top* in ball and stick form and **c** *Front* wire frame models for zigzag (35 × 0) SWCZNT

be and ***e*** defines the element. The file is imported into ANSYS (APDL 15.0). Alternatively, this can also be conducted by inserting the data as a macro in the command line. The model created in ANSYS is illustrated in Fig. 5.24 together with that of 20 × 20. With the model of the nanotube transferred into ANSYS, further editing and simulation can be carried out.

The Zr and O_2 atoms are joined mainly with ionic bonds and have a hexagonal lattice along (111) miller index [38]. The input sectional properties for the element of SWZNT compared to that of SWCNT [39] are shown in Table 5.3.

```
REMARK   Materials Studio PDB file
REMARK   Created:  Sat Jul 05 03:22:30 Malay Peninsula Standard Time 2014
ATOM      1  O   MOL     1       3.057  -0.191  -2.121  1.00  0.00          O2-
ATOM      2  O   MOL     1       1.222   2.792  -2.104  1.00  0.00          O2-
ATOM      3 Zr   MOL     1       3.823   1.677  -1.450  1.00  0.00          Zr4+
ATOM      4  O   MOL     1       4.513   3.533  -0.679  1.00  0.00          O2-
ATOM      5 Zr   MOL     1      -0.349   4.084  -1.479  1.00  0.00          Zr4+
ATOM      6  O   MOL     1      -1.930   5.301  -0.753  1.00  0.00          O2-
ATOM      7 Zr   MOL     1       2.426   3.945  -0.761  1.00  0.00          Zr4+
ATOM      8  O   MOL     1      -2.355   1.919  -2.113  1.00  0.00          O2-
ATOM      9 Zr   MOL     1      -3.001   3.460  -0.777  1.00  0.00          Zr4+
ATOM     10  O   MOL     1      -2.680  -1.537  -2.127  1.00  0.00          O2-
:
:
:
:
ATOM    816  O   MOL     1       2.010  -5.383 102.467  1.00  0.00          O2-
ATOM    817 Zr   MOL     1       0.531  -4.042 103.193  1.00  0.00          Zr4+
ATOM    818 Zr   MOL     1       3.042  -3.522 102.524  1.00  0.00          Zr4+
ATOM    819  O   MOL     1       2.270  -1.991 103.804  1.00  0.00          O2-
ATOM    820 Zr   MOL     1       3.960  -0.840 103.215  1.00  0.00          Zr4+
TER     821
CONECT    1    3   20
CONECT    2    5    7
CONECT    3    1    4
CONECT    4    3    7   23
:
:
:
:
CONECT  816  797  817  818
CONECT  817  814  816
CONECT  818  816  799  819
CONECT  819  818  820
CONECT  820  819  801
END
```

Fig. 5.21 PDB File for 5 × 5 SWCZNT from *Material Studio*

5.3.7 Meshing the Generated Nanotube

The mesh used for a simulation is critical in determining the accuracy of the output as too many elements may lead to longer computation time and too little may lead to inaccurate result. Before meshing a model, and even ahead of creating the model, it is vital to decide whether a free mesh or a mapped mesh is appropriate for the analysis. A *free* mesh has no limits in relation to element shapes, and has no definite pattern. In comparison to a free mesh, a *mapped* mesh is constrained in relation to element shape and the pattern of the mesh [40]. Beam elements will connect each pair of neighboring nodes. Nanotube modeler can provide us with a list of connections as well. We use list of connections and create another simple macro to insert beam elements into ANSYS. The path followed is: **Main**

```
### get atoms cordinates from PDB file and write them as
###ANSYS keypoints
line_value = 0
node_value = 0
file = open('C:\\xyz\\5x5.pdb','r')
igot = file.readlines()
output_file = open('C:\\xyz\\ZNT5x5.txt',"a") # needs input for distinct file
output_file.write('/PREP7'+"\n") #open pre-processing menu
output_file.write('CSYS,0'+"\n") #activate global cartesian
for line in igot:
   if line.find("ATOM") > -1:
            node_value = node_value + 1
            kv = str(node_value)
            xyz =  line.split()
            #print kv,",", xyz[6], ",", xyz[7],
            line_i="k" + ', '+ kv + ', ' + xyz[5] + ', ' + xyz[6] + ' , ' + xyz[7] + "\n"
            print (line_i)
            output_file.write(line_i)
 ### reads connect records
   elif line.find("CONECT") > -1:
            con =  line.split()
            line_value = line_value + 1
            #print line_value
            #print con[2]
            line_j = "l" + ', ' + str(line_value) + ', ' + con[2] + "\n"
            output_file.write(line_j)
            print (line_j)
            try:
                  line_i = "l" + ', ' + str(line_value) + ', ' + con[3] + "\n"
                  output_file.write(line_i)
                  print (line_i)
                  line_k = "l"+ ', ' + str(line_value) + ', ' + con[4] + "\n"
                  print (line_k)
                  output_file.write(line_k)
            except IndexError:
               continue
```

Fig. 5.22 *Python* script for extracting required data to model SWCZNT

Fig. 5.23 Output file in macro APDL for modeling 35 × 0 SWCZNT

```
/prep7
n, 1, 13.560, 0.607,0.658
n, 2, 14.697, 1.984,1.204
n, 3, 14.831, 0.665,3.705
:
:
n, 3358, 13.254, -3.027,101.248
n, 3359, 13.829, -1.873,102.814
n, 3360, 13.586, -0.610,101.245
e, 1, 2
e, 1, 137
e, 2, 1
e, 2, 4
e, 3, 6
e, 3, 140
:
:
:
e, 3359, 3360
e, 3360, 3223
e, 3360, 3359
e, 3360, 3357
```

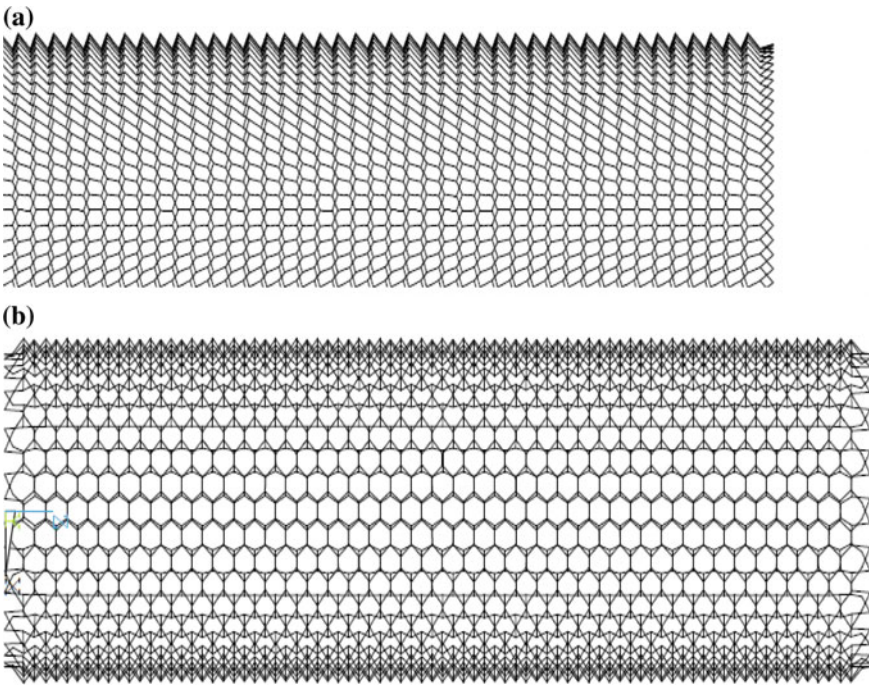

Fig. 5.24 FE model of **a** 35 × 0 and **b** 20 × 20 SWCZNTs having equal diameter

Table 5.3 Input properties of the SWZNT element compared to that of CNT

	SWZNT	SWCNT
Cross-sectional area, A	1.28579 $Å^2$	1.68794 $Å^2$
Moment of inertia, $I_{YY} = I_{ZZ} = I$	0.131496 $Å^4$	0.22682 $Å^4$
Polar moment of inertia, I_{XX}	0.26298 $Å^4$	0.453456 $Å^4$
Elastic modulus of beam element, E	5.09×10^{-10} N/$Å^2$	5.488×10^{-8} N/$Å^2$
Shear modulus of beam element, G	0.8569×10^{-9} N/$Å^2$	8.711×10^{-9} N/$Å^2$

Menu > Preprocessor > Meshing > Size Cntrls > ManualSize > Lines > All Lines with the options indicated in Fig. 5.25 (lines); Fig. 5.26 (picking of lines); Fig. 5.27 (creation of elements) and Fig. 5.28 (plotting of nodes).

Similar method is applicable to inorganic nanotubes. Mapped mesh has been used for zirconia nanotubes with the shape been the same as what was obtained during the solid modeling using *Material Studio*. The shape is similar to that of the nanosheet obtained by cleaving the supercell along the (111) miller index. Element shape testing was conducted and the warning and error limits found out to be 0 %, meaning the setting used for the meshing is acceptable [41].

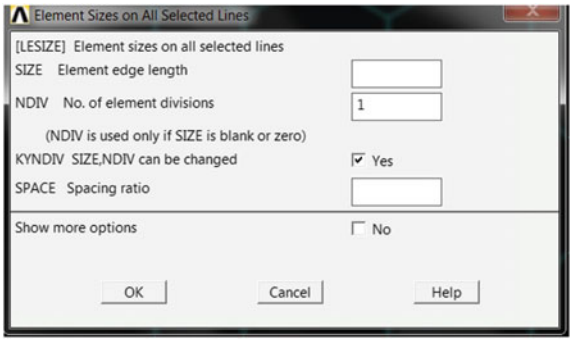

Fig. 5.25 Options for meshing CNT model

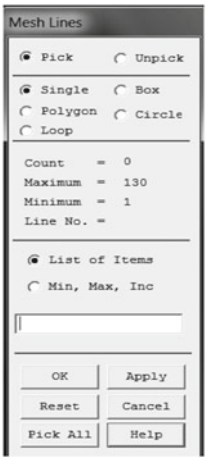

GUI command: Main Menu>Preprocessor>Meshing>Mesh>Lines

Fig. 5.26 Selection of lines to be meshed

5.3.8 Boundary Conditions

After generating the geometric models, specific conditions have to be given in relation to the constraints at both translational and rotational degrees of freedom on the nodes at ends needed for simulation. At this step, we will simulate the nanotube behavior under axial tension. In order to do this through *ANSYS*, we need to fix one end of the nanotube in x,y,z directions and pull the other end in axial direction which is z axis in this case (Fig. 5.29).

The selected end is fixed by constraining all degree of freedoms (DOFs) by setting all displacement to be zero ($U_x = U_y = U_Z = 0$) as indicated in Fig. 5.30.

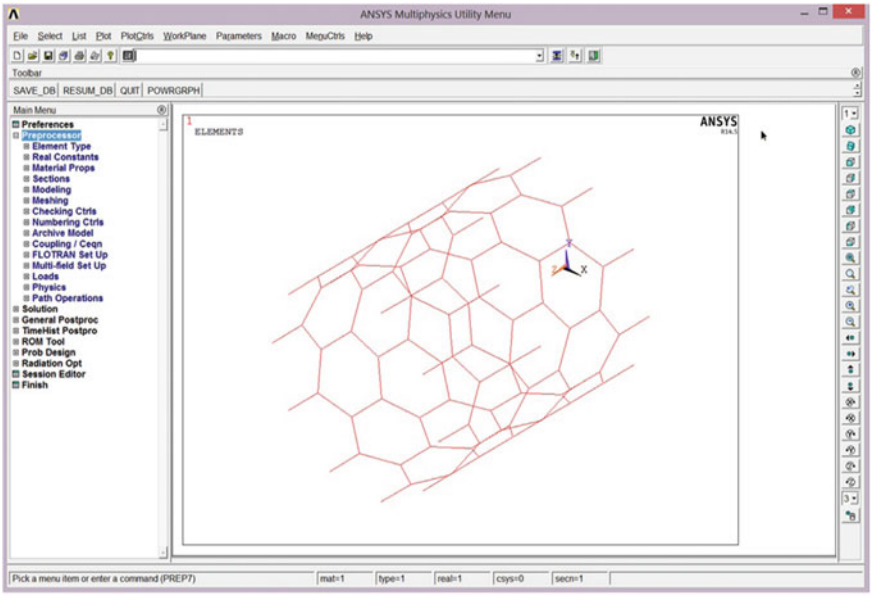

GUI command:
Main Menu>Preprocessor>Meshing>Mesh>Lines

Fig. 5.27 Creation of lines to be meshed

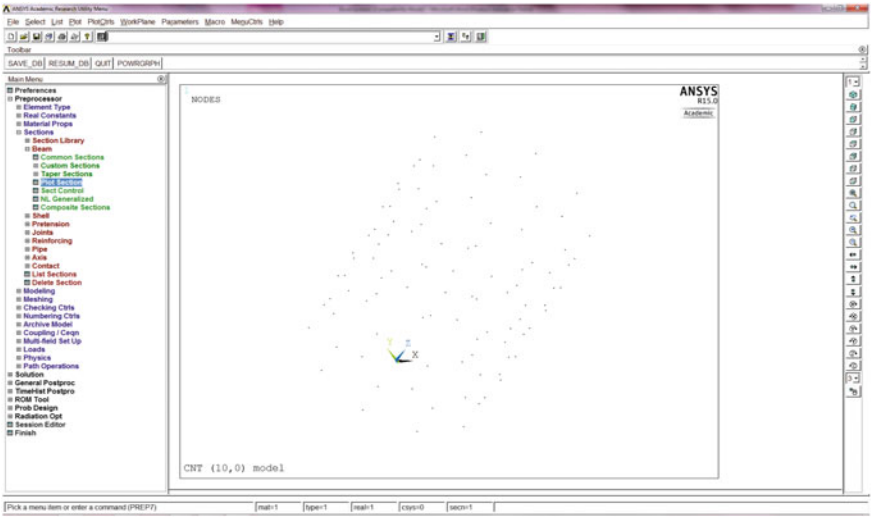

GUI command: Utility Menu>Plot>Nodes

Fig. 5.28 Plotting of nodes in the meshing

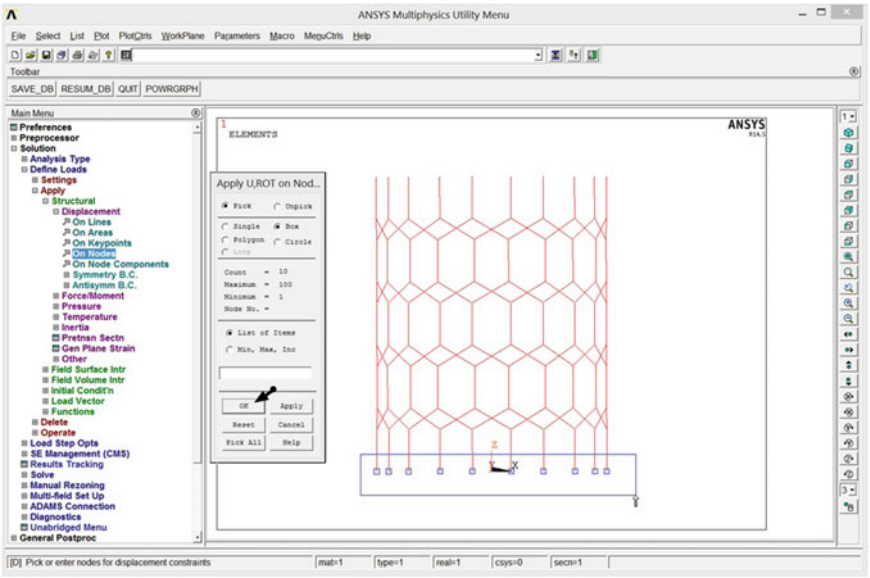

Fig. 5.29 Selection of the fixed nodes of (10,0) CNT

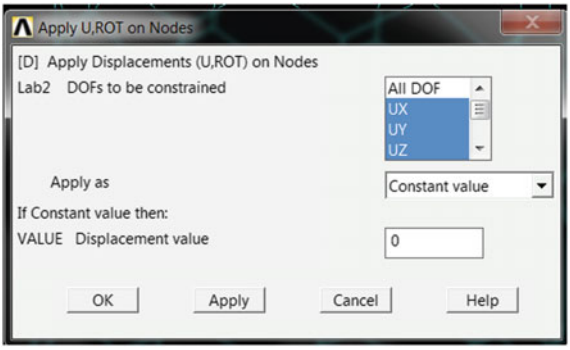

Fig. 5.30 Constraining displacement of the selected nodes in the CNT

Then, known magnitude of displacement is applied in z direction to the nodes on the other end of the model to simulate tension condition (Fig. 5.31). It should be noted that the direction where displacement is applied depends the orientation of the triad, thus it can be in the x, y or z direction; the displacement in Fig. 5.31 was applied in the z direction as it coincides with axial direction.

The way boundary conditions and forces are shown can be changed by selecting the **Symbols** option under **PlotCtrls** in the **Main Menu** and thereafter obtaining the details as indicated Fig. 5.32.

To save your model, select **Utility Menu Bar** → **File** → **Save As** *Jobname.db*. Your model will be saved in a file called *jobname.db*, where *jobname* is the name

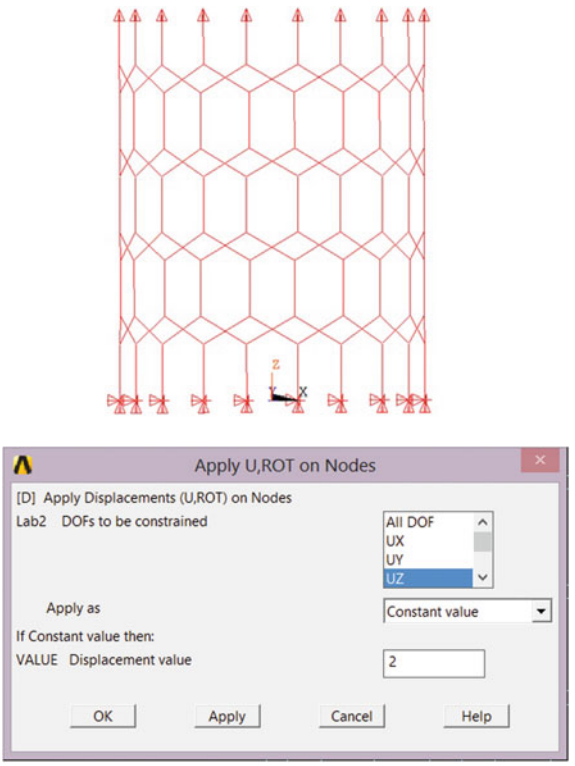

Fig. 5.31 Modelled (10,0) CNT with boundary conditions applied

that you specified in the *Launcher* when you first started *ANSYS*. It is a good idea to save your job at different times throughout the building and analysis of the model to back up your work in case of a system crash or other unforeseen problems.

Frequently you want to start up *ANSYS* and recall and continue a previous job. There are two methods to do this:

1. Using the *Launcher*...
   (1) In the *ANSYS Launcher*, select Interactive… and specify the previously defined *jobname*.
   (2) Then when you get ANSYS started, select **Utility Menu → File → Resume** *Jobname.db*.
   (3) This will restore as much of your database (geometry, loads, solution, etc.) that you previously saved.
2. Or, start ANSYS and select **Utitily Menu → File → Resume from**… and select your job from the list that appears.

Similar procedure is also followed for applying boundary conditions for inorganic nanotubes as illustrated in Fig. 5.33 for zirconia nanotube.

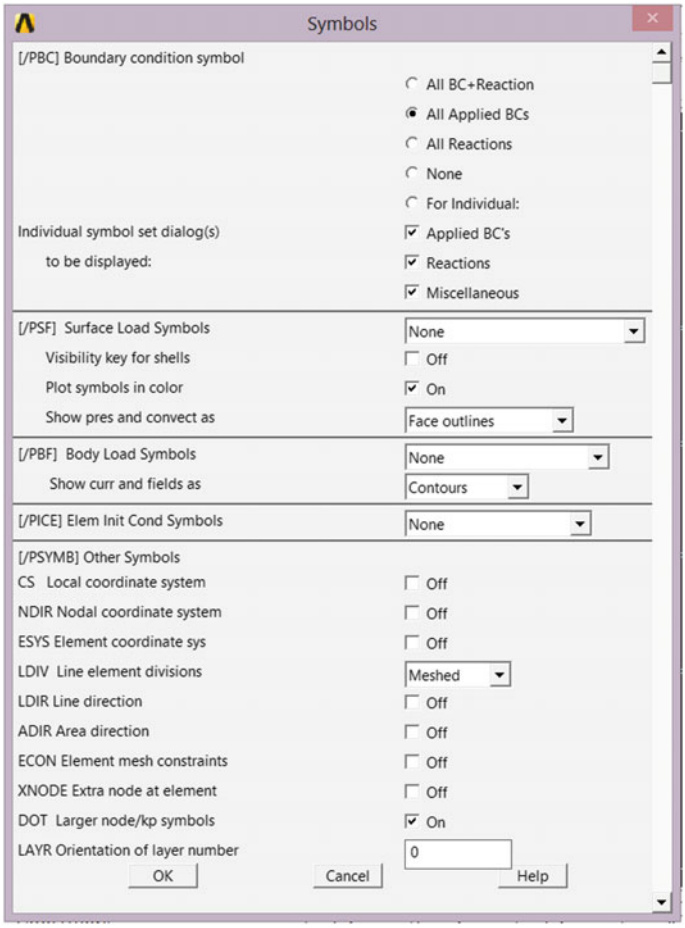

Fig. 5.32 Details and options available for the boundary conditions

5.3.9 Initiation of Solution for Nanotube Model

During the solution process, the computer takes over and solves the relevant equations that the finite element method generates. The results of the solution are:

- nodal degree-of-freedom values, which form the primary solution
- derived values, which form the element solution

Several methods of solving the simultaneous equations are available in the *ANSYS* program. You can select a solver using one of the following:

GUI: Main Menu > Preprocessor > Loads > Analysis Type > Analysis Options Main Menu > Solution > Load Step Options > Sol'n Control (: Sol'n Options Tab)

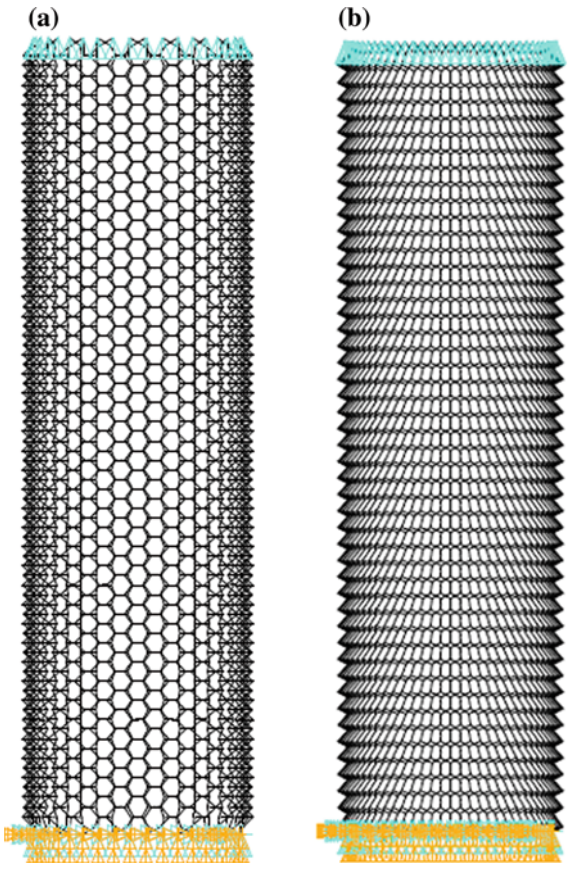

Fig. 5.33 **a** Armchair (20 × 20) and **b** zigzag (35 × 0) SWZNT with tensile loading at *top end* and fixed at the *bottom*

Main Menu > Solution > Analysis Options
Main Menu > Solution > Unabridged Menu > Analysis Options
After all the boundary conditions are applied select:
Main Menu > Solution > Solve > Current LS (Fig. 5.34).
When the solution is done, close the notification window (Fig. 5.35).

5.3.10 Post Processing

In relation to *ANSYS*, Post Processing signifies evaluating the results of an analysis. It is perhaps the most vital phase in the analysis, because it is related to understanding how the applied loads affect designs/models, how acceptable the selected finite element mesh is, and so on. Post processing is divided in three main groups [42]:

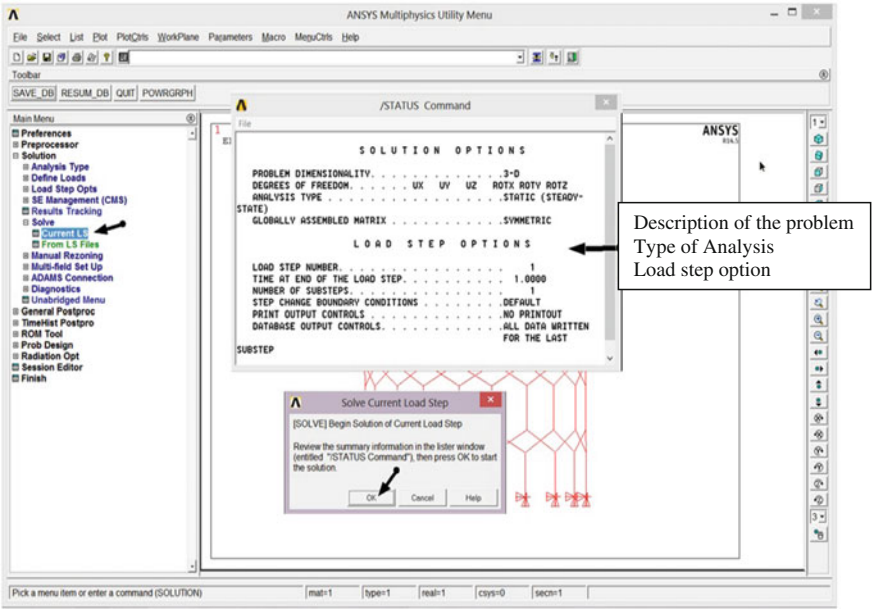

Fig. 5.34 Details of the solution options

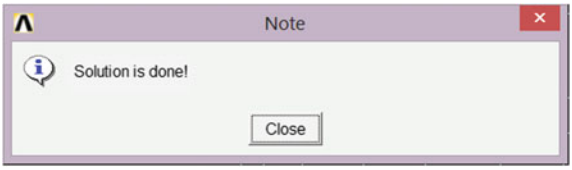

Fig. 5.35 End of the Solution

(i) Post Processors: two postprocessors are available for reviewing your results: POST1, the general postprocessor, and POST26, the time-history postprocessor. POST1 allows you to review the results over the entire model at specific load steps and substeps (or at specific time-points or frequencies). In a static structural analysis, for example, you can display the stress distribution for load step 3. Or, in a transient thermal analysis, you can display the temperature distribution at time = 100 s. POST26 allows you to review the variation of a particular result item at specific points in the model with respect to time, frequency, or some other result item. In a transient magnetic analysis, for instance, you can graph the eddy current in a particular element versus time. Or, in a nonlinear structural analysis, you can graph the force at a particular node versus its deflection.

Table 5.4 Primary and derived data for different disciplines [42]

Discipline	Primary data	Derived data
Structural	Displacement	Stress, strain, reaction, etc.
Thermal	Temperature	Thermal flux, thermal gradient, etc.
Magnetic	Magnetic potential	Magnetic flux, current density, etc.
Electric	Electric scalar potential	Electric field, flux density, etc.
Fluid	Velocity, pressure	Pressure gradient, heat flux, etc.

(ii) Result file: The name of the results file depends on the analysis discipline: *Jobname.RST* for a structural analysis; *Jobname.RTH* for a thermal analysis; *Jobname.RMG* for a magnetic field analysis and *Jobname.RFL* for a FLOTRAN analysis.

(iii) Types of data files available for post processing: the solution phase calculates two types of results data, namely

(a) *Primary data* consist of the degree-of-freedom solution calculated at each node: displacements in a structural analysis, temperatures in a thermal analysis, magnetic potentials in a magnetic analysis, and so on (Table 5.4). These are also known as nodal solution data.

(b) *Derived data* are those results calculated from the primary data, such as stresses and strains in a structural analysis, thermal gradients and fluxes in a thermal analysis, magnetic fluxes in a magnetic analysis, and the like. They are typically calculated for each element and may be reported at any of the following locations: at all nodes of each element, at all integration points of each element, or at the centroid of each element. Derived data are also known as element solution data, except when they are averaged at the nodes. In such cases, they become nodal solution data.

In order to plot the deformed shape of CNT after the boundary conditions has been applied and simulation carried out, press **Main Menu > General Postproc > Plot Results > Deformed Shape**. Then select the type of plot needed (Fig. 5.36).

The output plot associated with these elements is as shown in Fig. 5.37 with the maximum nodal displacement (DMX) equal to 2.00654 units.

We can list or plot the results from the **General Postproc Menu**. For example, select **Nodal Solution** from **Contour Plot** and follow the steps in Fig. 5.38 to plot the displacement of the nanotube under axial load.

After selecting the required option and pressing **OK**, the plot will be created (Fig. 5.39) indicating variation of displacement along the CNT as indicated numerically by the legend.

Thereafter, the nodal displacements can be listed by the following steps: **Main Menu > General Postproc > List Results > Nodal Solution** (Fig. 5.40).

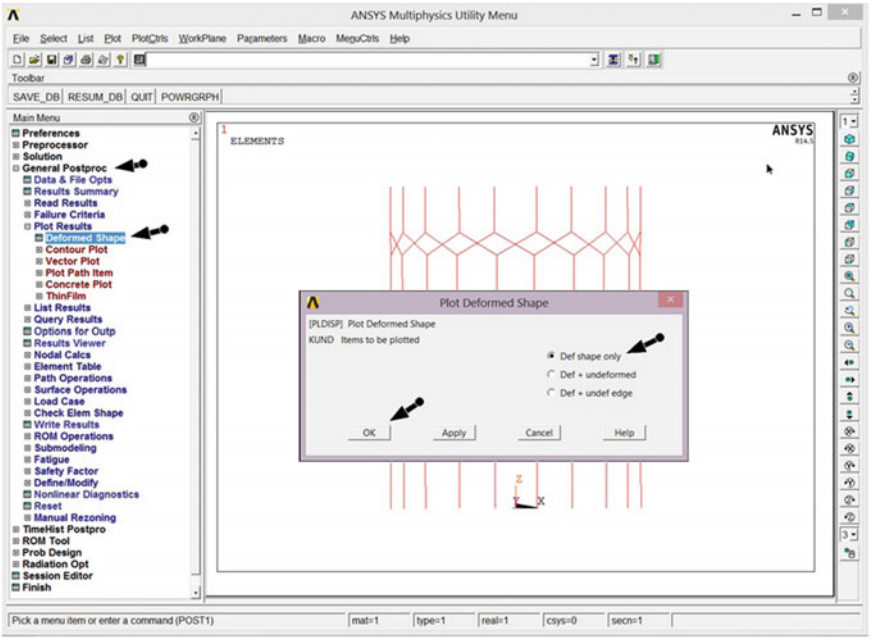

Fig. 5.36 Plotting of the deformed shape for CNT

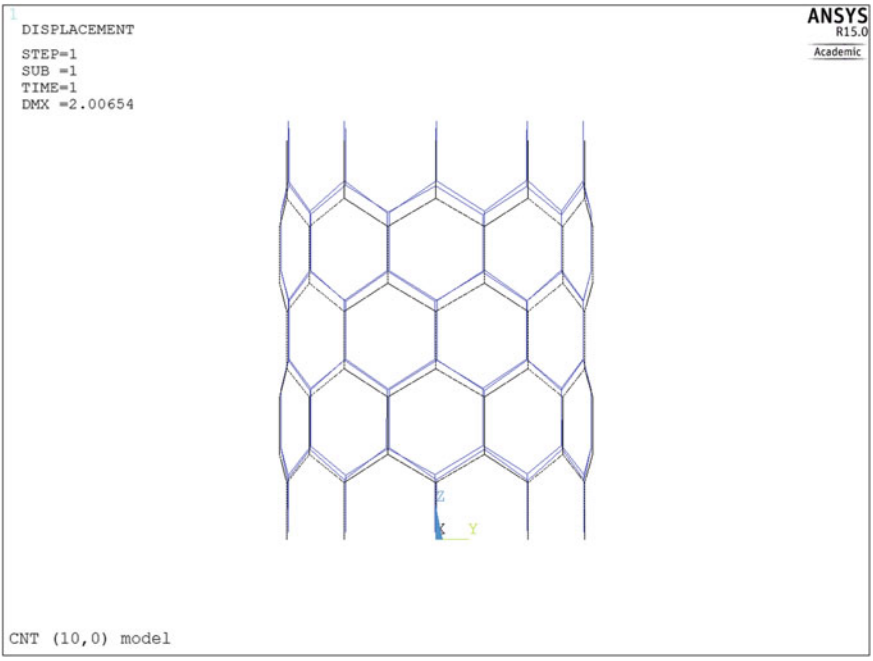

Fig. 5.37 Deformed (*blue*) and undeformed (*black*) plot for (10,0) CNT

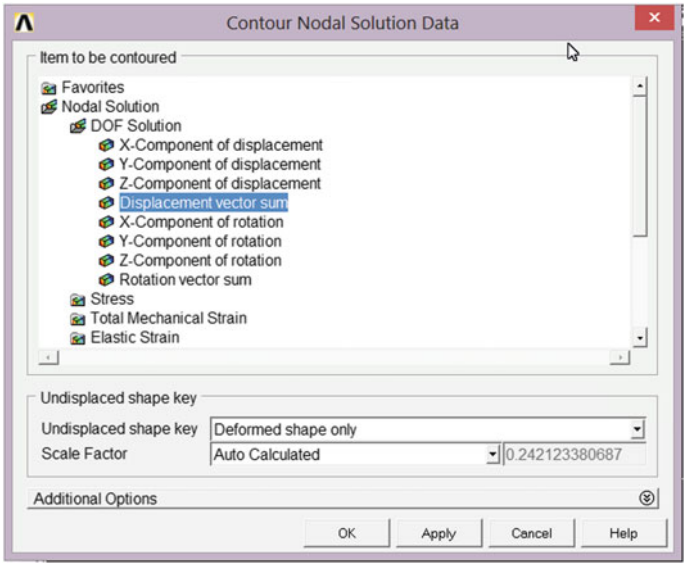

Fig. 5.38 Steps for plotting displacement vector sum

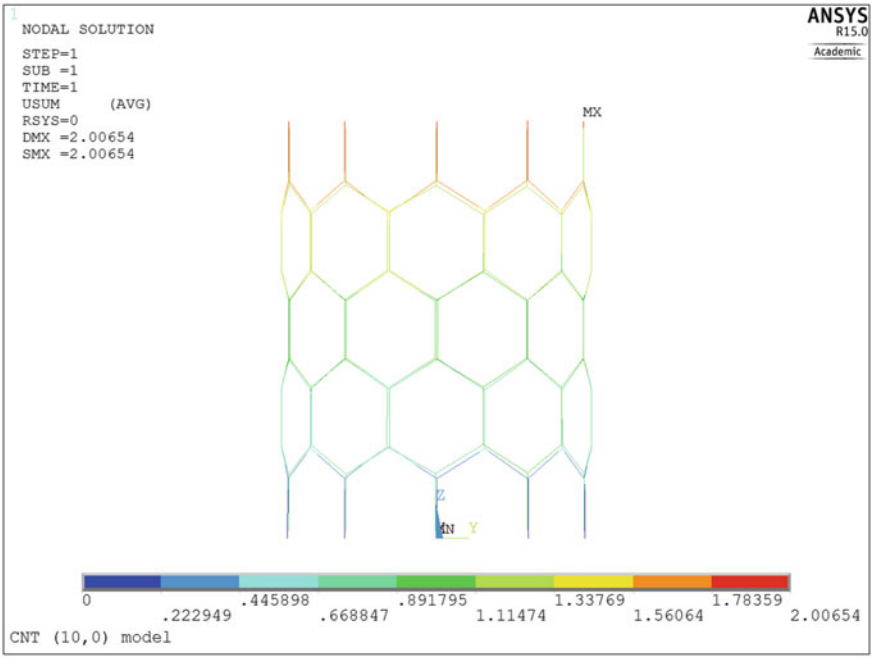

Fig. 5.39 Displacement contour plot for (10,0) CNT

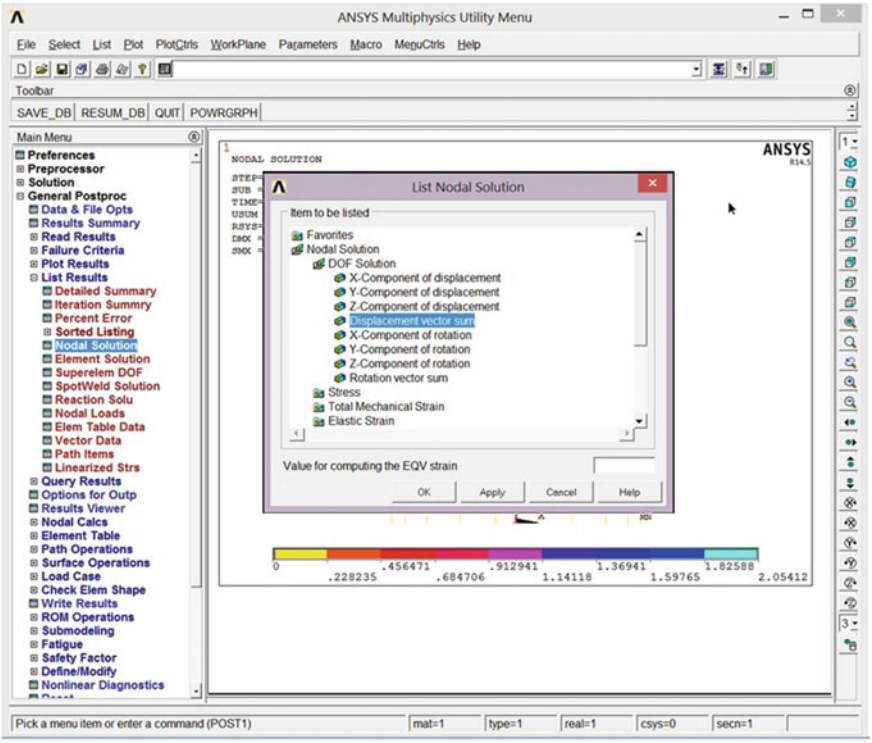

Fig. 5.40 Listing results obtained during simulation of CNT

The displacement values for all the nodes obtained after simulation are shown in Fig. 5.41. It should be noted that there are 100 nodes in (10,0) CNT having 10 Å length. The maximum absolute values are indicated in in Fig. 5.42.

5.3.11 Element Table

To review other results, such as forces and stresses in the elements, we must sort the results into element tables. The item labels and sequence numbers were given in Table 4.4 when element of BEAM188 type was described. For beam elements, the values of internal forces, stresses and strains calculated by ANSYS, can be looked up by assigning user defined labels. For example, we will assign the internal stress in beam elements, as computed by ANSYS to a user defined label *Elmstrain*. It should be noted that there are limitation on the number of defined label characters, which is eight.

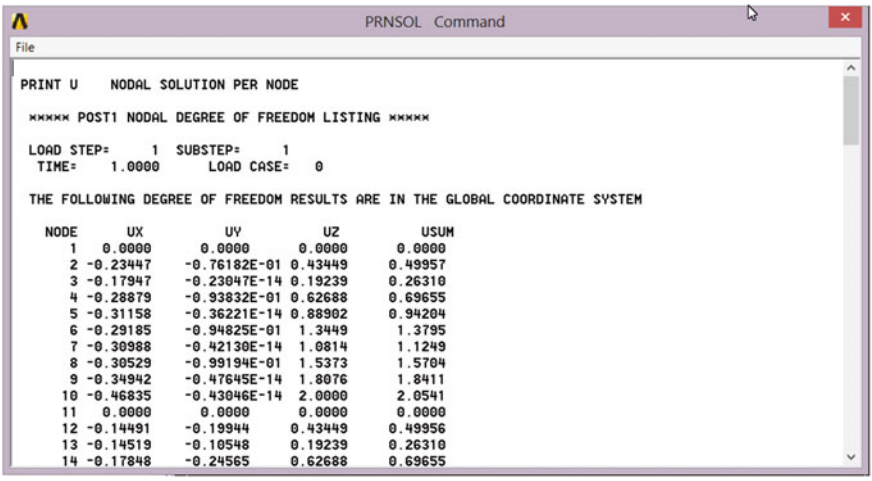

Fig. 5.41 Individual nodal displacement for (10,0) CNT

In order to sort results into element table, follow the sequence: **Main Menu > General Postproc > Element Table > Define Table** as visualized in Figs. 5.43 and 5.44.

After clicking OK and returning to the previous window, the defined table is listed with its parameters (Fig. 5.45). Several tables for other parameters can also be defined by referring to their sequence numbers and following the same steps.

Now we can plot or list the stress values in the elements by selecting Plot Elem Table and List Elem Table, respectively. For example, we plot the internal stress values for the nanotube structure: **Main Menu > General Postproc > Element Table > Plot Elem Table** (Fig. 5.46) with the element solution obtained in Fig. 5.47.

From the data generated so far after simulation of (10,0) CNT that was subjected to uniaxial loading, its Young's modulus can be computed. This requires the retrieval of the axial reaction forces at the top nodes of the nanotube by selecting the specific nodes and listing the reaction forces by following this sequence: **Utility Menu > Select > Entities** leading to options in a dialogue box (Fig. 5.48). Click Ok. In next window, Select Nodes, select Box option and now select the 10 nodes at top end of the tube (Fig. 5.49).

Click OK and go to the Reaction Solution section using the following sequence: **Main Menu > General Postproc > List Results > Reaction Solutions**. Then Pick F_Z (Fig. 5.50) item from the list and click OK.

List of selected Nodes and reaction forces on those nodes will be appear as shown in Fig. 5.51.

Now that we have the reaction forces, the Young's modulus of the nanotube can be calculated by using below equations,

```
    PRINT U    NODAL SOLUTION PER NODE

     ***** POST1 NODAL DEGREE OF FREEDOM LISTING *****

     LOAD STEP=     1  SUBSTEP=     1
      TIME=    1.0000       LOAD CASE=   0

     THE FOLLOWING DEGREE OF FREEDOM RESULTS ARE IN THE
GLOBAL COORDINATE SYSTEM

       NODE      UX           UY           UZ           USUM
          1   0.0000       0.0000       0.0000       0.0000
          2 -0.87560E-01 0.26555E-02 0.45961      0.46789
          3 -0.75354E-01 0.43425E-01 0.25331      0.26782
          4 -0.10441     0.62639E-02 0.65837      0.66663
          5 -0.13039     0.89872E-01 0.91421      0.92782
        :
        :
        :
         97 -0.12261     0.17743      1.0473       1.0692
         98 -0.12846     0.17521      1.3471       1.3645
         99 -0.13354     0.14969      1.2672       1.2830
        100 -0.13354     0.14969      1.2672       1.2830

    MAXIMUM ABSOLUTE VALUES
    NODE         58           86           10           30
    VALUE   0.19422     0.17792      2.0000       2.0065
```

Fig. 5.42 Post1 nodal degree of freedom listing for (10,0) CNT

$$\mathrm{E} = \frac{\mathrm{FL}}{\mathrm{AL}} = \frac{\mathrm{FL}}{\pi \mathrm{Dt} \Delta \mathrm{L}} \tag{5.12}$$

where E, F and A are the Young's modulus, net reaction force, cross sectional area, of the nanotube. In this case, cross section of the nanotube can be calculated by πDt (D and t are the nanotube diameter and thickness, respectively). It should be noted that the length (L) of the CNT was 10 Å during modeling with *Nanotube Modeler* but was measured in *ANSYS* as 9.947 10 Å. Applied displacement or extension (ΔL) during simulation in *ANSYS* was 2 Å. So, the Young's modulus of the nanotube using finite element modeling is:

$$E = \frac{0.12605 \times 10^{14} \times 9.947}{\pi \times 7.834 \times 3.4 \times 2} = 7.49191 \times 10^{11}\,\mathrm{Pa} \sim 0.75\,\mathrm{TPa} \tag{5.13}$$

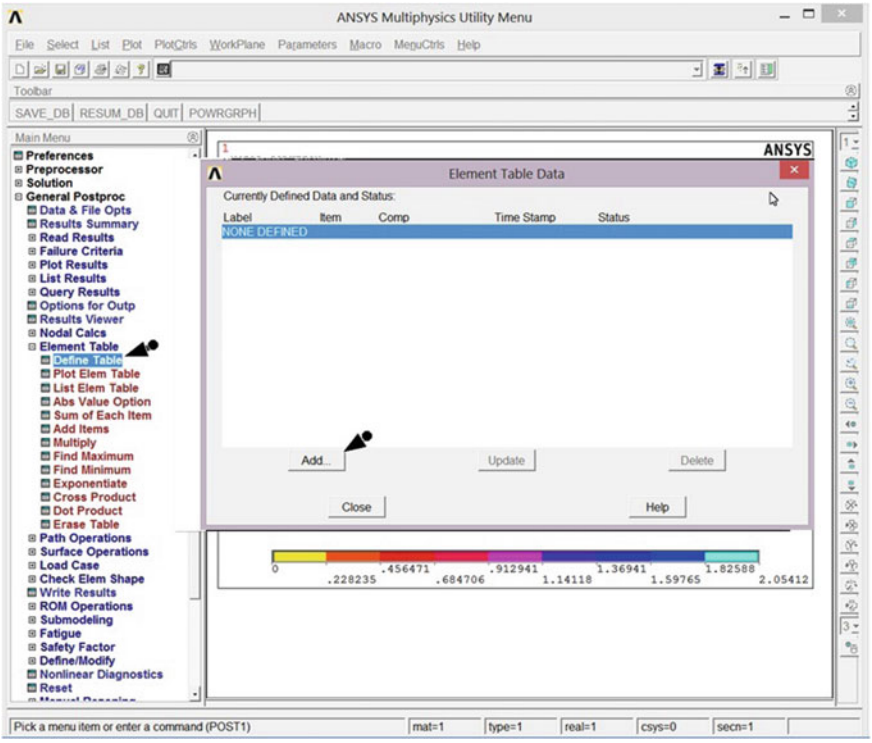

Fig. 5.43 Settings for defining element table

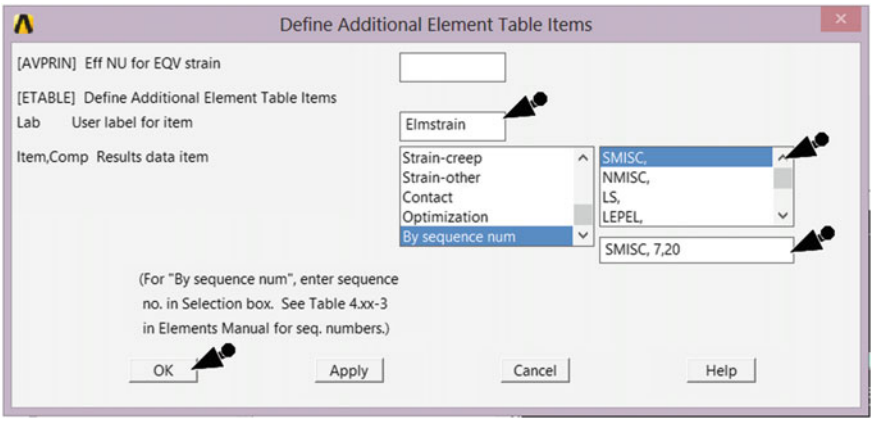

Fig. 5.44 Defining the label (*Elmstrain*) and other parameters

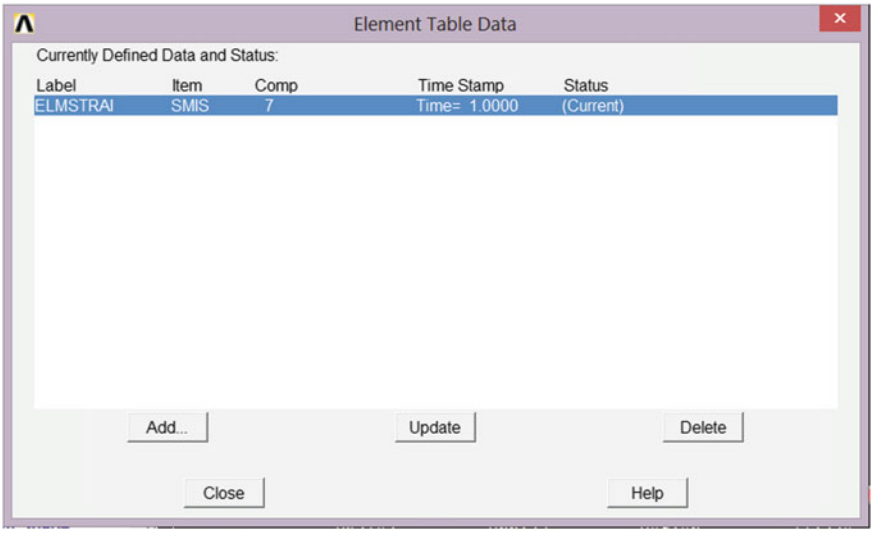

Fig. 5.45 Defined data with status for *Elstrain* label

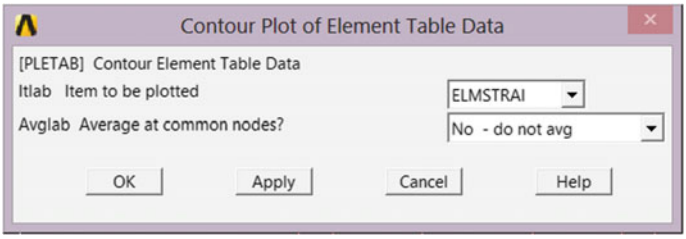

Fig. 5.46 Selecting the element table data for *Elstrain* label

5.4 Simulating Other Mechanical Behaviors for Nanotubes

Other properties of nanotubes such as mechanical and thermal can be studied using similar approach as carried on the elastic properties of the nanotube (Sect. 5.3). This requires the creation of the correct geometry of the nanotube and thereafter relates an equivalency between chemical potentials with structural mechanics. After importing the geometry and replacing chemical bonds with elements in the ANSYS, specific boundary conditions are applied depending on the type of property to be simulated.

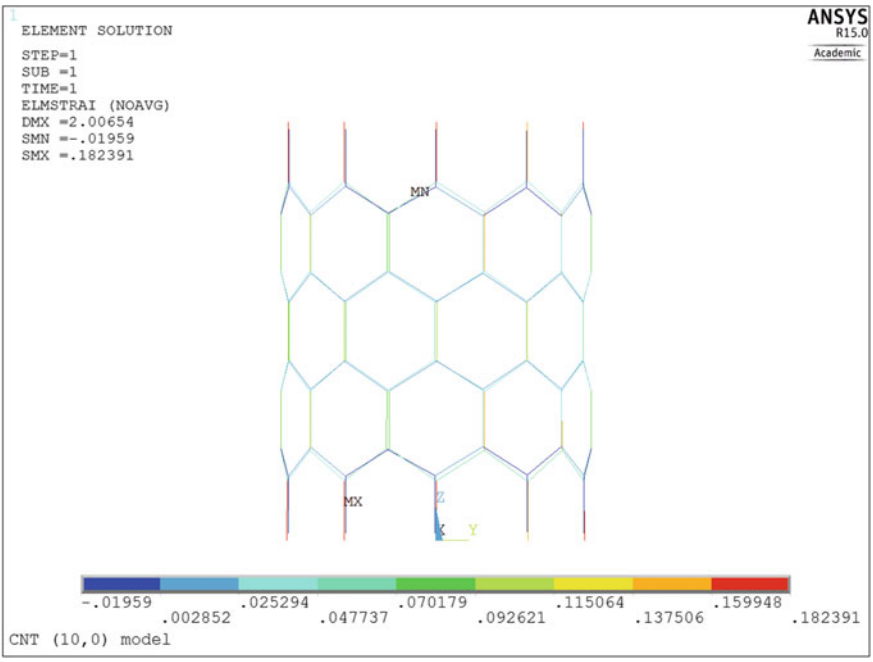

Fig. 5.47 Contour plot of element table data for (10,0) CNT

Fig. 5.48 Dialogue box to select entities for CNT

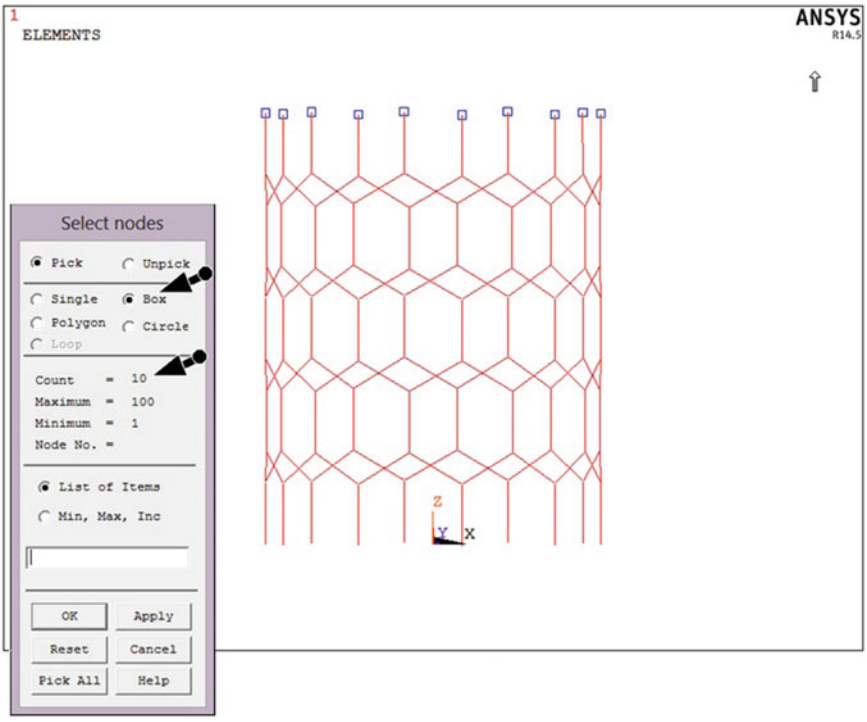

Fig. 5.49 Selected nodes at top of CNT

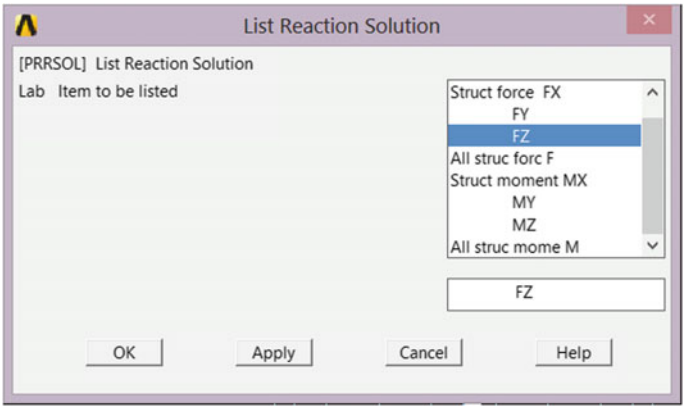

Fig. 5.50 Selecting the type of structural force to be used in reaction solution

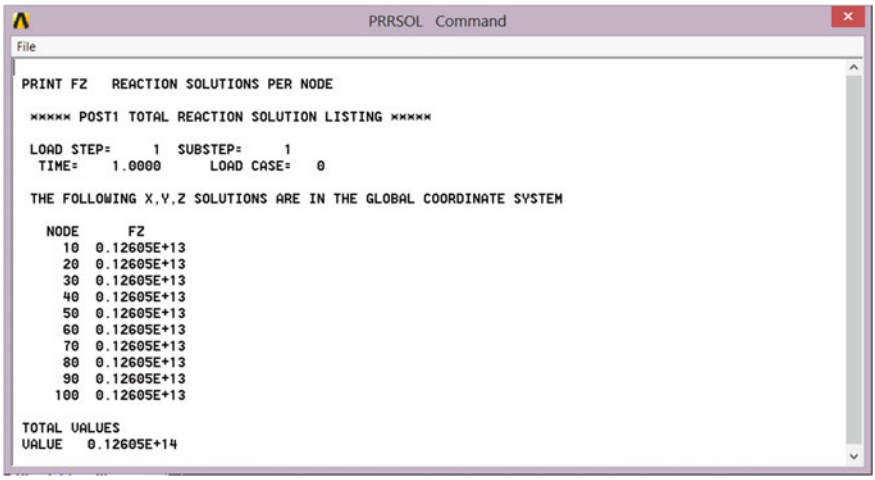

Fig. 5.51 Reaction forces on the selected nodes net/resultant force

5.4.1 *Buckling Behavior*

The buckling behaviour of nanotubes involves applying compressive displacement or force at the free end of the nanotube with the necessary boundary conditions as detailed in Fig. 5.52.

The buckling behavior of nanotubes can be analyzed using the Euler model. The general form of the Euler equations for a straight column under uniaxial compression is [43]:

$$P_{cri} = \frac{C\pi^2 EI}{L^2}, \tag{5.14}$$

where C represents the end form of the column, E is Young's modulus of elasticity, L is the length, and I is the moment of inertia and equal to $(\pi/64)\ (D_o^4 - D_i^4)$ for hollow NNTs. Also, D_o is the exterior diameter and Di is the interior diameter of the NNT.

Also, P_{cri} can be computed as

$$P_{cri} = AE\varepsilon_{cri} \tag{5.15}$$

with $A = (\pi/4)\ (D_o^2 - D_i^2)$ represent the area of the nanotubes and ε_{cri} is the critical strain. Thus,

$$\sigma_{cri} = E\varepsilon_{cri} = \frac{P_{cri}}{A}, \tag{5.16}$$

where σ_{cri} is the critical stress.

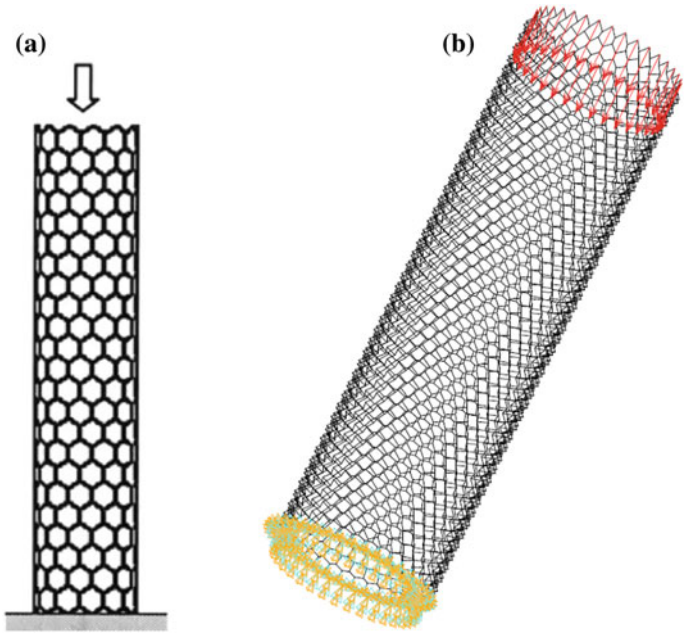

Fig. 5.52 Compressive loading, **a** illustrative and **b** on 35 × 0 zirconia nanotube

5.4.2 Bending Behavior

In order to simulate the bending effect, the free end of SWZNT was exposed to a little transverse displacement (δ) as indicated in Fig. 5.53.

Afterward the maximum force at right angles to cross section at the fixed support nodes of nanotube is recorded. Then, the bending elasticity modulus (E_B) was estimated from [43]:

$$E_B = \frac{FL^3}{3I\delta} \tag{5.17}$$

where F, L, δ and I are bending force, nanotube length, deflection at the free end, and the second moment of inertia, respectively. E_B is also referred to as flexural modulus.

5.4.3 Torsional Behavior

In order to study the torsional behavior of nanotubes, the Cartesian coordinates were substituted with cylindrical coordinates. Afterwards, a slight twist angle is applied to the free end of the nanotube whereas the other end was fixed (Fig. 5.54).

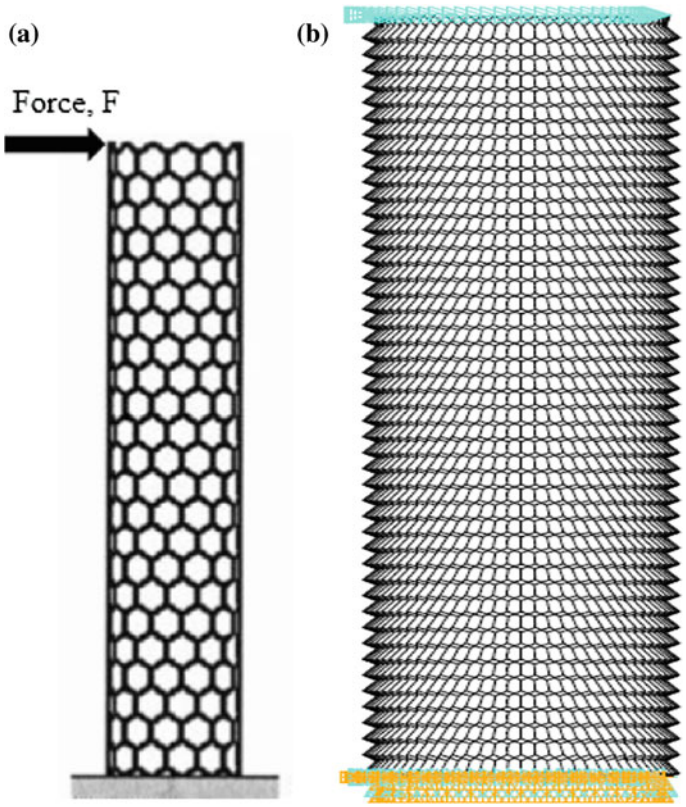

Fig. 5.53 Bending loading, **a** illustrative and **b** on (35 × 0) zirconia nanotube

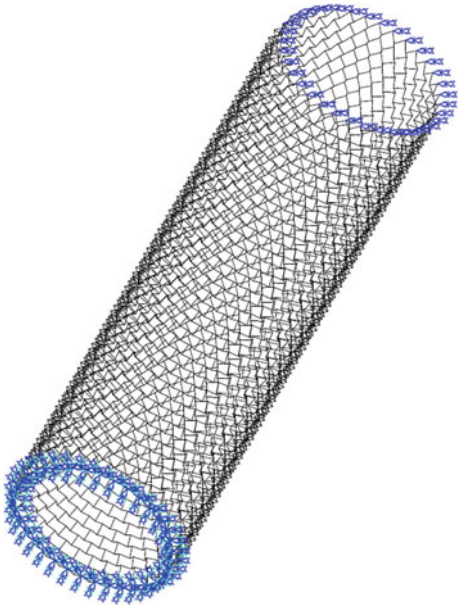

Fig. 5.54 Torsional loading at the free end of (35 × 0) zirconia nanotube

Following the application of the torsion, the sum of generated torsional torque at the fixed end of SWZNT was established and torsional modulus G determined from [44]:

$$G = \frac{TL}{J\phi} \tag{5.18}$$

where T, L, J and ϕ are torsional moment, nanotube length, polar moment of inertia and twist angle, respectively.

5.4.4 Modal Behavior

The modal analysis can be carried out to determine the behavior of SWZNT when exposed to vibration. The mode extraction method used was the Block Lanczos due to its ability for extract large modes [44]. After generating the model, analysis types and options were imposed and then the boundary conditions were set together with the density of the nanotube. The simulation can then be carried out for different settings: fixed-free, free-free and fixed-fixed. At the end of the simulation, the outputs to be recorded include natural frequencies, mode shapes and mode participation factors.

References

1. N.L. Allinger, Conformational analysis. 130. MM2. A hydrocarbon force field utilizing VI and V2 torsional terms. J. Am. Chem. Soc. **99**, 8127–8134 (1977)
2. T. Chang, H. Gao, Size-dependent elastic properties of a single-walled carbon nanotube via a molecular mechanics model. J. Mech. Phys. Solids **51**, 1059–1074 (2003)
3. G.M. Odegarda, T.S. Gatesb, L.M. Nicholsonc, K.E. Wised, Equivalent-continuum modeling of nano-structured materials. Compos. Sci. Technol. **62**, 1869–1880 (2002)
4. C. Li, A structural mechanics approach for the analysis of carbon nanotubes. Int. J. Solids Struct. **40**, 2487–2499 (2003)
5. C.W. Fan, Y.Y. Liu, C. Hwu, Finite element simulation for estimating the mechanical properties of multi-walled carbon nanotubes. Appl. Phys. A **95**, 819–831 (2009)
6. Z. Han, A. Fina, Thermal conductivity of carbon nanotubes and their polymer nanocomposites: a review. Prog. Polym. Sci. **36**, 914–944 (2010)
7. K. Ahmad, W. Pan, Dramatic effect of multiwalled carbon nanotubes on the electrical properties of alumina based ceramic nanocomposites. Compos. Sci. Technol. **69**, 1016–1021 (2009)
8. E.W. Wong, P.E. Sheehan, C.M. Lieber, Nanobeam mechanics: elasticity, strength and toughness of nanorods and nanotubes. Science **277**, 1997 (1971)
9. T. Shokuhfar, G.K. Arumugam, P.A. Heiden, R.S. Yassar, C. Friedrich, Direct compressive measurements of individual titanium dioxide nanotubes. ACS Nano **3**(10), 3098–3102 (2009)
10. I. Kaplan-Ashiri, R. Tenne, Mechanical properties of WS_2 nanotubes. J. Cluster Sci. **18**(3), 549–563 (2007)

11. S. Bertolazzi, J. Brivio, A. Kis, Stretching and breaking of ultrathin MoS_2. ACS Nano **5**(12), 9703–9709 (2011)
12. A.P. Suryavanshi, M.F. Yu, J. Wen, C. Tang, Y. Bando, Elastic modulus and resonance behavior of boron nitride nanotubes. Appl. Phys. Lett. **84**(14), 2527–2529 (2004)
13. A.K. Rappe, C.J. Casewit, K.S. Colwell, W.A. Goddard, W.M. Skiff, UFF, a full periodic table force field for molecular mechanics and molecular dynamics simulations. J. Am. Chem. Soc. **114**, 10024–10035 (1992)
14. N.L. Allinger, *Molecular Structure: Understanding Steric and Electronic Effects from Molecular Mechanics*: Wiley, Hoboken (2010)
15. H. Wan, F. Delale, A structural mechanics approach for predicting the mechanical properties of carbon nanotubes. Meccanica **45**, 43–51 (2010)
16. T. Belytschko, S.P. Xiao, G.C. Schatz, R.S. Ruoff, Atomistic simulations of nanotube fracture. Phys. Rev. B **65**, 235–430 (2002)
17. J. Xiao, B. Gama, J. Gillespiejr, An analytical molecular structural mechanics model for the mechanical properties of carbon nanotubes. Int. J. Solids Struct. **42**, 3075–3092 (2005)
18. K. Tserpes, P. Papanikos, G. Labeas, S. Pantelakis, Multi-scale modeling of tensile behavior of carbon nanotube-reinforced composites. Theoret. Appl. Fract. Mech. **49**, 51–60 (2008)
19. M. Rossi, M. Meo, On the estimation of mechanical properties of single-walled carbon nanotubes by using a molecular-mechanics based FE approach. Compos. Sci. Technol. **69**, 1394–1398 (2009)
20. G. Cao, X. Chen, J.W. Kysar, Thermal vibration and apparent thermal contraction of single-walled carbon nanotubes. J. Mech. Phys. Solids **54**, 1206–1236 (2006)
21. M.A. Caravaca, J.C. Mino, V.J. Pérez, R.A. Casali and C.A.Ponce, Ab initio study of the elastic properties of single and polycrystal TiO_2, ZrO_2 and HfO_2 in the cotunnite structure. J. Phys. Condens. Matter **21**(1) (2009)
22. M.C. Payne, M.P. Teter, D.C. Allan, T.A. Arias, J.D. Joannopoulos, Iterative minimization techniques for ab initio total-energy calculations: molecular dynamics and conjugate gradients. Rev. Mod. Phys. **64**(4), 1045 (1992)
23. G.V. Lewis, C.R.A. Catlow, Potential models for ionic oxides. J. Phys. C: Solid State Phys. **18** (6), 1149–1156 (1985)
24. D. Fang, Z. Luo, S. Liu, T. Zeng, L. Liu, J. Xu, W. Xu, Photoluminescence properties and photocatalytic activities of zirconia nanotube arrays fabricated by anodization. Opt. Mater. **35** (7), 1461–1466 (2013)
25. S.J. Clark, M.D. Segall, C.J. Pickard, P.J. Hasnip, M.I. Probert, K. Refson, M.C. Payne, First principles methods using CASTEP. Z. Kristallogr. **220**, 567–570 (2005)
26. A.R. Yavari, J.J. Lewandowski, J. Eckert, Mechanical properties of bulk metallic glasses. MRS Bull. **32**(08), 635–638 (2007)
27. A. Dwivedi, A.N. Cormack, A computer simulation study of the defect structure of calcia-stabilized zirconia. Philos. Mag. A **61**(1), 1–22 (1990)
28. R.W. Clough, Original formulation of the finite element method. Finite Elem. Anal. Descrip. **7**, 89–101 (1990)
29. P. Kohnke (ed.), *ANSYS Theory Reference*. (ANSYS, 1999)
30. M. Saeed, *Finite Element Analysis: Theory and Application with ANSYS*. Pearson Education, India, 2003
31. ANSYS Release, *10.0 Documentation* (ANSYS Inc., Canonsburg, PA, 2005)
32. Fluent, ANSYS. 12.0 User's guide. *User Inputs for Porous Media* 6, 2009
33. E. Mohammadpour, Numerical and experimental evaluation of carbon nanotube/polypropylene composites using nonlinear finite element modeling, Ph.D. thesis, Universiti Teknologi Petronas, 2013
34. K. Tserpes, P. Papanikos, Finite element modeling of single-walled carbon nanotubes. Compos. B Eng. **36**, 468–477 (2005)
35. C.-W. Fan, J.-H. Huang, C. Hwu, Y.-Y. Liu, Mechanical properties of single-walled carbon nanotubes—a finite element approach. Adv. Mater. Res. **33–37**, 937–942 (2008)

36. S. Nulaka, A.R. Allam, S. Kopparthi, Python program to generate atom records from PDB protein files for drug design studies. J. Bioinform. Res. **1**, 36–40 (2012)
37. A.N. Enyashin, S. Gemming, G. Seifert, Simulation of Inorganic Nanotubes, in *Materials for Tomorrow: Theory. Experiments and Modeling*, ed. by S. Gemming, M. Schreiber, J.-B. Suck (Springer, Berlin, 2010)
38. A.V. Bandura, R.A. Evarestov, Ab initio structure modeling of ZrO_2 nanosheets and single-wall nanotubes. Comput. Mater. Sci. **65**, 395–405 (2012)
39. A.L. Kalamkarov, A.V. Georgiades, S.K. Rokkam, V.P. Veedu, M.N. Ghasemi-Nejhad, Analytical and numerical techniques to predict carbon nanotubes properties. Int. J. Solids Struct. **43**(22), 6832–6854 (2006)
40. BEAM188 3-D Linear Finite Strain Beam [Online] 2009. http://mostreal.sk/html/elem_55/chapter4/ES4-188.htm. Accessed 22 Sept 14
41. I.D. Muhammad, Non-linear finite element modeling of mechanical behaviour of single-walled Zirconia nanotubes, (Ph.D. thesis), Universiti Teknologi Petronas, 2015
42. Release, ANSYS "12.0." *ANSYS Theory Reference,* (2009)
43. M. Zakeri, M. Shayanmehr, On the mechanical properties of chiral carbon nanotubes. J. Ultrafine Grained Nanostruct. Mater. **46**(1), 1–9 (2013)
44. J.H. Lee, B.S. Lee, Modal analysis of carbon nanotubes and nanocones using FEM. Comput. Mater. Sci. **51**(1), 30–42 (2012)

Chapter 6
Non-linear Finite Element Analysis of Nanotubes

6.1 Introduction

Structural analysis is possibly the utmost common application of the finite element method with several options available. For example, in ANSYS there are seven types of structural analyses available: static analysis, modal analysis, harmonic analysis, harmonic analysis, spectrum analysis, buckling analysis, explicit dynamic analysis and others for special-purpose features [1]. Static analysis has wider applications and is used to determine the displacements, stresses, strains, and forces in structures or components caused by loads that do not induce significant inertia and damping effects. *Steady* loading and response conditions are assumed; that is, the loads and the structure's response are assumed to vary slowly with respect to time. The kinds of loading that can be applied in a static analysis include: externally applied forces and pressures, steady-state inertial forces (such as gravity or rotational velocity), imposed (nonzero) displacements, temperatures (for thermal strain) and others [2].

A linear elastic model is not always suitable for numerical simulations of adapted mechanical elements [3]. Such set ups has enormous permanent deformations, and call for material models that should take into consideration the correlation concerning stress and strain.

Nonlinear structural behavior arises from a number of causes, which can be grouped into these principal categories [2]:

(i) Changing Status (Including Contact): Many common structural features exhibit nonlinear behavior that is *status-dependent*. Status changes might be directly related to load or they might be determined by some external cause. Situations in which *contact* occurs are common to many different nonlinear applications. Contact forms a distinctive and important subset to the category of changing-status nonlinearities.

M. Awang et al., *Finite Element Modeling of Nanotube Structures*,
Engineering Materials, DOI 10.1007/978-3-319-03197-2_6

(ii) Geometric Nonlinearities: If a structure experiences large deformations, its changing geometric configuration can cause the structure to respond nonlinearly. Geometric nonlinearity is characterized by "large" displacements and/or rotations.

(iii) Material Nonlinearities: Nonlinear stress-strain relationships are a common cause of nonlinear structural behavior. Many factors can influence a material's stress-strain properties, including load history (as in elastoplastic response), environmental conditions (such as temperature), and the amount of time that a load is applied (as in creep response).

For nanotubes, non-linear structural behaviors are attributed mainly to material properties [3] and are solved using different approaches. For example, ANSYS employs the "Newton-Raphson" approach to solve nonlinear problems. In this approach, the load is subdivided into a series of load increments. The load increments can be applied over several load steps. Figure 6.1 illustrates the use of Newton-Raphson equilibrium iterations in a single DOF nonlinear analysis [2].

There are several models used to designate the elasto-plastic description of materials. Each model has its feature and is suitable to a specific problem. Examples of models are [4]:

(1) Linear elastic,
(2) Elastic-perfectly plastic,
(3) Elasto-plastic with linear or nonlinear hardening,
(4) Isotropic or kinematic hardening.

Several models can be used for describing plasticity behavior in ANSYS. This work will deal with only the Multilinear Isotropic Hardening (MISO) model. The MISO is option uses the von Mises yield criteria coupled with an isotropic work hardening assumption. It is called multilinear [5] because several lines define the stress-strain curve (Fig. 6.2).

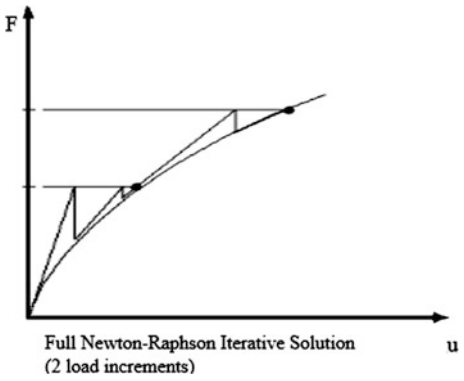

Fig. 6.1 Newton-Raphson approach for solving non-linear problems [2]

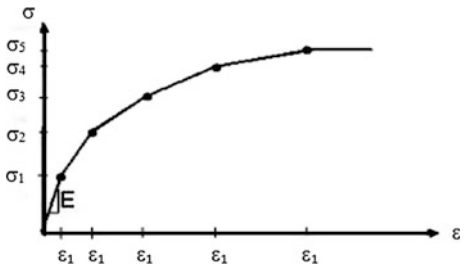

Fig. 6.2 Uniaxial stress-strain curve for a MISO model [3]

6.2 Non-linear Simulation of Carbon Nanotube

6.2.1 Problem Description

Let us consider an armchair carbon nanotube (12,12) with length of 10 nm (100 Å). This nanotube has 1968 carbon atoms which are connected through 2928 covalent bonds. We will study the tensile stress-strain behavior of the nanotube using ANSYS. Recall that for the large deformation of the carbon-carbon bonds, we must employ more complicated potentional such as Modified Morse potentials. The Modified Morse potential was discussed in Sect. 2.3. The geometry of the mentioned nanotube is shown in Fig. 6.3.

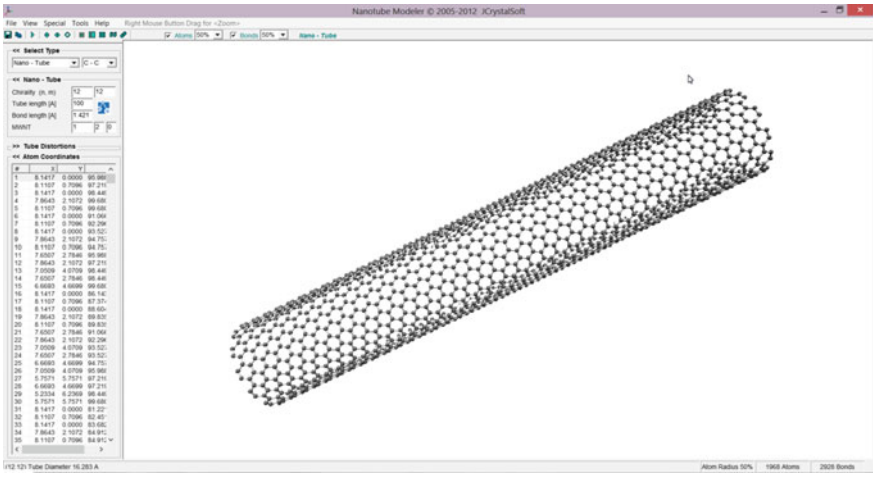

Fig. 6.3 Geometry of (12,12) CNT with L = 10 nm in *Nanotube Modeler*

6.2.2 Defining Element Type

Enter the ANSYS program by using the Launcher and create a title for the problem. This title helps to identify the displays. Use the following command sequences: **Utility Menu > File > Change Title**.

Then select the BEAM188 element. BEAM 188 element supports nonlinear material models such as large deflection, large strain, plasticity, stress stiffening, user-defined material. This element is capable enough to handle nonlinear material properties corresponding to the interatomic Morse potential functions. These functions were already introduced in Sect. 5.3.3.

6.2.3 Defining Material Properties

In general, a number of factors can cause your structure's stiffness to change during the course of an analysis. Nonlinear stress-strain relationships cause a structure's stiffness to change at different load levels. We have to use this concept in order to make the equivalency between chemical PEF and structural analysis (Fig. 6.4).

If a material displays nonlineary, we can use the TB family of commands (TB, TBTEMP, TBDATA, TBPT, TBCOPY, TBLIST, TBPLOT, TBDELE) to define the nonlinear material property relationships in terms of a data table. The precise form of these commands varies depending on the type of nonlinear material behavior being defined.

Consider a C–C bond which can be expressed by Morse potential functions. Under axial tension, bond stretching potential dominates the nanotube deformation. Based on the stress-strain curve of a single C–C bond (Fig. 6.5), the Multi-linear Isotropic Hardening (TB, MISO) option is recommended for large strain analyses of the nanotube. The MISO option can contain up to 20 different temperature curves, with up to 100 different stress-strain points allowed per curve. Strain points can differ from curve to curve.

The corresponding material model (TB, MISO) consists of two main parts. Isotropic elastic and non-linear isotropic hardening model. For the elastic section, axial Young's modulus and Poisson ratio were obtained from the elastic formulation. Based on the Eq. (3.4), the stretching force for a C–C bond has defined. Stress-strain relationship for bond stretching can be calculated by dividing the stretching force by bond cross section. The diameter of C–C covalent

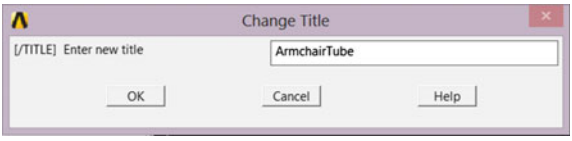

Fig. 6.4 Title for the (12,12) CNT

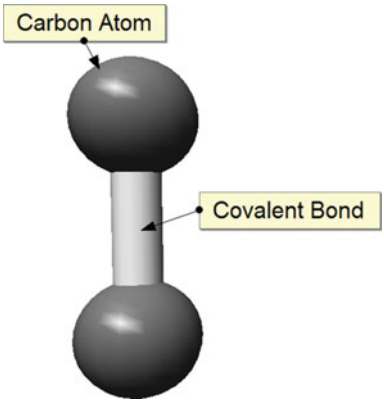

Fig. 6.5 Simplified structural model of the carbon-carbon bond

Bond is 1.47 Å, so the cross section would be $\pi D^2/4$. *Microsoft Excel* is used to make the calculations.

The initial modulus of the covalent bond is 7.99087 TPa and passion ratio is 0.3. The nonlinear model is responsible for large deformation of the bond at larger strains.

```
/PREP7
MP,EX,1,6.7E12      !ISOTROPIC ELASTIC YOUNG'S MODULUS
MP,PRXY,1,,0.3      !ISOTROPIC ELASTIC POISSON'S RATIO

TB,MISO,1,1,15          !DEFINE NONLINEAR ISOTROPIC HARDEDING MATERIAL
TBPT,DEFI,0.00499999999999998,39954313058.2701      !STRAIN, STRAIN
TBPT,DEFI,0.0249999999999999,187641262616.324
TBPT,DEFI,0.0449999999999998,312850209775.058
TBPT,DEFI,0.065,418218409215.675
TBPT,DEFI,0.085,506099953999.886
TBPT,DEFI,0.105,578595037687.637
TBPT,DEFI,0.125,637576246657.843
TBPT,DEFI,0.145,684712181362.927
TBPT,DEFI,0.165,721488675333.018
TBPT,DEFI,0.185,749227853819.524
TBPT,DEFI,0.205,769105249732.323
TBPT,DEFI,0.225,782165172711.396
TBPT,DEFI,0.245,789334507540.674
TBPT,DEFI,0.265,791435100441.428
TBPT,DEFI,0.28,790245382980.451
```

Now, check the material models which should indicate two options: Linear Isotropic and Multilnear Isotropic (Fig. 6.6).

The MISO table can be reviewed together with revised strain and stress values if necessary by double clicking **Multilinear Isotropic** to see the window in Fig. 6.7.

Click **Graph** to plot the defined strain-stress data. It should be noted that MISO material model does not support negative slops in the defined curve. The initial

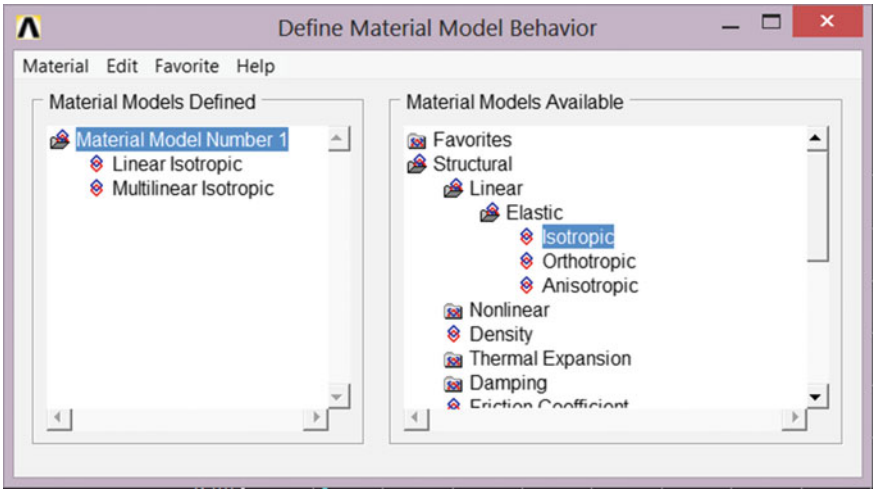

Fig. 6.6 Material models defined for CNT

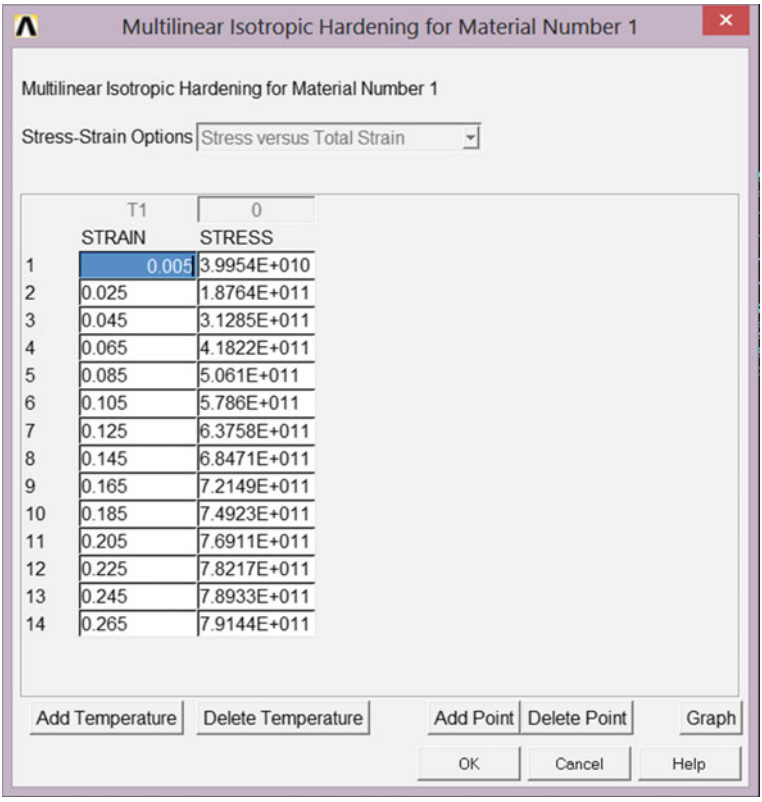

Fig. 6.7 Defined strain-stress data for C–C bond

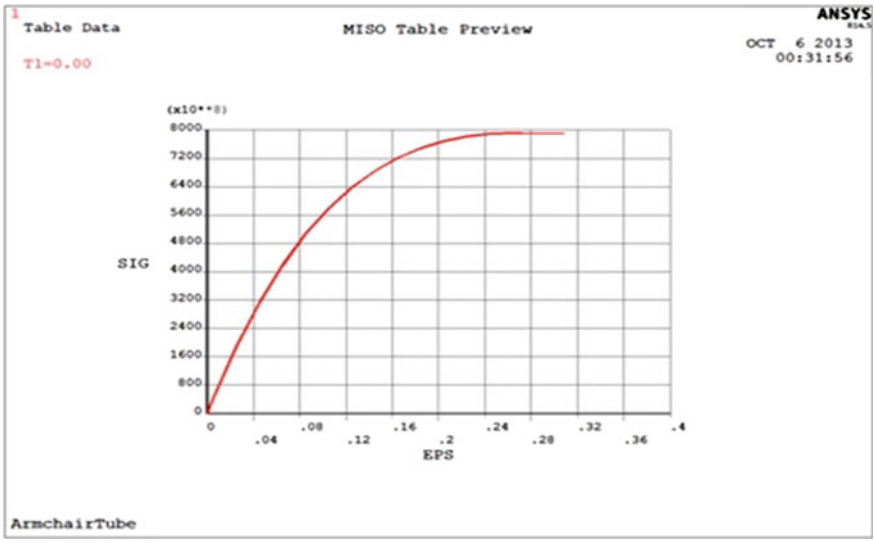

Fig. 6.8 Stress-strain curve for C–C bond based on MISO model

point of the graph will be used by ANSYS to calculate the initial Young's modulus. So, the elastic isotropic Young's modulus should be exactly similar to this value from the curve. Otherwise, there would be some errors (Fig. 6.8).

6.2.4 Defining the Element Cross Section

The cross section of the beam elements according to the simplified structural model of the carbon-carbon bond is indicated in Fig. 6.9, see details in Sect. 5.3.4.

6.2.5 Creating the Nanotube Geometry

After creating the (12,12) nanotube as indicated in Fig. 6.3, then *Microsoft Excel* is used to list the commands for Nodes and Elements in ANSYS. Carbon atoms will be replaced by nodes and covalent bonds will be substitute with beam elements. Figure 6.10 shows a section of text file consist of nodes definition commands, since we have almost 2000 nodes having the format: N, NODE, X, Y, Z, THXY, THYZ, THZX. Then follow the sequence **Main Menu > Preprocessor > Modeling > Create > Nodes > In Active CS** to create the nodes.

Now we use the *text editor* to replace spaces with ",". The result would be a list of node definition commands as partially shown in Fig. 6.11. Then copy the list and

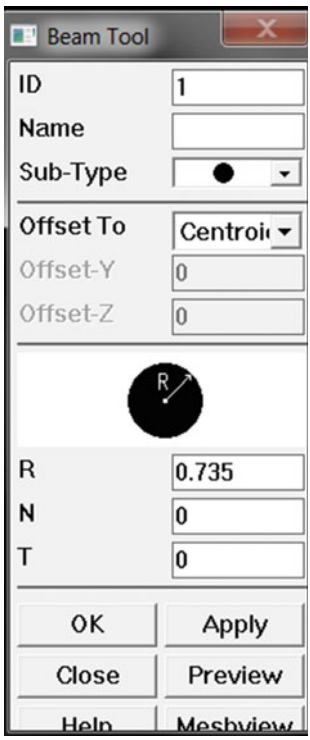

Fig. 6.9 Selected cross section of C–C bond (*BEAM188*)

paste it at the command prompt in ANSYS and press ENTER to obtain the geometrical model of (12,12) as shown in Fig. 6.12.

After we defined the nodes, elements will be defined to connect adjacent nodes and create the honeycomb structure of the armchair nanotube. We must use following command, in order to create the beam elements: **Main Menu > Preprocessor > Modeling > Create > Elements > Auto Numbered > Thru Nodes** having the format: E, I, J, K, L, M, N, O, P with *E* representing "element" and *I, J, K* indicating x, y, z coordinates of the nodes (atoms). Then from *Microsoft* Excel, import bonds list (Fig. 6.13).

Now replace the spaces with "," in the *text editor* (Fig. 6.14a) and paste the list to the command prompt in ANSYS. Then, plot the elements in the (12,12) CNT as defined as shown in Fig. 6.14b.

6.2.6 Boundary Conditions and Loads

Apply boundary condition with the following commands: **Main Menu > Solution > Define Loads > Apply > Structural > Displacement > On Nodes**. Procedures for applying the boundary condition can be reduced and making the process more convenient by using a series of commands and tools in APDL.

Fig. 6.10 Nodes and coordinates of (12,12) CNT in *Microsoft Excel*

	A	B	C	D	E
1	Command	Node Number	X	Y	Z
2	n	1	8.1417	0	95.9885
3	n	2	8.1107	0.7096	97.2191
4	n	3	8.1417	0	98.4498
5	n	4	7.8643	2.1072	99.6804
6	n	5	8.1107	0.7096	99.6804
7	n	6	8.1417	0	91.066
8	n	7	8.1107	0.7096	92.2967
9	n	8	8.1417	0	93.5273
10	n	9	7.8643	2.1072	94.7579
11	n	10	8.1107	0.7096	94.7579
12	n	11	7.6507	2.7846	95.9885
13	n	12	7.8643	2.1072	97.2192
14	n	13	7.0509	4.0709	98.4498
15	n	14	7.6507	2.7846	98.4498
16	n	15	6.6693	4.6699	99.6804
17	n	16	8.1417	0	86.1436
18	n	17	8.1107	0.7096	87.3742
19	n	18	8.1417	0	88.6048
20	n	19	7.8643	2.1072	89.8354
21	n	20	8.1107	0.7096	89.8354
22	n	21	7.6507	2.7846	91.066
23	n	22	7.8643	2.1072	92.2967
24	n	23	7.0509	4.0709	93.5273
25	n	24	7.6507	2.7846	93.5273
26	n	25	6.6693	4.6699	94.7579
27	n	26	7.0509	4.0709	95.9885
28	n	27	5.7571	5.7571	97.2192
29	n	28	6.6693	4.6699	97.2192
30	n	29	5.2334	6.2369	98.4498

For commands in APDL, components must be created which would be useful through the rest of the analysis. A component is a grouping of some geometric entity that can then be conveniently selected or unselected. A component may be redefined by reusing a previous component name. The following entity types may belong to a component: nodes, elements, keypoints, lines, areas, and volumes. A component may contain only 1 entity type, but an individual item of any entity may belong to any number of components. Once defined, the items contained in a component may then be easily selected or unselected [CMSEL]. Components may be listed [CMLIST], modified [CMMOD] and deleted [CMDELE]. Components may also be further grouped into assemblies [CMGRP]. Other entities associated with the entities in a component (e.g., the lines and keypoints associated with areas) may be selected by the ALLSEL command.

The steps for creating component(s) are illustrated in Figs. 6.15, 6.16, 6.17, 6.18.

Then click Ok to return to the Component Manager window which shows a list of existing components (Fig. 6.19).

N,·NODE,·X,·Y,·Z

```
1  n,1,8.1417,0,95.9885
2  n,2,8.1107,0.7096,97.2191
3  n,3,8.1417,0,98.4498
4  n,4,7.8643,2.1072,99.6804
5  n,5,8.1107,0.7096,99.6804
6  n,6,8.1417,0,91.066
7  n,7,8.1107,0.7096,92.2967
8  n,8,8.1417,0,93.5273
9  n,9,7.8643,2.1072,94.7579
10 n,10,8.1107,0.7096,94.7579
11 n,11,7.6507,2.7846,95.9885
12 n,12,7.8643,2.1072,97.2192
13 n,13,7.0509,4.0709,98.4498
14 n,14,7.6507,2.7846,98.4498
15 n,15,6.6693,4.6699,99.6804
16 n,16,8.1417,0,86.1436
17 n,17,8.1107,0.7096,87.3742
18 n,18,8.1417,0,88.6048
19 n,19,7.8643,2.1072,89.8354
20 n,20,8.1107,0.7096,89.8354
21 n,21,7.6507,2.7846,91.066
22 n,22,7.8643,2.1072,92.2967
23 n,23,7.0509,4.0709,93.5273
```

Fig. 6.11 Nodes and coordinates of (12,12) CNT in *text editor/notepad*

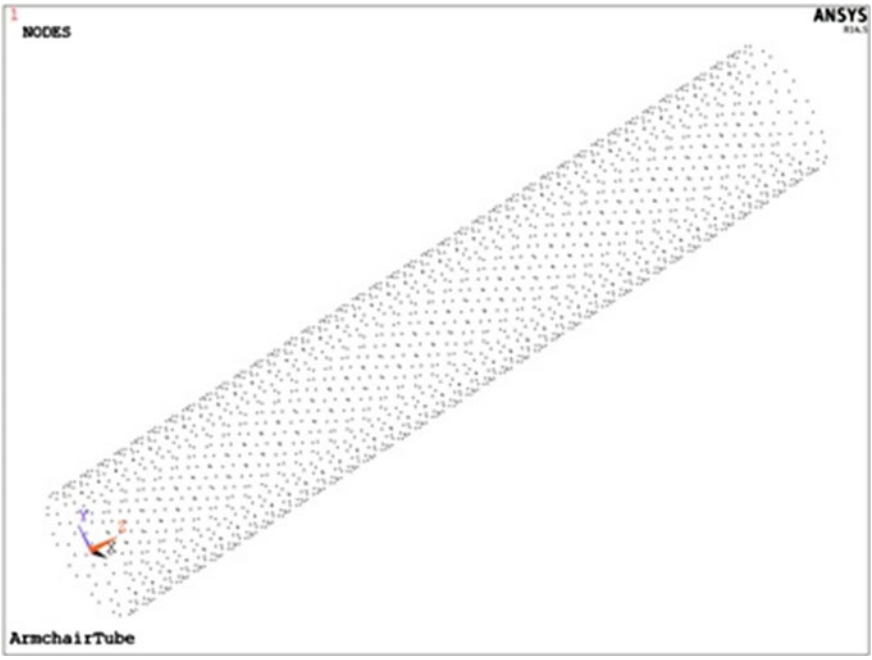

Fig. 6.12 Structural geometry of (12,12) CNT

	A	B	C	D
1	Command	Node I	node J	
2	e	1	2	
3	e	1	10	
4	e	1	996	
5	e	2	3	
6	e	2	12	
7	e	3	5	
8	e	3	899	
9	e	4	5	
10	e	4	14	
11	e	6	7	
12	e	6	20	
13	e	6	1092	
14	e	7	8	
15	e	7	22	
16	e	8	10	
17	e	8	994	
18	e	9	10	
19	e	9	11	
20	e	9	24	

Fig. 6.13 Elements/bonds list for (12,12) CNT

In other to create another component from the 24 nodes at the bottom top of the nanotube and name it "Bottom_nodes", follow the same procedure in Figs. 6.15, 6.16, 6.17, 6.18 as obtained in Fig. 6.20.

Alternatively, we can use command on *notepad* to select the components and apply boundary conditions to the nanotube model by following the below commands,

```
CMSEL, s, Bottom_Nodes      !select component of BOTTOM NODES
CMPLOT                      !PLOT THE COMPONENT
D, All,UX                   !CONSTRAIN STRUCTURAL DISPLACEMENT IN X DIRECTION
D,ALL,UY                    !CONSTRAIN STRUCTURAL DISPLACEMENT IN Y DIRECTION
D,ALL,UZ                    !CONSTRAIN STRUCTURAL DISPLACEMENT IN Z DIRECTION
CMSEL, s, Top_Nodes         !select component of TOP NODES
CMPLOT
D,ALL,UZ,10                 !APPLY DISPLACEMENT IN Z DIRECTION
ALLSEL,ALL                  !SELECT EVERYTHING
```

(a)

```
e,1,2
e,1,10
e,1,996
e,2,3
e,2,12
e,3,5
e,3,899
e,4,5
e,4,14
e,6,7
e,6,20
e,6,1092
e,7,8
e,7,22
e,8,10
e,8,994
e,9,10
e,9,11
e,9,24
e,11,12
e,11,26
e,12,14
```

(b)

Fig. 6.14 **a** Elements in APDL format for (12,12) CNT; **b** (12,12) CNT FE model

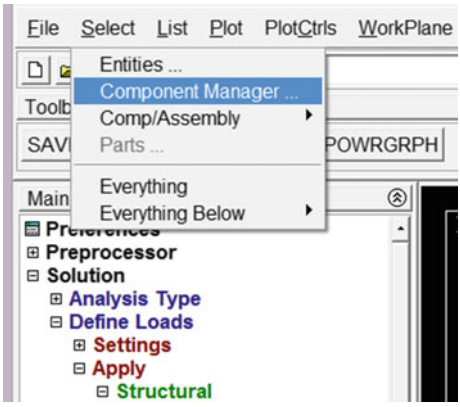

Fig. 6.15 Selecting component manager from the Select menu

Copy the entire list and paste them at the command prompt in ANSYS toolbar.

Using the GUI or command option, model with boundary conditions is generated as shown in Fig. 6.21.

After setting the boundary conditions, we must define the load step options. Select the Solution Control form the Analysis Type. Enter the solution controls and change the small deformation to large deformation option. It is recommended to work with large deformation option when non-linear material models is active. We need to set the following parameters (Fig. 6.22):

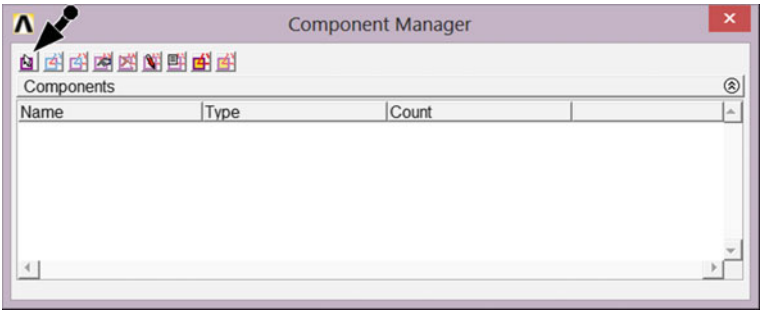

Fig. 6.16 Creating component(s)

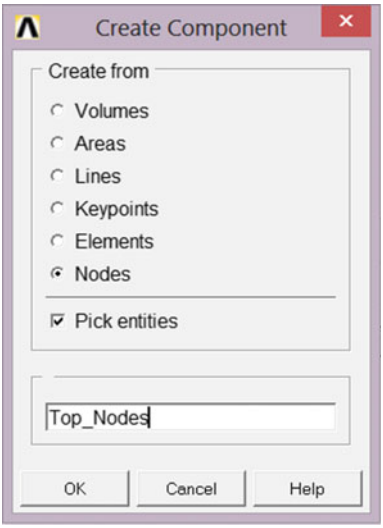

Fig. 6.17 Picking entities and renaming the component as "Top_Nodes"

Analysis Options: Large Displacement
Time at end of loadstep: 100
Automatic time stepping: On
Number of substeps: 200
Max no. of substeps: 300
Min no. of substeps: 100
Frequency: Write every substep

Then choose solve current LS and wait until the solving ends. Waiting time is highly depends on the computing power of your unit.

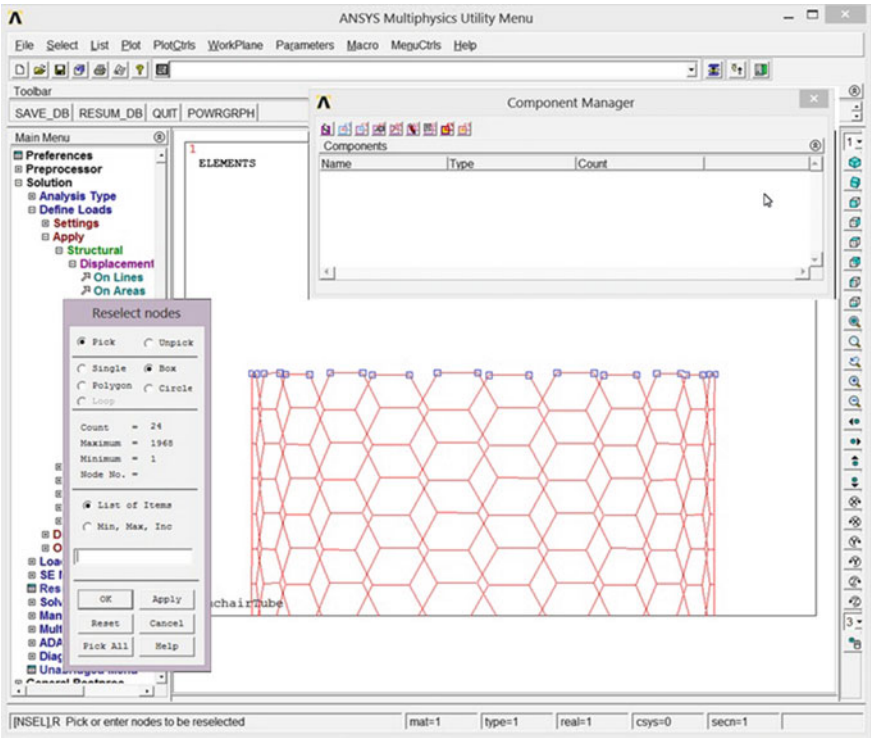

Fig. 6.18 Reselecting nodes at *top end* of the (12,12) carbon nanotube

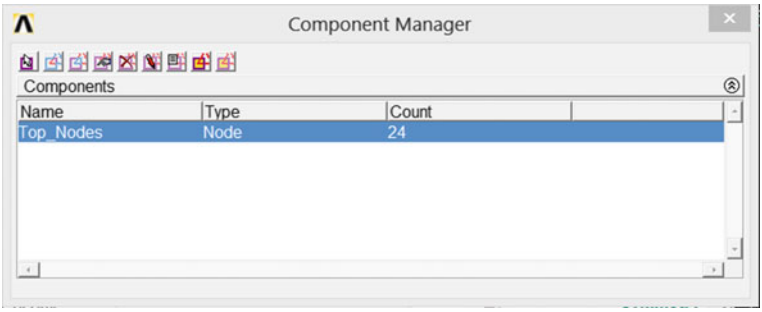

Fig. 6.19 List of existing components in (12,12) CNT

6.2.7 Non-linear Solution

The Graphical Solution Tracking plot is shown in Fig. 6.23. The title of the graph is the time value of the last calculated iteration. For example, the time at the end of the analysis was set to 100. This can be changed with the Time command before the

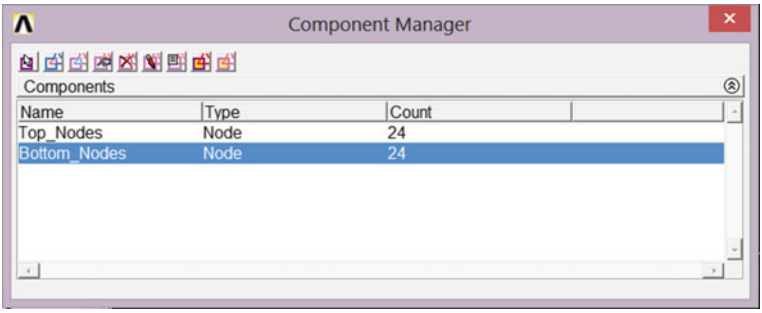

Fig. 6.20 *Top* and *bottom* components for the (12,12) CNT

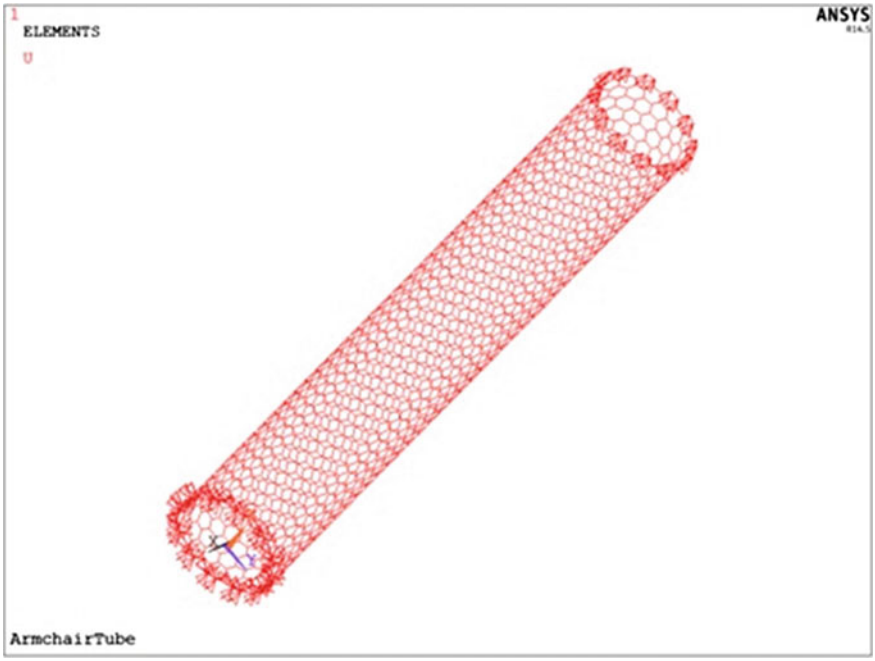

Fig. 6.21 carbon nanotube (12,12) with applied boundary conditions

Solve command is issued. For more information regarding setting the time value, and many other solution control option, see Chapter on Structural Analysis Guide in the ANSYS Help documents [1, 2, 6].

In the plot (Fig. 6.23), the *x-axis* is labeled *Cumulative Iteration Number*. As ANSYS steps through non-linear analysis, it uses a solver, *Newton-Raphson* as illustrated in Fig. 6.1. If the problem is relatively linear, very little iteration will be required and thus the length of the graph will be small. However, if the solution is highly non-linear, or is not converging, much iteration will be required. The length

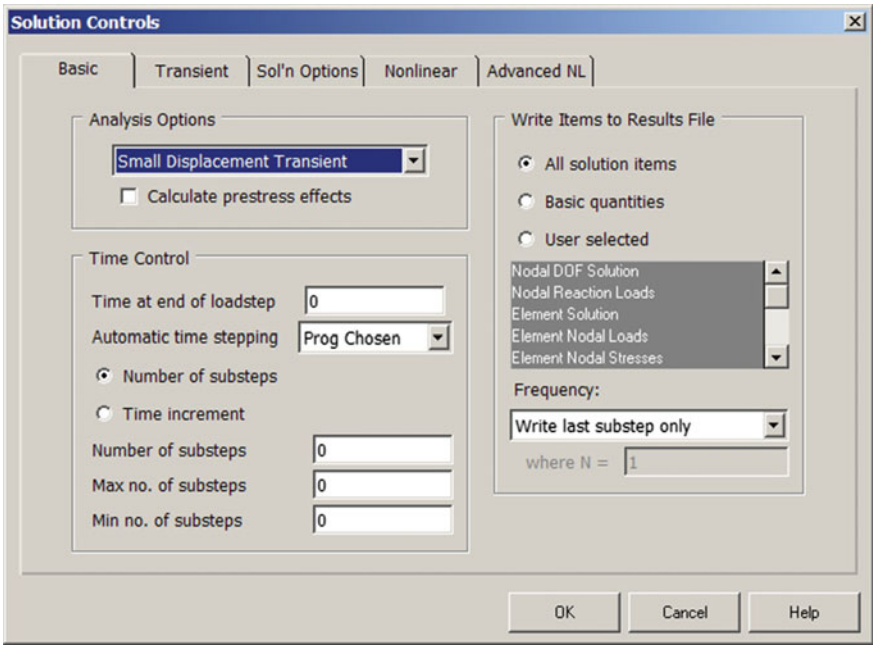

Fig. 6.22 Setting the solutions control for non-linear analysis

of the graph in these cases can be quite long. Again, for more information about changing iteration settings, see Chapter on Structural Analysis Guide in the ANSYS Help documents [1, 2, 6].

The *y-axis* is labeled *Absolute Convergence Norm*. In the case of a structural analysis, which this graph is taken from, this absolute convergence norm refers to non-normalized values (i.e. there are units associated with these values). Some analyses use normalized values. In reality it does not really matter because it is only a comparison that is going on.

6.2.7.1 Curves and Legend

As can be guessed from the legend labels, the graph in Fig. 6.23 relates to forces and moments. These values are plotted because they are the corresponding values in the solution vector for the DOF's that are active in the elements being used. If this graph were from a thermal analysis, the curves may be for temperature. For each parameter, there are two curves plotted. For ease of explanation, we will look at the force curves.

The **F CRIT** curve refers to the convergence criteria force value. This value is equal to the product of **VALUE** times **TOLER**. The default value of **VALUE** is the square root of the sum of the squares (SRSS) of the applied loads, or **MINREF**

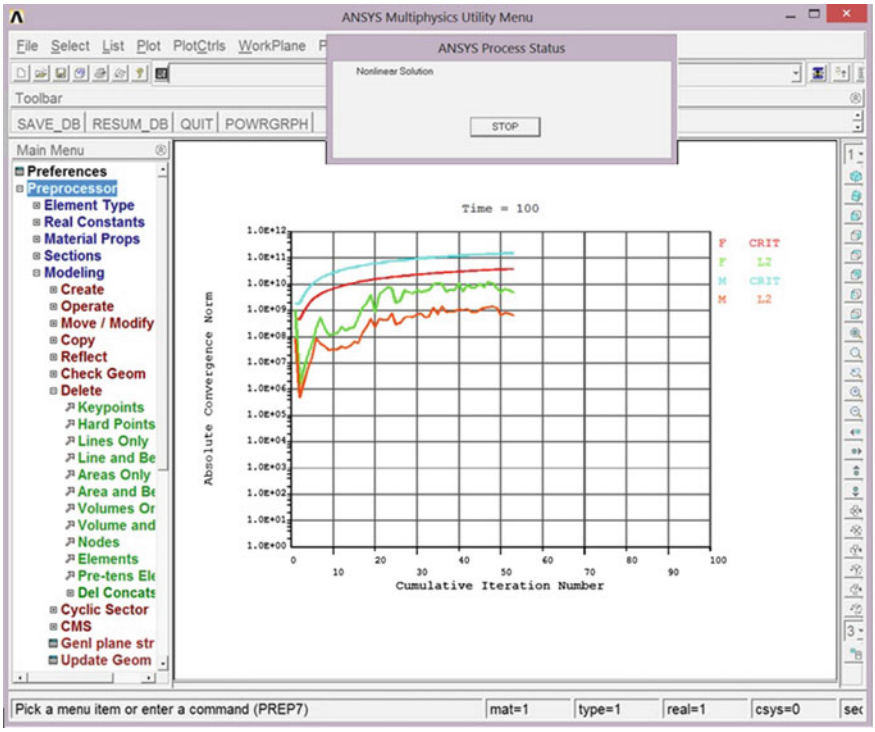

Fig. 6.23 Graphical solution tracking plot for (12, 12) CNT

(which defaults to 0.001), whichever is greater. This value can be changed using the **CNVTOL** command, which is discussed in the help file. The value of **TOLER** defaults to 0.5 % for loads.

One may inquire why the **F CRIT** value increases as the number of iterations increases. This is because the analysis is made up of a number of substeps. In the case of a structural example, such as this, these substeps are basically portions of the total load being applied over time. For instance, a 100 N load broken up with 20 substeps means 20, 5 N loads will be applied consecutively until the entire 100 N is applied. Thus, the **F CRIT** value at the start will be 1/20th of the final **F CRIT** value.

The F L2 curve refers to the L2 Vector Norm of the forces. The L2 norm is the SRSS of the force imbalances for all DOF's. In simpler terms, this is the SRSS of the difference between the calculated internal force at a particular DOF and the external force in that direction.

For each substep, ANSYS iterates until the **F L2** value is below the **F CRIT** value. Once this occurs, it is deemed the solution is within tolerance of the correct solution and it moves on to the next substep. Generally, when the curves peak this is the start of a new substep. As can be seen in the graph above, a peak follow every time the L2 value drops below the **CRIT** value, as expected.

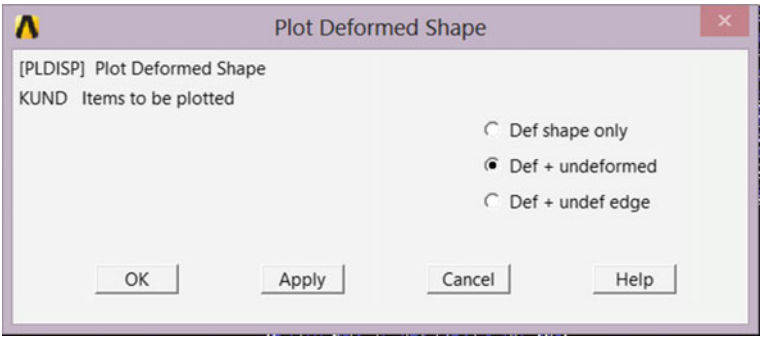

Fig. 6.24 Options for plotting deformed shape

6.2.8 Post Processing

In order to obtain/view the results from the simulation of the nanotube, follow the command sequence path: **Main Menu > General Postproc > Plot Results > Deformed Shape**. Then select the **Def + undeformed** option (Fig. 6.24) to obtain the displacement vector sum (Fig. 6.25).

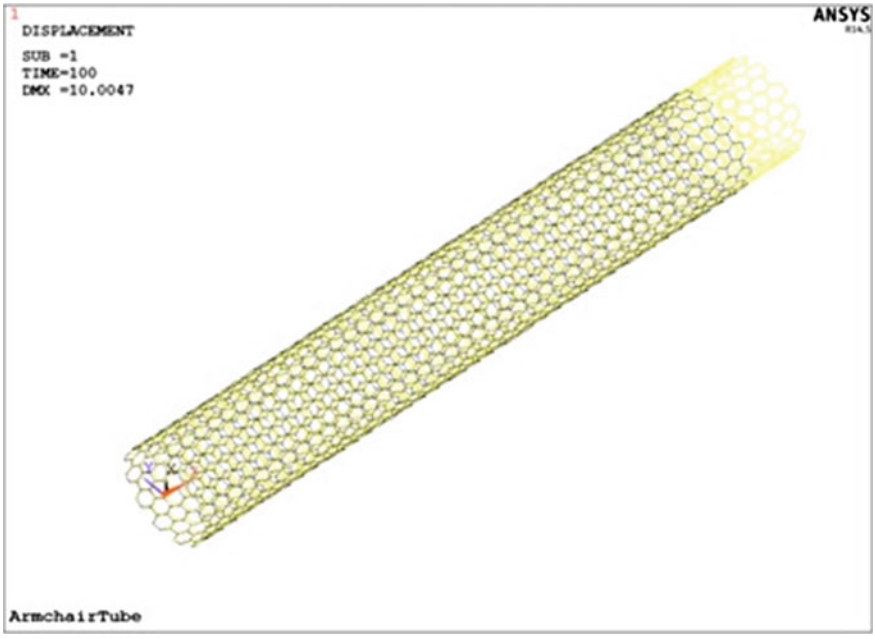

Fig. 6.25 Plot result for the displacement vector sum from the nodal solution

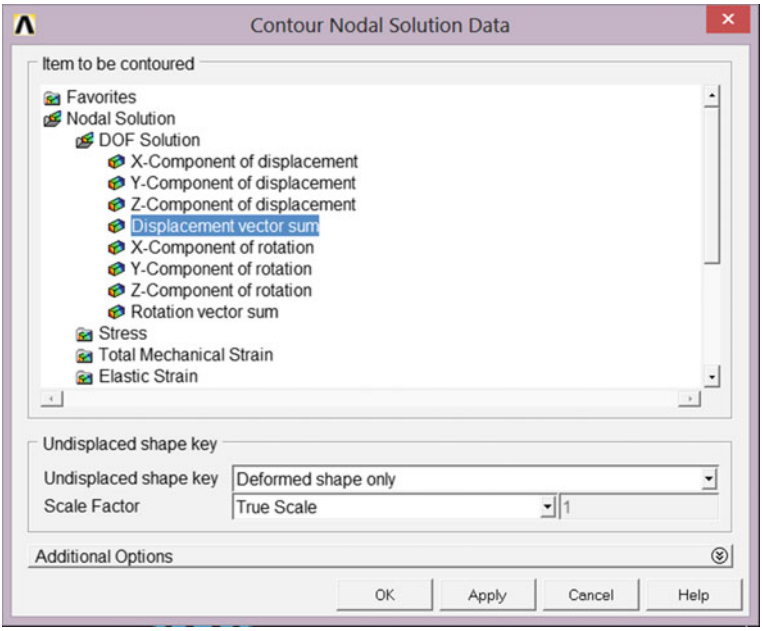

Fig. 6.26 Options for contour plotting

Then, in order to obtain the contour results from the simulation of the nanotube, follow the command sequence path: **Main Menu > General Postproc > Plot Results > Contour Plot > Nodal Solu**. Then select the **DOF Solu** option (Fig. 6.26) to obtain the displacement vector sum (Fig. 6.27).

In order to review the effect of axial displacement, we must define the axial strain and internal stress using element tables. We can define the tables through the Element Table under General Post processing menu. The more convenient option is to use a series of ANSYS commands and command prompt. We will use the following commands to define and plot the element strains and stresses:

Main Menu > General Postproc > Element Table > Define Table
ETABLE, Lab, Item, Comp
Main Menu > General Postproc > Element Table > Plot Elem Table
PLETAB, Itlab, Avglab
Use a *text editor* and type following sequence of commands,

```
1  ETABLE, AxStrain, SMISC, 7
2  PLETAB, AxStrain, NOAV
3
4  ETABLE, InStress, SMISC, 31
5  PLETAB, InStress, NOAV
6
7
```

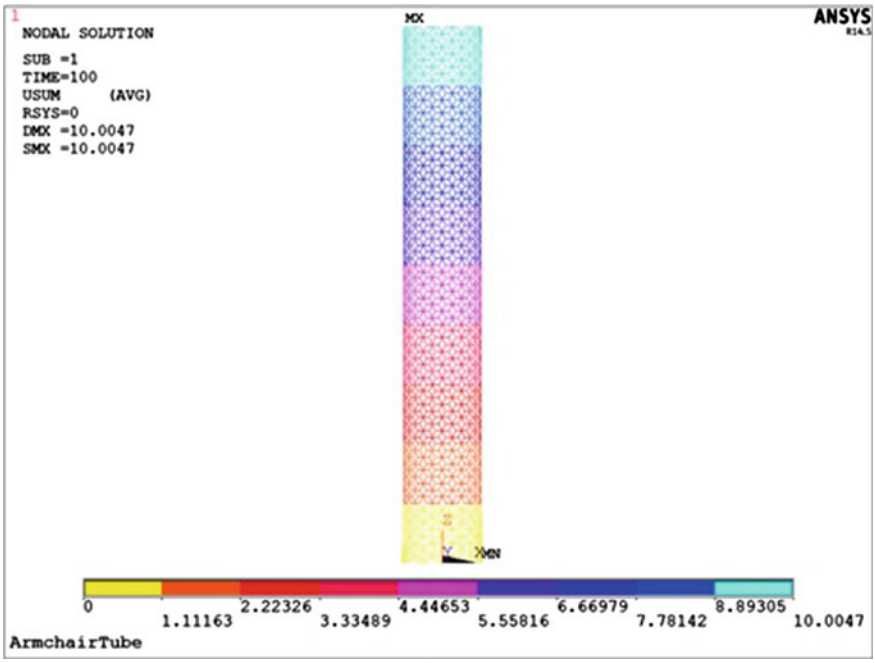

Fig. 6.27 Contour plot result for the displacement vector sum options for (12,12) CNT

The bonds strain based on Modified Morse potential are shown in Fig. 6.29 similar to what was obtained in Fig. 6.28.

6.2.9 Stress-Strain Curve of the Nanotube

Now that we have incorporated a more precise potential function, it is possible to study the stress-strain relationship of the nanotube under axial displacements. Based on the defined parameters at Solution Control section, we have applied the axial displacement at 100 equal steps. List of substeps can be found in the General Post processing menu by this sequence: **Main Menu > General Postproc > Read Results > By Pick** with the output in Fig. 6.29.

We must calculate the reaction forces on all nodes at top end of the nanotube at each substep. There are several ways to review the stored solution data using command prompt. *GET command is a general command to obtain a specific data from the solutions. We can use it at different section of the analysis by employing appropriate set of parameters. These parameters can be listed from the Help Topics at main menu.

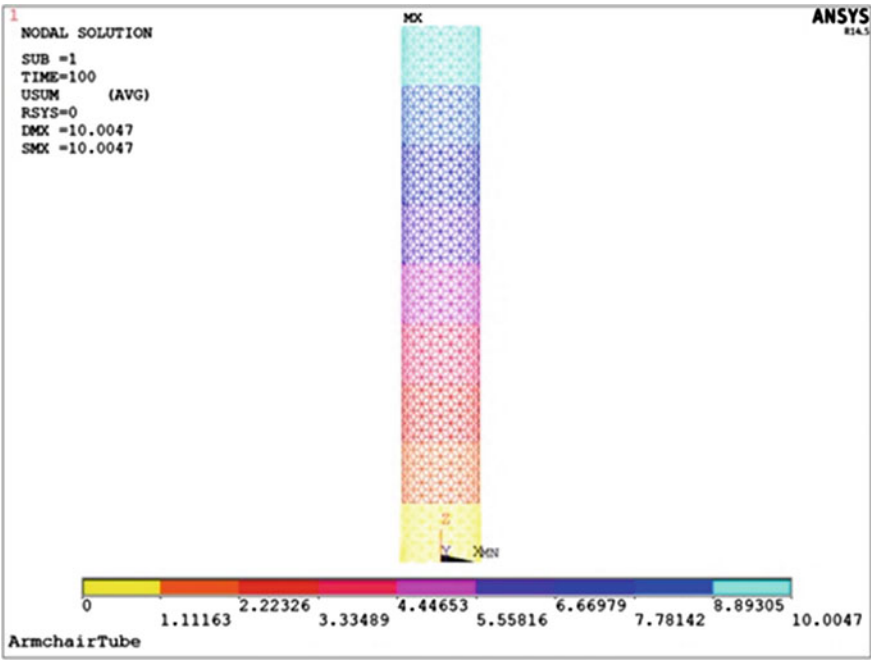

Fig. 6.28 Contour plot for the element strain of (12,12) CNT

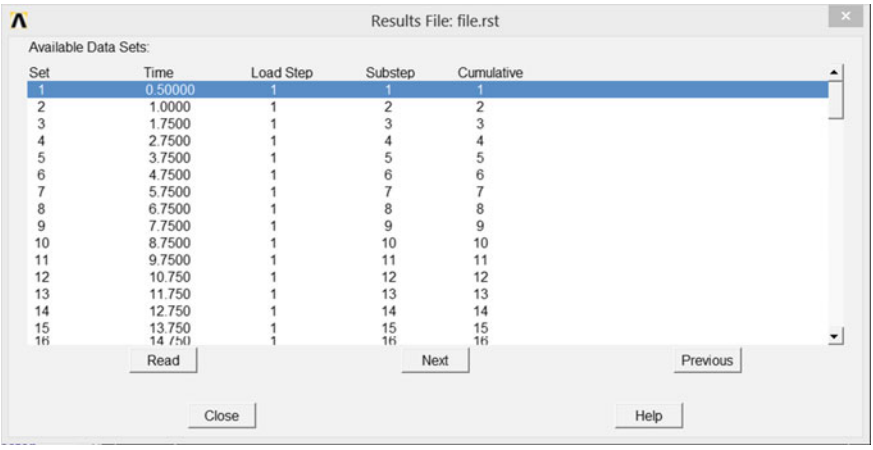

Fig. 6.29 List of substeps for (12,12) CNT

***GET**, *Par*, *Entity*, *ENTNUM*, *Item1*, *IT1NUM*, *Item2*, *IT2NUM*

GET command retrieves a value for a specified item and stores the value as a scalar parameter, or as a value in a user-named array parameter. An item is identified by various keyword, label, and number combinations. The usage is similar to

the *SET command except that the parameter values are retrieved from previously input or calculated results. For example, A, ELEM, 5, CENT, X returns the centroid x-location of element 5 and stores the result as parameter A. *GET command operations, along with the associated Get functions return values in the active coordinate system unless stated otherwise. A Get function is an alternative in-line function that can be used to retrieve a value instead of the *GET command (see Using In-line Get Functions for more information). The sequence is: **Utility Menu > Parameters > Get Scalar Data**.

We will use *GET command to retrieve reaction forces and strains at top end of the nanotube. For additional information regarding other mentioned commands, please referee to the ANSYS documents from Help Topics. Use a text editor and type the commands as shown in Fig. 6.30. This macro, Macro_1, will store the reaction forces and nanotube strain under axial tension in a text file which named "output.txt".

After creating the Macro_1, save it into the working directory and rename it to "lib_1.txt". Use the text editor to define below commands,

```
*ULIB,lib_1,txt
*USE,Macro_1
```

Copy both lines and paste them into the command prompt. Wait till the process is accomplished. Now, we can import output.txt into *Microsoft Excel* (Fig. 6.31) and used to plot the stress-strain curve (Fig. 6.32) with the slope been the Young's modulus.

```
Macro_1         !Name of macro
/POST1
CMSEL,S,TOP_NODES,NODES         !Recall the TOP_NODES component
CMPLOT                          !Plot the component
*CFOPEN,D:\output,txt,,loc      !Create the TEXT file
*VWRITE,'step_num','Z_Strain','Z_Stress'
(A8,',',A8,',',A8)
A_ =208.2373974             !Cross section of the nanotube
L_=99.74268451                  !length of the nanotube
*GET,step_num,ACTIVE,0,SET,NSET,,Loadstep           !Retrieve the number of substeps
*DO,j_,1,step_num
   m_=0
   n_=0
   rx_sum = 0
   ry_sum = 0
   rz_sum = 0
   SET,,,,,,,j_
   numnp_ = NDINQR(0,13)                            !Retrieve the number of selected nodes
   *DO,i_,1,numnp_
      n_ = NDNEXT(n_)                               !retrieve the next node in the selection
      rf_i = 0.
      *GET,rf_i, NODE,n_,RF,FZ                      !Retrieve the reaction force in axial direction at each substep
      rz_sum = rz_sum + rf_i
         *IF,m_,EQ,0,then
            *GET,U_Z,NODE,n_,U,Z                    !retrieve the displacement in axial direction at each substep
            z_=U_Z/L_
            m_=1
         *ENDIF
      Z_Stress = rz_sum / A_
   *ENDDO
*VWRITE,j_,z_,Z_Stress
(F4.0,',',F10.5,',',F20.5)
*ENDDO
*CFCLOSE
/eof                        !End of Macro_1
```

Fig. 6.30 Macro to retrieve reaction forces and strains at the top of (12,12) CNT

Fig. 6.31 Retrieved stress and strain for (12,12) CNT

	A	B	C	D	E
1	step_num	Z_Strain	Z_Stress		
2	1	0.0005	432738580.4		
3	2	0.001	865427150.9		
4	3	0.00175	1514980883		
5	4	0.00276	2381686522		
6	5	0.00376	3249108892		
7	6	0.00476	4117237203		
8	7	0.00576	4986060701		
9	8	0.00677	5855491462		
10	9	0.00777	6725326413		
11	10	0.00877	7595332883		
12	11	0.00978	8465056629		
13	12	0.01078	9291600235		
14	13	0.01178	10133030787		
15	14	0.01278	10962837100		
16	15	0.01379	11801216189		
17	16	0.01479	12640113840		
18	17	0.01579	13479653658		
19	18	0.01679	14319558882		
20	19	0.0178	15157631017		
21	20	0.0188	15993049372		
22	21	0.0198	16826652895		
23	22	0.0208	17658806178		
24	23	0.02181	18488982337		
25	24	0.02281	19317750696		
26	25	0.02381	20165766919		
27	26	0.02481	21076583878		
28	27	0.02582	21840010198		
29	28	0.02682	22665672662		
30	29	0.02782	23600688691		

Fig. 6.32 Plot the stress values against the strain values

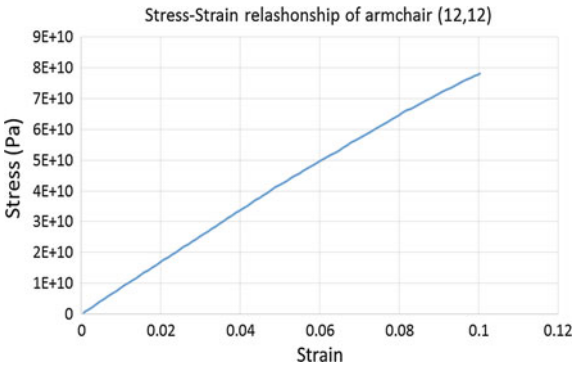

6.3 Non-linear Simulation of Inorganic Nanotubes

The procedure for simulation of mechanical properties of inorganic nanotubes is similar to that used for carbon nanotube with some differences in relation to specifications. For example, the input sectional properties for the element of single walled zirconia nanotube compared to that of carbon nanotube are shown in Table 5.3.

The diameter and Poisson ratio for the element (Zr-O bond) were determined to be 0.018 nm and 0.1897 respectively using *CrystalMaker* and *CASTEP*. While for C–C bond, the diameter and Poisson ratio are 0.147 nm and 0.3 respectively.

Differentiating Eq. (2.26), the force between Zr-O bond is:

$$F = \left(-\frac{Ae^{-\frac{r}{\rho}}}{\rho}\right) + \left(\frac{6C}{r^7}\right) - \left(\frac{Q_{Zr}Q_{o_2}}{4\varepsilon_0\pi r^2}\right) \tag{6.1}$$

In relation to ZrO_2, $\varepsilon_o = 0.55263614 \times 10^{-12}$ $C^2eV^{-1}Å^{-1}$, $Q_{Zr} = 4e$, $Q_{O2} = -2e$, where e is magnitude of electronic charge = 1.602×10^{-19} C and the parameters of pairs of interactions of atoms in ZrO_2 are presented in Table 6.1.

For Zr-O bond, the relationship between stress and strain is shown in Fig. 6.32 and was obtained by calculating the element's cross-sectional area to be $2.545 \times 10^{-20}m^2$. The Zr-O bond displays nonlinear or rate-dependent stress-strain and the problem is reduced by using *MISO* model for the element. The slope along the linear section of the curve represents the Young's modulus of the Zr-O bond, which is the same as the element of the nanotube.

Table 6.1 Computed constants for interactions of pairs of atoms in ZrO_2 [7]

Pair *ij*	*A ij* (eV)	ρ*ij* (Å)	*C* (eVÅ^6)
Zr-O	985.87	0.3760	0.0
O-O	22764.3	0.1490	27.89
Zr-O	0.0	0.0	0.0

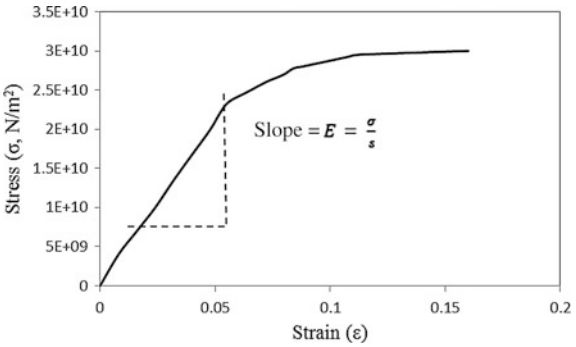

Fig. 6.33 Stress and strain curve for Zr-O bond/element as MISO model

From the curve in Fig. 6.33, Young's modulus of the Zr-O element was computed to be 5.01×10^{11} Pa (501 GPa), representing the slope in the linear region, and the value is similar to 491 GPa that was obtained for bulk ZrO2 by first principle calculations using CASTEP [8].

Thereafter, the subsequent procedures are same for simulating inorganic nanotubes as conducted for carbon nanotubes (Sects. 6.2.1–6.2.9).

References

1. Release, A.N.S.Y.S "14.0", (Ansys Inc, Canonsburg, PA, USA, 2013)
2. Release, A. N. S. Y. S. "12.0", *ANSYS Theory Reference*, 2009
3. E.J. Hearn, *Mechanics of Materials 2: The Mechanics of Elastic and Plastic Deformation of Solids and Structural Materials*, (Vol. 2) (Butterworth-Heinemann, 1997)
4. A.L. Kalamkarov, A.V. Georgiades, S.K. Rokkam, V.P. Veedu, M.N. Ghasemi-Nejhad, Analytical and numerical techniques to predict carbon nanotubes properties. Int. J. Solids Struct. **43**(22), 6832–6854 (2006)
5. A. Desai, M. Haque, Mechanics of the interface for carbon nanotube–polymer composites. Thin-Wall. Struct. **43**, 1787–1803 (2005)
6. A.N.S.Y.S. Release, *10.0 Documentation* (ANSYS Inc, Canonsburg, 2005)
7. X.L. Xia, Computational modeling study of yttria-stabilized zirconia, Doctoral dissertation, University College London, 2010
8. I.D. Muhammad, M. Awang, O. Mamat, Z.B. Shaari, First-principles calculations of the structural, mechanical and thermodynamics properties of cubic zirconia. World J. Nano Sci. Eng. **4**(2), 97–103 (2014)

Chapter 7
Effect of Geometrical Parameters on Tensile Properties of Nanotubes

7.1 Introduction

There is a large variation of mechanical properties, such as Young's moduli for nanotubes as indicated from both experimental and theoretical studies. From an early study [1], the experimental values of Young's modulus of the carbon nanotubes was 1.3 −0.4/+0.6 TPa. While, in another study [2] measured value for Young's modulus of nanotubes as 0.816 ± 0.41 TPa. The wide variation in the experimental results may be due to the several factors including (i) presence of defects in nanotube specimens and (ii) inherent limitations of current experimental techniques.

Contradicting theoretical results have also been observed [3–6] due to various definitions and constants involved, for example, the wide range of effective thickness of nanotube and different potential functions with different algorithms. During a simulation the thickness of 0.066 nm for C-C bond was used resulting in the graphite Young's modulus of 5.5 TPa [7] as opposed to 0.34 nm used in several studies [3–5].

To calculate the stress, one CNT's end was restrained and axial displacement was applied on the other end. The axial strain, ε_z, is defined as tube length at each substep, l, divided by initial length of the tube, l_o. The corresponding external force, F, is calculated from the summation of nodal reactions at fixed end. Then, the properties can be calculated as follows:

$$\varepsilon_z = \frac{u}{l_0} = \frac{l - l_0}{l_0} \tag{7.1}$$

$$\sigma = \frac{F}{A} \tag{7.2}$$

$$E = \frac{d\sigma}{ds} \tag{7.3}$$

M. Awang et al., *Finite Element Modeling of Nanotube Structures*,
Engineering Materials, DOI 10.1007/978-3-319-03197-2_7

$$\upsilon = \frac{(r - r_0)/r_0}{u/l_0} \tag{7.4}$$

where E, σ, F, A, v, r, r_o are the Young's modulus, axial stress, reaction force, cross sectional area, Poisson's ratio, current and initial radius of the tube.

The stress–strain relationship of nanotubes is predicted using the above procedures up to the inflection point (i.e. the maximum of the interatomic force) only, though the procedure is able to give the post failure [8]. However, the predicted post failure of the generated model may not be reliable because the model together with the simple interatomic potential function is not capable of describing the behaviors of the nanotube after the bonds are broken, such as formation of new bonds, rehybridization and structural transformations. From the experimental [9] and theoretical [10] studies on the tensile behaviors of nanotubes, it was found that the stress exhibits a sudden drop to zero when stress reaches the ultimate tensile strength and the fracture is brittle. Therefore, there is the need to study the effect of geometrical parameters with respect to mechanical behaviors of nanotubes.

7.2 Effect of Nanotube Length on its Mechanical Behavior

There have been several theoretical investigations leading to conclusion that that Young's moduli are size-dependent at small tube diameters with studies based on lattice-dynamical [11], atomistic-based continuum mechanics [12], structural mechanics [13], and analytical molecular mechanics [14]. Due to the limitations of current experimental techniques, it is hard to validate/extract such dependence experimentally.

It was assumed that length to radius ratio smaller than 10 may affect the simulation results. As mentioned earlier, one end of CNT is fixed in all degree of freedom while the other end is axially stretched. Hence, a series of simulations were performed to determine the possible effects of boundary conditions on different length to diameter ratio (L/D). Figure 7.1 shows the Young's modulus variation with length of nanotubes for zigzag (10,0) and armchair (5,5) which have almost same diameters.. The tube lengths and estimated Young's modulus are listed in Table 7.1 together with the number of atoms and elements for each model are also mentioned for comparison purposes.

In agreement with previous observations, results shows that armchair configuration is stiffer than zigzag. However, their stiffness decreases sharply when L/D ratio increase. This effect is a result of applied boundary conditions. As one end is completely fixed, the transverse displacement is also restricted which affect the stiffness of the nanotube structure.

It should be noted that all above-mentioned Young's moduli are the initial tangent modulus of carbon nanotubes. Secant moduli at different strains will be

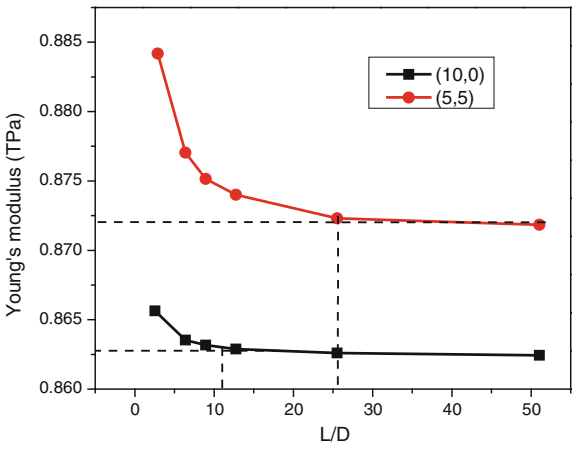

Fig. 7.1 Young's modulus variation with CNT length for zigzag (10,0) and armchair (5,5) SWCNTs

Table 7.1 Axial Young's modulus of SWCNTs with different L/D ratio

Chilarity	*L/D*	Length (Å)	*E* (TPa)	No. of atoms/nodes	No. of bonds/elements
(10,0)	2.55	17.76	0.86	190	270
(10,0)	6.38	47.60	0.86	470	690
(10,0)	8.93	66.78	0.86	660	970
(10,0)	12.76	98.75	0.86	950	1410
(10,0)	25.52	196.80	0.86	1880	2800
(10,0)	51.05	397.16	0.86	3760	5620
(5,5)	2.901	19.69	0.88	170	245
(5,5)	6.38	43.07	0.87	360	530
(5,5)	8.93	60.30	0.87	500	740
(5,5)	12.76	86.14	0.87	710	1055
(5,5)	25.52	173.51	0.87	1420	2120
(5,5)	51.05	345.80	0.87	2820	4220

presented later to illustrate the degree of nonlinearity in the stress–strain curve predicted prior to failure.

Figure 7.2 shows the calculated initial Young's modulus of nanotubes from the Modified Mores potential functions. The predicted Young's modulus of graphene sheet is 1.13 TPa (corresponding to an in-plane stiffness of 383 J/m^2), which agrees well with the experimental value and other theoretical values mentioned above. Differences between the experimental and theoretical graphite results may be due to the potential function and associated parameters.

It is seen from Fig. 7.2 that the feature of the size-dependent Young's moduli is captured by the present simple model and Young's moduli for both armchair and zigzag nanotubes decrease with decreasing tube diameter and approach the predicted graphite value when the tube diameter is increased.

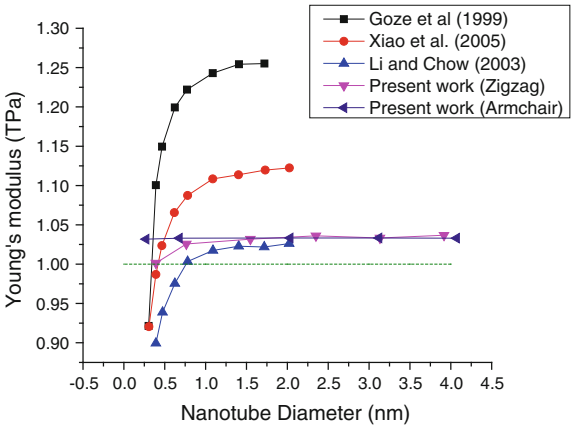

Fig. 7.2 Size-dependent Young's moduli for both armchair and zigzag nanotubes

For a given tube diameter, Young's modulus of armchair tubes is slightly larger than that of zigzag tubes. The maximum difference of armchair nanotube's moduli is less than 5 % and could be considered size-independent. At small diameter (<2 nm), zigzag nanotubes exhibit a higher sensitivity of moduli to tube diameter as shown in Fig. 7.2 with a difference up to 19 % and also compared with results from other simulations. The present model gives almost same trend as those of the tight-binding formulation [11] and continuum structural mechanics [14] although there exists difference at the area of stability level. It is interesting that when different values are normalized by their corresponding asymptotic value (i.e. predicted graphite value for large tube diameters), one obtains almost identical curves as shown in Fig. 7.2. In summary, the present values for single-walled nanotubes are in reasonable agreement with other theoretical and experimental values.

The dependence of Poisson's ratio to the tube diameter is shown in Fig. 7.3. The present predicted Poisson's ratio for both armchair and zigzag tubes decrease with

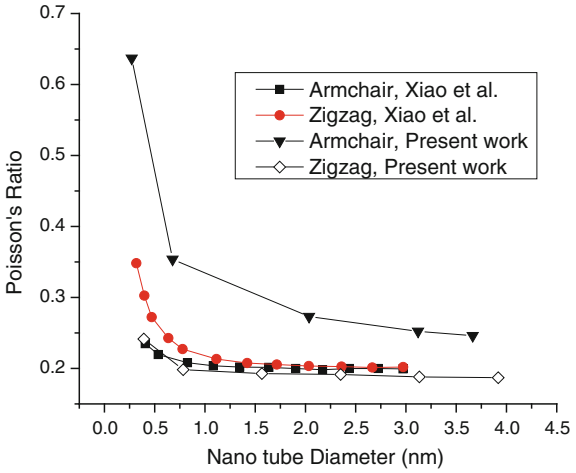

Fig. 7.3 Dependence of nanotube diameter on *Poisson's* ratio of CNT

increasing tube diameter, approaching the limit value of 0.20 for graphene sheet. It is seen that Poisson's ratio for zigzag tubes is more sensitive to the tube diameter than the armchair tubes.

The results given in earlier [15] show the same trend as the present results for armchair tubes, but a different trend for zigzag tubes. It should be noted that the present prediction for large diameter nanotubes (>2 nm) and graphite is almost constant and in excellent agreement with the theoretical value (0.21) obtained based on a lattice-dynamics model [15]. Although many investigations for *Poisson's* ratio of nanotubes have been conducted, there is no unique opinion that is widely accepted. Another study [14] showed that *Poisson's* ratio for single-walled nanotubes is almost constant (0.28). The tight-binding calculations [11] gave values of 0.247, 0.256 for (6,6), (10,10) armchair tubes, respectively and values of 0.275, 0.270 for (10,0), (20,0) zigzag tubes, respectively.

7.3 Effect of Wall Curvature on Strength of CNTs

Although there is discrepancy on Young's modulus of nanotubes it has been commonly recognized that nanotubes with large diameters have the same modulus as that of graphite and small diameter nanotubes exhibit some size-dependence. Experimental value for graphite [16] is about 1.06 TPa (corresponding to an in-plane stiffness of 360 J/m^2).

Available theoretical graphite values include 1.16 TPa (also size-independent nanotube value [10]) using molecular mechanics/dynamics with the modified Morse potential and 1.50 TPa [17] using MD with the Keating potential. Based on a lattice dynamics model with empirical force-constants, Young's modulus for graphite (also nanotubes) was calculated to be about 0.972 TPa [18] and around 1.0 TPa for graphite [15]. The Young's modulus of carbon nanotube with larger diameters was also simulated as 1.025 TPa using structural mechanics [13]. In relation to graphite value of 1.06 TPa (360 J/m^2) for the Young's modulus using the same analytical structural model [14] as the present investigation, but with force-constants (harmonic potential). The tight-binding methods also showed significant scatter in Young's modulus values with variations from 0.676 TPa [19] to 1.27 TPa [11]. There are also many other predictions available from other simulations conducted.

An armchair (10,10) with length of 100 nm was chosen to study the SWCNT under tension. A relatively long CNT is selected to minimize effect of boundary conditions. Figure 5.17 shows snapshots of the finite element model of a CNT. All atoms at lower end of CNTs are held fixed in 6 degree of freedom while the other end displaced outward to simulate axial tension. To keep the tubular shape of CNT ends, radial constrains were applied to both ends. Displacement was applied and solution completed in almost 500 substeps followed by equilibrium for each of them. The applied boundary conditions are depicted in Fig. 7.4.

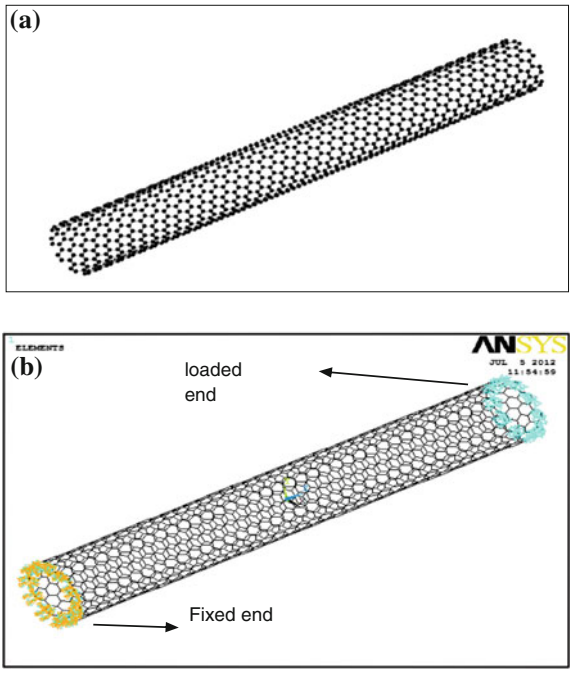

Fig. 7.4 **a** Schematic of CNTs studied in this work armchair (10,10), **b** finite element model of (10,10) CNT

In Fig. 7.5a the reaction forces at extreme nodes is displayed for the last substep. Figure 7.5b shows the recorded reaction force for a selected node at the fixed end during deformation. Equations (7.1)–(7.4) were used to compute stress and strain values at each substep of the solution. Figure 7.5a shows the stress-strain plot for tensile loading of (10,10). The CNT behavior under tension was assumed to be nonlinear for strains higher than 10 %. Therefore, for better accuracy both the tangent modulus at zero strain and the secant modulus were studied. The secant modulus at higher strains is depicted in Fig. 7.5b.

In the modified Morse potential formulation, nonlinear exponential functions were employed to estimate mechanical behaviors of C-C bonds when the bond stretching is dominant. Obviously, the stiffness of the C-C bonds becomes weaker when the interatomic distance increase. Thus, CNTs became weaker when deformation increases. This is the direct effect of modified Morse potential functions in bond stretching simulations. It also suggests that harmonic equations which merely assume linear functions are not precise tools for studying large strains such as tensile fracture of CNTs. Present calculations showed large differences between the tangent modulus at near zero strain and the secant modulus in higher strains. According to the results, the elastic formulations seem only suitable for very small strains. Young's modulus as an indicator of mechanical response remains constant in values less than 0.018 and 0.010 for armchair and zigzag CNTs, respectively. At larger strains, CNTs regardless of the chirality tends to become weaker. Figure 7.6b

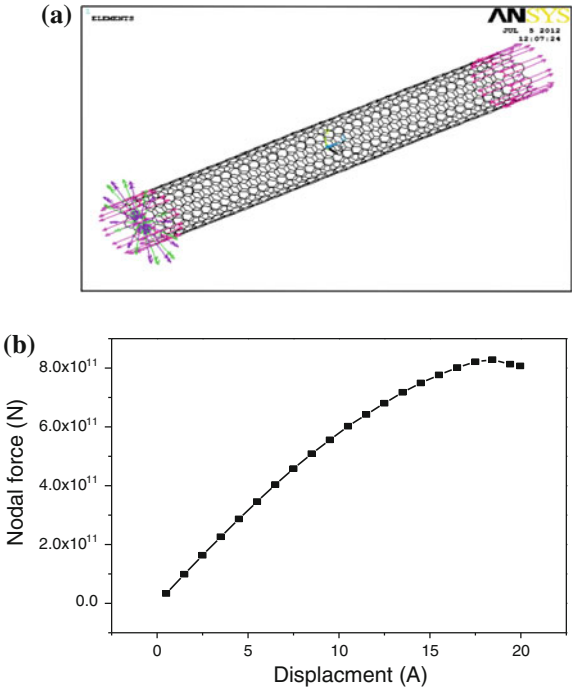

Fig. 7.5 **a** Reaction forces at extreme nodes for the last substep, **b** recorded reaction force for a selected node at the fixed end during deformation

depicts the secant modulus of a (10,10) armchair SWCNT under tensile load. Hence, it is recommended to use more versatile formulations such as Morse potential [20, 21] or Brenner many-body potential [10] in large deformation studies.

Figure 7.7 shows a comparison of secants modulus reported by different authors. It can be seen clearly that the results are in good agreement with previous models. Present atomic model can provide wide range of information about the CNTs subjected to loads. For example, radial displacement and bond stretching for a typical CNT under tensile load are illustrated in Fig. 7.8.

Unlike a planar graphene sheet, the carbon atom and its three closest neighbors carbon atoms on a CNT wall form a tetrahedron because of the curvature effect [8]. Since the CNT is built by rolled graphene sheet in specific direction, the armchair SWCNT was unrolled to a two-dimensional planar sheet of graphene as shown in Fig. 7.9. This can be simply done by cutting the CNT along on its axial direction and then unrolling to a plane without stretching as shown in Fig. 7.9b. Consequently, the bond distance between each pair of atoms in the unrolled plane is similar to its matching arc length on the CNT wall. Then, the same tensile load was applied to the graphene sheet and the tensile behavior was compared with the corresponding CNT configuration. The stress-strain curve of (10,10) graphene sheet along (10,10) SWCNT were depicted in Fig. 7.10. The effect of curvature

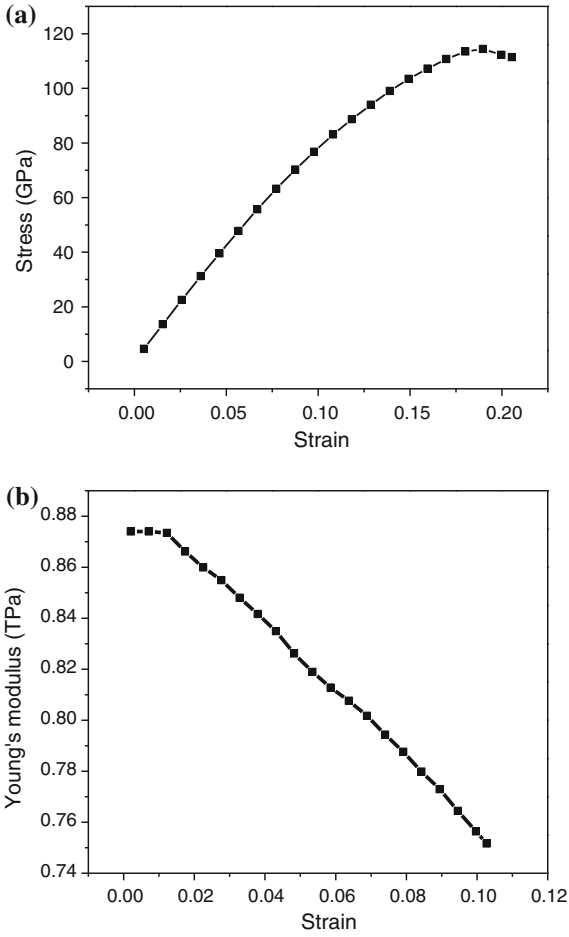

Fig. 7.6 SWCNT (10,10) under axial tention: **a** Stress–strain response, and **b** secant modulus

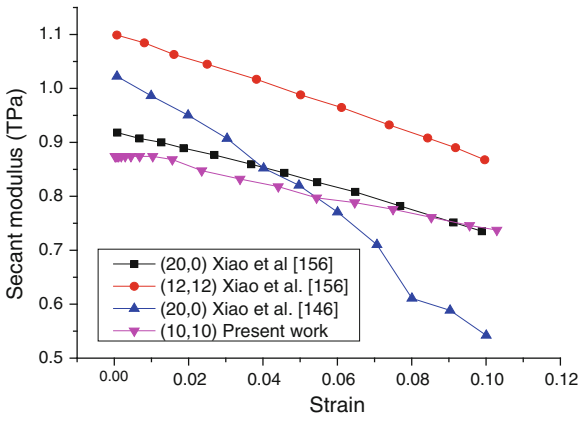

Fig. 7.7 Secant modulus of SWCNTs versus strain from different studies

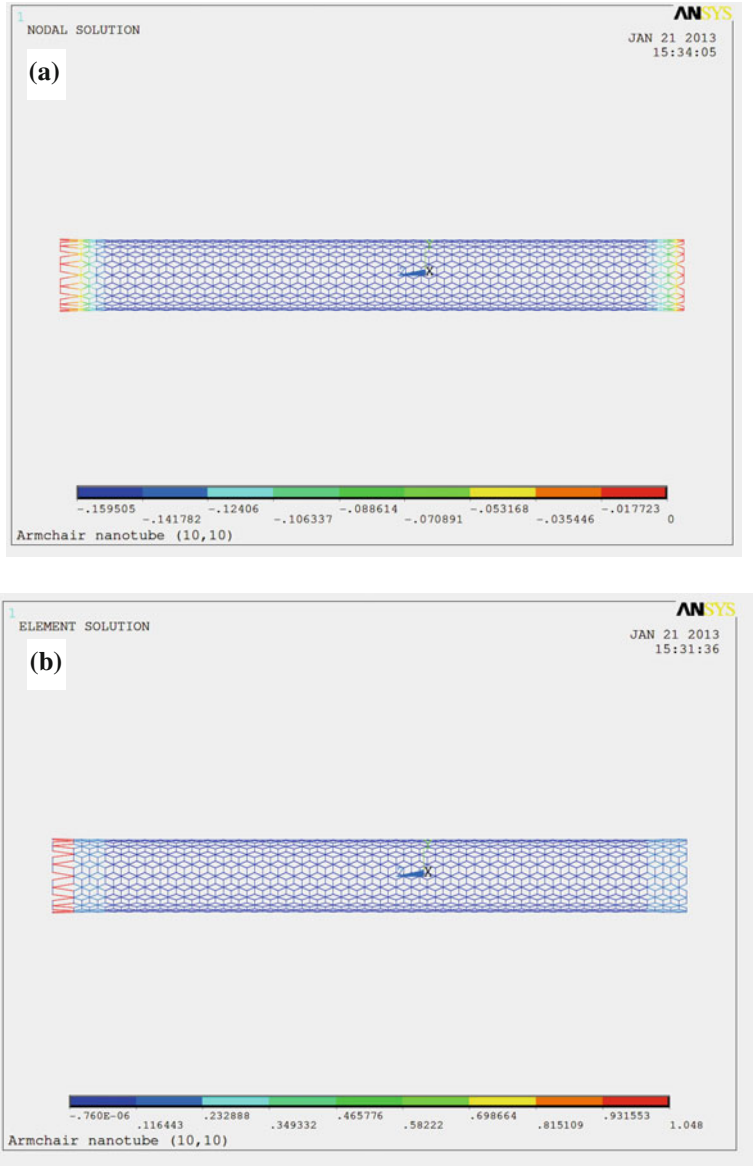

Fig. 7.8 Radial displacement and bonds strain at the final substep of axial loading

introduced by rolling carbon sheets could be seen clearly [22]. As it was expected, the graphene sheet showed higher tensile strength at equal strains comparing to matching CNT and its ultimate strength of 124.69 GPa obtained at about 20 % strain.

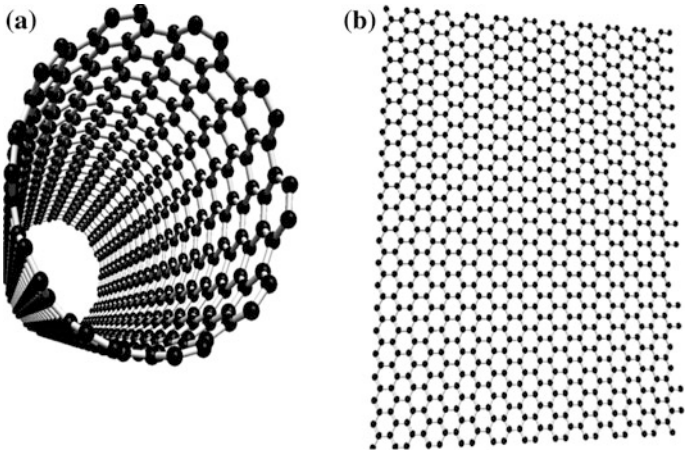

Fig. 7.9 Schematic of **a** a (10,10) CNT configuration, **b** a planar, "unrolled" (10,10) graphene sheet

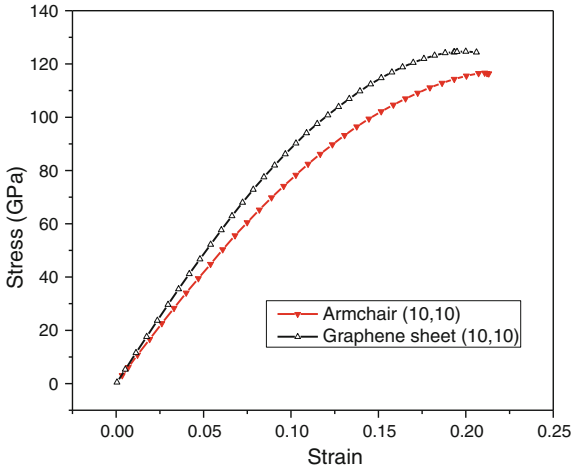

Fig. 7.10 The stress–strain diagrams for graphene sheet and SWCNT of armchair (10,10) under tensile load

Simulation result gave a value of about 1 TPa for the Young's modulus of graphene sheet. The graphene layer thickness is assumed equal to 3.4 Å. Values of 1.06 and 1.04 TPa were reported using the same analytical structural model [14]. From a molecular mechanics approach, a predicted the value of 1.16 TPa was also obtained [10]. Figure 7.11 shows the variation of secant modulus for (10,10) SWCNT and graphene sheet.

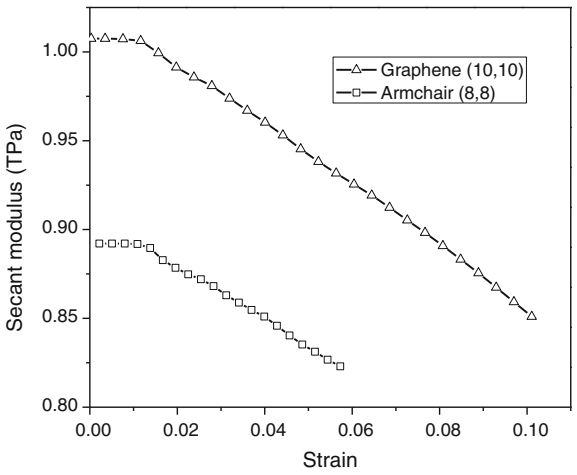

Fig. 7.11 Secant modulus of graphene (10,10) and (8,8) SWCNT under tensile load

7.4 Effect of Chirality on Strength of CNTs

In this section, the effects of chirality on the tensile behavior of SWCNTs were investigated. The influences of the CNT length and diameter were also studied in the following sections. Armchair and zigzag SWCNTs were tested under tension to see how significant does chirality affect their behavior. Armchairs (10,10) and zigzags (18,0) configuration were selected for illustration purposes. Figure 7.12 shows the stress–strain curves for the armchair and the zigzag CNTs. The average Young's modulus for the simulated CNTs in the range of 0–0.01 strain were 0.89 and 0.87 TPa for armchair and zigzag configuration, respectively. For the armchair (10,10) and zigzag (18,0) CNTs, a maximum stress equal to 116.64 and 94.96 GPa were found at around 21.48, 17.79 % of strain, respectively.

SWCNTs with different atomic configuration of (5,5), (8,8), (10,10), (14,14), (16,16), (8,0), (14,0), (18,0) and (22,0) were analyzed and results are presented in Table 7.2. In addition, plane sheets of graphene with atomic structure of (10,0) and (10,10) were also evaluated to show the effect of curvature of the CNT wall on the tensile behavior.

Results showed that the elastic properties of carbon nanotubes at small deformations were almost unaffected by CNT chirality during tension. The Poisson's ratio for (14,14) and (22,0) configuration was calculated as 0.20. They are comparable with reported values of 0.19 [23] based on the Brenner potential force field function. Average Young's modulus was also predicted as 0.91 TPa by using Morse potential force fields [24]. They utilized spring elements to simulate both C-C bonds and angle bending force fields.

Generally, two contrary trends have been reported for size dependent Young's modulus of CNTs based on numerical studies. Although some researchers found that the elastic properties of CNTs tend to decline when their diameter is increasing, few studies predicted an opposite trend [25]. The present results suggested that the

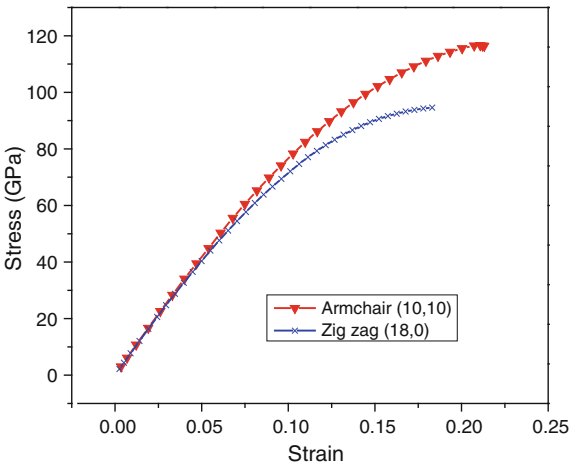

Fig. 7.12 Stress–strain diagrams for armchair (10,10) and zigzag (18,0) SWCNTs under tensile load

Table 7.2 Axial Young's modulus of SWCNTs and graphene sheets

Helicity	Diameter (Å)	Young's modulus (TPa)	Strain (%)	Ultimate strength (GPa)
(5,5)	6.78	0.86	21.12	115.86
(8,8)	10.84	0.89	21.48	116.53
(10,10)	13.56	0.89	21.31	116.64
(14,14)	18.98	0.90	21.12	116.58
(16,16)	21.69	0.97	21.12	131.14
Graphene sheet (10,10)	∞	1.00	19.99	124.69
(8,0)	6.26	0.84	17.91	94.17
(14,0)	10.96	0.87	17.64	94.02
(18,0)	14.09	0.87	17.79	94.96
(22,0)	17.22	0.88	17.85	94.41
Graphene sheet (10,0)	∞	1.00	17.73	111.28

Young's modulus of CNTs slightly increased when tube diameter raised [26] as shown in Table 7.2. In general, results showed that the zigzag configurations lead to a lower tensile strength as compared to the armchair configuration with almost similar diameter. These results were in agreement with what was obtained in other simulations [24, 27, 28].

Secant modulus is a useful tool for stiffness analysis at larger strains. It can be seen that graphene is stiffer than SWCNTs as shown in Fig. 7.13. Armchair configuration results in more tensile stiffness in comparison to zigzag structures.

A comparison between the present simulations results and previous studies is shown in Fig. 7.14. It can be seen that the curve shape is in good agreement with

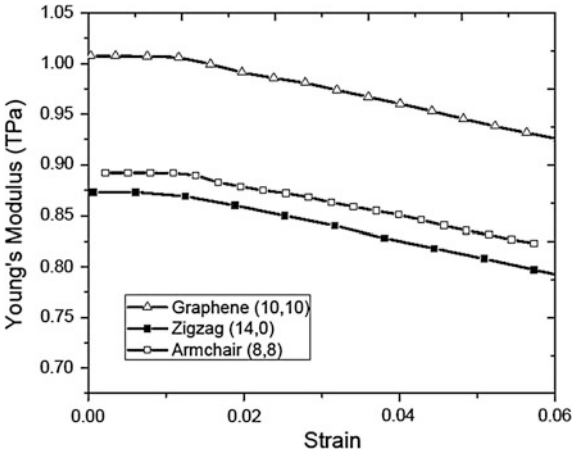

Fig. 7.13 Secant modulus variation for armchair and zigzag CNTs under tensile loading

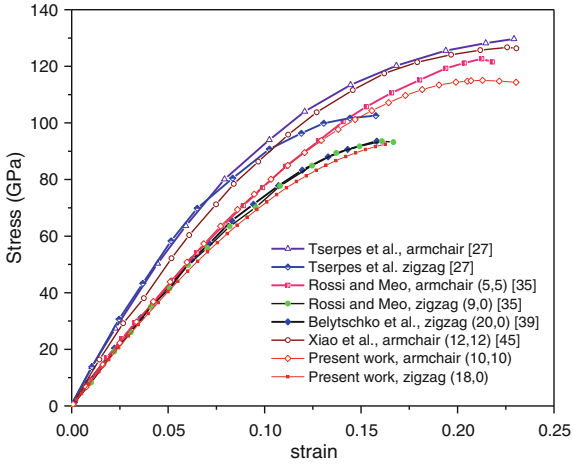

Fig. 7.14 Comparison between present simulation results and previous studies on the tensile behaviour of SWCNTs

current studies [10, 20, 21, 28]. The predicted nonlinear behaviors of CNTs were similar to calculated results from molecular dynamics [10]. The predicted ultimate failure strains of 17–21 %, were dramatically larger than the experimental values reported earlier [9]. This difference between predictions and experiential values could be partly explained by various defects that reduce stiffness and strength. Recently, the effects of imperfection of tube wall caused by defects have been investigated [28].

On the other hand, the results showed a very slight dependence between tensile properties and SWCNT radius. Moreover, it could be observed that with increasing diameter of CNT it becomes stronger and come closer to the calculated value for graphene sheets with infinite diameter. The calculated value for graphene sheets is around 1 TPa which is comparable with previous studies.

7.5 Effect of Geometric Parameters on the Mechanical Behaviors of Inorganic Nanotubes

The effects of geometrical parameters on mechanical properties of inorganic nanotubes are not exactly same as that of carbon nanotubes. For example, zirconia nanotube (ZNT) in relation to diameter and length depends on chirality, with chiral type having the highest followed by the zigzag and then armchair. The variations are similar to that of Boron Nitride nanotubes (BNNT) and CNT [29, 30], but the values are less than that of ZNT which have longer and thicker atomic bond. Details of the geometrical parameters of some ZNTs are stated in Table 7.3.

The symmetry of the SWZNT is not uniform compared to CNT. The orientation depends on the chirality, with armchair having more uniform diameter across the tube and zigzag having variations leading to depressions across the tube and in some cases less diameter at the ends. The ZNT is not a cylindrical tube as in CNT, but irregular as referred to polygonal tube which is similar to other inorganic nanotubes [31]. The difference in geometrical orientation of ZNT compared to CNT is illustrated in Fig. 1.9, both have the same number of bonds/elements and approximately same diameter.

It has been established that some mechanical properties of CNTs are influenced by size and chirality (Sects. 7.2–7.4). Similar trend occurs in relation to ZNT as indicated in Fig. 7.15 showing changes of Young's modulus of armchair and zigzag nanotubes with diameter. The curve indicates significant effect of diameter on the value of E, especially in relation to small diameters. The zigzag ZNTs have higher Young's modulus in comparison with armchair ZNT's with similar diameters, but the pattern of increase in is the same for all nanotubes. The increase in Young's modulus as the diameter increases is attributed to the effect of nanotube curvature [20, 32].

As the nanotube diameter increases, the effect of curvature reduces and Young's modulus, E converges to a value. For a variation of diameter from 1.05 to 6.18 nm for the armchair SWZNTs and between 1.09 and 6.13 nm for the zigzag SWZNTs, the values of Young's modulus E vary from 217 to 385 GPa and from 309 to 431 GPa, respectively. The findings indicate that the Young's modulus computed for both armchair and zigzag SWZNTs is constant for diameters ranging from 3.8 to 6.13 nm and is approximately 380 and 427 GPa for armchair and zigzag, respectively.

In contrast, the Young's modulus of the SWZNTs decreases as the aspect ratio (L/d) increases as shown in Fig. 7.16. This indicates that increasing the aspect ratio will negatively affect the structural stability of the nanotubes as in other inorganic nanotubes [32]. Thus in relation to optimum Young's modulus, minimal diameter is required.

With respect to length and aspect ratio, similar pattern was observed for (35,0) SWZNT as illustrated in Fig. 7.17. There was tremendous increase in the Young's modulus initially until the optimum value of 297 GPa was attained at 10 nm length and aspect ratio of 2 and thereafter convergence occurred.

Table 7.3 Geometrical parameters for modeled ZNT

Chirality (nxm)	Diameter (Å)	Length (Å)	Atoms/nodes	Bonds/elements	Bond length (Å)		
					Minimum	Maximum	Mean
5 × 5	10.461	100.84	820	1220	1.95	2.263	2.118
9 × 0	10.872	102.84	768	1293	1.932	2.364	2.093
8 × 8	16.738	100.84	1312	1952	2.012	2.295	2.136
14 × 0	16.911	102.84	1344	1988	1.972	2.165	2.032
10 × 10	20.923	100.84	1640	2440	1.978	2.143	1.997
17 × 0	20.535	102.84	1728	2431	1.949	2.103	1.996
14 × 14	29.292	100.84	2296	3416	1.961	2.157	1.972
24 × 0	28.991	102.84	2304	3432	1.881	2.114	1.964
16 × 16	33.476	100.84	2624	3904	1.95	2.157	1.962
28 × 0	33.823	102.84	2784	4147	1.873	2.11	1.958
					1.873	2.263	2.0229

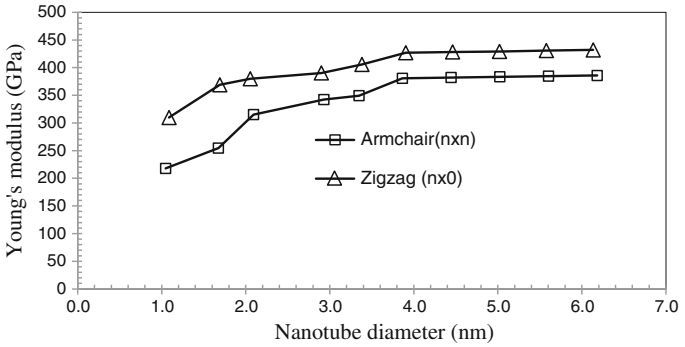

Fig. 7.15 Effect of diameter on the Young's modulus of SWZNT

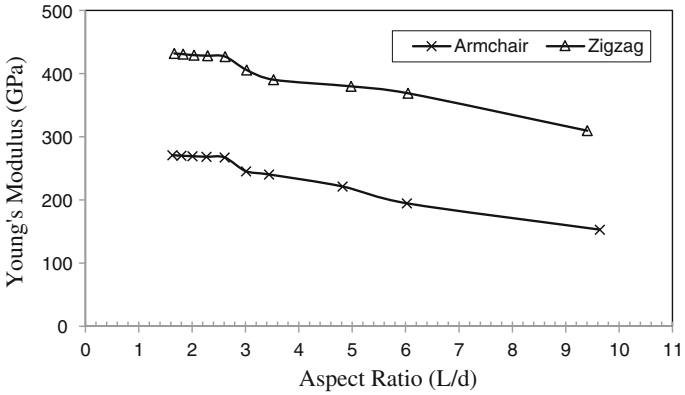

Fig. 7.16 Effect of aspect ratio (L/d) on the Young's modulus of SWZNT

As illustrated in Fig. 1.9, the ZNT is not a cylindrical tube but polygonal tube. Thus the thickness of the tube is not assumed to be equivalent to the thickness of the bond/element as in CNT, but is defined as difference of radial spaces between the farthest and inmost (oxygen) atoms in the optimized structures [29]. The wall thickness of SWZNT modelled from cubic nanosheet varies between 0.194 and 0. 680 nm depending on symmetry and chirality [29]. As was obtained in CNT [21], the wall thickness has substantial influence on the computed Young's modulus as shown in Fig. 7.18.

From the simulation results, it was noted that the greater the wall thickness of SWZNTs, the lesser the value of Young's modulus, E computed. For a variation of t from 0.05 to 0.2 nm, the value of Young's modulus, E varied from 565 to 67 GPa for the (35,0) nanotube and from 431 to 53 GPa for the (20,20) nanotube. Thus the result confirms what was obtained during nanoindentation of ZNT where thicker arrays were found out to be softer than their thinner equivalents [33].

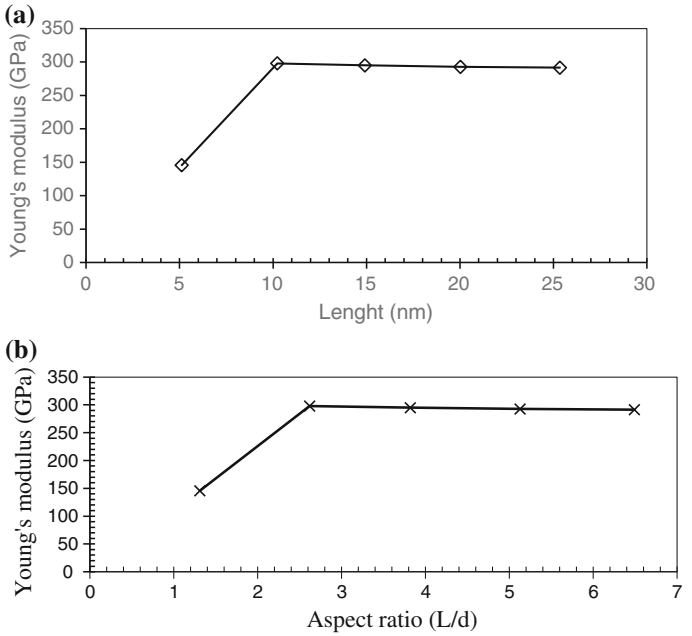

Fig. 7.17 Variation of Young's modulus of (35,0) SWZNT with length (**a**) and aspect ratio (**b**)

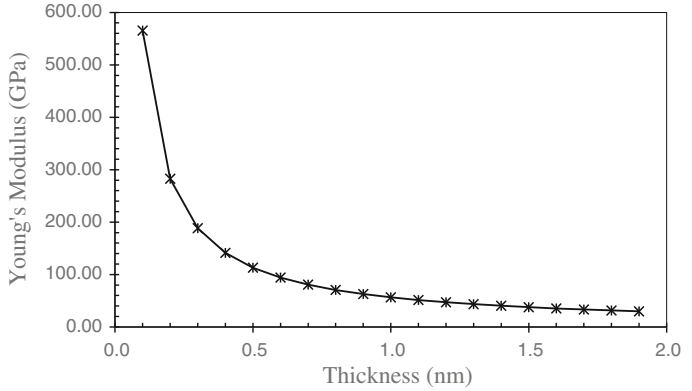

Fig. 7.18 Effect of thickness on the Young's modulus of (35,0) SWZNT

It has been established that for any tube wall thickness, t and chirality, there occurs a diameter. d below which the NT develops instability and experiences impulsive damage or destruction [29]. In order to maintain uniformity in the parametric studies of ZNT, the value of 0.194 was adopted for t which is equivalent to the thickness of cubic zirconia nanosheet cleaved along (111) plane [34].

7.6 Convergence and Mesh Independence Study

In the finite element analysis (FEA), a finer mesh often results in a more accurate solution. While engineers cannot typically obtain the exact solution for a model, an approximation can be obtained with very high accuracy using finite-element methods. However, as a mesh is made finer and accuracy increased, computational intensity also increases, often leading to longer solution times. This conundrum begs the question: Just how fine of a mesh is fine enough to accurately represent the real-world event? The question cannot be answered categorically. To find the solution that best balances computational capacity and accuracy; we should perform a mesh convergence study.

A mesh convergence study is an empirical process that compares the results of one meshed model with those of another. As such, one of the easiest and best ways to start is with the fewest, yet reasonable number of elements. That is, begin by meshing the model as coarsely as seems reasonable and analyze it. Then, recreate the mesh with a denser element distribution, re-analyze it and compare the results to those of the more coarsely-meshed model. Are the results similar? If not, then the coarse mesh is not very accurate. Increase the mesh density and re-analyze the model.

Keep increasing the mesh density and re-analyzing the model until the results converge satisfactorily. That is, when we reach a point at which finer meshing no longer yields appreciably different results, the mesh may be considered fine enough. This type of mesh convergence study can help us to obtain an accurate solution with a mesh that is sufficiently dense and yet not overly demanding of computer resources.

A zigzag nanotube with 100 length will be studied. We need to change the mesh from coarse to fine and study its influence on the a constant property such as Young's modulus of the tube.

We start with very coarse element size. In order to change the meshing parameters, go to meshing section (Fig. 7.19):

Main Menu > Preprocessor > Meshing > Size Cntrls > ManualSize > Lines > All Lines

The lines can be meshed from the mesh submenu: **Main Menu > Preprocessor > Meshing > Mesh > Lines** and Pick all lines. Better observation can be made on the nodes and elements if we change the elements size and shape. To do so, chose from main menu **PlotCtrl > Style > Size and Shape** and apply the changes (Fig. 7.20). After replotting, nodes and element divisions illustrated in a better view (Fig. 7.21).

Each pair of nodes is connected via a beam element. This pattern repeated throughout the structure of the nanotube. Then the Young's modulus of the nanotube is computed using the established procedure (Sects. 6.2.2–6.2.9). After which the element divisions for all lines are increased from 1 to 3, 5, 10 with the view of division 5 shown in Fig. 7.22 and the effect of the changes on Young's modulus illustrated in Fig. 7.23.

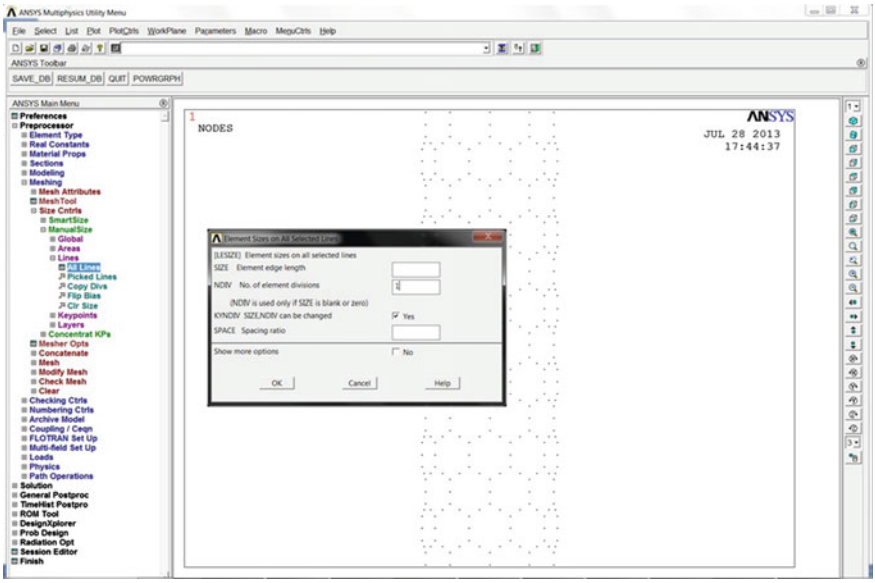

Fig. 7.19 Changing the meshing parameters

Fig. 7.20 Changing the shape and/or size of the meshing

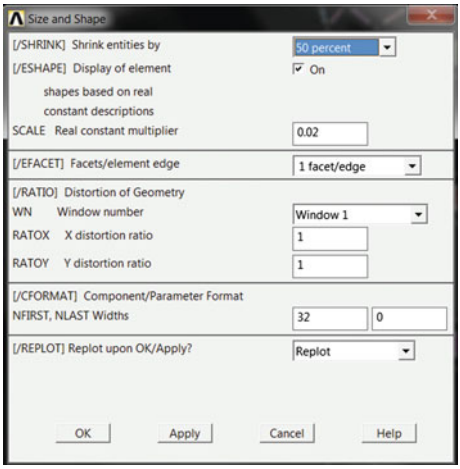

Result similar illustrated in Fig. 7.23 for CNT was obtained after convergence test on (35,0) ZNT (Fig. 7.24). The plots (Figs. 7.23 and 7.24) indicate the results are converging to a particular value or approaching a value. From Fig. 7.24, convergence starts at 5 divisions of the element having Young's modulus as 141.64 GPa compared to 297.96 GPa when division of the elements was 1 which is about 110 % reduction. Dividing the elements further up to 10 units gave a

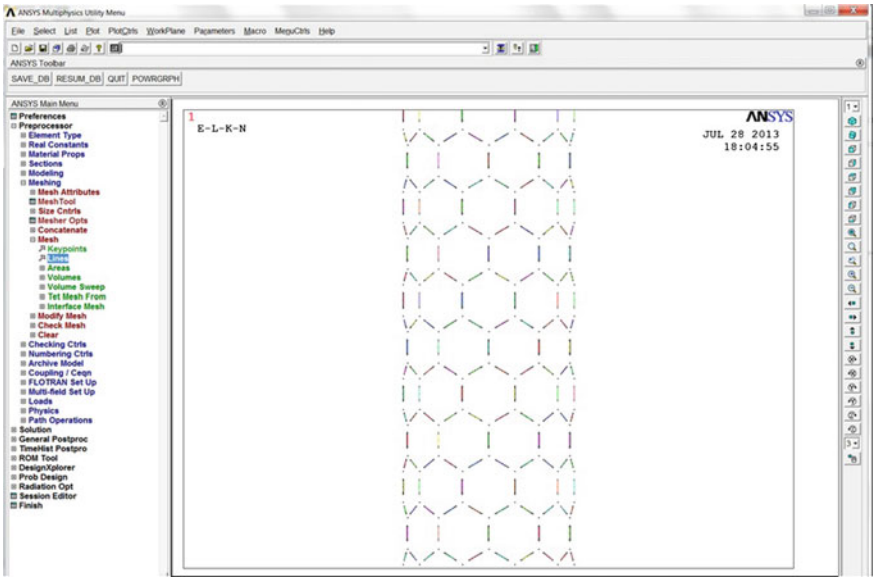

Fig. 7.21 Element division of 1for the CNT

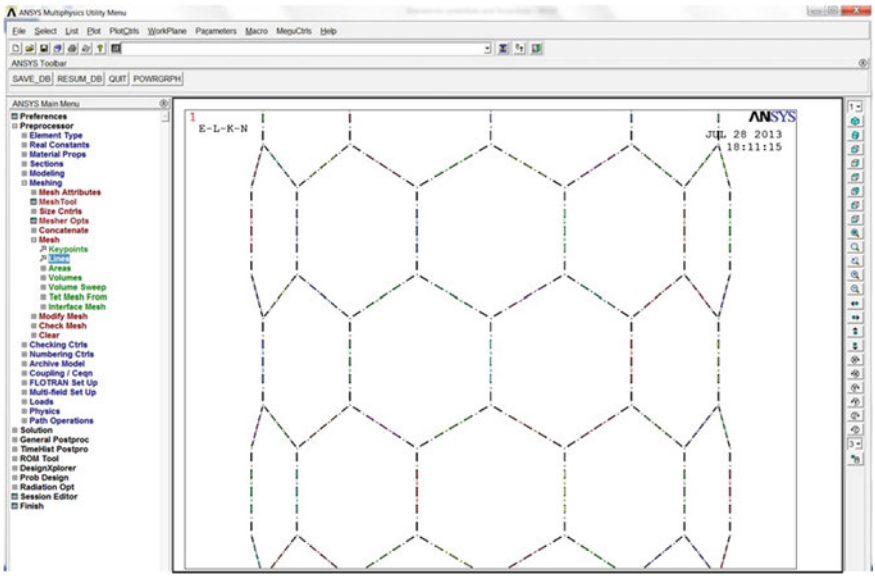

Fig. 7.22 Element division of 5 for the CNT

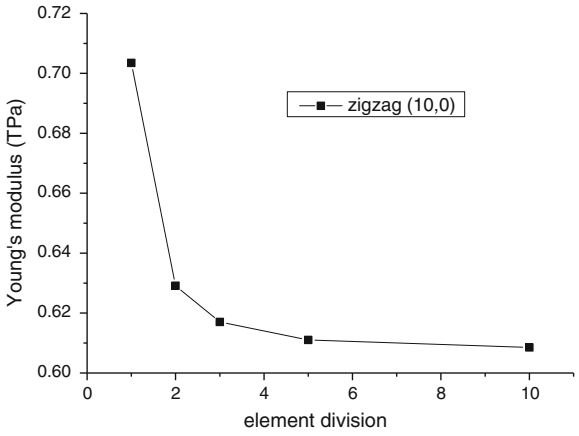

Fig. 7.23 Effect of variation of element division on the Young's modulus of CNT

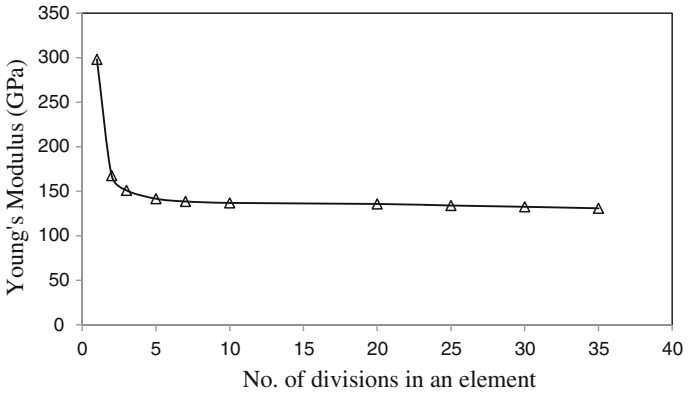

Fig. 7.24 Curve obtained from convergence test for 35 × 0 SWZNT

difference of 3 % from what was obtained for 5 divisions of the elements. Thus the value at 5 or 10 element division is selected as the approximate Young's modulus of the nanotube.

References

1. A. Krishnan, E. Dujardin, T.W. Ebbesen, P.N. Yianilos, M.M.J. Treacy, Young's modulus of single-walled nanotubes. Phys. Rev. B **58**(20), 14013 (1998)
2. J.P. Salvetat, G.A.D. Briggs, J.M. Bonard, R.R. Bacsa, A.J. Kulik, T. Stöckli, L. Forró, Elastic and shear moduli of single-walled carbon nanotube ropes. Phys. Rev. Lett. **82**(5), 944 (1999)

3. E. Mohammadpour, in *Numerical And Experimental Evaluation Of Carbon Nanotube/Polypropylene Composites Using Nonlinear Finite Element Modeling*, Ph. D. thesis, Universiti Teknologi Petronas, 2013
4. A.L. Kalamkarov, A.V. Georgiades, S.K. Rokkam, V.P. Veedu, M.N. Ghasemi-Nejhad, Analytical and numerical techniques to predict carbon nanotubes properties. Int. J. Solids Struct. **43**(22), 6832–6854 (2006)
5. J.H. Lee, B.S. Lee, Modal analysis of carbon nanotubes and nanocones using FEM. Comput. Mater. Sci. **51**(1), 30–42 (2012)
6. E.J. Hearn, in *Mechanics of Materials 2: the mechanics of elastic and plastic deformation of solids and structural materials,* vol. 2 (Butterworth-Heinemann, Oxford, 1997)
7. B.I. Yakobson, C.J. Brabec, J. Bernholc, Structural mechanics of carbon nanotubes: from continuum elasticity to atomistic fracture. J. Comput. Aided Mater. Des. **3**, 173–182 (1996)
8. H. Jiang, P. Zhang, B. Liu, Y. Huang, P.H. Geubelle, H. Gao, The effect of nanotube radius on the constitutive model for carbon nanotubes. Comput. Mater. Sci. **28**, 429–442 (2003)
9. M.-F. Yu, B.S. Files, S. Arepalli, R.S. Ruoff, Tensile loading of ropes of single wall carbon nanotubes and their mechanical properties. Phys. Rev. Lett. **84**, 5552–5555 (2000)
10. T. Belytschko, S.P. Xiao, G.C. Schatz, R.S. Ruoff, Atomistic simulations of nanotube fracture. Phys. Rev. B **65**, 235–430 (2002)
11. L. Vaccarini, C. Goze, L. Henrard, E. Hernández, P. Bernier, A. Rubio, Mechanical and electronic properties of carbon and boron-nitride nanotubes. Carbon **38**, 1681–1690 (2000)
12. L. Jiang, W. Guo, A molecular mechanics study on size-dependent elastic properties of single-walled boron nitride nanotubes. J. Mech. Phys. Solids **59**(6), 1204–1213 (2011)
13. C. Li, T.-W. Chou, Elastic moduli of multi-walled carbon nanotubes and the effect of van der Waals forces. Compos. Sci. Technol. **63**, 1517–1524 (2003)
14. T. Chang, H. Gao, Size-dependent elastic properties of a single-walled carbon nanotube via a molecular mechanics model. J. Mech. Phys. Solids **51**, 1059–1074 (2003)
15. V.N. Popov, V.E. Van Doren, M. Balkanski, Elastic properties of single-walled carbon nanotubes. Phys. Rev. B **61**(4), 3078 (2000)
16. O.L. Blakslee, D.G. Proctor, E.L. Seldin, G.B. Spence, T. Weng, Elastic constants of compression-annealed pyrolytic graphite. J. Appl. Phys. **41**(8), 3373–3382 (1970)
17. G. Overney, W. Zhong, D. Tomanek, Structural rigidity and low frequency vibrational modes of long carbon tubules. Zeitschrift für Physik D Atoms (Mol. Clust.) **27**(1), 93–96 (1993)
18. C.-W. Fan, J.-H. Huang, C. Hwu, Y.-Y. Liu, Mechanical Properties of single-walled carbon nanotubes—a finite element approach. Adv. Mater. Res. **33–37**, 937–942 (2008)
19. C.Y.J Cai, T. Yu, S. Yu, Wall thickness of single-walled carbon nanotubes and its Young's modulus, Phys. Scr. **79** (2009)
20. K. Tserpes, P. Papanikos, G. Labeas, S. Pantelakis, Multi-scale modeling of tensile behavior of carbon nanotube-reinforced composites. Theoret. Appl. Fract. Mech. **49**, 51–60 (2008)
21. K. Tserpes, P. Papanikos, Finite element modeling of single-walled carbon nanotubes. Compos. B Eng. **36**, 468–477 (2005)
22. E. Mohammadpour, M. Awang, Nonlinear finite-element modeling of graphene and single-and multi-walled carbon nanotubes under axial tension. Appl. Phys. A **106**(3), 581–588 (2012)
23. B.I. Yakobson, C.J. Brabec, J. Bernholc, Nanomechanics of carbon tubes: instabilities beyond linear response. Phys. Rev. Lett. **76**, 2511–2514 (1996)
24. M. Rossi, M. Meo, On the estimation of mechanical properties of single-walled carbon nanotubes by using a molecular-mechanics based FE approach. Compos. Sci. Technol. **69**, 1394–1398 (2009)
25. S. Xiao, W. Hou, Studies of size effects on carbon nanotubes' mechanical properties by using different potential functions. Fuller. Nanotub. Carbon Nanostruct. **14**, 9–16 (2006)
26. A.K. Rappe, C.J. Casewit, K.S. Colwell, W.A. Goddard, W.M. Skiff, UFF, a full periodic table force field for molecular mechanics and molecular dynamics simulations. J. Am. Chem. Soc. **114**, 10024–10035 (1992)

27. J. Xiao, B. Gama, J. Gillespiejr, An analytical molecular structural mechanics model for the mechanical properties of carbon nanotubes. Int. J. Solids Struct. **42**, 3075–3092 (2005)
28. J.R. Xiao, J. Staniszewski, J.W. Gillespie Jr, Fracture and progressive failure of defective graphene sheets and carbon nanotubes. Compos. Struct. **88**, 602–609 (2009)
29. A.V. Bandura, R.A. Evarestov, Ab initio structure modeling of ZrO_2 nanosheets and single-wall nanotubes. Comput. Mater. Sci. **65**, 395–405 (2012)
30. D. Dass, R. Prasher, R. Vaid, Analytical study of unit cell and molecular structures of single walled carbon nanotubes. Int. J. Comput. Eng. Res. **2**, 1447–1457 (2012)
31. K. Tibbetts, R. Doe, G. Ceder, Polygonal model for layered inorganic nanotubes. Phys. Rev. B **80**(1), 014102 (2009)
32. R. Ansari, S. Rouhi, M. Mirnezhad, F. Sadeghiyeh, Studying the buckling and vibration characteristics of single-walled zinc oxide nanotubes using a nanoscale finite element model. Appl. Phys. A **112**(3), 767–774 (2013)
33. L.N. Wang, L. Jing-Li, Fabrication and mechanical properties of anodized zirconium dioxide nanotubular arrays. J. Phys. D Appl. Phys. **44**(7), 075301 (2011)
34. L. Boldrin, F. Scarpa, R. Chowdhury, S. Adhikari, Effective mechanical properties of hexagonal boron nitride nanosheets. Nanotechnology **22**(50), 505702 (2011)

Chapter 8
Finite Element Analysis of Multi-walled Nanotubes

8.1 Introduction

There are two types of nanotubes: single-walled nanotubes (SWCNTs) and multiwalled nanotubes (MWCNTs), which differ in the arrangement of their graphene cylinders. SWCNTs have only one single layer of graphene cylinders; while MWCNTs have many layers (approximately 2–50). Multi-walled tube with the separation between the sheets around $d + t$ [1] where d = is the diameter of the inner tube and t is the thickness of the nanotube. Figure 8.1 shows a SWCNT and MWCNT. The relative geometry of (10, 0) CNT having 25 Å length, 1.421 Å and different walls as shown in Table 8.1.

8.2 Modeling Multi-walled Carbon Nanotubes

In order to model MWCNTs one should take into account the van der Waals forces between CNTs layers. Van der Waals term include a variety of interactions such as permanent electric dipoles, permanent multipoles and short lived multipoles. The latter term caused some attraction forces among nuclei which is opposed by repulsion anytime the two nuclei approach each other. Maximum stabilization is occurred at the van der Waals radius. At any distances less than it, the van der Waals potential emerges a repulsive force and the atoms repel each other. However, at larger distances atoms attract each other. The main impact of van der Waals term is to stabilize the molecular structure. At interatomic distances smaller than the van der Waals radius when repulsion is noticeable, van der Waals interactions merely results in a more stabilized molecule.

The pair wise potential energy between two nonbonded atoms can be conveyed in term of internuclear separation. It is convenient to represent van der Waals interactions by the Lennard-Jones (LJ) "6–12" potential [2–5]. The LJ potential

M. Awang et al., *Finite Element Modeling of Nanotube Structures*,
Engineering Materials, DOI 10.1007/978-3-319-03197-2_8

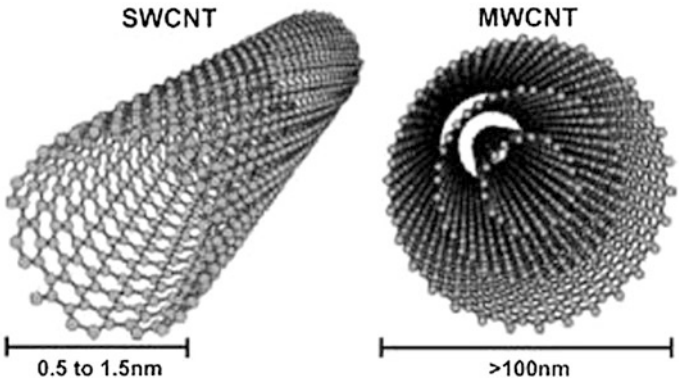

Fig. 8.1 Single-walled nanotube and muti-walled nanotube [1]

Table 8.1 Geometry of SWCNT and MWCNT

Type and layers	Chirality of walls	Diameter (Å)
SWCNT, 1	(10,0)	7.834
MWCNT, 2	(10,0), (12,0) = [(10,0)-(12,0)]	9.401
MWCNT, 3	(10,0), (12,0), (14,0) = [(10,0)-(14,0)]	10.968
MWCNT, 4	(10,0), (12,0), (14,0), (16,0) = [(10,0)-(16,0)]	12.535
MWCNT, 5	(10,0), (12,0), (14,0), (16,0),(18,0) = [(10,0)-(16,0)]	14.102

attract two uncharged atoms which are approaching one another from a distance. In contrast, it changes to strong repulsive force when the two atoms approach too close. Consequently, the pair of atoms tend to keep a separation distance that corresponds to the minimum of the LJ potential;

$$U_{LJ} = 4\varepsilon\left[\left(\frac{\sigma}{r}\right)^{12} - \left(\frac{\sigma}{r}\right)^{6}\right] \tag{8.1}$$

where U_{LJ} is the energy between a pair of atoms of distance r, ε is the bond energy at the equilibrium distance and σ is a constant. The first part of the equation, $(\sigma/r)^{12}$ describes the repulsive forces between particles while the latter part, $(\sigma/r)^{6}$ denotes attraction. For a pair of carbon atoms, the bond energy and σ are 0.002390 eV and σ = 0.3415 nm, respectively [5]. To a limited extent, the Morse potential function can be employed to quantify the van der Waals potential. It must be noted that Morse potential was specially developed to describe interactions of a pair of atoms [6, 7]. Morse function for van der Waal potential can be expressed as in Eq. (8.2).

$$U_{vdw} = D_M\left(1 - e^{-\alpha(r-R)}\right)^2 \tag{8.2}$$

where D_M is atomic separation energy and α is a constant ($6/r_o$). Figure 8.2 depicts that both for near equilibrium and long range, the LJ 12-6 and Morse behave in a similar way at minimum well depths. It also clearly indicates that the van der Waals forces between two carbon atoms are vividly nonlinear.

Therefore, nonlinear spring elements were used connecting the atoms. Load against displacement relationship for spring elements according to Morse potential is shown in Fig. 8.3. The spring element is capable of uniaxial tension and compression. The opted elements offer three degrees of freedom at each node which are x, y and z nodal translations. Two nodes and a non-linear force–displacement relationship can properly specify them for this purpose.

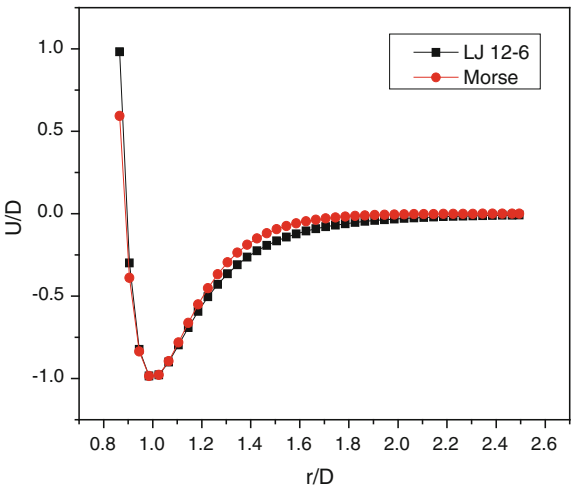

Fig. 8.2 The van der Waals interactions for CNTs

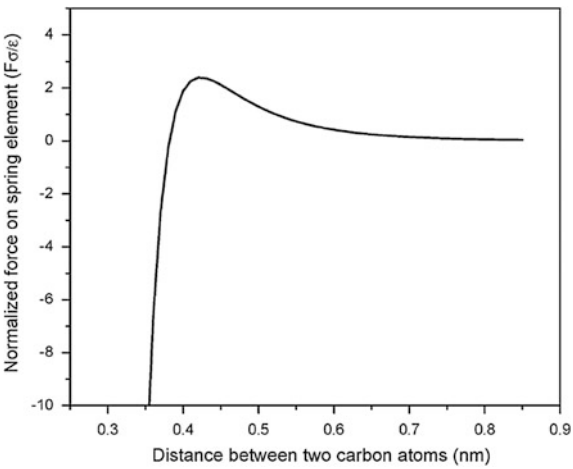

Fig. 8.3 Load-displacement for the spring element according to Morse van der Waals potential

Two multi-walled nanotubes were studied: (12,0)-(21,0) and (5,0)-(14,0)-(23,0). The finite element models for these two MWCNTs depicted in Fig. 8.4a, b. The spring elements which simulate van der Waals are shown in the models and the interaction illustrated in Fig. 8.5.

A triple walled CNT was also modeled. The schematic illustration of the MWCNT and finite element model is shown in Fig. 8.6 with Van der Waals interactions in Fig. 8.7.

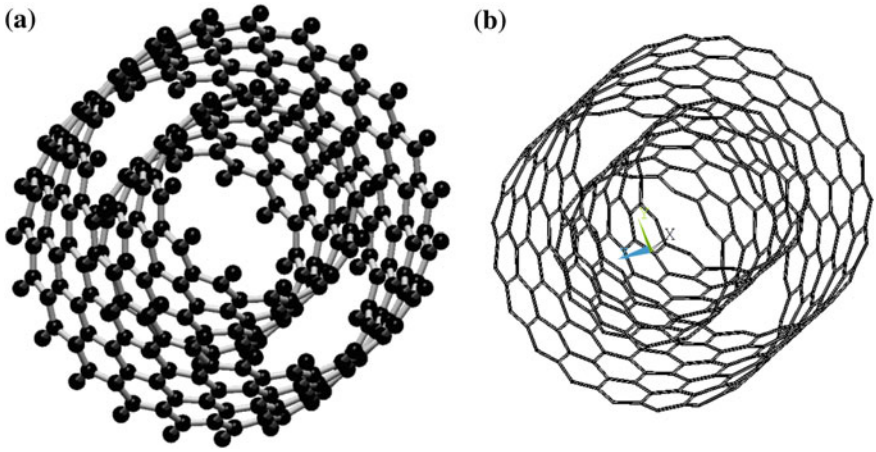

Fig. 8.4 **a** Atomic structure and **b** corresponding FE model of (12,0)-(21,0)

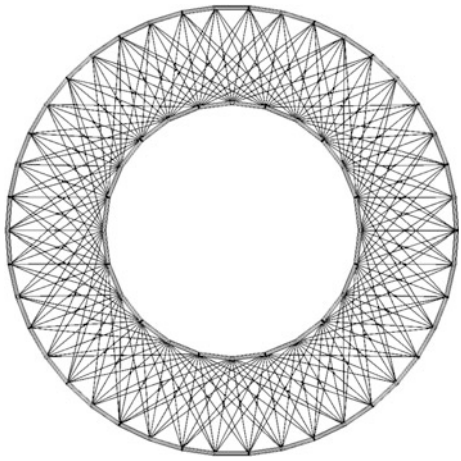

Fig. 8.5 Van der Waals interactions in (12,0)-(21,0)

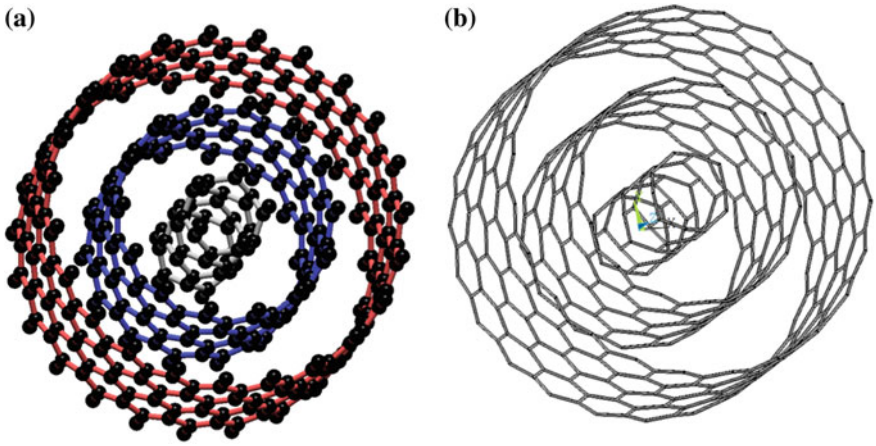

Fig. 8.6 **a** Atomic structure and **b** corresponding FE model of (5,0)-(14,0)-(23,0) CNT

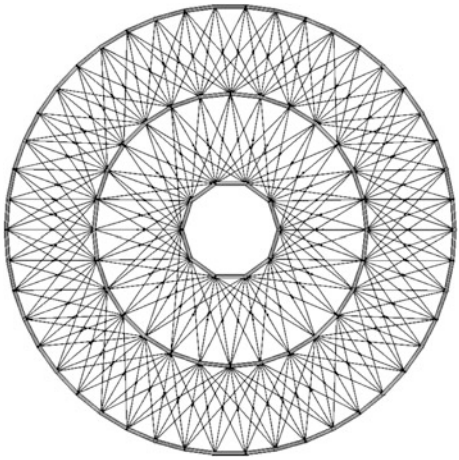

Fig. 8.7 van der Waals interactions of (5,0)-(14,0)-(23,0)

8.3 Tensile Behavior of MWCNT

There have been studies on the tensile loading of MWCNTs using different configurations and conditions [8, 9]. In the aforementioned works, the CNTs were fixed to two opposing AFM tips and undergone tensile load. In particular, the outermost tube of a MWCNT failed under external tension and then the inner CNTs are pulled out in so-called 'sword and sheath' telescoping failure mechanism [10, 11]. Thus, only the outer CNT layer was considered as load bearing member in this work. Weak van der Waals forces are responsible for inner layer interactions in the present model. This is in contrast with another model [12] where the tensile load was

applied to all layers of a MWCNT. The finite element model of double-walled CNT is generated with two concentric CNTs, (12, 0)-(21, 0). The nodes were connected by non-linear spring elements when the pair distance was less than 4 Å but greater than 3.3 Å. Mechanical response of FE models were investigated under small strain tensions.

Simulation of pure tension was achieved by constraining all degrees of freedom on the nodes at one end of the CNT, while the other end was loaded in axial tension. Figure 8.8 shows the atomic configuration of double-wall CNT (12,0)-(21,0) and corresponding modeling concepts, respectively.

Based on the formulation described above, Young's modulus was calculated for MWCNTs and the results are listed in Table 8.2 [8]. The measured tensile strengths of the outermost layer are between 11 and 63 GPa, while elastic modulus was scattered between 270 and 950 GPa. It has also been reported that average value of 1.8 TPa was obtained using AFM-based method [13]. These data are comparable to the present Young's modulus prediction of 0.95 TPa. Finally, the above modeling work has shown that the tensile behavior of MWCNTs is different from that of SWCNTs induced by the presence of van der Waals forces. It suggested that such behaviors could not be simplified with the average of the modulus of the individual SWCNTs building the MWCNT. Moreover, the result showed that when the load was put only on the outmost layer, the inner layers demonstrated very small axial

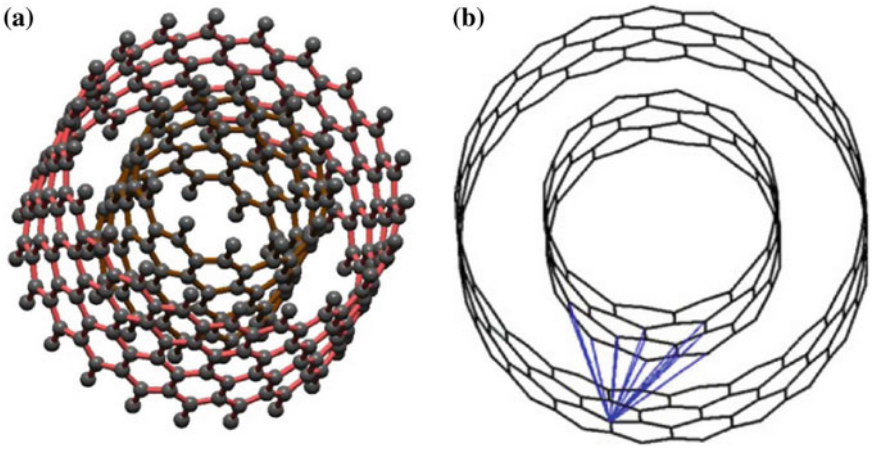

Fig. 8.8 MWCNT (12, 0)–(21, 0): **a** atomic structure and **b** typical FE model for the van der Waals interactions

Table 8.2 Axial Young's modulus of double-walled *CNT*s

Helicity	Young's modulus (TPa)
(5,0)–(14,0)	0.9514
(12,0)–(21,0)	0.9531

displacement. It means that the outer layer cannot transfer the applied force to the inner layers because of weak van der Waals interactions. This behavior confirms the "sword-sheath" mechanism observed by experimental studies [8].

References

1. E.N. Ganesh, "Single -walled and multi walled carbon nanotube structure, synthesis and applications", in *International Journal of Innovative Technology and Exploring Engineering (IJITEE) ISSN*, pp. 2278–3075 (2013)
2. P. Zhang, Y. Huang, H. Gao, K.C. Hwang, Fracture nucleation in single-wall carbon nanotubes under tension: a continuum analysis incorporating interatomic potentials. J. Appl. Mech. **69**, 454–458 (2002)
3. L. Jiang, Y. Huang, H. Jiang, G. Ravichandran, H. Gao, K. Hwang et al., A cohesive law for carbon nanotube/polymer interfaces based on the van der Waals force. J. Mech. Phys. Solids **54**, 2436–2452 (2006)
4. H. Tan, L. Jiang, Y. Huang, B. Liu, K. Hwang, The effect of van der Waals-based interface cohesive law on carbon nanotube-reinforced composite materials. Compos. Sci. Technol. **67**, 2941–2946 (2007)
5. W. Lu, J. Wu, J. Song, K. Hwang, L. Jiang, Y. Huang, A cohesive law for interfaces between multi-wall carbon nanotubes and polymers due to the van der Waals interactions. Comput. Methods Appl. Mech. Eng. **197**, 3261–3267 (2008)
6. T.-C. Lim, The relationship between lennard-jones (12–6) and morse potential functions. *Zeitschrift für Naturforschung,* 58a, pp. 615–617 (2003)
7. M. W. Hyer, S. R. White, *Stress analysis of fiber-reinforced composite materials* (DEStech Publications Inc, Lancaster, 2009)
8. M.-F. Yu, O. Lourie, M. J. Dyer, K. Moloni, T. F. Kelly, R. S. Ruoff, Strength and breaking mechanism of multiwalled carbon nanotubes under tensile load. *Science* **287,** 637–640 (2000)
9. J. Vera-Agullo, A. Glória-Pereira, H. Varela-Rizo, J.L. Gonzalez, I. Martin-Gullon, Comparative study of the dispersion and functional properties of multiwall carbon nanotubes and helical-ribbon carbon nanofibers in polyester nanocomposites. Compos. Sci. Technol. **69**, 1521–1532 (2009)
10. E.T. Thostenson, T.-W. Chou, Aligned multi-walled carbon nanotube-reinforced composites: processing and mechanical characterization. J. Phys. D Appl. Phys. **35**, 77–80 (2002)
11. J.N. Coleman, U. Khan, Y.K. Gun'ko, Mechanical reinforcement of polymers using carbon nanotubes. Adv. Mater. **18**, 689–706 (2006)
12. C. Li, T.-W. Chou, Elastic moduli of multi-walled carbon nanotubes and the effect of van der Waals forces. Compos. Sci. Technol. **63**, 1517–1524 (2003)
13. E.W. Wong, P.E. Sheehan, C.M. Lieber, Nanobeam mechanics: elasticity, strength and toughness of nanorods and nanotubes. Science **277**, 1997 (1971)

Chapter 9
Influence of Defects on the Strength of Graphene and Carbon Nanotube

9.1 Introduction

As with every material, the presence of a crystallographic defect influences the material properties. Defects can occur in various forms with significant effect. With high levels of such defects can lower the tensile strength by up to 85 % [1]. In general, three types of defects are reported in the CNTs [2, 3]:

1. Topological defects, such as the Stone-Wales transformations (Fig. 9.1). A Stone–Wales defect is the rearrangement of the six-membered rings of graphene into pentagons and heptagons [1]. This rearrangement is a result of π/2 (90°) rotation of a C–C bond. A Stone–Wales defect is a crystallographic defect that occurs on carbon nanotubes and graphene and is thought to have important implications for the mechanical properties of carbon nanotubes.
2. Rehybridization defects, which refer to the change from sp^2 to sp^3 of a C–C bond due to highly localized deformation (Fig. 9.2),
3. Incomplete bonding (vacancy) and other defects, such as impurity attachments and substitutions (Fig. 9.3).

It has been discovered that carbon nanotube (CNT) defects can be found at different steps of its fabrication and purification process [4, 5], during device or composite production [6, 7], or under mechanical strains [8]. It was also reported that even few number of defects in the atomic structure of the CNT will result in deterioration of mechanical or electrical properties of the CNT [9, 10]. At present, the studies of the defective CNTs and atomistic effects of these imperfections has been a great challenge from both experimental and numerical aspects.

In order to simulate the mechanical behavior of carbon-carbon bonds beyond bond breaking, a complex interatomic potential function is needed. For instance, the *Brenner* potential function is mentioned as an accurate model [11]. A continuum mechanics approach directly incorporating the *Brenner* potential function has been developed [12, 13]. The process involves modeling elastic properties and

M. Awang et al., *Finite Element Modeling of Nanotube Structures*,
Engineering Materials, DOI 10.1007/978-3-319-03197-2_9

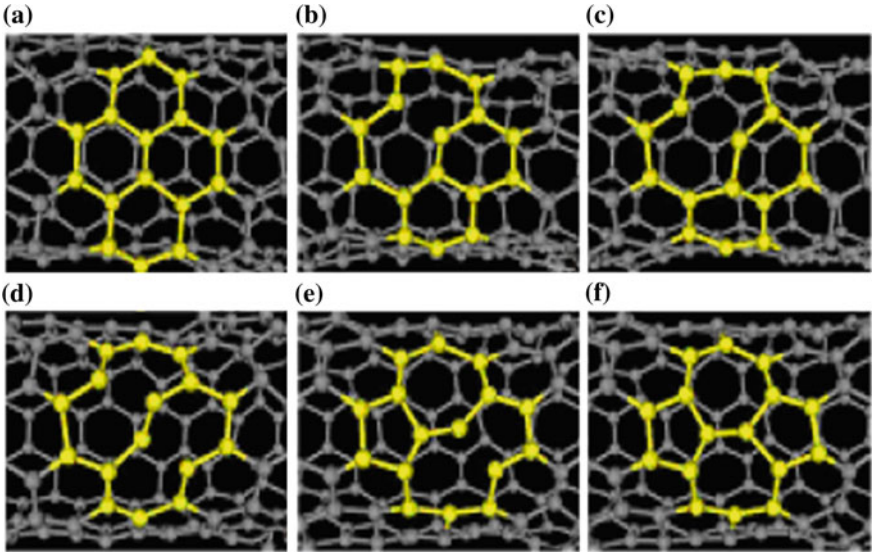

Fig. 9.1 Topological defect (*Stone-Wales)* in CNT [2]

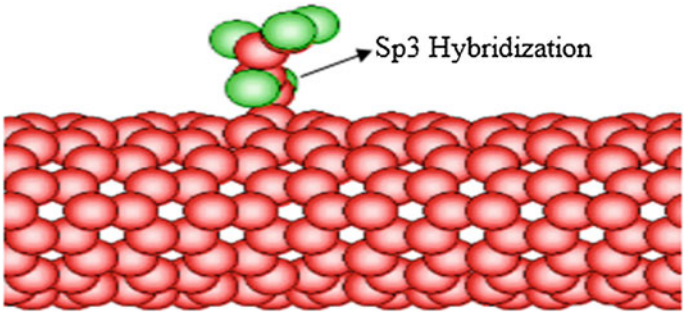

Fig. 9.2 Hybridization defect in CNT (Sp^2 to Sp^3) [3]

stress–strain relationships of carbon nanotubes based on a modified *Cauchy–Born* rule. An analytical molecular structural mechanics model [14] incorporating the modified *Morse* potential function [15] has been developed by model defect-free CNTs under tensile loadings.

From the studies conducted so far, continuum mechanics based models have not been fully developed for predicting the effects of defects on mechanical properties of CNTs and nanotube composites. The quantum mechanics and molecular dynamics (MD) simulations are the main approaches for modeling the effects of defects on mechanical [9, 10] and thermal properties [16] of CNTs. One attempt using a continuum based atomistic model to study defect nucleation in carbon nanotubes under mechanical loadings have been carried out [15]. Also, the effect of

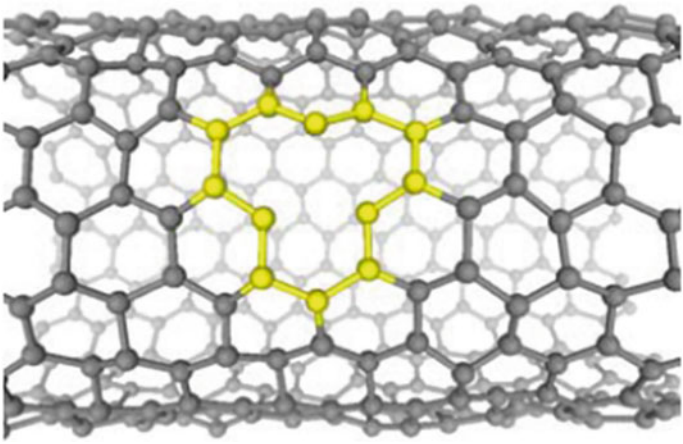

Fig. 9.3 A vacancy defect on a (10,10) SWCNT [2]

defects on fracture of nanotubes has been studied [16] using the finite element (FE) based model where the dimensions of the nanotube structures were assumed to remain unchanged after the formation of defects, which may not be true as atoms redistribute to minimize energy.

9.2 Problem Description

The finite element method is to be used for evaluating the mechanical behavior of defective CNTs and graphene sheets. *Stone-Wales* (SW) defect (5-7-7-5) [17] and vacancies in SWCNTs and graphene sheets with different chilarities will be studied under axial load. Then, the stress–strain relationship of defective structures containing different number of defects is predicted by using the established finite element model based on the modified *Morse* potential function. Effects of defects on the tensile strength of carbon nanostructures are thereafter analyzed. The process involves comparing obtained outputs after simulations with other numerical results such as molecular dynamics for armchair and zigzag carbon nanotubes and graphene.

9.3 Modeling of Defective CNT and Graphene Structures

The process for modeling defective CNT and graphene was conducted through the same method used defect free CNT and other nano-structures as detailed in Sects. 6.2.2–6.2.9. The boundary conditions for the models are shown in Fig. 9.4.

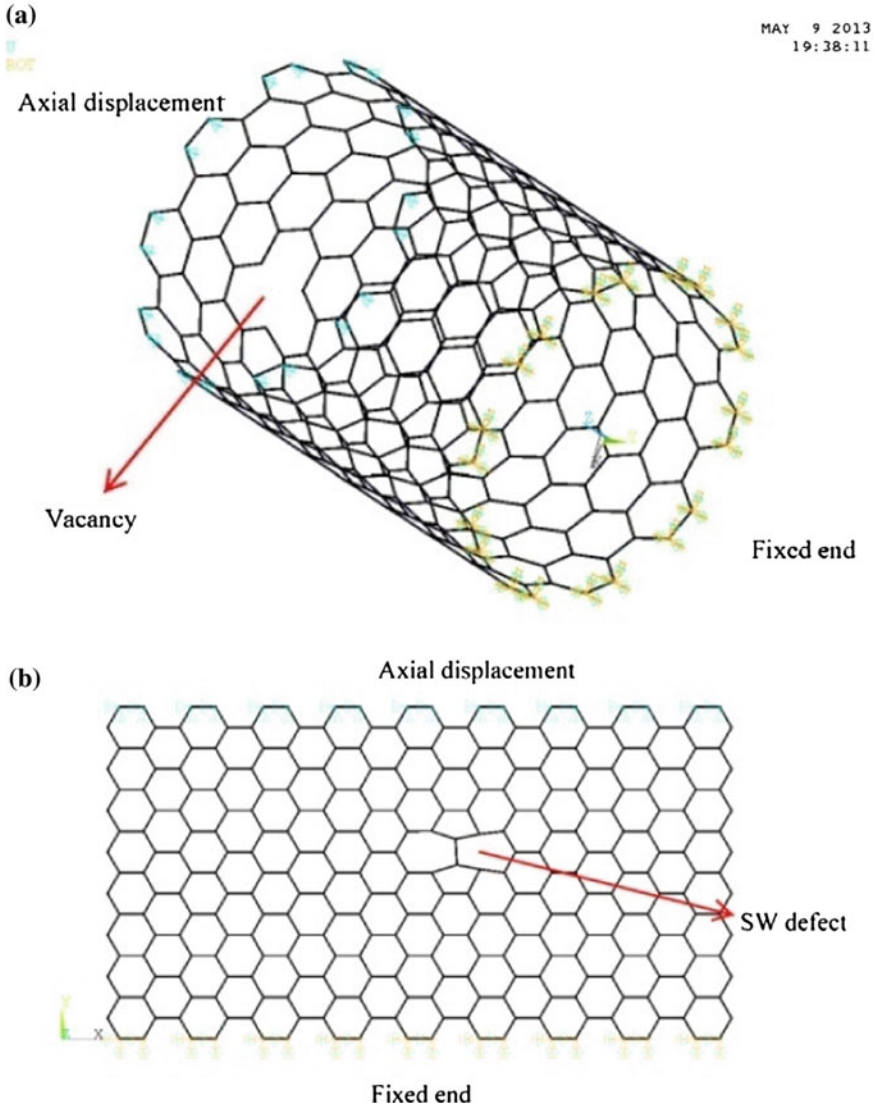

Fig. 9.4 **a** Vacancy in a SWCNT and **b** SW defect in a graphene sheet

The atoms on the bottom edge of the tube were fixed in all directions. The other end of the CNT was axially displaced incrementally to introduce load into the tube.

The interatomic force is calculated for all atoms along the end of the nanotube where the displacement is prescribed. The axial strain of the CNT is computed as $\varepsilon = \Delta l/l_o$, where l_o is the initial length of the CNT or graphene. The force–strain relationship of nanotubes is predicted using modified Morse potential as outlined earlier. It should be noted that the present method does not require a tube thickness

to be defined. However, in order to compare the results with others, a conventional modulus and strengths can be calculated using wall thickness of 0.34 nm for CNTs and graphene sheets. The total force carried by the CNTs can be extracted from the simulation results and then the stress can be computed as $\sigma = F/A$ and the Young's modulus as $E = F \cdot l/\Delta l \cdot A$, respectively.

9.4 Post Processing for Defective CNT and Graphene

The predicted nonlinear behaviors of nanotubes are very similar to results calculated from MD approach [12]. From earlier studies [12, 13], the predicted strengths and failure strains are significantly higher than the experimental values, that is 11–63 GPa for strength and 10–13 % for failure strain [18]. This difference can be partially explained by the presence of defects that reduce stiffness and strength.

Various types of defects exist in CNTs and graphene such as vacancies and SW (5-7-7-5). Graphene sheets and SWCNTs of armchair (12,12) and zigzag (20,0) were modeled in length of 10 nm. It was shown before that the Young's moduli for both armchair and zigzag nanotubes decrease with decreasing tube diameter and approach the predicted graphite value when the tube diameter is increased. Effect of tube curvature were neglected because (12,12) and (20,0) nanotubes have similar tube diameter. In this simulation, the displacement was increased gradually until carbon-carbon (C–C) bonds reach inflation point and bonds breaks. Bond strain and stress can be extracted from the simulation results. Figure 9.5 shows effect of vacancies on the graphene (12,12) and SWCNT (12,12).

Different numbers of vacancies were analyzed to these structures in order to study the effect of vacancy density on the mechanical behavior of graphene sheets and nanotubes. Figure 9.6 Shows stress-strain relationships for graphene (12,12) and SWCNT (12,12) containing different amount of vacancies. It can be seen when the number of vacancies increases from 0 to 50, both structures become less resistance to stress. The same behavior was observed from simulation results of graphene (20,0) and SWCNT (20,0). Based on the results, it can be concluded that vacancies can badly deteriorate mechanical properties of carbon nanostructures.

Figure 9.7 shows the calculated Young's modulus of defective nanotubes and graphene sheets with different chilarities. Young's modulus of nanotubes and graphene sheets are reduced from 0.88 to 0.72 TPa when the number of vacancies increased from 1 to 50, respectively.

Results show that such reduction is highly depends on the chilarity. Armchair structures have greater mechanical strength comparing to zigzag structures. Obviously graphene sheet (12,12) shows remarkable resistance to vacancies in comparison with other nanostructures. Zigzag configurations are weaker and more sensitive to defects as deduced from simulation results.

The Stone–Wales 5-7-7-5 defect involves the 90° rotation of a carbon bond with a new configuration. Figure 9.7 shows two graphene sheet (12,12) with one and three SW defect. Bond strains under tensile loading are depicted in Fig. 9.8.

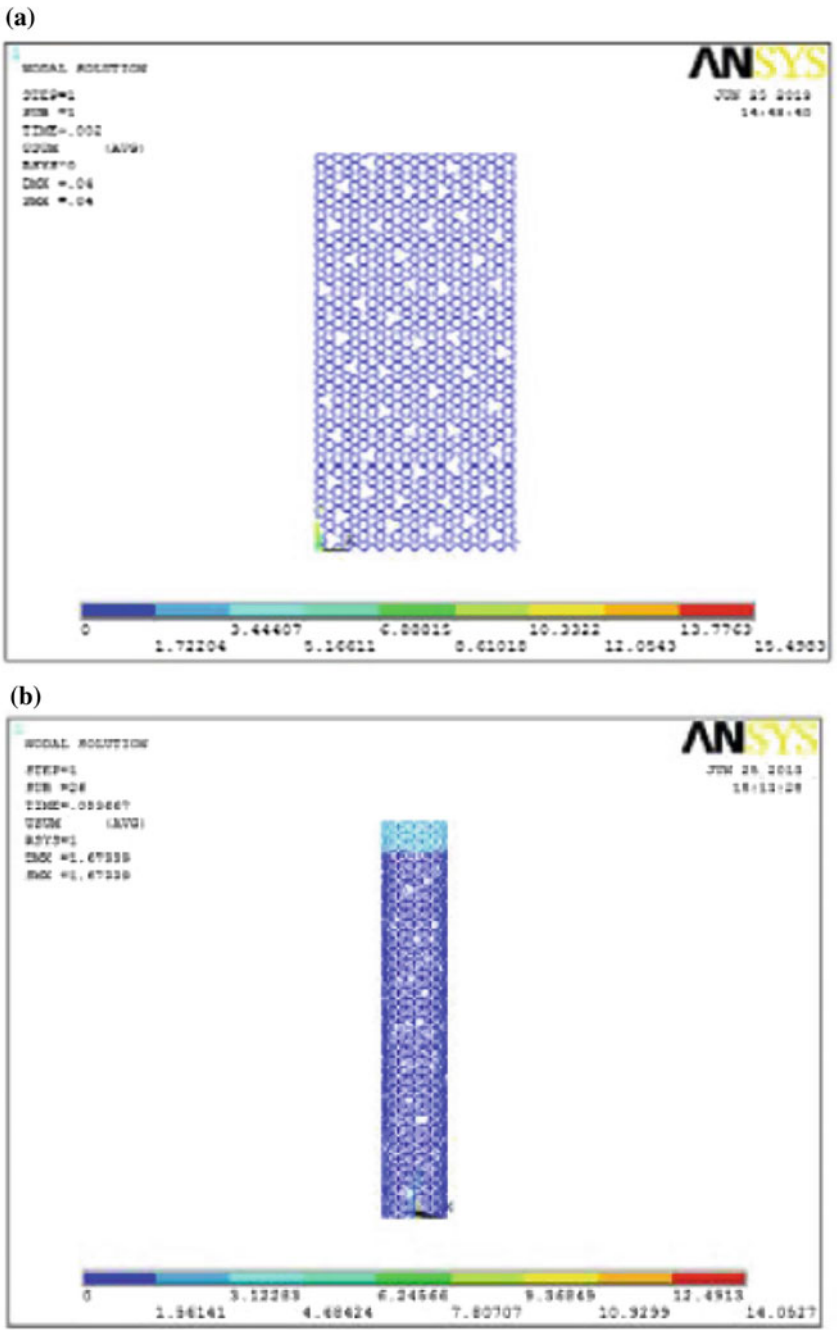

Fig. 9.5 Effect of 26 vacancies on the graphene and SWCNTs: **a** graphene (12,12) and **b** SWCNT (12,12)

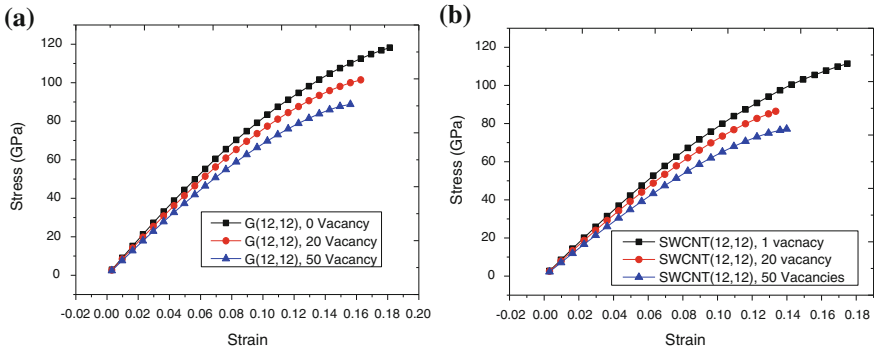

Fig. 9.6 Stress-strain curves for **a** Graphene (12,12), **b** SWCNT (12,12)

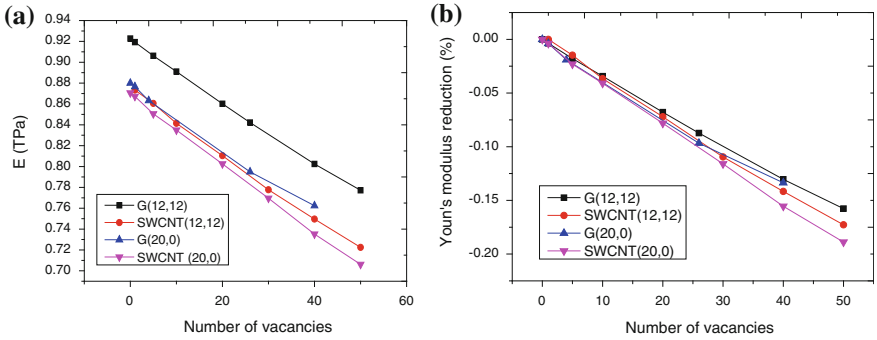

Fig. 9.7 **a** Effect of number of vacancies on the Young's modulus of SWCNTs and graphene sheets, **b** reduction of Young's modulus caused by vacancies

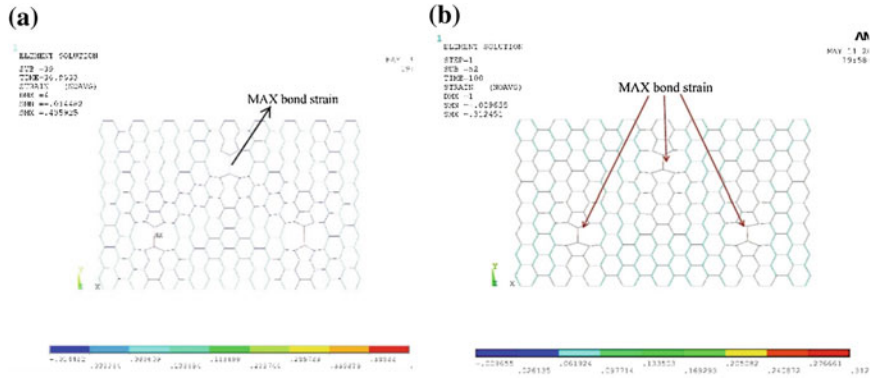

Fig. 9.8 Effect of SW defects on graphene (12,12), **a** 1 SW and **b** 3 SW

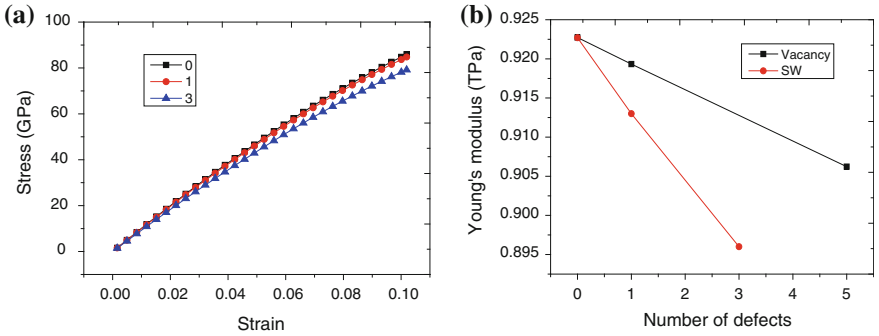

Fig. 9.9 **a** Stress-strain curves of defect-free and defective graphene sheet (12,12), **b** effect of different point defects on the Young's modulus of graphene sheet (12,12)

It seems that SW defect is the weakest part in a graphene sheet. In addition, the effect of the SW defect on the configuration is found out to be local and limited to atoms in the neighborhood of the defect.

Atoms far away from the defect undergo uniform deformation and their geometry configurations are the same as the defect-free tubes. Stress-strain curves of prefect graphene sheets and defected graphene sheets are shown in Fig. 9.8. Results show that SW defect has significant effect on the tensile behavior of graphene.

Figure 9.9a shows the calculated stress–strain relationships for armchair nanotubes with and without SW defects. As can be seen from Fig. 9.9b, when three SW defect were introduced to a (12,12) graphene sheet, its Young's modulus decreases from 0.9227 to 0.896 TPa which is more effective than vacancies. The predicted tensile strength as 85.9 GPa of defect free graphene is much greater than that 75 GPa of defective graphene.

From the results obtained after simulating defective CNT and graphene, it can be concluded that:

1. The present approach is capable of predicting Young's modulus, and stress–strain relationship of graphene sheets and nanotubes with or without vacancy/SW defects.
2. Results show that CNTs and graphene structures are sensitive to vacancies. However armchair graphene structures have significant resistance to defect under tensile load. Moreover, armchair structures for both CNTs and graphene sheets are stronger than zigzag ones.
3. Effects of the SW defect on the Young's modulus, fracture and failure of defective CNTs have been investigated. Using the present approach, it is feasible to model multiple defects and their interaction in both SWCNT and MWCNT since the present approach is much simpler and computationally efficient than the classical molecular dynamics model.

References

1. J.C. Charlier, Defects in carbon nanotubes. Acc. Chem. Res. **35**(12), 1063–1069 (2002)
2. A.L. Kalamkarov, A.V. Georgiades, S.K. Rokkam, V.P. Veedu, M.N. Ghasemi-Nejhad, Analytical and numerical techniques to predict carbon nanotubes properties. Int. J. Solids Struct. **43**, 6832–6854 (2006)
3. Q. Lu, Influence of random defects on the mechanical behavior of carbon Nanotubes through atomistic simulation. Ph.D. thesis, Delaware University (2005)
4. R. Andrews, D. Jacques, D. Qian et al., Purification and structural annealing carbon nanotubes at graphitization temperatures. Carbon **39**, 1681 (2001)
5. D.B. Mawhinney, V. Naumenko, A. Kuznetsova et al., Surface defect site density on single walled carbon nanotubes by titration. Chem. Phys. Lett. **6**, 213 (2000)
6. F.H. Gojny, J. Nastalczyk, Z. Roslaniec et al., Influence of different carbon nanotubes on the mechanical properties of epoxy matrix composites–a comparative study. Chem. Phys. Lett. **370**, 820 (2003)
7. F.H. Gojny, K. Schulte, Functionalisation effect on the thermo-mechanical behaviour of multi-wall carbon nanotube/epoxy-composites. Comp. Sci. Tech. **64**, 2303 (2004)
8. M.B. Nardelli, J.L. Fattebert, D. Orlikowski et al., Mechanical properties, defects and electronic behavior of carbon nanotubes. Carbon **38**, 1703 (2000)
9. M. Sammalkorpi, A. Krasheninnikov, A. Kuronen et al., Mechanical properties of carbon nanotubes with vacancies and related defects. Phys. Rev. B **70**, 245 (2004)
10. Q. Lu, B. Bhattacharya, Effect of randomly occurring stone–wales defects on mechanical properties of carbon nanotubes using atomistic simulation. Nanotechnology **16**, 555 (2005)
11. D.W. Brenner, Empirical potential for hydrocarbons for use in simulating the chemical vapor deposition of diamond films. Phys. Rev. B **42**, 9458 (1990)
12. T. Belytschko, S.P. Xiao, G.C. Schatz, R.S. Ruoff, Atomistic simulations of nanotube fracture. Phys. Rev. B **65**, 235–430 (2002)
13. J. Xiao, B. Gama, J. Gillespiejr, An analytical molecular structural mechanics model for the mechanical properties of carbon nanotubes. Int. J. Solids Struct. **42**, 3075–3092 (2005)
14. P. Zhang, Y. Huang, P.H. Geubelle et al., The elastic modulus of single-wall carbon nanotubes: a continuum analysis incorporating interatomic potentials. Int. J. Solids Struct. **39**, 3893 (2002)
15. H. Jiang, P. Zhang, B. Liu et al., The effect of nanotube radius on the constitutive model for carbon nanotubes. Comput. Mater. Sci. **28**, 429 (2003)
16. M. Rahmandoust, A. Öchsner, Influence of structural imperfections and doping on the mechanical properties of single-walled carbon nanotubes. J. Nano Res. **6**, 185–196 (2009)
17. A.J. Stone, D.J. Wales, Theoretical studies of icosahedral C60 and some related structures. Chem. Phys. Lett. **128**, 501 (1986)
18. M.F. Yu, B.S. Files, S. Arepalli et al., Tensile loading of ropes of single wall carbon nanotubes and their mechanical properties. Phys. Rev. Lett. **84**, 5552 (2000)

Chapter 10
Mechanical Behavior of Carbon Nanotube-Reinforced Polymer Composites

10.1 Introduction

Nanocomposite is a multiphase solid material where one of the phases has one, two or three dimensions of less than 100 nm, or structures having nano-scale repeat distances between the different phases that make up the material. In the broadest sense this definition can include porous media, colloids, gels and copolymers, but is more usually taken to mean the solid combination of a bulk matrix and nano-dimensional phase(s) differing in properties due to dissimilarities in structure and chemistry. The mechanical, electrical, thermal, optical, electrochemical, catalytic properties of the nanocomposite will differ markedly from that of the component materials [1–3].

In mechanical terms, nanocomposites differ from conventional composite materials due to the exceptionally high surface to volume ratio of the reinforcing phase and/or its exceptionally high aspect ratio. The reinforcing material can be made up of particles (e.g. minerals), sheets (e.g. exfoliated clay stacks) or fibres (e.g. CNT or electrospun fibres). The area of the interface between the matrix and reinforcement phase(s) is typically an order of magnitude greater than for conventional composite materials. The matrix material properties are significantly affected in the vicinity of the reinforcement [4].

Examples on nanocomposites include:

1. *Ceramic-matrix nanocomposites*: In this group of composites the main part of the volume is occupied by a ceramic, i.e. a chemical compound from the group of oxides, nitrides, borides, silicides etc. In most cases, ceramic-matrix nanocomposites encompass a metal as the second component. Ideally both components, the metallic one and the ceramic one, are finely dispersed in each other in order to elicit the particular nanoscopic properties. Nanocomposites from these combinations were demonstrated in improving their optical, electrical and magnetic properties as well as tribological, corrosion-resistance and other protective properties [5].

M. Awang et al., *Finite Element Modeling of Nanotube Structures*,
Engineering Materials, DOI 10.1007/978-3-319-03197-2_10

2. *Metal-matrix nanocomposites*: Metal matrix nanocomposites can also be defined as reinforced metal matrix composites. This type of composites can be classified as continuous and non-continuous reinforced materials. One of the more important nanocomposites is CNT metal matrix composites, which is an emerging new material that is being developed to take advantage of the high tensile strength and electrical conductivity of carbon nanotube materials [6].
3. *Polymer-matrix nanocomposites*: These are obtained by adding nanoparticulates to a polymer matrix to enhance its performance, often dramatically, by simply capitalizing on the nature and properties of the nanoscale filler. Nanoparticles such as graphene, CNTs, molybdenum disulfide and tungsten disulfide are being used as reinforcing agents to fabricate mechanically strong biodegradable polymeric nanocomposites for bone tissue engineering applications. In general, two-dimensional nanostructures can reinforce the polymer better than one-dimensional nanostructures, and inorganic nanomaterials are better reinforcing agents than carbon based nanomaterials. In addition to mechanical properties, multi-walled carbon nanotubes based polymer nanocomposites have also been used for the enhancement of the electrical conductivity [7, 8].

In the large field of nanotechnology, polymer matrix based nanocomposites have become a prominent area of current research and development. Since the last decade, research activities in the area of nanocomposites have been increased dramatically [9]. Extensive efforts have been dedicated to a deep understanding of CNT/polymer composites [10–16]. CNTs have been well respected as reinforcement that can enhance mechanical, thermal and electrical properties of polymer-based composite [17]. Their properties such as one-dimensional structure, small size, low density, high aspect ratio, great flexibility and supreme mechanical strength make them an attractive additive in a polymer matrix [18–20]. Nevertheless, many parameters influence the effective properties of CNT/polymer composites such as structure, orientation, dispersion, diameter of CNTs and matrix properties including stiffness and toughness.

10.2 Computational Modeling of CNT Based Composites

Computational approach can significantly assist the development of the CNT-based composites and improve their analysis and design [20]. It is difficult to provide an analytical model at nanoscale. However, even available models are often too complicated and cannot be solved easily. Experimental tests are also costly and involve technical difficulties. Due to these limitations, computational modeling of nanocomposites can be an efficient tool for characterizing the mechanical properties of CNT based composites [21].

It has been established that individual CNTs are widely simulated via MD simulations which have been a great help toward understanding the mechanical and electrical behaviors of the CNTs. However, MD limitations in length and time

scales dramatically affect their application for larger length scales in nanocomposites. For instance, a composite cube with an edge length of 1 μm could contain up to 10^{12} atoms which demands huge computing powers for a simple MD analysis [22]. Practically, advanced materials and nanocomposites in particular should primarily be evaluated at nano scale. They can be extended to macro length scales. It is believed that a combination of MD with other methods is the best approach for this purpose [23].

A multi-constituent material, composites in particular, could be successfully homogenized through the combination of the continuum approaches with micromechanics models [24]. This combination bridges microscale properties to the macroscale. Micromechanics is based on continuum mechanics and specialized for small deformations. Material properties should be uniform in continuum mechanics. However, it is impossible to hold uniformity at microscale. Thus, the micromechanics method must be employed instead. In this way, one can express the continuum quantities of very small elements by using the structural properties of micro constituents [23].

Interaction between CNTs and polymer has been studied and various bonding in the interface were reported [25]. However, most of the observations indicate that strong bonding commonly occurs [25]. A suitable interface is defined as a strong interface which efficiently transfers the load from the chosen matrix to the fibers via a stiff interface [26]. It was argued that atomic interaction and micromechanical interlock in the CNTs/matrix interface are the main factors in the interfacial strength [27].

Based on several factors, a multi-scale representative volume element (RVE) has been used for modeling the tensile behavior of carbon nanotube-reinforced composites [28]. Between the nanotube and the matrix a perfect bonding was assumed until the interfacial shear stress exceeds the corresponding strength which simulated the debonding effect. With isotropic assumption for resultant composite, a typical RVE for CNT composite is shown in Fig. 10.1.

Technical difficulties at nano scale are the main barrier in the way to a comprehensive measurement of the interfacial strength between CNT and polymer matrix [29]. These inconveniences have incited the application of theoretical approaches to evaluate the load transfer ability of the nanocomposites [30]. It has been reported [24] that there are two main types of stress at the interface. The elastic shear stress in the perfectly bonded area and frictional stress at debonded interfaces with the variation for interfacial stress is depicted in Fig. 10.2.

Based on simulation conducted so far, computational approaches are powerful tools in the field of CNT and related composites. However, they cannot simulate many experimental observations which lead to over predicted or underestimated properties of the composites. Micromechanical and continuum models exhibited good potentials in mechanical characterization of composite RVEs. However, results shows that enormous challenges still remain in the development of such an accurate and efficient nanocomposite model.

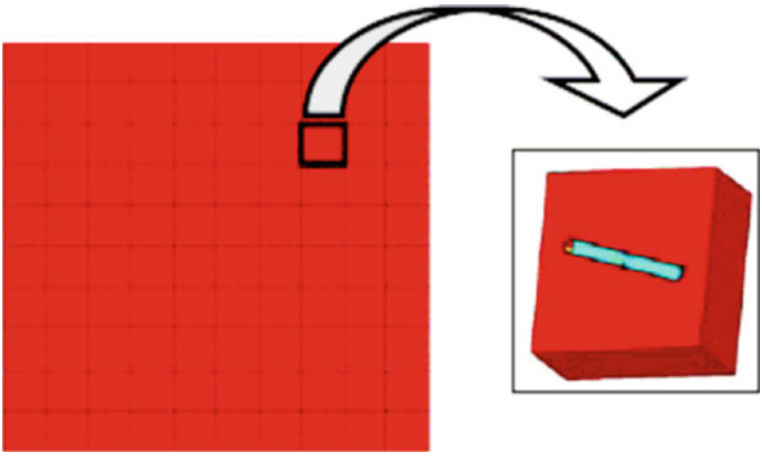

Fig. 10.1 Modeling the effective module of composite by representative volume element [17]

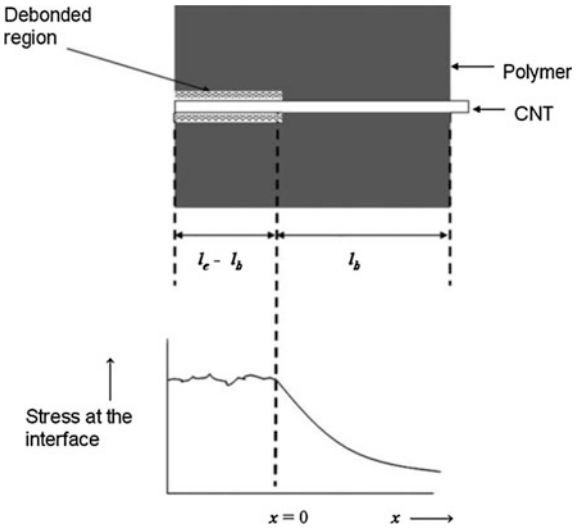

Fig. 10.2 Interfacial stress measurement based on micromechanics modeling [31]

10.3 Modeling Procedure for RVE

Bulk CNTs are a combination of different sizes and forms. As mentioned in previous chapter, they can be a few nanometers in length and can reach micrometers. They are in different shapes, for example, a CNT can be straight, twisted or curled in the bundle of ropes. Moreover, their distribution and orientation in the matrix can be uniform and unidirectional or random. All these parameters make the simulations of CNT-based composites extremely difficult.

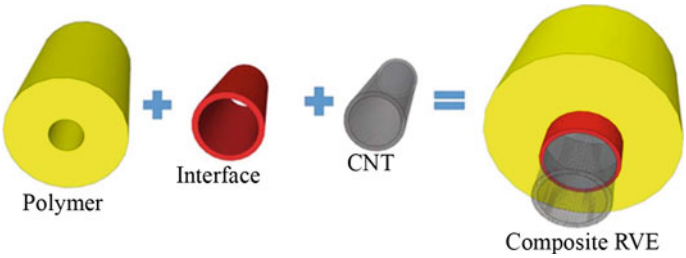

Fig. 10.3 RVE consists of polymer, interface and CNT

The concept of unit cells or RVE has been applied successfully in the studies of microscale fiber-reinforced composites [32, 33]. In the RVE, CNT with surrounding matrix were modeled. Proper attention should be made to boundary and interfacial conditions to consider the effects of the constituent materials. The mechanical responses of these RVEs under tensile load would be analyzed using finite element and ANSYS code. Different constituents of nanoscale RVEs are shown in Fig. 10.3 [16].

At the onsett, finite element models should be constructed for each of the components. Molecular mechanics are employed to create a nonlinear model for tensile behavior of CNTs as described in Sects. 6.2.2–6.29. The Polymer (Polypropylene) was modeled with solid elements which support plasticity with available experimental data adopted for the material behavior of elements. Interfacial region needs careful attention due to its important role in the load transfer issue. As noted before, interface has been simulated differently through spring or joint elements. Although they have leaded to acceptable, modeling process were inefficient in terms of computing power and required time. Therefore, a new approach was opted to overcome these difficulties. Figure 10.4 demonstrates the finite element modeling steps for CNT and composite RVEs.

This RVE can efficiently be utilized to study the load transfer mechanism and interactions of CNTs with the polymer. Stress distributions along the interface can be extracted from the results as well. The chemical bonding between SWCNTs and the PP may results in too complicated solutions. Therefore, chemical interactions in the interface were neglected. To be more specific, the aim was to evaluate the influences of nonbonded interactions on interfacial stress transfer which is a common phenomenon in CNT/polymer composites.

It is a common practice to assume all the phases as homogeneous and isotropic. The material deformation was integrated into elements for material and geometrical nonlinearities. Full Norton-Raphson method was chosen to solve the nonlinear finite element equations. The stress generated in the RVE was calculated using the nodal and elemental stresses by accounting for all phases present in the RVE. The mechanical properties of composite RVE were calculated via extracted nodal data. For example, modulus of the composite was calculated from the values of the axial.

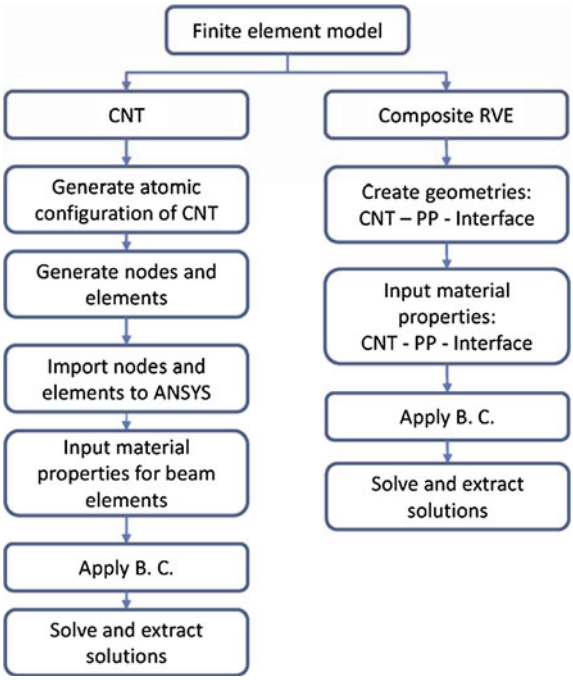

Fig. 10.4 Modeling strategy adopted for CNT and composite RVEs

10.3.1 Polymer Matrix

The volume fraction of CNTs in a typical composite should be small, since CNTs tends to agglomerate. Therefore, the volume percent of polymer matrix is much higher than that of CNTs at molecular scale. As a reasonable assumption, a continuum medium is expected to be accurate enough for modeling of surrounding polymer. In this work, solid elements are utilized to simulate the polypropylene matrix. A 3-D higher order elements with 20-node, SOLID186, was employed for this purpose. The nodes have 3 translational degrees of freedom in x, y and z directions. The element support nonlinear material behavior and according to the ANSYS conditions is a prefect medium to model curved boundaries.

The simulated resin was treated as a nonlinear isotropic material. Young's modulus and Poisson's ratio was set according to the experimental data. Multilinear Isotropic Hardening (MISO) material model was utilized to include nonlinear plasticity of PP work or isotropic hardening has been adopted. The hardening rule describes the changing of the yield surface with progressive yielding, so that the conditions such as stress states for subsequent yielding can be established. For materials with isotropic plastic behavior this is termed isotropic hardening and is shown in Fig. 10.5a. The CNT volume percent is altered by changing the cross sectional area of PP matrix.

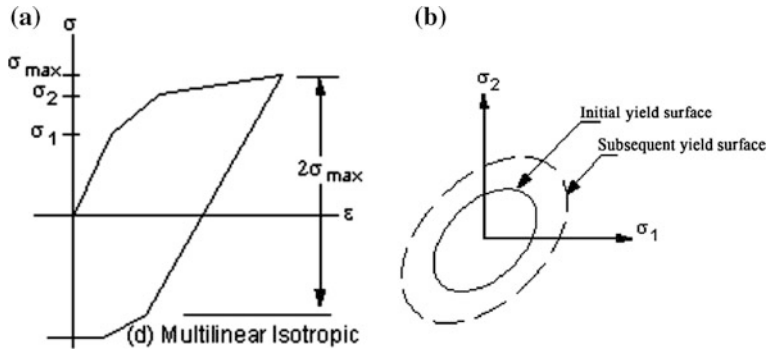

Fig. 10.5 **a** Stress-strain behavior of the multilinear isotropic plasticity, **b** Isotropic work hardening rule [34]

10.3.2 CNT Polymer Interaction

The interfacial region between the CNTs and polymer is a crucial factor. Proper adhesion ensures the maximum load carrying capacity from polymer. All these issues make them the most challenging problem for any simulation approaches. Therefore, it was one of the objectives to explore the load transfer issues and its effects on the tensile behavior of CNT/PP composite.

Although continuum models have been developed for CNT/polymer composite, simulation of CNT/polymer interface has remained as a challenge topic for further investigations [35]. It is difficult to account for the van der Waals force in continuum models in an efficient and accurate method [36].

Cohesive zone models have been successfully employed in the continuum modeling of interface stresses in composites [37]. In this work, a cohesive zone model is adopted to relate interfacial shear tractions and the sliding displacements. The proposed interface model is capable of simulating interface functions. With respect to presented formulation, the interface is modeled using augmented Lagrangian method. A typical cohesive zone with a relatively course mesh is shown in Fig. 10.6. A combination of CONTA174 and TARGE170 elements were used to model stress transfer behavior of the interface.

10.3.3 Boundary Conditions and Assumptions for RVE

To conduct a comprehensive study, two types of RVEs were represented containing long and short CNTs. The schematic illustrations of 3D RVE with applied boundary conditions are shown in Fig. 10.7. Tensile behavior of CNT/PP composites is investigated under uniform extension. For each model, one end is constrained in the all directions and the other end ($z = L$), where L is the length of RVE, is free to

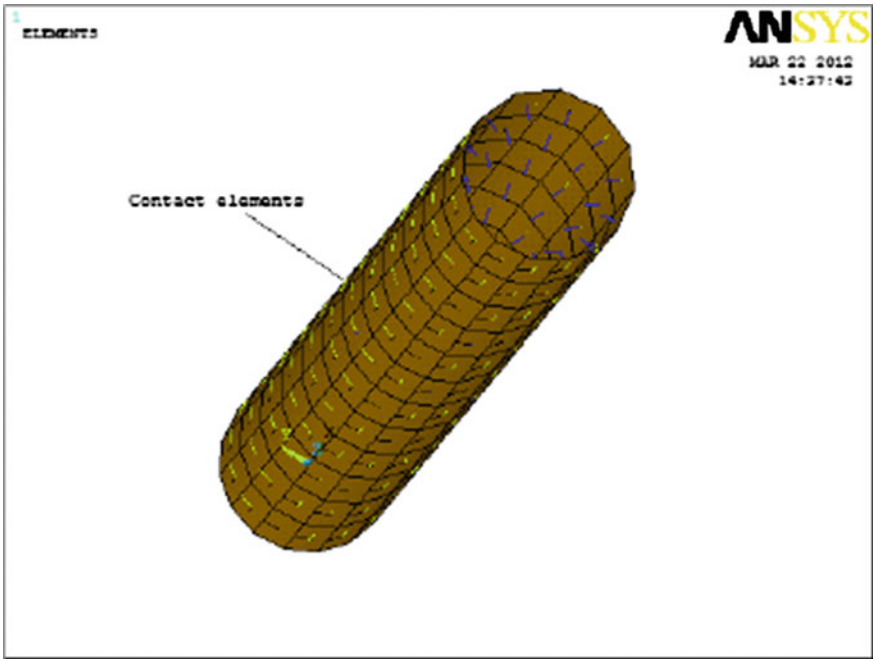

Fig. 10.6 Contact elements representing CNT/polymer interface

move in the z directions. An axial displacement is applied to all nodes on the end surface to simulate external tension on the top surface.

10.3.3.1 CNT Through the Length of the RVE

In this case embedded CNT is relatively long and represent one with large aspect ratio. Therefore, a segment of the composite can be modeled using a 3D RVE as shown in Fig. 10.7a. The volume fraction of the CNT was calculated from the RVE geometry as:

$$V_f = \frac{r_o^2 - r_i^2}{R^2 - r_i^2} \tag{10.1}$$

One can simply obtains the following expression for the Young's modulus in the axial direction of a fiber-reinforced composite,

$$E_C = E_f V_f + E_M(1 - V_f) \tag{10.2}$$

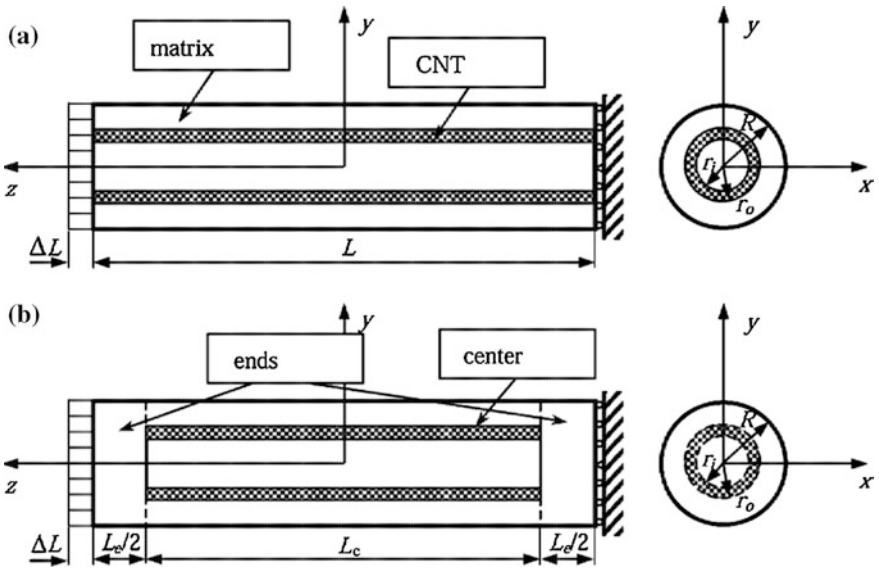

Fig. 10.7 3D RVEs with the applied boundary conditions for **a** long and **b** short CNTs

where *Ec*, *Em* and *Ef* are the Young's modulus of the composite, matrix and CNT, respectively. This is the same rule of mixtures as applied for predicting the Young's modulus in the CNT direction.

However, in the proposed model, as matrix and CNT do not attach directly, it is assumed that they can deform independently under the stretch ΔL. It means the simplified formulation is not applicable in this work. Only for comparison purposes, the results will be compared with the rule of mixtures. This will be compared with the rule of mixtures. This may clarify the distortion of the simplified formulation.

10.3.3.2 CNT Inside the RVE

In this case, the CNT is comparatively short and completely surrounded with polymer as illustrated in Fig. 10.7b. According to role of mixture, the RVE can be divided into two segments. One segment accounting for the two ends with total length L_e and Young's modulus E_m; and another segment accounting for the center part with length L_c and Young's modulus E_c. The two hemispherical end caps of the CNT have been ignored in this derivation, since they do not contribute to the composite strength. The center part can be similarly visualized by a RVE similar to Fig. 10.7a, thus its Young's modulus can be found by using Eq. 10.3. The volume fraction of the CNT is given by Eq. 10.3 is computed based on merely the center part of the RVE with length of L_c. Once again, one can find the Young's modulus in

the axial direction by applying the compatibility of strains and equilibrium of stresses. The expression can be written as:

$$\frac{1}{E_C} = \frac{1}{E_M}\left(\frac{L_e}{L}\right) + \frac{1}{E_C}\left(\frac{L_C}{L}\right)\left(\frac{A}{A_C}\right) \tag{10.3}$$

in which the areas are $A = \pi R^2$ and $A_c = \pi(R^2 - r^2)$. Equation 10.3 could be viewed as an extended version of rule of mixtures compared to that given in Eq. 10.2. It can be used to estimate the Young's modulus when CNT is inside the RVE as shown in Fig. 10.7b.

10.4 Tensile Loading of the RVEs

To evaluate the tensile properties of a CNT-based nanocomposite, the cylindrical RVE consisting of SWCNT, PP matrix and interface was studied using the finite element method. Tensile behavior of PP and a typical CNT was compared in Fig. 10.8.

As mentioned earlier, solid elements were utilized to model RVE. The nonlinear behavior of PP and CNT were integrated with solid elements by using Multilinear Isotropic Hardening (MISO) material model. This model is recommended for large strain deformations. In order to calculate stress values at each substep, reaction forces at surface nodes were divided by cross section of the polymer model.

In Fig. 10.9, a comparison between tensile behavior of fabricated net PP samples and calculated behavior from FE model is shown. It can be seen that they match perfectly up to 10 % strain.

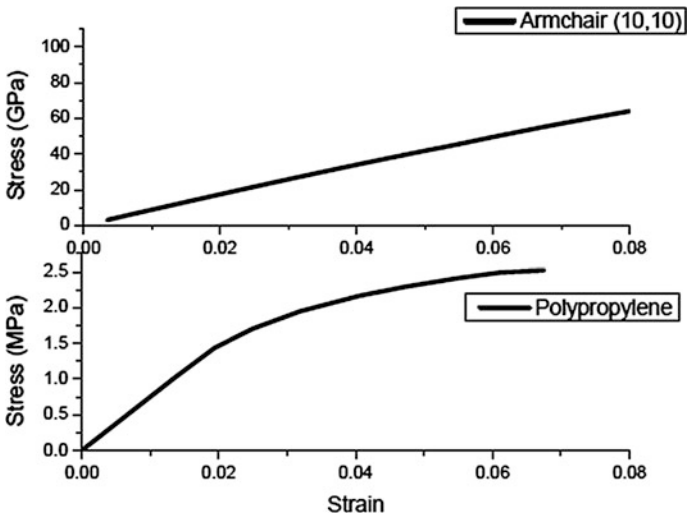

Fig. 10.8 Stress-strain curves of armchair SWCNT and pure PP

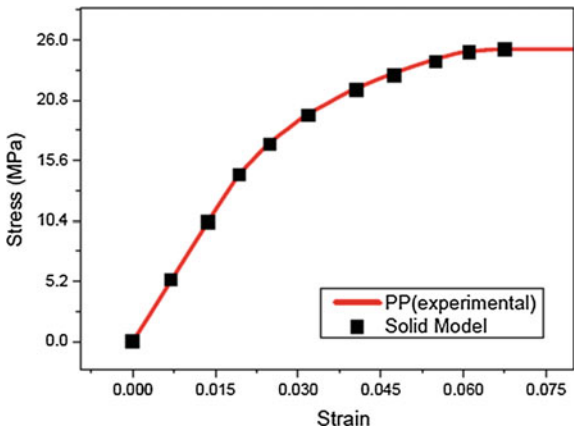

Fig. 10.9 Stress-strain curves obtained from FE model and experiments for pure PP

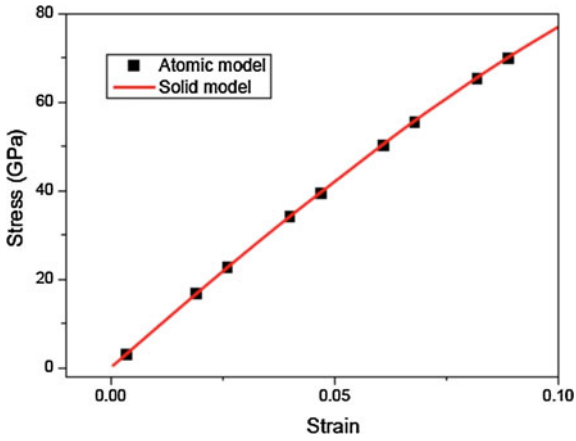

Fig. 10.10 Stress-strain curves obtained from solid and atomic models for armchair SWCNT (5,0)

In order to reduce computing cost, the CNT were also replaced with solid elements in shape of a hollow cylinder. Stress values for at each substep were calculated from the reactions forces at surface nodes. The tensile behavior of solid model is compared with tensile respond of molecular model based on modified Morse functions and shown in Fig. 10.10.

10.4.1 Effect of CNT Length on the Modulus of CNT/PP Composites

To start with, perfect bonding between CNT and PP was assumed. As noted previously, it is not impossible to create such a strong bond via functionalization methods in a CNT-based composite. The interface model was adjusted to account

the full bonded condition between the CNTs and matrix. RVE containing a long CNT was studied. The RVE with applied boundary conditions is illustrated in Fig. 10.11. Axial displacement were constrained at z = 0. Axial displacement was applied in axial direction to simulate deformation of the RVE under tension. The nodal displacement and reaction forces were computed for the described boundary conditions. These data were used to calculate the stress-strain relationships of RVEs. As demonstrated in Fig. 10.11, the CNT went all the way through the RVE length. Material constants and dimensions of RVE are listed in Table 10.1. The material behavior for CNT is assigned to the solid elements. The values of the dimensions and material constants can be modified for any specific case in other simulations. Equations 3.7–3.10 were employed to compute the Young's modulus (E), ultimate strength (σ_{uts}) and Poisson's ratios (ν) for the RVE.

As mentioned earlier, two case studies are presented that covers long and short CNTs in the polymer. In all the cases, full 3-D FEM models were built. The finite element meshing has been done with different element sizes. The optimum mesh size was chosen according to the accuracy and efficiency of the model as demonstrated in Fig. 10.12. CNT is meshed with two layers of elements. It was concluded that it was fine enough to produce converged solutions.

Surrounding matrix does not require small elements comparing to CNT. The polymer meshed with relatively courser element. However, it was necessary to avoid elements with large aspect ratios. Section of the proposed model is shown in Fig. 10.13.

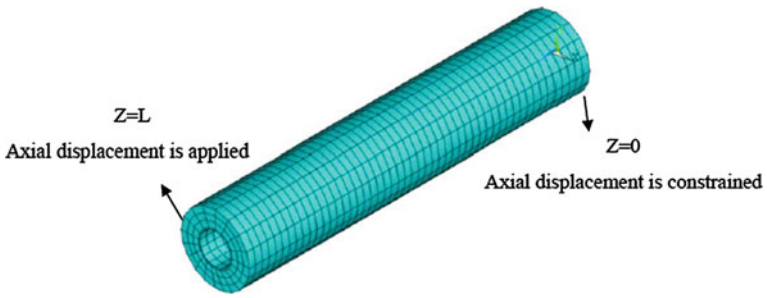

Fig. 10.11 RVE with applied boundary conditions

Table 10.1 Dimensions and material constants of the RVE

Dimensions	PP	CNT
Length (nm)	100	100
Inner radius (nm)	5	4.6
Outer radius (nm)	10	5
E (GPa)	0.475	861
σ_{uts} (GPa)	0.028	94.86
ν	0.42	0.3

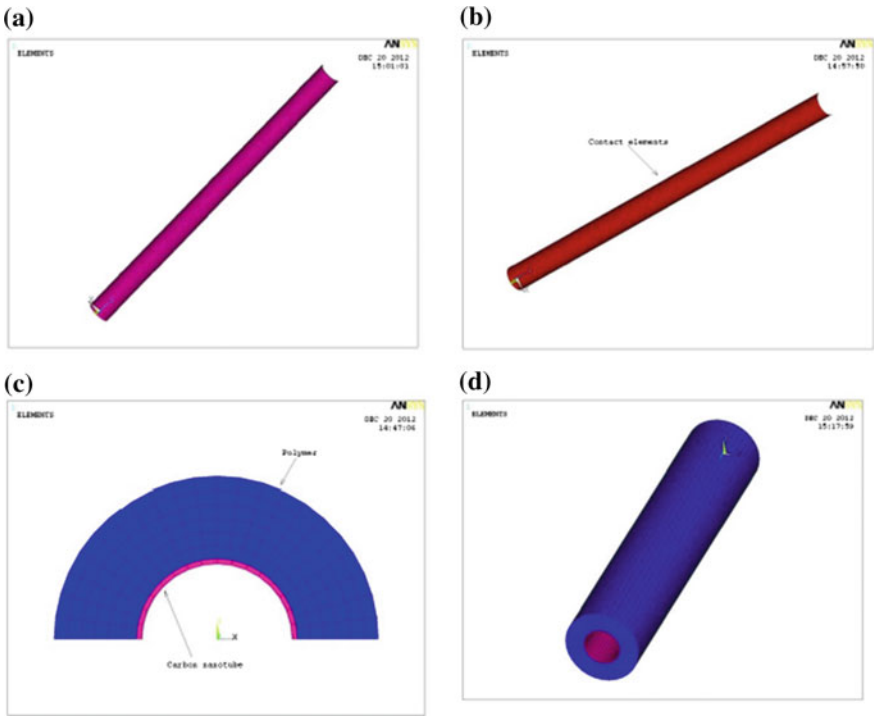

Fig. 10.12 3-D RVE of SWCNT/PP composite with long CNT

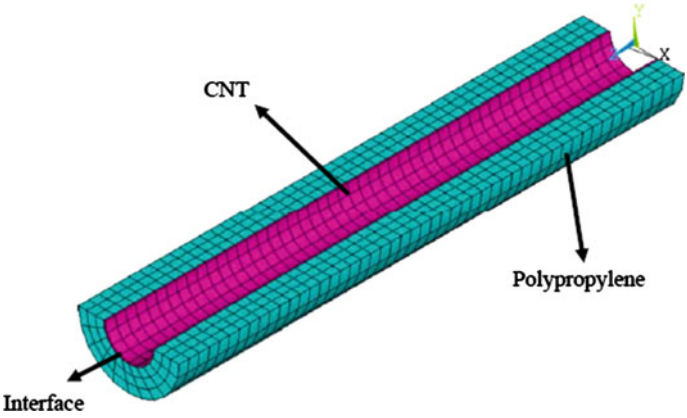

Fig. 10.13 Section of the FE model for RVE with long CNT

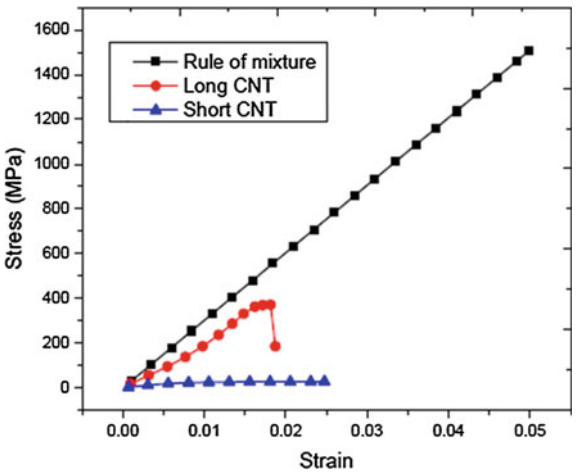

Fig. 10.14 Comparison between the FEA results and rule of mixture predictions

The volume facture of the presented RVE was calculated from Eq. (10.2) as 0.033. Thus, the rule of mixture in Eq. (10.3) yielded *Emix* = 28.7 GPa which predicts a significant improvement in the composite mechanical response. However, the calculated value form more elaborated Halpin-Tsai equation [38] leads to E_{H-T} = 475 MPa. This value is closer to the experimental observation. The difference is much obvious in the plots illustrated in Fig. 10.14. The lower values of material constants obtained from FEA, compared with that of the results of rule of mixture and Halpin-Tsai model, suggested that the effect of material nonlinearity caused by both material properties and geometry of the RVE cannot be neglected.

Then a RVE containing short CNT was built. The same concept was utilized while the CNT total length reduced to 50 nm. The finite element was meshed as shown in Fig. 10.15. Two layers of elements were used to mesh the thickness of the

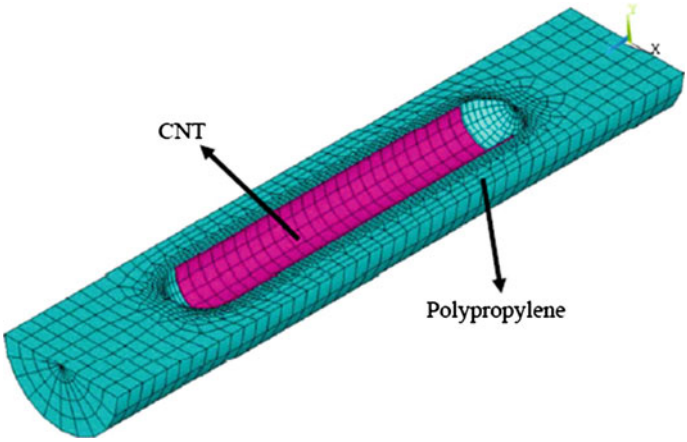

Fig. 10.15 Section of the FE model for RVE with short CNT

CNT due to complexity of the geometry and to obtain a reasonable element shape. The interface was adjusted accordingly to simulate prefect bonding. DOF constraint was imposed to both end surfaces. All DOFs for the bottom surface was constrained while axial displacement was applied to other end so that all nodes on that surface displaced the same amount in the axial direction to simulate the tensile load.

If we consider the rule of mixture equation for short CNTs [16], calculation from $v_f = 0.016$, $E_f = 861$ GPa and $E_m = 0.475$ GPa yields $E_{mix} = 0.912$ GPa. While, the extracted value form the RVE was $E_c = 603$ MPa. The difference could be seen much clearly in the plots illustrated in Fig. 10.14. The lower value of Young's modulus and ultimate strength (σ_{uts}) obtained from FEA, compared with that of the rule of mixture, suggests that we cannot neglect the effect of material nonlinearity caused by both material properties and geometry for the composite RVE.

Figure 10.16 represented deformation contours of RVEs under tensile load. The displacement results showed the deformed shape of RVE model after the solution. The color contours demonstrated the magnitude of deformation from the original shape. The color contours corresponded to the values defined by the color bar.

To find out the effect of CNT length on the tensile properties of composites, the stress-strain curves for both cases were plotted in Fig. 10.17. It can be seen that RVE with long CNTs shows several order higher strength comparing to other RVE. This conclusion is in good agreement with other reports [16, 20, 40]. However, both of these studies were based on elastic models.

According to the results, radial deformation mostly happens in the areas with smallest mechanical strength. In RVE containing large CNT, the deformation mostly happen in the polymer near the $z = L$. It can be seen that the tensile load was applied to this end. For short CNT, deformation concentrated in the polymer close to the CNT ends. Stress concentration at these regions can explain this behavior. Displacement vector sum for both RVEs are shown in Fig. 10.17.

Von Mises stresses in Fig. 10.18 used color contours to show the stresses calculated during the solution for RVE models. The deformed model was displayed. The color contours corresponded to the values defined by the color bar.

It can be seen that the stress distribution is not uniform in the RVEs. Based on the theoretical models, it was expected that polymer transfer external stress to the CNT in a prefect composite. Stress distribution in the RVEs in Fig. 10.19 is the evidence that confirm theoretical prediction. In both cases, stress is concentrated mainly in the CNT. Maximum transferred stress in RVE containing short CNT is 1.16 GPa, while this value for RVE containing long CNT is several magnitude larger and equals to 21.8 GPa. Strain mostly happen in the regions with larger stress tensor. Strain distribution in the RVEs with prefect bonding is depicted in Fig. 10.19. Von Mises strain in the RVEs matches perfectly with the predictions.

In order to realize the deformation mechanism of RVEs under tensile load, each component of the RVE was studied separately. Figure 10.20 shows the stress distribution in the matrix. Interestingly, in both cases the maximum stress value is almost 33 MPa. It can be seen that polymer is merely a medium which transfer the stress. Thus, it cannot resist the external stress sufficiently. Therefore, CNTs are

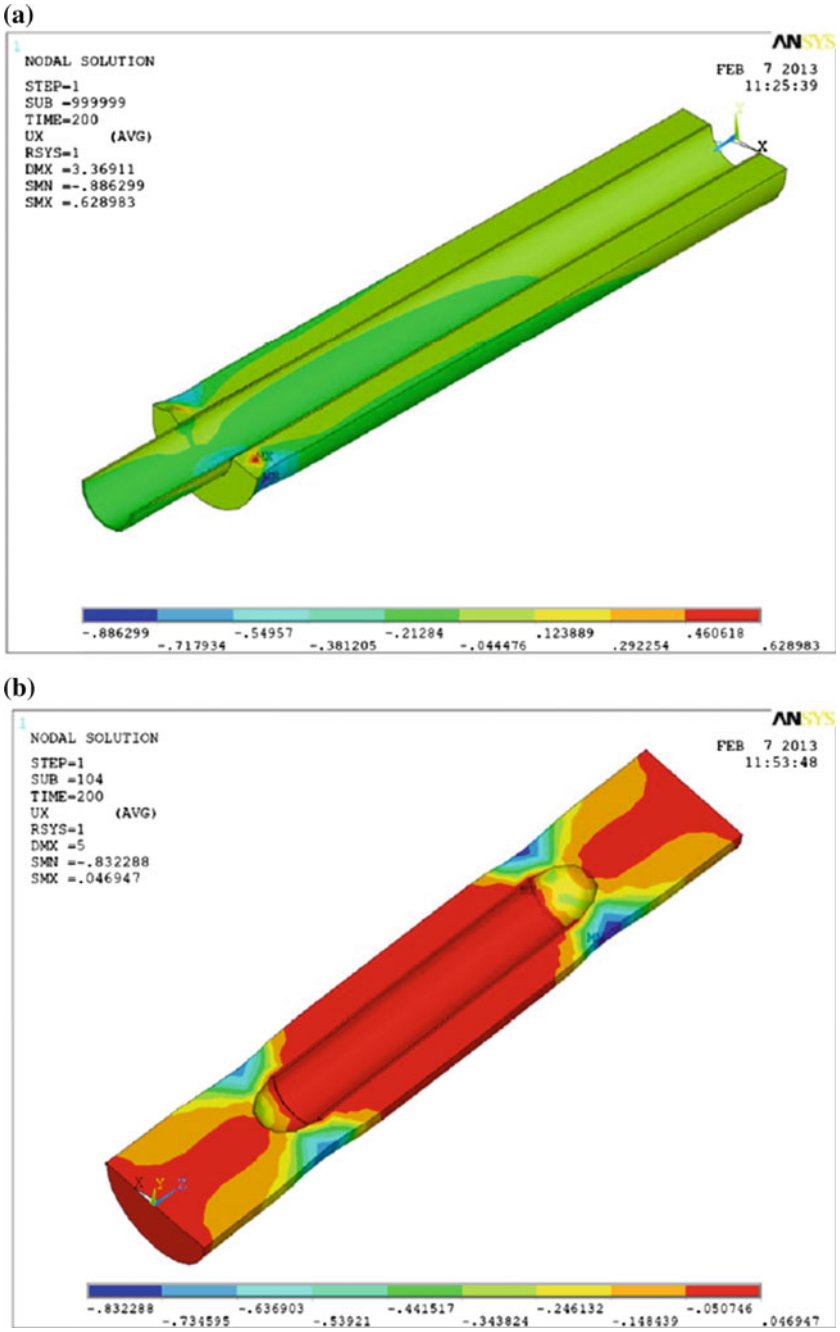

Fig. 10.16 Radial displacement of the RVEs for prefect bonding: **a** long and **b** short CNTs

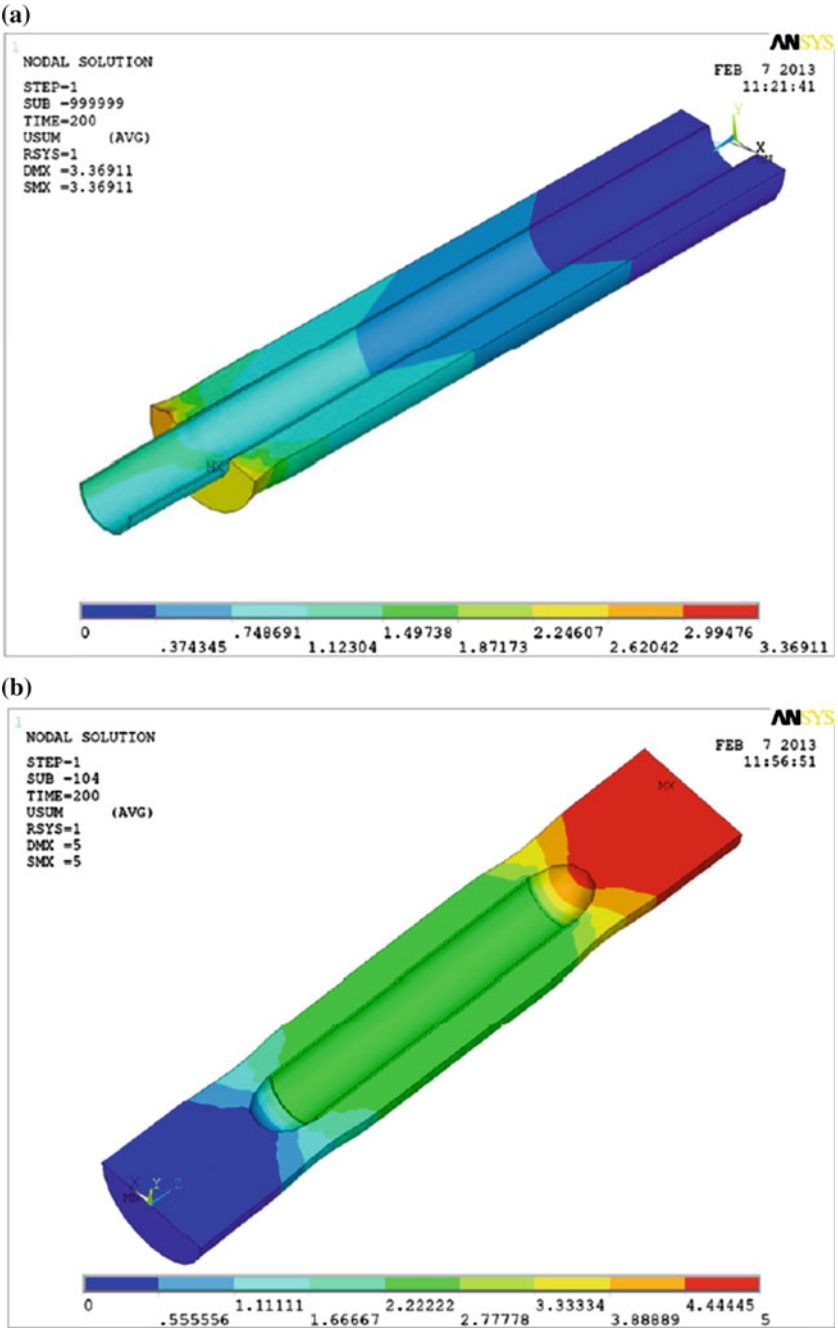

Fig. 10.17 Displacement vector sum of the RVEs for prefect bonding: **a** long and **b** short CNTs

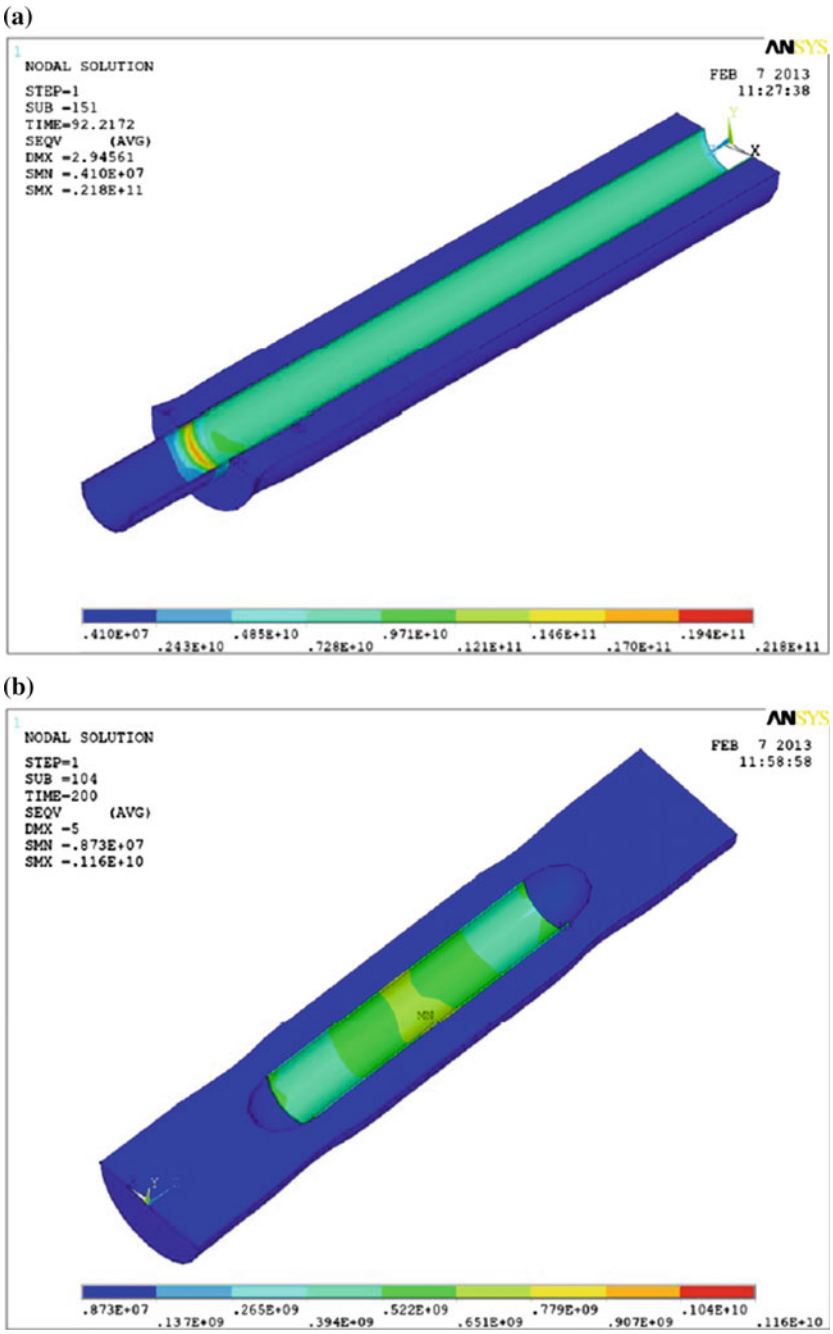

Fig. 10.18 Von Mises stress distribution in the RVEs for perfect bonding: **a** long and **b** short CNTs

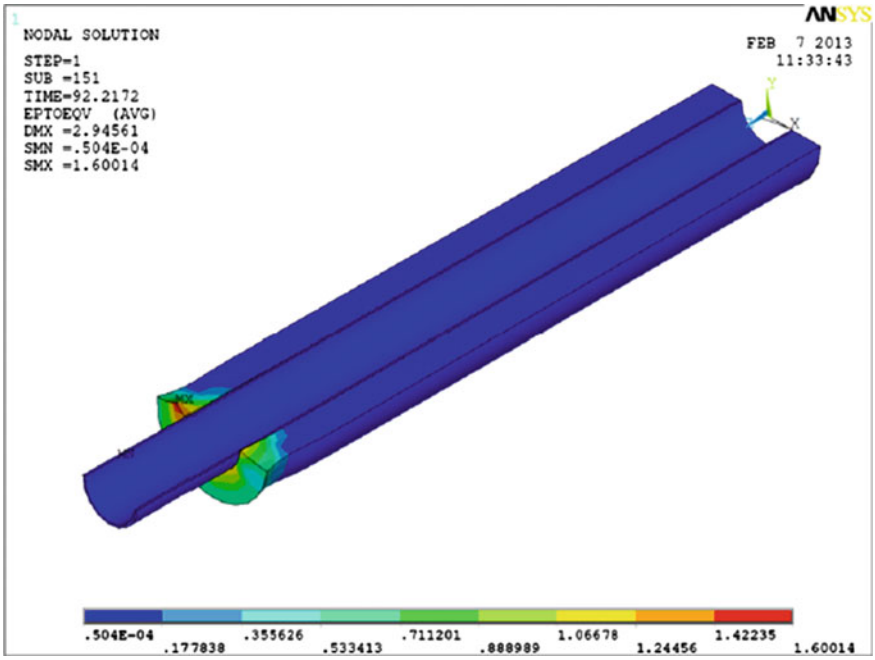

Fig. 10.19 Von Mises strain distribution in the RVEs with long CNT for perfect bonding

essential parts of the composite and carry great part of the applied stress as shown in Fig. 10.21. Prefect bonding in the interface enables the composite to withstand large external stress before matrix fails under tension.

As depicted in Fig. 10.22, results showed that the maximum stress located in the middle of the CNT for short CNT. The maximum stress happened at $z = 0$ of the CNT. It is mostly the result of displacement constrains applied to the extremes.

Perfect bonding condition in the proposed RVE with long CNT results in a large local strain up to 1.6 nm/nm as depicted in Fig. 10.23. Due to complete adhesion between CNT and polymer, similar strain was observed in most of the length of the RVE less than 0.006 nm/nm. Superior mechanical strength of the CNT successfully resist against the external stress at these areas. At $z = L$, stress gradually increases until the polymer fails under the tension and undergoes a large strain.

For RVE containing short CNT, maximum strain located in the polymer close to the CNT ends as shown in Fig. 10.24. Based on the theoretical studies, the shear stress at these regions should be maximum which introduce strain to the polymer with lower mechanical strength.

Since CNTs are remarkably stronger than polymer, their displacement under tension is very small. Von Mises total strain distribution in the CNTs are illustrated in Fig. 10.25. Total strain in the CNTs are smaller than the polymer in

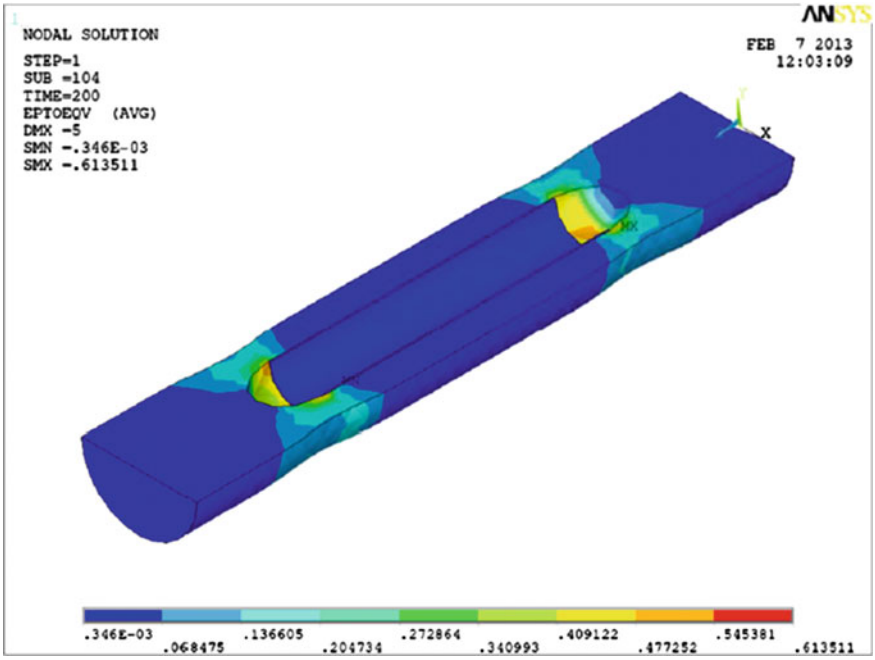

Fig. 10.20 Von Mises strain distribution in the RVEs with short CNTs for perfect bonding

corresponding RVEs. Maximum strain in RVE with short CNT located in the middle of the CNT which has highest amount of normal stress. Due to fixed ends of the RVE with long CNT, the maximum strain expected to occur at the z = 0 end with highest stress value.

The first principal stress gives the value of stress that is normal to the plane in which the shear stress is zero. The first principal stress helps to understand the maximum tensile stress induced in the part due to the loading conditions. Figures 10.26 and 10.27 shows the first principal stress distribution thorough the RVEs. The obtained data showes that CNTs are vital when tensile strength is needed in such a composite. Significant portion of the applied tensile stress was transferred to the CNT through the polymer in both cases.

However, the shifted tensile load of 17.5 GPa is smaller than the von Mises stress of 21 GPa. Their difference indicates that other tensile forces also exist in the RVEs. This difference is more obvious for RVE with short CNT. The maximum detected tensile tension is equal to 1.1 GPa which is remarkably smaller than von Mises value of 11.6 GPa. It can be the main reason for the failure of the RVE under tensions much faster than the RVE with long CNT. The tensile stress distribution of the RVE with short CNT is shown in Fig. 10.27.

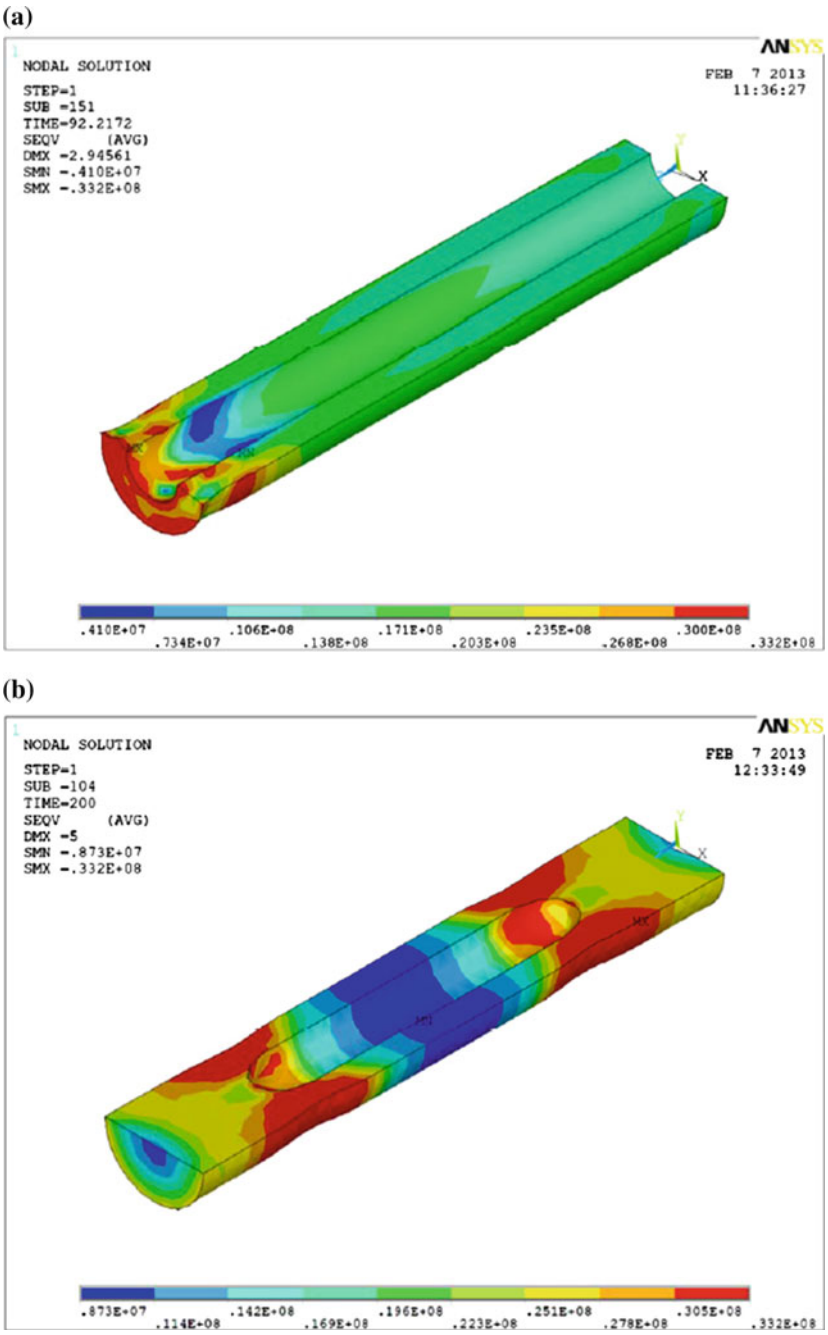

Fig. 10.21 Von Mises stress distribution in PP for prefect bonding: **a** long and **b** short CNTs

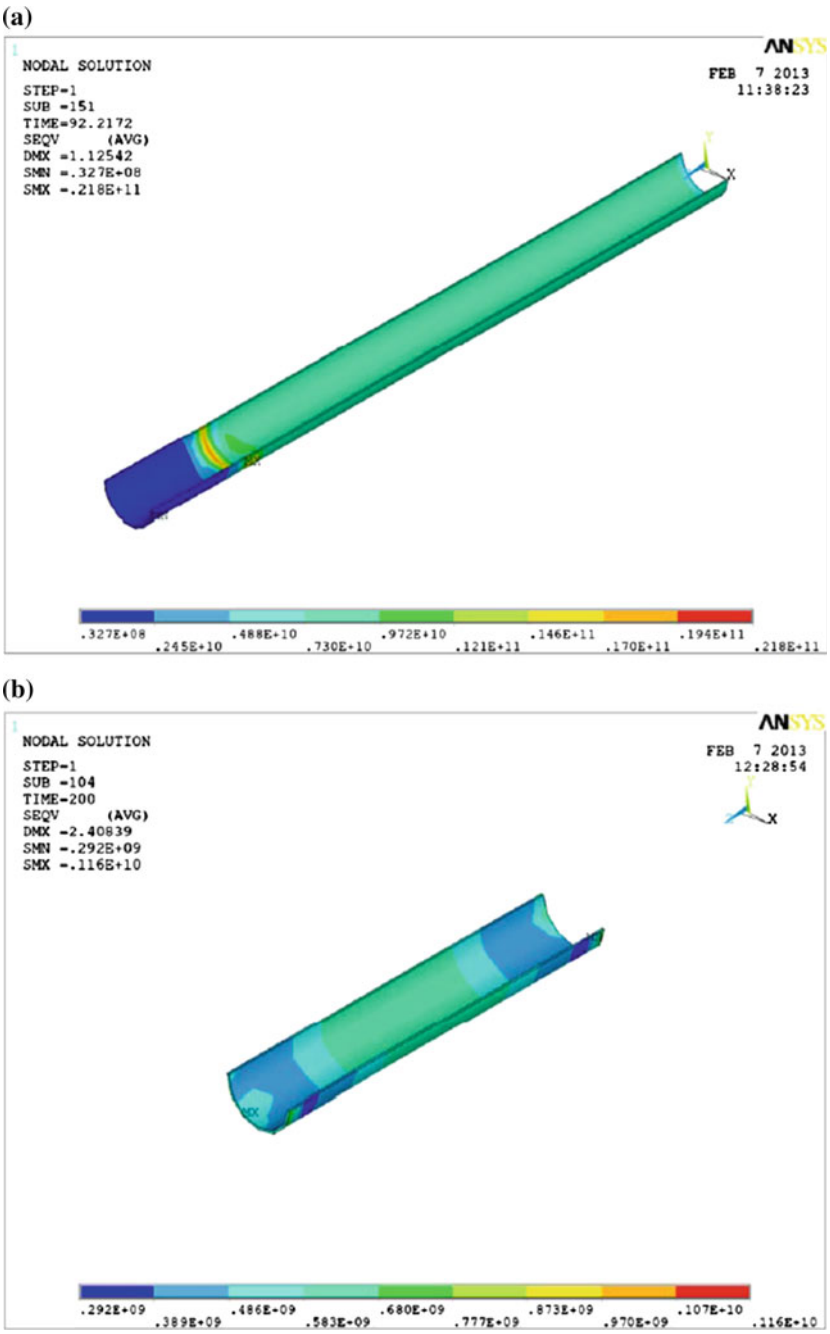

Fig. 10.22 Von Mises stress distribution in CNT for prefect bonding: **a** long and **b** short CNTs

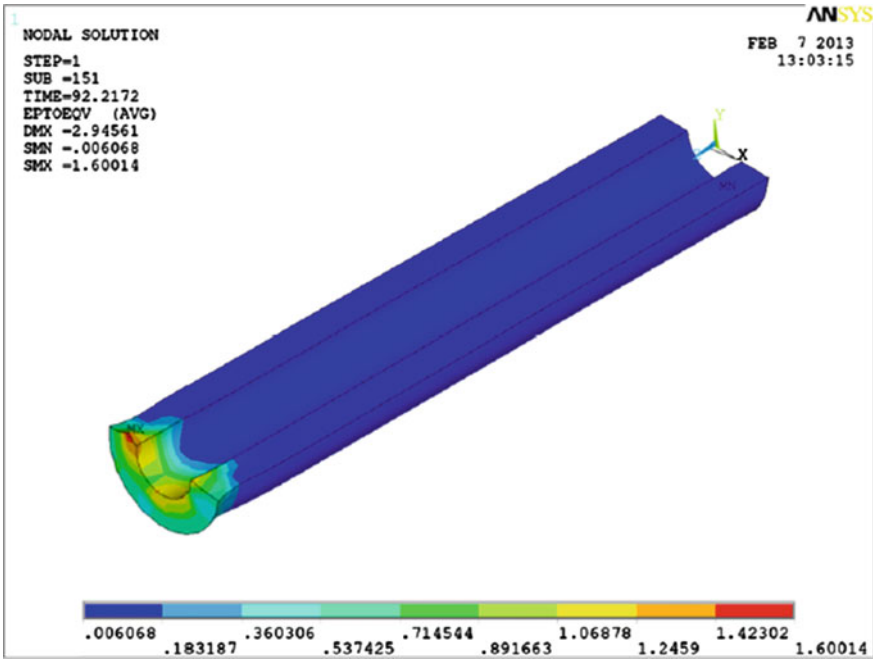

Fig. 10.23 Von Mises total strain in the PP for prefect bonding: **a** long and **b** short CNTs

10.4.2 Effect of Interface on the Modulus of CNT/PP Composites

It has been established that the prefect interface can lead to a significantly improved mechanical respond of the entire composite [24–27, 29, 32, 33, 36, 39–46]. However, in most cases qualitative Atomic Force Microscopy (AFM) and Scanning Electron Microscope (SEM) studies showed that the interface is the weakest component of the composite. To investigate the efficiency of the RVE, a parametric study has been performed to illustrate the influence of interface strength on the behavior of entire RVE. Different interface strength values were successfully adjusted to contact elements. The interface modulus was varied from no-bonding to very strong bonding.

Different values of shear strength was adjusted to the interface to simulate the shear stress filed around the CNT. The values in between were adopted from available experimental observations which were listed in Table 10.1.

Figure 10.28a shows the RVE with disabled interface. It means that the shear strength of the interface is zero. It can be seen that polymer move freely around the CNT and deformation is completely uniform in the entire matrix. In the contrary, when the interface strength increased to 10 MPa, stress transfer dominates and polymer cannot move independently. So there would be localized severe

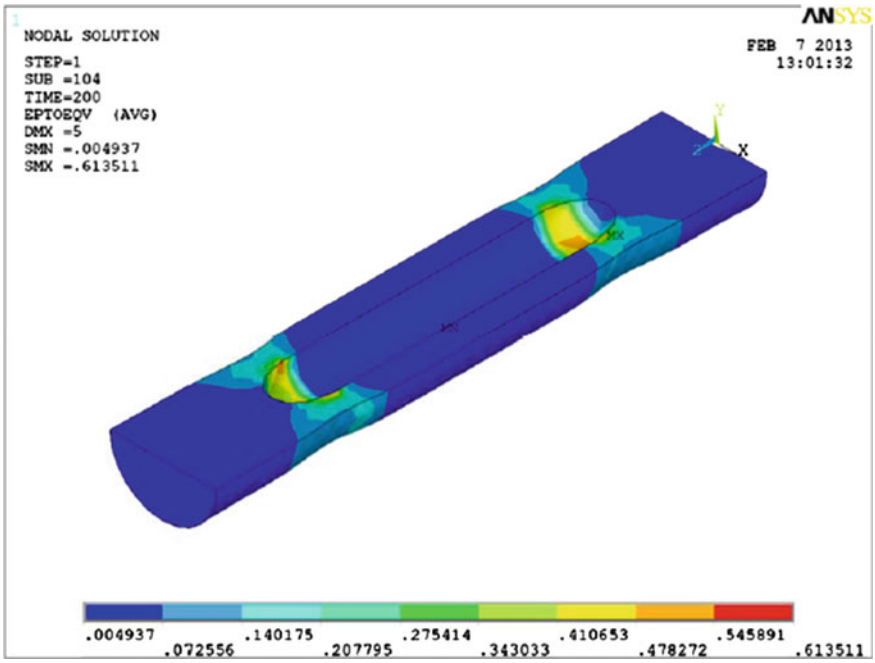

Fig. 10.24 Von Mises total strain in the PP for prefect bonding: **a** long and **b** short CNTs

deformation as demonstrated in Fig. 10.28b. Stress analysis illustrated that the shear transfer between polymer and CNT could be almost zero and polymer deformed uniformly under the stress increment as shown in Fig. 10.29a.

Von Mises stress distribution for RVE with ISS value of 10 MPa is shown in Fig. 10.29b. It seems that, polymer transfer the stress up to 10 MPa and beyond that interface fails and polymer undergo the remaining stress. This leads to intensive strain at the area neighboring the broken interface. The maximum stress in case of disabled interface was detected on the edges of the polymer of almost 68.1 MPa, while the stress value less than 35 MPa at most spots. These results can explain the weak stress-strain relationship of the RVE as depicted in Fig. 10.29a. Maximum stress of 732 MPa was calculated when the ISS = 10 MPa in Fig. 10.29b. It clearly shows the effect of interface on the composite. In addition, von Mises stress distribution showed that stress is successfully transferred to the CNT through the interface and CNT carries a great proportion of the stress. Stress-strain curves for RVEs with disabled interface and ISS = 10 MPa are shown in Fig. 10.30.

Similar studies have been conducted for various ISS values. The mechanical response of the RVEs was extracted and analyses. Stress-strain curves for different ISS value was calculated from the FE model. These curves are shown in Fig. 10.31. Results showed that the effect of interface on the Young's modulus and tensile strength is significant.

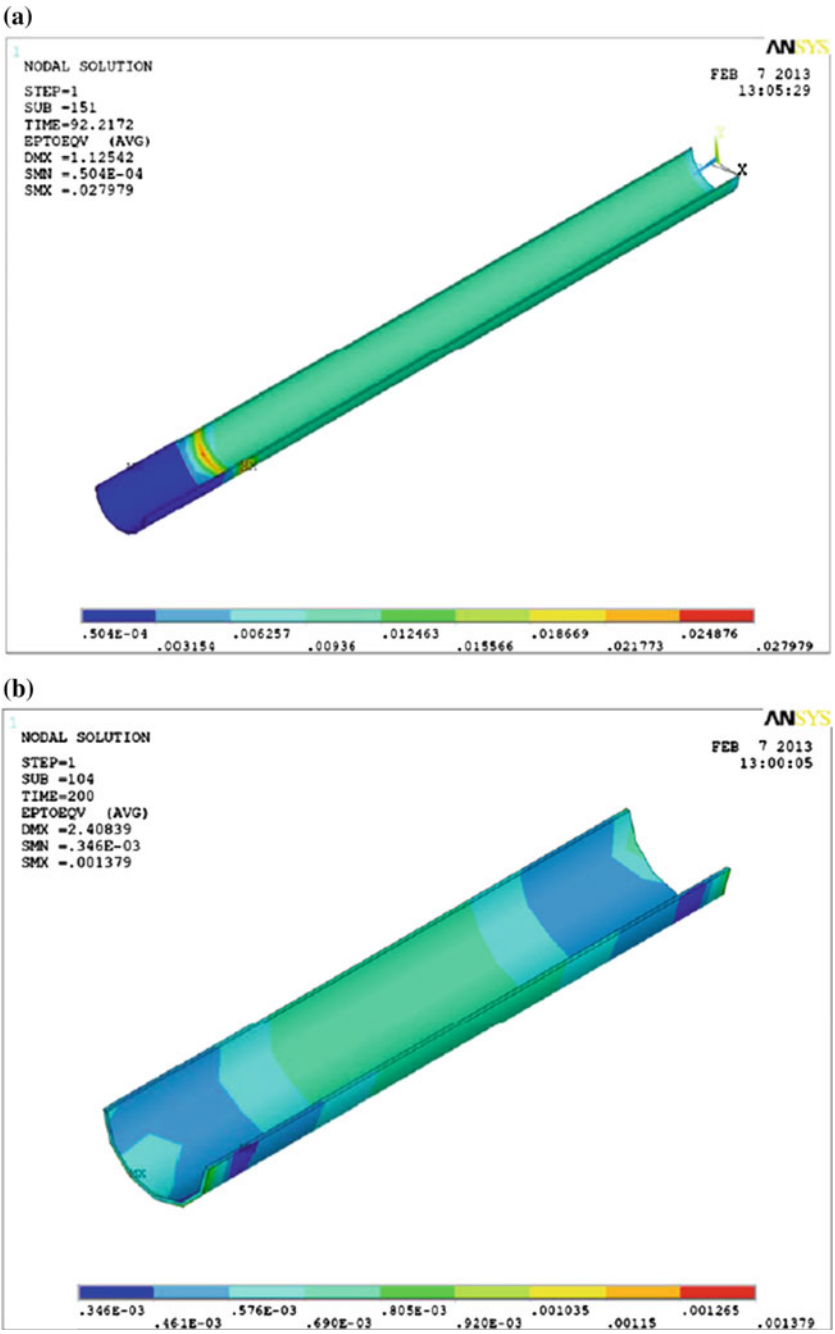

Fig. 10.25 Von Mises total strain in the CNT for prefect bonding: **a** long and **b** short CNTs

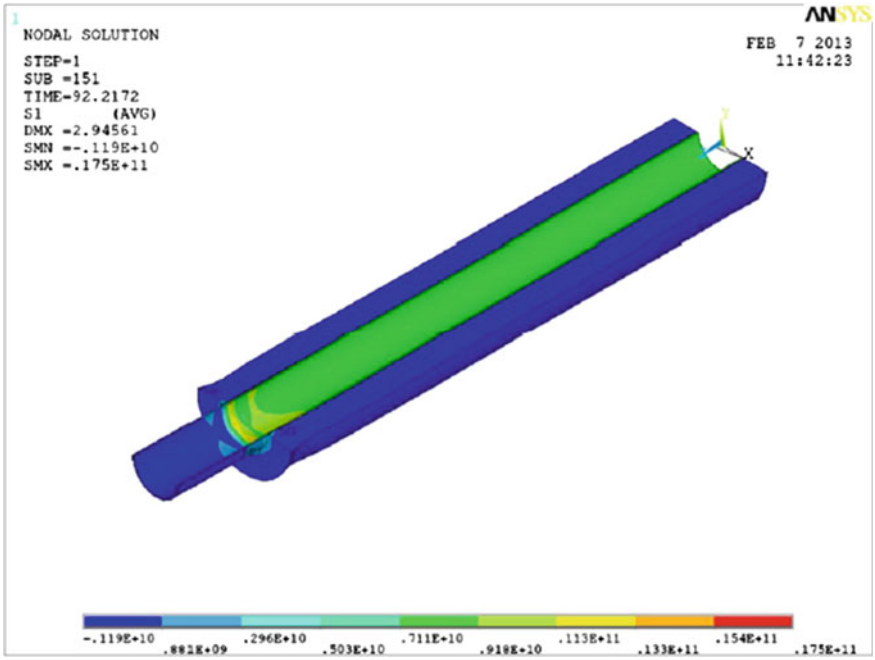

Fig. 10.26 First principal stress distribution in the RVE with long CNT for perfect bonding

The material constants were computed using the FEM results for the RVEs under the tension. The Young's modulus and ultimate strength of CNT/PP composite as a function of the ISS value are listed in Table 10.2 for RVE containing long CNT. It can be deduced from the Fig. 10.31 that bigger ISS values leads to larger composite stiffness. For example, the strength of the composite were almost two times bigger than RVE without interface bonding when ISS is 50 MPa. Lower values of ISS results in decreased modulus for the composites. However, these are remarkably smaller in comparison with the prefect interface bonding case. Based on the results, the obtained stiffness in the axial direction from rule of mixtures equation is far from the FEA solutions. So, the rule of mixtures could not serve as an accurate tool to estimate the stiffness of CNT-based composites in the axial direction.

The results in Table 10.2 confirm that the stiffness of the composite increases substantially in the CNT axial direction. By addition of about 3.28 % volume fraction of the CNT, the Young's modulus of the composite in the axial direction increases by more than 7 times compared with pure PP, when Ef is much larger than Em (CNTs in a polymer matrix).

The cohesive zone model (CZM) adopted for interface has various capabilities which are depicted in Fig. 10.32. Contact status is a useful indicator which shows whether, the polymer is sticking or sliding at any stage of the tension. Total stress

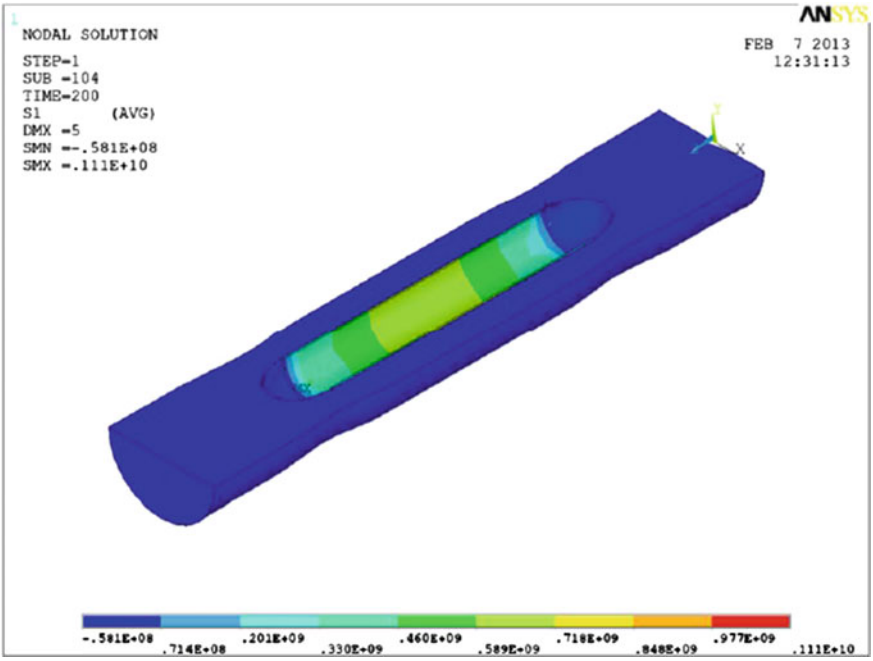

Fig. 10.27 First principal stress distribution in the RVE with short CNT for perfect bonding

and strain that transfer to the CNT from the surrounding PP could be retrieved simply as shown in Fig. 10.32b, c.

For short CNTs, likewise, different cases were studies. For a non-perfect bonding between CNT and PP, different amount of ISS were assumed between the CNTs and matrix. Figure 10.33 shows stress distribution in the RVE with ISS value of 10 MPa.

Extracted values for tensile properties of these RVEs are listed in Table 10.3. The properties of the CZM interface region can be adjusted by appropriate values. Results showed that at a similar interfacial strength, the RVE behavior completely depends on the CNT length. For example, for ISS value of 10 MPa, the RVE containing long CNT depicted higher strength comparing to the other. Von Mises stress values in Figs. 10.29 and 10.33 clearly show the influence of CNT length on the mechanical response of the composite. The stress-strain curves for long and short CNTs with similar ISS value are shown in Fig. 10.34.

Von Mises stress value in the matrix for RVE containing short CNT is almost 8.1 MPa while the same value in RVE with long CNT is about 2.5 MPa. The stress value inside the CNT on the other hand follows an opposite trend. Indeed, larger values of stress transferred to the long CNT of 73.5 MPa comparing to 50.3 MPa for short CNT. This difference shows that polymer transfer more stress to longer CNTs which leads to higher stress values in same strains comparing to short CNTs.

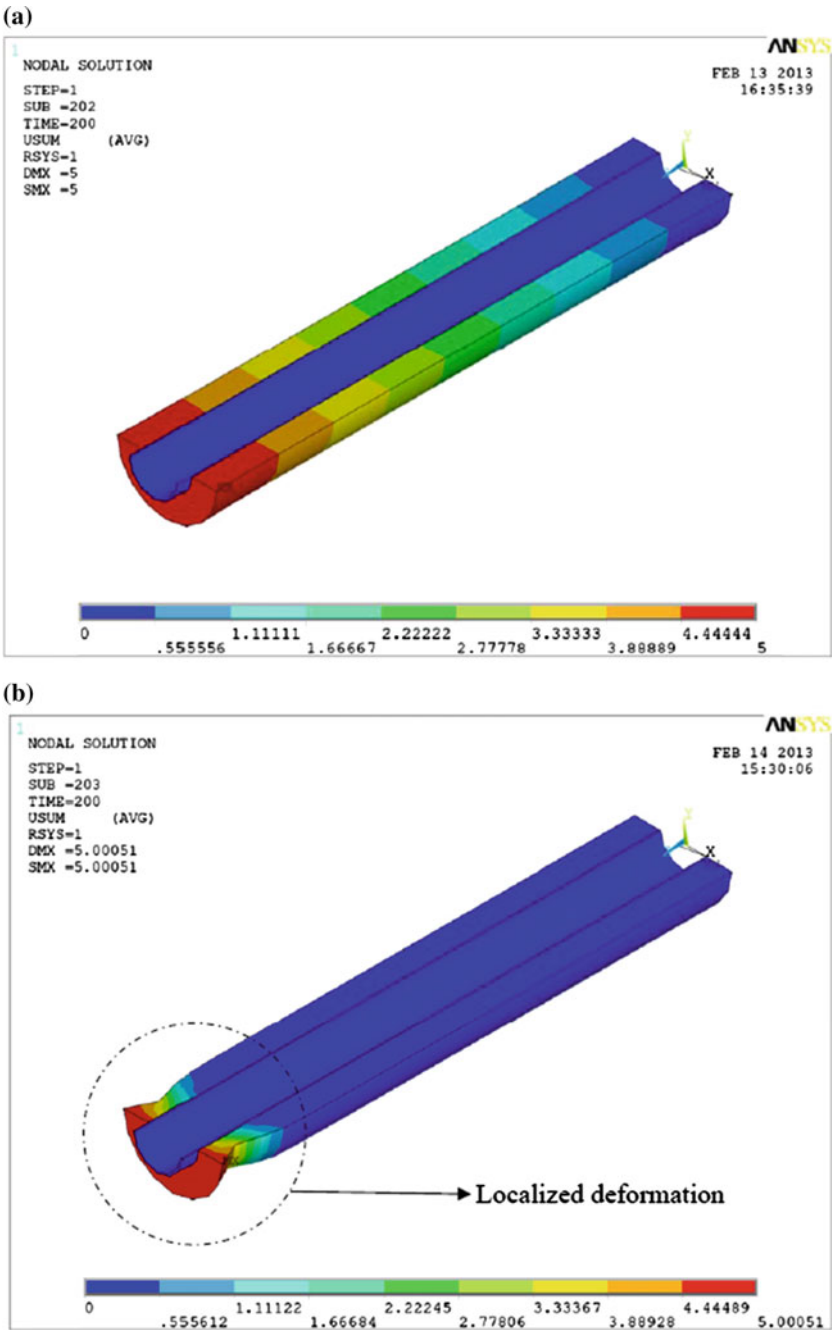

Fig. 10.28 Displacement vector sum for RVE with **a** disabled interface and **b** ISS = 10 MPa

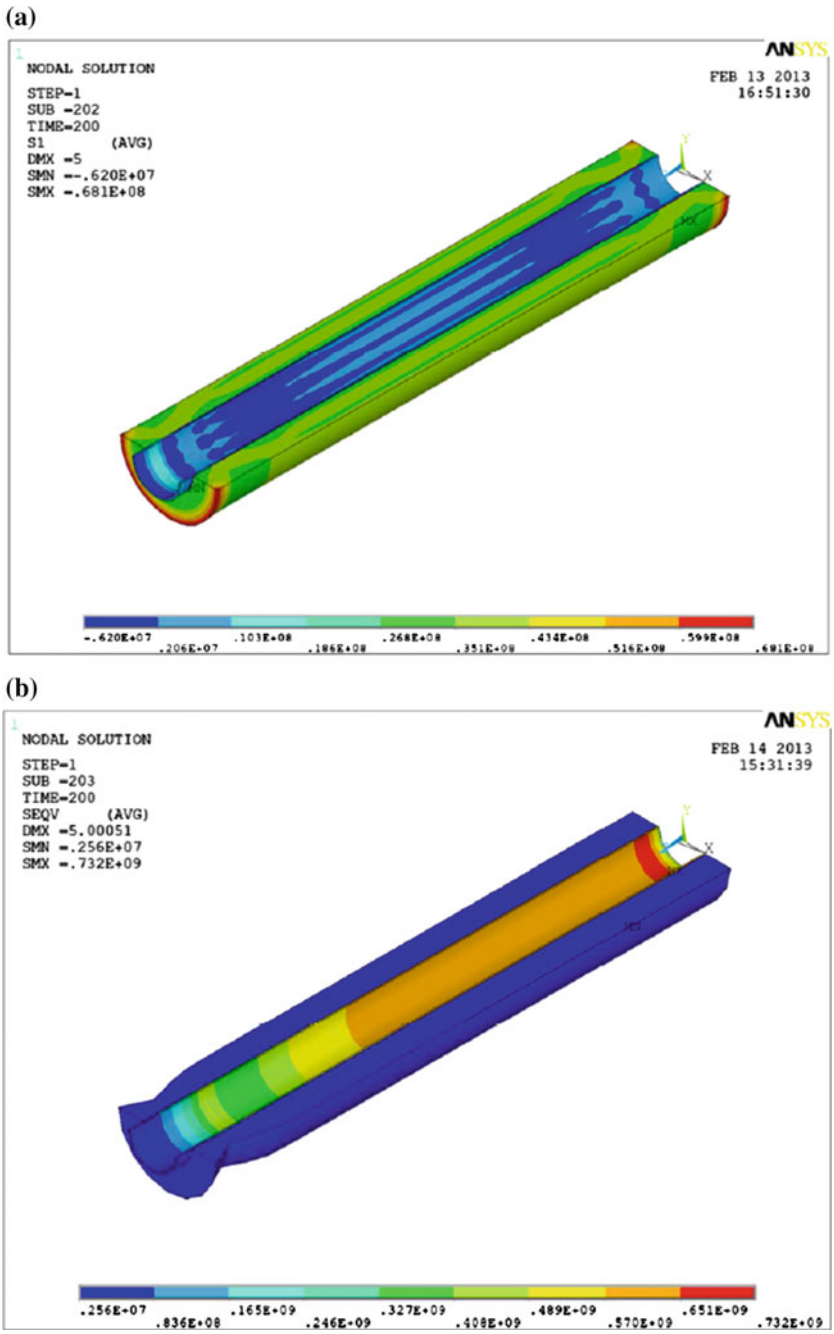

Fig. 10.29 Von Mises stress distribution in RVE with **a** disabled interface and **b** ISS = 10 MPa

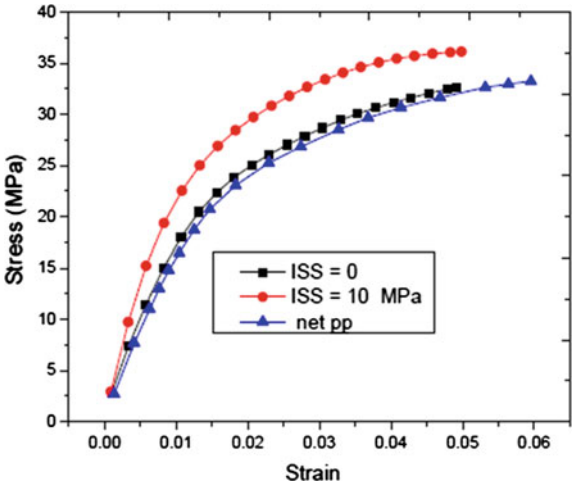

Fig. 10.30 Stress-strain curves of the long CNT/RVE with different interfacial strength

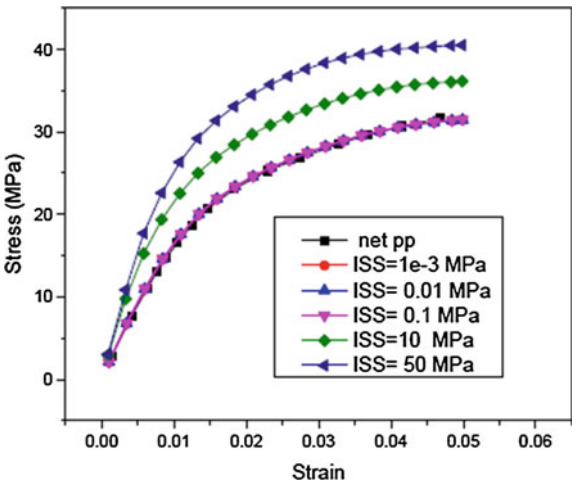

Fig. 10.31 Stress-strain curves of RVE containing long CNT as a function of the ISS value

Table 10.2 Computed Young's modulus and tensile strength for RVE with long CNT

ISS (MPa)	*E* (MPa)	Relative change (%)	σ_{uts} (MPa)	Relative change (%)
0.001	495	4.2	31.4	0.64
0.01	497	4.7	31.5	0.62
0.1	505	6.4	31.5	0.44
0	587	23.6	32.1	1.3
10	817	72.0	36.1	14.1
50	844	77.6	40.5	28.0

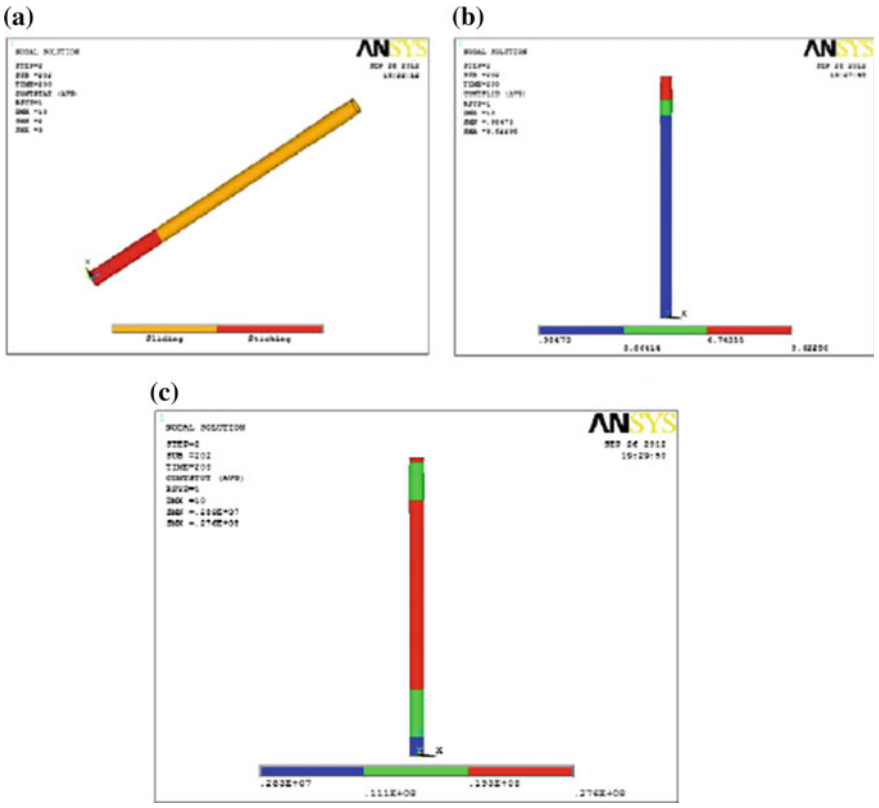

Fig. 10.32 **a** Contact status, **b** sliding distance at final step and **c** total stress at the interface at final load step

The results showed that the increases of the mechanical properties in axial direction were significant for different ISS values and even for small volume fraction of the CNT. For example, when ISS = 50 MPa, the composite modulus was 553 MPa which is 16 % higher than pure PP samples. It reveals that the increase of the stiffness of the composite can be significant in the CNT axial direction. Once again, very low interfacial strength leads to smaller Young's modulus and tensile strength. According to the results, there is no significant mechanical enhancement for the composite if the ISS value is below 1 MPa.

On the other hand, a comparison between mechanical improvement of RVEs containing long and short CNTs shows a noticeable difference. In all cases, long CNT results in higher Young's modulus and stress values in same strains. It means that reinforcement length plays a remarkable role in the composite stiffness, where longer CNTs with higher interfacial surface area lead to larger stiffness and elastic modulus. Although, presence of CNT in the matrix leads to better tensile strength in all cases, results showed that short CNT cannot be as effective as long CNT in a

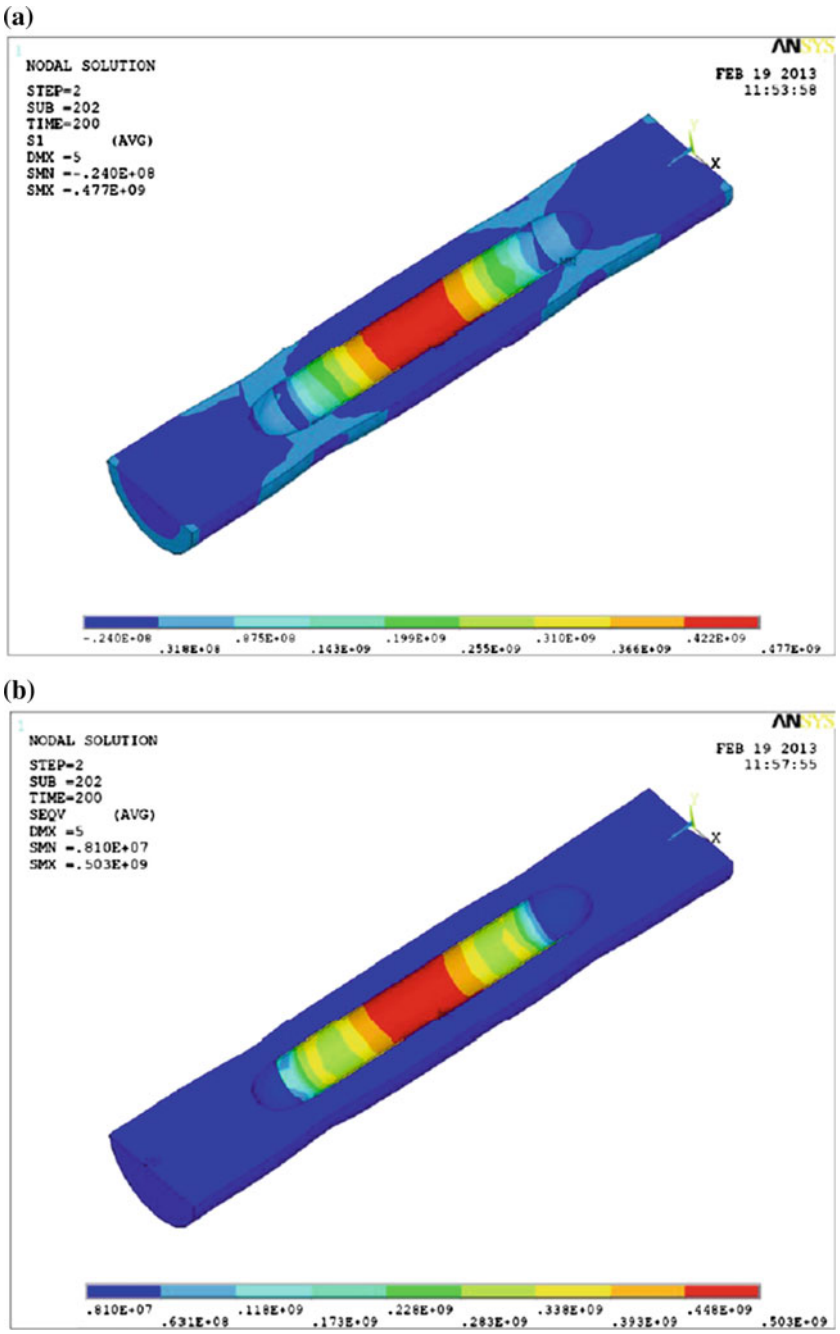

Fig. 10.33 First principal stress distribution in the RVE containing short CNT and ISS = 10 MPa

Table 10.3 Computed Young's modulus and tensile strength for RVE with short CNT

ISS (MPa)	*E* (MPa)	Relative change (%)	σ_{uts} (MPa)	Relative change (%)
0.001	480	1.1	24.0	0.13
0.01	481	1.3	24.3	7.7
0.1	494	4.0	24.4	7.9
0	534	12.6	24.4	13.7
10	543	14.2.0	25.1	14.3
50	553	16.4	28.3	15.7

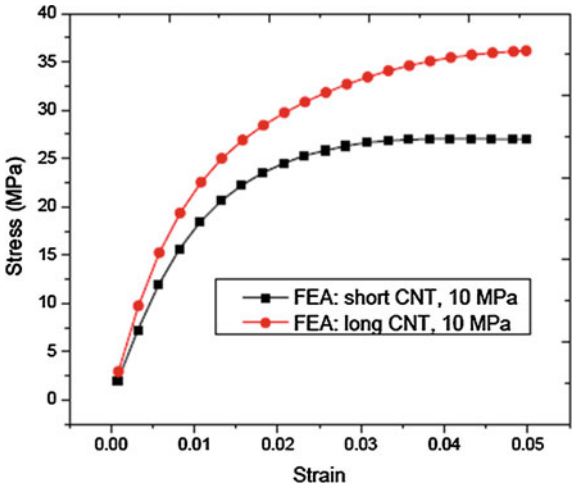

Fig. 10.34 Stress-strain curves of RVEs with ISS = 10 MPa

polymer matrix for reinforcing purposes. Figures 10.35 and 10.36 show the effect of ISS and CNT length on the mechanical response of RVEs.

It can be deduced from the results that the composite stiffness in the axial direction calculated from the rule of mixtures is not coincident with the FEM solutions which are based on nonlinear RVEs. Therefore, it seems the rule of mixtures equations could not be employed as an accurate tool to predict the Young's modulus of CNT-reinforced composites in the axial direction.

At this stage RVEs were built based on the nonlinearity of materials and cohesive zone interface. These RVEs were further used to estimate the tensile properties of CNT/PP composites in the axial direction. In this section for the convenience of comparison, the numerical results found by the FEM were validated by experimentally data. Although the proposed FEM is not completely accurate for stress distribution in the RVE, it is fairly accurate and efficient in predicting the composite properties in the axial direction of the RVEs. The main emphasis of the work was on the interfacial stress transfer issue which was addressed successfully through cohesive zone model.

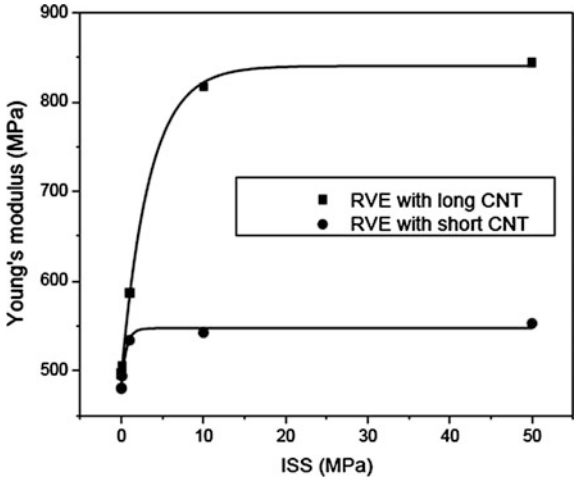

Fig. 10.35 Comparison between Young's modulus of RVEs containing long and short CNT

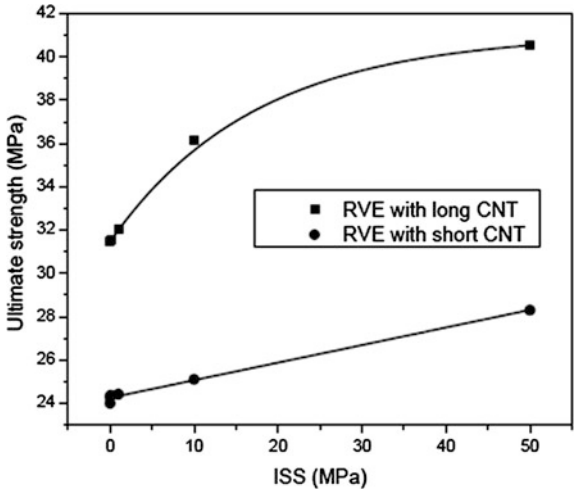

Fig. 10.36 Comparison between tensile strength of RVEs containing long and short CNT

The modelling results and experimental data were compared in terms of the stress-strain curve overall shape and material constants such as Young's modulus and tensile strength. Figure 10.37 shows stress-strain curves of functionalized MWCNTs/PP composites obtained from tensile tests for various amount of CNTs.

To compare experimental data with numerical results, weight percent of MWCNTs should be converted to volume percent. Therefore, bulk and true density of MWCNTs of 0.27 g/cm3 and 2.1 g/cm3 were taken into account, respectively. Table 10.4 shows weight to volume conversions used in this study.

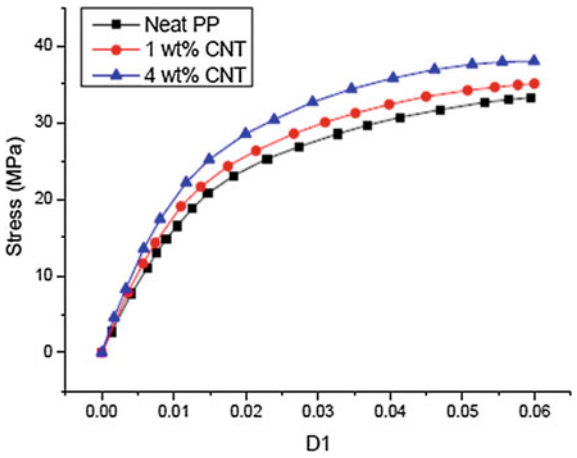

Fig. 10.37 Stress-strain plot of MWCNT/PP composites

Table 10.4 Percentage by weight to percentage by volume

Percentage by weight	Percentage by volume
0.5	0.23
1	0.45
2	0.91
3	1.37
4	1.84
5	2.32

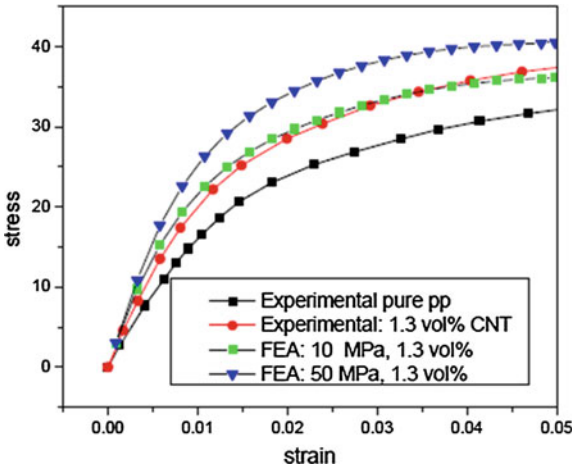

Fig. 10.38 Comparison between FEA results for long CNTs RVEs and experimental data

By using the Table 10.4, the experimentally obtained data were converted in a way in which they are comparable with theoretical results from FEM. Figure 10.38 shows a comparison between FEA results of RVE with long CNT and experimental data from tensile tests.

In case of RVEs with long CNT, it could be deduced that most of CNT effect will happen below 0.03 strain. However, for RVEs with short CNTs, reinforcing continued up to 0.05 strain.

Furthermore, RVEs with no interface shear strength illuminated similar tensile behavior of pure polymer samples. Although accounting for the imperfect CNT/PP contact leads to a reduced modulus of the composites comparing to perfect bonding case, the computational results still overestimate the modulus compared to the experimental values. It indicates that there are other experimentally observed characteristics including CNT agglomerates, poor CNT dispersion within the PP matrix and CNT alignment with respect to the applied load direction that should also be accounted for in the future computational analysis.

References

1. M.L. Jose-Yacaman, L. Rendon, J. Arenas, M.C.S. Puche, Maya blue paint: an ancient nanostructured material. Science **273**(5272), 223–225 (1996)
2. B.K.G. Theng, *Formation and Properties of Clay Polymer Complexes* (Elsevier, New York, 1979)
3. P.M. Ajayan, L.S. Schadler, P.V. Braun, *Nanocomposite Science and Technology* (Wiley, 2003)
4. Zhiting Tian, Hu Han, Ying Sun, A molecular dynamics study of effective thermal conductivity in nanocomposites. Int. J. Heat Mass Transfer **61**, 577 (2013)
5. S. Zhang, D. Sun, Y. Fu, H. Du, Recent advances of superhard nanocomposite coatings: a review. Surf. Coat. Technol. **167**(2–3), 13–119 (2003)
6. S. R. Bakshi, D. Lahiri, A. Argawal, *Carbon nanotube reinforced metal matrix composites—A Review*. Int. Mater. Rev. **55** (2010)
7. Evangelos Manias, Nanocomposites: stiffer by design. Nat. Mater. **6**(1), 9–11 (2007)
8. K. Lau, C. Gu, D. Hui, A critical review on nanotube and nanotube/nanoclay related polymer composite materials. Compos. B Eng. **37**, 425–436 (2006)
9. Z. Spitalsky, D. Tasis, K. Papagelis, C. Galiotis, Carbon nanotube–polymer composites: chemistry, processing, mechanical and electrical properties. Prog. Polym. Sci. **35**, 357–401 (2010)
10. S. Iijima, Helical microtubules of graphite carbon. Nature **354**, 56–58 (1991)
11. B.I. Yakobson, P. Avouris, Mechanical properties of carbon nanotubes. Topics Appl. Phys **80**, 287–327 (2001)
12. E.W. Wong, P.E. Sheehan, C.M. Lieber, Nanobeam mechanics: elasticity, strength, and toughness of nanorods and nanotubes. Science **277**, 1971–1975 (1997)
13. J.-P.B. Salvetat, G.A.D. Briggs, J.-M. Bonard, R.R. Bacsa, A.J. Kulik, T. Stöckli, N.A. Burnham, L. Forró, Elastic and shear moduli of single-walled carbon nanotube ropes. Phys. Rev. Lett. **82,** 944–947 (1999)
14. D.A. Walters, L.M. Ericson, M.J. Casavant, J. Liu, D.T. Colbert, K.A. Smith, R.E. Smalley, Elastic strain of freely suspended single-wall carbon nanotube ropes. Appl. Phys. Lett. **74**, 3803–3805 (1999)
15. H. Wan, F. Delale, A structural mechanics approach for predicting the mechanical properties of carbon nanotubes. Meccanica **45**, 43–51 (2009)
16. X.L.C.Y.J. Liu, Evaluations of the effective material properties of carbon nanotube-based composites using a nanoscale representative volume element. Mech. Mater. **35**, 9–81 (2003)
17. M.S. Dresselhaus, G. Dresselhaus, R. Saito, Physics of carbon nanotubes. Carbon **33**, 883–891 (1995)

18. G.M. Odegarda, T.S. Gatesb, L.M. Nicholsonc, K.E. Wised, Equivalent-continuum modeling of nano-structured materials. Composites Science and Technology **62**, 1869–1880 (2002)
19. C. Li, A structural mechanics approach for the analysis of carbon nanotubes. Int. J. Solids Struct. **40**, 2487–2499 (2003)
20. X.L. Chen, Y.J. Liu, Square representative volume elements for evaluating the effective material properties of carbon nanotube-based composites. Comput. Mater. Sci. **29**, 1–11 (2004)
21. R. Andrews, D. Jacques, D. Qian et al., Purification and structural annealing carbon nanotubes at graphitization temperatures. Carbon **39**, 1681 (2001)
22. T. Gates, G. Odegard, S. Frankland, T. Clancy, Computational materials: multi-scale modeling and simulation of nanostructured materials. Compos. Sci. Technol. **65**, 2416–2434 (2005)
23. D.B. Mawhinney, V. Naumenko, A. Kuznetsova et al., Surface defect site density on single walled carbon nanotubes by titration. Chem. Phys. Lett. **6**, 213 (2000)
24. A. Desai, M. Haque, Mechanics of the interface for carbon nanotube–polymer composites. Thin-Walled Struct. **43**, 1787–1803 (2005)
25. C.A. Cooper, S.R. Cohen, A.H. Barber, H.D. Wagner, Detachment of nanotubes from a polymer matrix. Appl. Phys. Lett. **81**, 3873–3875 (2002)
26. D. Qian, E.C. Dickey, Load transfer and deformation Mechanisms in carbon nanotube-polystyrene composites. Phys. Lett. **76** (2000)
27. A. Fereidoon, E. Saeedi, B. Ahmadimoghadam, in *World Congress on Engineering,* pp. 1381–1385. Comparison between different finite element methods for foreseeing the elastic properties of carbon nanotube reinforced epoxy resin composite, 2008
28. K. Tserpes, P. Papanikos, G. Labeas, S. Pantelakis, Multi-scale modeling of tensile behavior of carbon nanotube-reinforced composites. Theoret. Appl. Fract. Mech. **49**, 51–60 (2008)
29. J. Gou, B. Minaie, B. Wang, Z. Liang, C. Zhang, Computational and experimental study of interfacial bonding of single-walled nanotube reinforced composites. Comput. Mater. Sci. **31**, 225–236 (2004)
30. C. Li, T.-W. Chou, Elastic moduli of multi-walled carbon nanotubes and the effect of van der Waals forces. Compos. Sci. Technol. **63**, 1517–1524 (2003)
31. I. Janowska, S. Hajiesmaili, D. Bégin, V. Keller, N. Keller, M.-J. Ledoux et al., Macronized aligned carbon nanotubes for use as catalyst support and ceramic nanoporous membrane template. Catal. Today **145**, 76–84 (2009)
32. M.R. Piggott, *Load Bearing Fibre Composites* (Kluwer Academic Publications, 2002)
33. M.W. Hyer, S.R. White, *Stress analysis of fiber-reinforced composite materials* (DEStech Publications, Inc, 2009)
34. Release, A. N. S. Y. S. 12.0. *ANSYS Theory Reference* (2009)
35. H. Jiang, P. Zhang, B. Liu, Y. Huang, P.H. Geubelle, H. Gao, The effect of nanotube radius on the constitutive model for carbon nanotubes. Comput. Mater. Sci. **28**, 429–442 (2003)
36. M.A. Bhuiyan, R.V. Pucha, M. Karevan, K. Kalaitzidou, Tensile modulus of carbon nanotube/polypropylene composites—A computational study based on experimental characterization. Comput. Mater. Sci. **50**, 2347–2353 (2011)
37. E.J. Hearn, *Mechanics of materials 2: The mechanics of elastic and plastic deformation of solids and structural materials,* vol. 2 (Butterworth-Heinemann, 1997)
38. E. Mohammadpour, Numerical and experimental evaluation of carbon nanotube/polypropylene composites using nonlinear finite element modeling (PhD Thesis, Universiti Teknologi Petronas, 2013)
39. S. Nemat-Nasser, M. Hori, M*icromechanics: overall properties of heterogeneous materials* Second Revised ed (Elsevier, 1999)
40. S.K. Georgantzinos, G.I. Giannopoulos, N.K. Anifantis, Numerical investigation of elastic mechanical properties of graphene structures. Mater. Des. **31**, 4646–4654 (2010)
41. P.K. Valavala, G.M. Odegard, Modeling techniques for determination of mechanical properties of polymer nanocomposites. Rev. Adv. Mater. Sci. **9**, 34–44 (2005)
42. M.M. Shokrieh, R. Rafiee, Prediction of Young's modulus of graphene sheets and carbon nanotubes using nanoscale continuum mechanics approach. Mater. Des. **31**, 790–795 (2010)

43. K.H. Kim, W.H. Jo, A strategy for enhancement of mechanical and electrical properties of polycarbonate/multi-walled carbon nanotube composites. Carbon **47**, 1126–1134 (2009)
44. J.-P. Salvetat-Delmottea, A. Rubioc, Mechanical properties of carbon nanotubes a fiber digest for beginners. Carbon **40**, 1729–1734 (2002)
45. T. Ogasawara, T. Tsuda, N. Takeda, Stress–strain behavior of multi-walled carbon nanotube/PEEK composites. Compos. Sci. Technol. **71**, 73–78 (2011)
46. P.-C. Ma, N.A. Siddiqui, G. Marom, J.-K. Kim, Dispersion and functionalization of carbon nanotubes for polymer-based nanocomposites: a review. Compos. A Appl. Sci. Manuf. **41**, 1345–1367 (2010)